

# Multivariable High-Precision Motion Control

## with Structured Modeling and Data-Driven Convex Optimization



**Masahiro Mae**



# Doctoral Dissertation

博士論文

## Multivariable High-Precision Motion Control with Structured Modeling and Data-Driven Convex Optimization

(構造的モデル化とデータ駆動凸最適化による  
多変数超精密位置決め制御)

**Masahiro Mae**

37-207078 前 匡鴻

Dissertation Submitted to

**Department of Electrical Engineering and Information Systems**

for the Degree of

**Doctor of Philosophy**

at

**The University of Tokyo**



**December 2022**

Supervisor

**Professor Hiroshi Fujimoto**





# Contents

<b>I</b>	<b>Introduction</b>	<b>1</b>
<b>1</b>	<b>Multivariable High-Precision Motion Control in Industrial Applications</b>	<b>3</b>
1.1	Advanced motion control in industrial applications . . . . .	3
1.2	Background of multivariable motion control . . . . .	5
1.3	Concept of multivariable high-precision motion control . . . . .	10
1.4	Contributions . . . . .	15
1.5	Outline of the dissertation . . . . .	16
<b>II</b>	<b>Multirate Feedforward Control in Multivariable Motion Systems</b>	<b>19</b>
<b>2</b>	<b>Multirate Feedforward Control with Non-Causal Inversion and Mode Selection</b>	<b>21</b>
2.1	Introduction . . . . .	21
2.2	Problem formulation . . . . .	22
2.3	Desired state trajectory generation . . . . .	25
2.4	Multirate feedforward control with mode decomposition . . . . .	29
2.5	Application to multi-modal motion system . . . . .	34
2.6	Conclusion . . . . .	41
<b>3</b>	<b>MIMO Multirate Feedforward Control with Generalized Controllability Indices</b>	<b>43</b>
3.1	Introduction . . . . .	43
3.2	Problem formulation . . . . .	45
3.3	Single-rate feedforward control for multi-input multi-output system . . . . .	46
3.4	Multirate feedforward control for multi-input multi-output system . . . . .	47
3.5	Comparison for intersample behavior analysis . . . . .	53
3.6	Application to MIMO motion system . . . . .	56
3.7	Conclusion . . . . .	60
<b>III</b>	<b>Fixed-Structure Sampled-Data Feedforward and Learning Control</b>	<b>61</b>
<b>4</b>	<b>Linearly Parameterized Feedforward Control with Sampled-Data Differentiator</b>	<b>63</b>
4.1	Introduction . . . . .	63
4.2	Problem formulation . . . . .	64
4.3	Structured feedforward using multirate zero-order-hold differentiator . . . . .	68
4.4	Comparison with multirate feedforward control . . . . .	72
4.5	Application to multi-modal motion system . . . . .	75

4.6	Conclusion . . . . .	77
<b>5</b>	<b>Iterative Learning Control with MIMO Sampled-Data Basis Functions</b>	<b>79</b>
5.1	Introduction . . . . .	79
5.2	Problem formulation . . . . .	80
5.3	Basis function design using multirate zero-order-hold differentiator . . . . .	82
5.4	Iterative learning control with MIMO structured basis functions . . . . .	86
5.5	Application to MIMO motion system . . . . .	89
5.6	Conclusion . . . . .	94
<b>IV</b>	<b>Feedback Controller Design using Frequency Response Data</b>	<b>95</b>
<b>6</b>	<b>Disturbance Rejection with Robust Performance in Dual-Stage Actuator</b>	<b>97</b>
6.1	Introduction . . . . .	97
6.2	Problem formulation . . . . .	98
6.3	Convex optimization of multiple resonant filters . . . . .	100
6.4	Application to dual-stage actuator hard disk drive . . . . .	103
6.5	Conclusion . . . . .	109
<b>7</b>	<b>Disturbance Rejection with Robust Stability in MIMO Motion Systems</b>	<b>111</b>
7.1	Introduction . . . . .	111
7.2	Problem formulation . . . . .	113
7.3	Convex optimization of rational peak filter . . . . .	116
7.4	Application to MIMO high-precision scan stage . . . . .	120
7.5	Conclusion . . . . .	127
<b>V</b>	<b>Closing</b>	<b>129</b>
<b>8</b>	<b>Conclusion</b>	<b>131</b>
	<b>Bibliography</b>	<b>135</b>
	<b>Publications</b>	<b>147</b>
	<b>Abstract (in Japanese)</b>	<b>153</b>
	<b>Acknowledgment (in Japanese)</b>	<b>157</b>
	<b>Curriculum Vitae</b>	<b>159</b>

# **Part I**

## **Introduction**



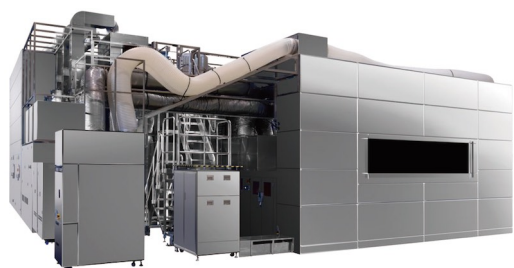
# Chapter 1

## Multivariable High-Precision Motion Control in Industrial Applications

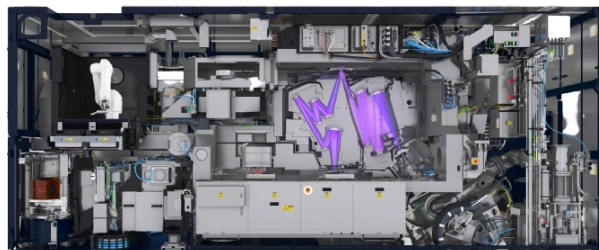
### 1.1 Advanced motion control in industrial applications

Control engineering is a hidden technology although in many industrial applications. Technology has an important role in modern society and many of them are based on control engineering. Control technologies are developed in both academics and industries, and bridging the gap between academics and industries makes a large impact on industrial development. Advanced motion control has an important role in the increasing demand for mechatronic systems in industrial applications such as shown in Fig. 1.1. FPD lithography system in Fig. 1.1(a) [1] and semiconductor lithography systems in Fig. 1.1(b) [2] are fundamentals of modern information societies and are used to manufacture PCs and smartphones. The accuracy of the high-precision stages in lithography systems directly leads to the improvement of the performance of semiconductors known as Moore's law [3]. Machine tools in Fig. 1.1(c) [4] and industrial robots in Fig. 1.1(d) [5] are widely used in industrial manufacturing processes such as making automobiles. The accuracy and task flexibility enable the manufacturing of high-value-added products with small quantities and large variety. Printers in Fig. 1.1(e) [6] are also used for modern manufacturing processes not only printing on paper but also additive manufacturing. Printing can be used to make an electric circuit and additive manufacturing technology is paid attention to space development. Hard disk drives in Fig. 1.1(f) [7] enable a modern information society based on big data. The accuracy of the magnetic head makes the volume of the data storage larger. Motor drives that are used in air conditioners Fig. 1.1(g) [8] and electric vehicles in Fig. 1.1(h) [9] make human life comfortable. The improvement of the current control in motor drives leads to both better performance and efficiency [10, 11]. Electric vehicles with in-wheel motors are paid attention to the degree-of-freedom of control that can be used to improve ride comfort [9, 12]. The control performance directly results in product quality and the controllers should be designed considering the limitation and requirements in actual setups and applicability for on-site engineers who implement these control techniques.

In most industrial applications, linear control is widely used because of the connection between theories and applications, and ease of implementation. The history of the linear control is shown in Fig. 1.2 [13]. Since the 1930s, classical control has been developing. Classical control is based on the frequency domain and the systems are represented in a transfer function. Classical control such as the Proportional–Integral–Derivative (PID) controller is intuitive for engineering skills



(a) FPD lithography system [1].



(b) Semiconductor lithography system [2].



(c) Machine tools [4].



(d) Industrial robot [5].



(e) Printer [6].



(f) Hard disk drive [7].



(g) Air conditioner [8].



(h) Electric vehicle [9].

Fig. 1.1: Mechatronic systems in industrial applications.

and is the most widely used in industrial applications. Since the 1960s after World War II, modern control has been developing. Modern control is based on the time domain and the systems are represented in state space. The development of modern control is connected to the development of computers that enables real-time optimization. Kalan filter which is widely for state estimation is developed during the Cold War and is said to be implemented in spacecraft in the Apollo program. Since the 1980s, robust control has been developing. It is because modern control with optimization is difficult to guarantee robust stability. Robust control models the uncertainty and considers it in controller design, and it is one of the uniqueness of control engineering. Although robust control has guaranteed robust stability, the controller can be designed conservatively and the performance is not enough in many applications.

To achieve both robust stability and robust performance, several advanced control approaches have been developed. Multivariable control [14] is developed for complex systems with many degree-of-freedom (DOFs) and considers the interaction. Sampled-data control [15] is the approach to minimize the gap between discrete-time implementation and continuous-time controlled system. Model predictive control [16] is used for the controlled system that needs real-time optimization with constraints. In summary, advanced motion control approaches are developed to improve the performance of industrial applications.

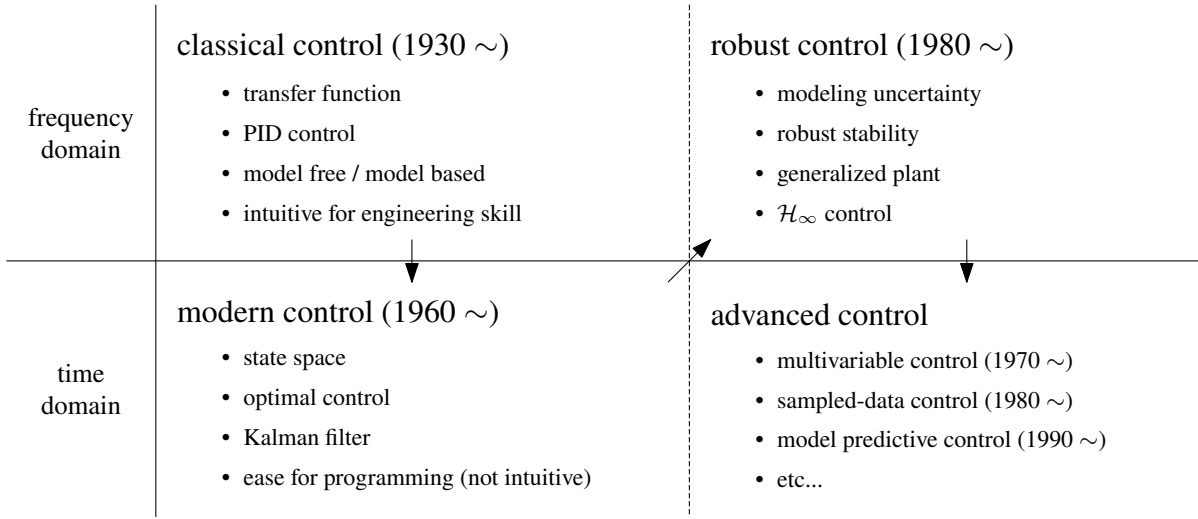


Fig. 1.2: History of linear control.

## 1.2 Background of multivariable motion control

To improve control performance, industrial mechatronic systems tend to be complicated and be extended from single-input single-output (SISO) systems to multi-input multi-output (MIMO) systems. As an example, the six-degree-of-freedom high-precision scan stage in the FPD lithography system is shown in Fig. 1.3. To make the tracking error of the high-precision scan stage in nm scale, multivariable motion control is applied. The basic controller design procedure for multivariable systems is as follows.

1. interaction analysis: choose the input and output pairs that are mainly used for control.
2. static decoupling: make the system diagonally dominant by using input and output decoupling matrix with real static values.
3. decentralized control: design the controllers diagonally with ensuring MIMO stability.

To deal with multivariable dynamics in controller design, several properties of multivariable systems should be considered.

### 1.2.1 Analysis of multivariable systems

To analyze the dynamics of multivariable systems, the basic properties such as pole and zeros, stability, and interaction are described [14].

The  $n_u$ -inputs  $n_y$  outputs  $n^{\text{th}}$  order continuous-time linear time-invariant system  $\mathbf{G}$  is given by

$$\mathbf{G} \stackrel{s}{=} \left[ \begin{array}{c|c} \mathbf{A} & \mathbf{B} \\ \hline \mathbf{C} & \mathbf{D} \end{array} \right] = \mathbf{C}(s\mathbf{I} - \mathbf{A})^{-1}\mathbf{B} + \mathbf{D} = \mathbf{C} \frac{\text{adj}(s\mathbf{I} - \mathbf{A})}{\det(s\mathbf{I} - \mathbf{A})} \mathbf{B} + \mathbf{D}, \quad (1.1)$$

where  $\mathbf{A} \in \mathbb{R}^{n \times n}$ ,  $\mathbf{B} \in \mathbb{R}^{n \times n_u}$ ,  $\mathbf{C} \in \mathbb{R}^{n_y \times n}$ , and  $\mathbf{D} \in \mathbb{R}^{n_y \times n_u}$ .  $\mathbf{G}$  is assumed to be controllable and observable and is given by minimal realization.

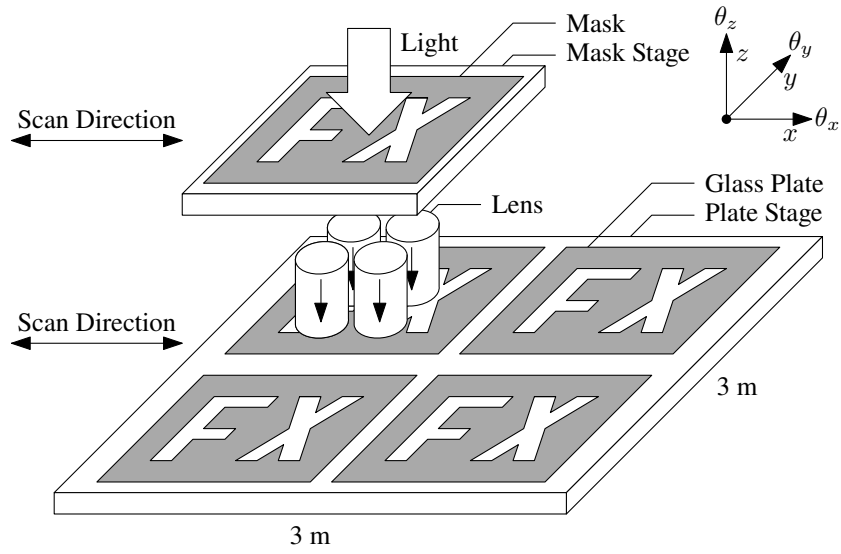


Fig. 1.3: A six-degree-of-freedom high-precision scan stage in an FPD lithography system.

The Smith-McMillan form of the system  $\mathbf{G}$  is given by

$$\mathbf{M}(s) = \mathbf{U}_1(s)\mathbf{G}(s)\mathbf{U}_2(s) = \begin{bmatrix} \frac{n_1(s)}{d_1(s)} & & & \mathbf{O} \\ & \ddots & & \\ & & \frac{n_r(s)}{d_r(s)} & \\ \mathbf{O} & & & \mathbf{O} \end{bmatrix}, \quad (1.2)$$

where  $\mathbf{U}_1$  and  $\mathbf{U}_2$  are unimodular,  $n_i$  and  $d_i$  are coprime, and  $r$  is the normal rank of  $\mathbf{G}$ .

### Poles

In the state space, the poles are defined as follows.

**Definition 1.1** (Poles in state space) : *The poles  $p_i$  of a system  $\mathbf{G}$  in state-space realization are the eigenvalues  $\lambda_i(\mathbf{A})$  ( $i = 1, \dots, n$ ) of the state matrix  $\mathbf{A}$ . The poles are the roots of the pole polynomial*

$$\phi(s) = \det(s\mathbf{I} - \mathbf{A}) = 0. \quad (1.3)$$

In the transfer function, the poles are defined as follows.

**Definition 1.2** (Poles in transfer function) : *The pole polynomial  $\phi(s)$  corresponding to a minimal realization of a system with transfer function  $\mathbf{G}(s)$  is the least common denominator of all non-identically zero minors of all orders of  $\mathbf{G}$ . The poles are the roots of the pole polynomial*

$$\phi(s) = \prod_{i=1}^r d_i(s) = 0. \quad (1.4)$$



### Zeros

In the state space, the zeros are defined as follows.

**Definition 1.3** (Zeros in state space) : *The system  $\mathbf{G}$  is given by*

$$\mathbf{\Pi}(s) \begin{bmatrix} \mathbf{x}(s) \\ \mathbf{u}(s) \end{bmatrix} = \begin{bmatrix} \mathbf{0} \\ \mathbf{y}(s) \end{bmatrix}, \quad (1.5)$$

where the Rosenbrock system matrix  $\mathbf{\Pi}(s)$  is defined as

$$\mathbf{\Pi}(s) = \begin{bmatrix} \mathbf{A} - s\mathbf{I} & \mathbf{B} \\ \mathbf{C} & \mathbf{D} \end{bmatrix} = \begin{bmatrix} \mathbf{A} & \mathbf{B} \\ \mathbf{C} & \mathbf{D} \end{bmatrix} - s \begin{bmatrix} \mathbf{I} & \mathbf{O} \\ \mathbf{O} & \mathbf{O} \end{bmatrix}. \quad (1.6)$$

The transmission zeros are the values for which the Rosenbrock system matrix loses rank.

Note that if  $\mathbf{D}$  is invertible, then

$$\begin{aligned} \det \left( \begin{bmatrix} \mathbf{A} - s\mathbf{I} & \mathbf{B} \\ \mathbf{C} & \mathbf{D} \end{bmatrix} \right) &= \det \left( \begin{bmatrix} \mathbf{A} - s\mathbf{I} & \mathbf{B} \\ \mathbf{C} & \mathbf{D} \end{bmatrix} \begin{bmatrix} \mathbf{I} & \mathbf{O} \\ -\mathbf{D}^{-1}\mathbf{C} & \mathbf{I} \end{bmatrix} \right) \\ &= \det \left( \begin{bmatrix} (\mathbf{A} - \mathbf{B}\mathbf{D}^{-1}\mathbf{C}) - s\mathbf{I} & \mathbf{B} \\ \mathbf{O} & \mathbf{D} \end{bmatrix} \right). \end{aligned} \quad (1.7)$$

Since  $\mathbf{D}$  is invertible, the transmission zeros are eigenvalues of  $\mathbf{A} - \mathbf{B}\mathbf{D}^{-1}\mathbf{C}$ .

In the transfer function, the zeros are defined as follows.

**Definition 1.4** (Zeros in transfer function) : *The zero polynomial  $\psi(s)$ , corresponding to a minimal realization of the system, is the greatest common divisor of all the numerators of all order  $r$  minors of  $\mathbf{G}(s)$ , where  $r$  is the normal rank of  $\mathbf{G}$ , provided that these minors have been adjusted in such a way as to have the pole polynomial  $\phi(s)$  as their denominator. The transmission zeros are the roots of the zero polynomial*

$$\psi(s) = \prod_{i=1}^r n_i(s) = 0. \quad (1.8)$$

### Stability

For the parametric model of the system, the stability of the system is determined by the poles.

**Definition 1.5** : *A linear dynamic system  $\dot{\mathbf{x}}(t) = \mathbf{A}\mathbf{x}(t) + \mathbf{B}\mathbf{u}(t)$  is stable if and only if all the poles are in the open left-half plane (LHP); that is,  $\text{Re}(p_i) = \text{Re}(\lambda_i(\mathbf{A})) < 0, \forall i$ .*

For the non-parametric model of the system such as frequency response data, the stability of the system is analyzed by Nyquist stability criteria. Let  $\mathbf{L}(s)$  be the open-loop transfer function matrix, Nyquist plot is given by an image of  $\det(\mathbf{I} + \mathbf{L}(s))$  as  $s$  goes clockwise around the Nyquist  $\mathcal{D}$ -contour in Fig. 1.4. In multivariable systems, the necessary and sufficient condition of the stability is defined in generalized (MIMO) Nyquist theorem and Eigenvalue Loci.

**Definition 1.6** (Generalized (MIMO) Nyquist theorem) : *Let  $P_{ol}$  denote the number of open-loop unstable poles in  $\mathbf{L}(s)$ . The closed-loop system with  $\mathbf{L}(s)$  and negative feedback is stable if and only if the Nyquist plot of  $\det(\mathbf{I} + \mathbf{L}(s))$*

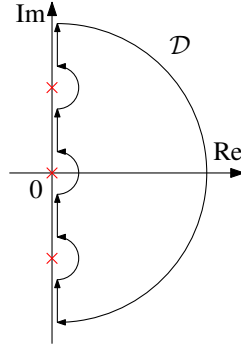


Fig. 1.4: Nyquist  $\mathcal{D}$ -contour.  $\times$  shows the poles on the imaginary axis.

- (i) makes  $P_{ol}$  anti-clockwise encirclements of the origin, and
- (ii) does not pass through the origin.

**Definition 1.7** (Eigenvalue loci) : Let  $P_{ol}$  denote the number of open-loop unstable poles in  $\mathbf{L}(s)$ . The closed-loop system with  $\mathbf{L}(s)$  and negative feedback is stable if and only if the characteristic loci  $1 + \lambda_i(j\omega)$ , taken together

- (i) makes  $P_{ol}$  anti-clockwise encirclements of the origin, and
- (ii) does not pass through the origin.

### Interaction

Relative Gain Array (RGA) of a non-singular square complex matrix  $\mathbf{G}$  is a square complex matrix defined as

$$\mathbf{A}(\mathbf{G}) \triangleq \mathbf{G} \circ (\mathbf{G}^{-1})^T, \quad (1.9)$$

where  $\circ$  is Hadamard product which means element-wise multiplication. The RGA is independent of input and output scaling and its rows and columns sum to 1. It is preferred to pair such that the rearranged system, with the selected pairings along the diagonal, has an RGA matrix close to identity around the frequencies of interest, and should avoid pairing on negative steady-state RGA elements.

The interaction index  $\lambda(j\omega)$  for the system  $\mathbf{G}$  is defined as a maximum eigenvalue of  $\mathbf{M}(j\omega|\mathbf{G})$ , where the matrix  $\mathbf{M}(j\omega|\mathbf{G})$  is given by

$$\mathbf{M}(j\omega|\mathbf{G}) = \begin{cases} 0 & (j = i) \\ \left| \frac{G_{ji}(j\omega)}{G_{ii}(j\omega)} \right| & (j \neq i) \end{cases}. \quad (1.10)$$

The interaction index is small if the system is diagonally dominant in that frequency. The radius  $r_i$  of the generalized Gershgorin bands in the axis  $i$  for the system  $\mathbf{G}$  with the diagonal feedback controller  $\mathbf{K}$  is given by

$$r_i(j\omega) = \lambda(j\omega) |G_{ii}(j\omega)K_{ii}(j\omega)|. \quad (1.11)$$

The open-loop frequency response of each axis  $i$  may move within the radius at each frequency point on the SISO Nyquist plot when MIMO systems have an interaction between each axis.

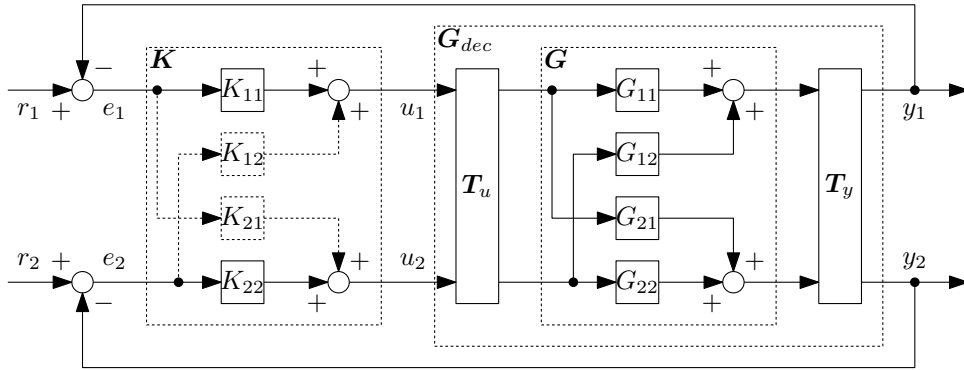


Fig. 1.5: Block diagram of the feedback control in the dual-input dual-output system.

### 1.2.2 Controller design for multivariable systems

The control strategy for multivariable systems is described in the example of the dual-input dual-output system that is shown in Fig. 1.5.

#### Static decoupling

In the decoupling process, static decoupling is basically used and the input decoupling matrix  $T_u$  and the output decoupling matrix  $T_y$  are designed as the static real value matrix to make the decoupled system  $T_y G T_u$  diagonally dominant so that the RGA is close to identity around the frequencies of interest. Dynamic decoupling that means  $T_u$  and  $T_y$  have dynamics also can be designed. Although the dynamic decoupling enables the perfect decoupling such as  $T_y G T_u = I$  in all frequencies, the dynamic decoupling may be very sensitive to modeling errors and uncertainties, and it is not recommended to use the dynamic decoupling in practice. If the system  $G$  is non-square, the Singular Value Decomposition (SVD)  $G_0 = U \Sigma V^T$  can be used as the input decoupling matrix  $T_u = V$  and the output decoupling matrix  $T_y = U^T$  where  $G_0$  is a real approximation of  $G(j\omega_0)$  at a frequency of interest  $\omega_0$ .

#### Decentralized control

After the decoupling process, the decentralized controller is basically designed for the diagonally dominant square system  $G_{dec} = T_y G T_u$ . In decentralized control, the off-diagonal term of the controller in Fig. 1.5 is  $K_{12} = K_{21} = 0$ . Decentralized control has the advantage that the diagonal term of the controller  $K_{11}$  and  $K_{22}$  is physically intuitive for the meaning of each axis and can be designed by the SISO controller design approach. Centralized control is also the approach for the feedback controller design of multivariable systems. In centralized control, off-diagonal term of the controller in Fig. 1.5 is  $K_{12} \neq 0$  and  $K_{21} \neq 0$ . Although centralized control has more degree of freedom for controller design and can actively change the interaction dynamics, the physical meaning of the controller is not intuitive and has difficulty in the tuning process. Note that decentralized control is normally used in the static-decoupled system that is diagonally dominant in low-frequency dynamics such as industrial mechatronic systems. The concept of decentralized control is extended to glocal control [17, 18] that can be applied to large-scale multivariable systems with interacted subsystems such as multi-agent dynamical systems and hierarchical networked systems.

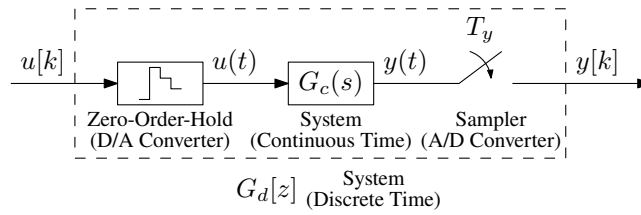


Fig. 1.6: Block diagram of the discretized system with sampler and zero-order-hold.

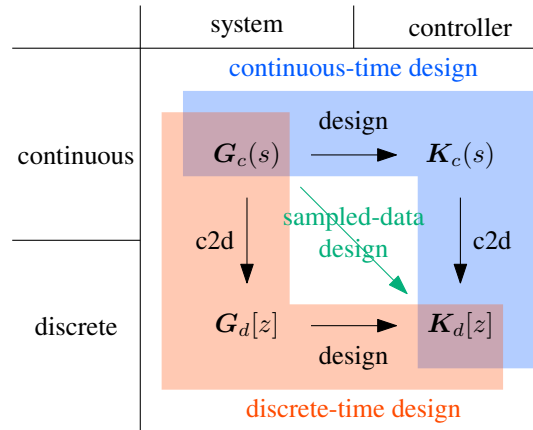


Fig. 1.7: Sampled-data controller design.

## 1.3 Concept of multivariable high-precision motion control

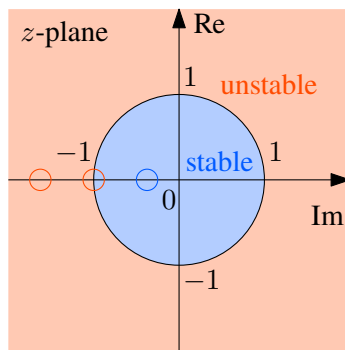
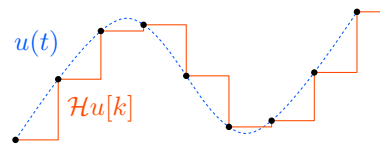
In the dissertation, the multivariable high-precision motion control is characterized by two concepts that are “sampled-data controller design for intersample performance” and “data-driven controller design with structured modeling”.

### 1.3.1 Sampled-data controller design for intersample performance

The designed controllers are implemented to actual setups in discrete time as shown in Fig. 1.6. Due to discretization, there is a performance limitation because of the sampling time. Fig. 1.7 shows the controller design methods in sampled-data systems. In the controller design for sampled-data systems, there are three controller design approaches that are continuous-time, discrete-time, and sampled-data design. In the continuous-time design, the continuous-time controller is designed for the continuous-time model and the discrete-time controller is designed by discretizing the designed continuous-time controller. Although the continuous-time design is simple and physically intuitive, it is difficult to consider the effect of discretization by sampler and zero-order-hold. In the discrete-time design, the discrete-time model is provided by discretizing the continuous-time model and the discrete-time controller is designed for the discrete-time model. Although the discrete-time design considers the effect of discretization by sampler and zero-order-hold, the designed controller ignores the continuous-time dynamics of the controlled system. Compared to the continuous-time and discrete-time design, the discrete-time controller is designed for the continuous-time model in the sampled-data design and it considers both the continuous-time dynamics of the controlled system and the effect of discretization by sampler and zero-order-hold. In high-precision motion control applications, the sampled-data controller

Table 1.1: Zeros of Euler-Frobenius polynomial [19].

relative degree	discretization zeros
2	-1
3	$-2 - \sqrt{3}, 1/(-2 - \sqrt{3})$
4	$-5 - 2\sqrt{6}, -1, 1/(-5 - 2\sqrt{6})$
$\vdots$	$\vdots$

(a) Discretization zeros on  $z$ -plane.

(b) Signal with zero-order-hold.

Fig. 1.8: Effect of discretization with sampler and zero-order-hold.

design is necessary to improve continuous-time tracking performance.

In a two-degree-of-freedom control approach, the feedforward controller is designed for tracking performance and the feedback controller is designed for disturbance rejection. The feedforward controller design is based on the model inversion and the feedforward controller becomes unstable when the model has nonminimum-phase zeros. The nonminimum-phase zeros are on the closed right-half plane (RHP) of  $s$ -plane in continuous time and on the outside of the closed unit circle of  $z$ -plane in discrete time. The challenge of the feedforward controller design is that the model discretized by sampler and zero-order-hold (ZOH) can have discretization zeros including nonminimum-phase zeros depending on the relative degree of the continuous-time model that is known as Euler-Frobenius polynomial in Table 1.1. Table 1.1 shows that the discretization zeros when the relative degree of the continuous-time model is more than 2. For example, the discretization zeros when the relative degree of the continuous-time model is 4 are shown in Fig. 1.8(a). Fig. 1.8(b) shows the constraint of the control input signal due to zero-order-hold. The difficulty of the zero-order-hold control input is that the discretization zeros around  $z = -1$  result in the oscillating feedforward input that deteriorates intersample performance even if the feedforward controller is stable. There are several implementation methods of the sampled-data controller design to improve the intersample performance. The state tracking approach is one of the solutions because it enables natural intersample interpolation for mechatronic systems considering the state trajectory tracking of the controlled system by multirate sampling control [20].

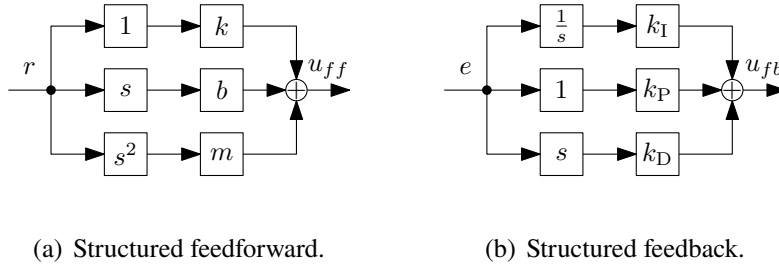


Fig. 1.9: Block diagram of the structured controller examples.

## 1.3.2 Data-driven controller design with structured modeling

### Structured parameterization

In industrial applications, the multivariable controllers have a lot of tuning parameters, and it leads to too much effort and time in the tuning process for on-site engineers. It results in the demand for data-driven controller design. Although the main tuning process is conducted by the optimization in data-driven controller design, the designed controller should be interpretable by the engineers for analysis and manual tuning in the implementation process in industrial mechatronic systems. In the dissertation, the structured controller is defined as follows.

**Definition 1.8** (Structured controller) : *The control input from the structured controller is defined as  $u = \Psi\theta$  that is linearly parameterized by the basis functions  $\Psi = [\psi_1 \ \cdots \ \psi_n]$  and the tuning parameters  $\theta = [\theta_1 \ \cdots \ \theta_n]^\top$ .*

The structured controller is interpretable if the basis functions  $\Psi$  and the tuning parameters  $\theta$  are physically intuitive. Examples of the structured controller are shown in Fig. 1.9. In Fig. 1.9(a), the feedforward signal consists of the basis functions  $\Psi = [r(t) \ \frac{d}{dt}r(t) \ \frac{d^2}{dt^2}r(t)]$ , that correspond to position, velocity, and acceleration of the reference  $r(t)$ , and the tuning parameters  $\theta = [k \ b \ m]^\top$ , that correspond to spring, damper, and mass coefficients of the continuous-time rigid body model. In Fig. 1.9(b), the feedback signal consists of the basis functions  $\Psi = [\int e(t)dt \ e(t) \ \frac{d}{dt}e(t)]$ , that correspond to integral, proportional, and derivative of the error  $e(t)$ , and the tuning parameters  $\theta = [k_I \ k_P \ k_D]^\top$ , that correspond to integral, proportional, and derivative gains of the PID feedback controller. The linearly parameterized controller has an advantage because it is preferable for convex optimization [21] during the tuning process.

### Iterative learning control

The structured feedforward controller can be optimized by the error data using iterative learning control [22, 23] as shown in Fig. 1.10. In the iterative learning control, the feedforward input in task  $j + 1$  is updated from the task  $j$  and is given by

$$f_{j+1} = Q(f_j + Le_j), \quad (1.12)$$

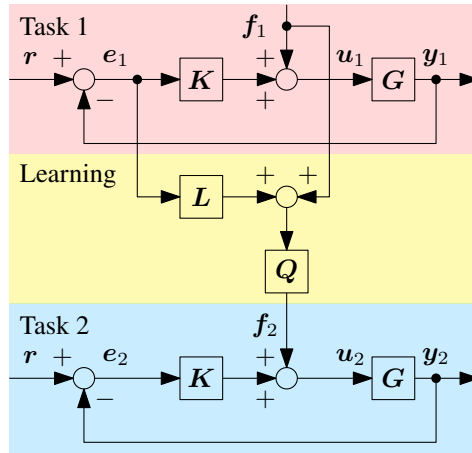


Fig. 1.10: Block diagram of iterative learning control.

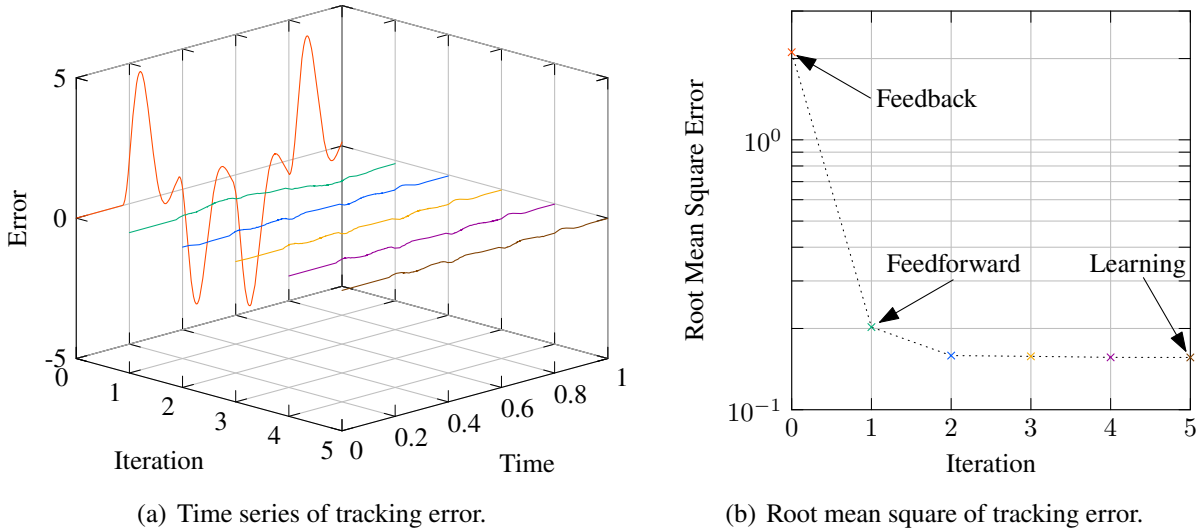


Fig. 1.11: Improvement of tracking error in iterative learning control through experiments.

where  $L$  is a learning filter and  $Q$  is a robustness filter. For simplification, the robustness filter is assumed to be  $Q = I$ . The error of the closed-loop system in task  $j + 1$  is given by

$$\begin{aligned}
 e_{j+1} &= \mathbf{S}r - \mathbf{S}\mathbf{G}f_{j+1} \\
 &= (e_j + \mathbf{S}\mathbf{G}f_j) - \mathbf{S}\mathbf{G}(f_j + \mathbf{L}e_j) \\
 &= (\mathbf{I} - \mathbf{S}\mathbf{G}\mathbf{L})e_j,
 \end{aligned} \tag{1.13}$$

where the sensitivity function is  $\mathbf{S} = (\mathbf{I} + \mathbf{G}\mathbf{K})^{-1}$ . It shows that  $e_{j+1} = \mathbf{0}$  if  $\mathbf{L} = (\mathbf{S}\mathbf{G})^{-1}$  and it has the same challenges as the feedforward controller design. The monotonic convergence condition requires  $\bar{\sigma}(\mathbf{I} - \mathbf{G}\mathbf{S}\mathbf{L}) < 1$  where  $\bar{\sigma}(\cdot)$  is a maximum singular value. In practice, there is a modeling error, and the robustness filter  $Q$  is used so that the monotonic convergence condition  $\bar{\sigma}(Q(\mathbf{I} - \mathbf{G}\mathbf{S}\mathbf{L})) < 1$  is satisfied. The iterative learning control improves the error  $e_j$  through iterations as shown in Fig. 1.11(a). Fig. 1.11(b) shows the comparison of the Root Mean Square (RMS) error in each iteration. Iteration  $j = 0$  is using the input that is from only the feedback controller and iteration  $j = 1$  is using the input that is approximately equal to the feedforward

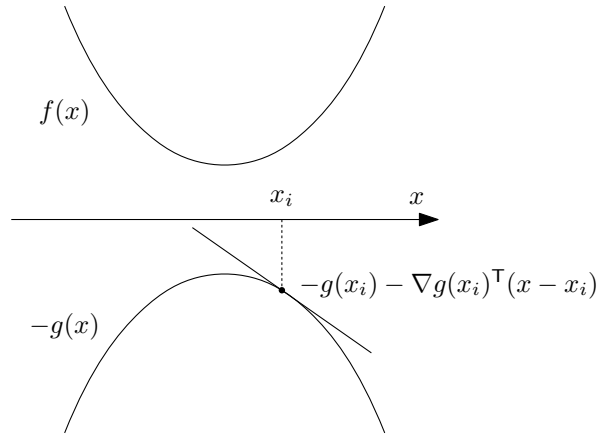


Fig. 1.12: Sequential linearization in concave-convex procedure.

and controller. It shows that the error is further reduced by learning through iterations when the monotonic convergence condition is satisfied.

Although the traditional iterative learning control achieves high performance for the specific reference signal, there is a trade-off of performance and flexibility compared to the traditional feedforward control. To achieve both performance and flexibility, iterative learning control with basis functions is developed [24,25]. Instead of learning the time-series feedforward input  $\mathbf{f}_j$ , the iterative learning control with basis functions updates the tuning parameter  $\boldsymbol{\theta}_j$  and the feedforward input  $\mathbf{f}_j$  is given by

$$\mathbf{f}_j = \mathbf{F}(\boldsymbol{\theta}_j)\mathbf{r}_j \quad (1.14)$$

where  $\mathbf{F}(\boldsymbol{\theta})$  is the feedforward controller and  $\mathbf{r}_j$  is the reference in Task  $j$ . The advantage of this parameterization is the learning is decoupled from the reference trajectory. In the iterative learning control with basis functions, structured parameterization can be applied to construct  $\mathbf{F}(\boldsymbol{\theta})$  so that the tuning parameters  $\boldsymbol{\theta}$  are physically intuitive.

### Data-driven convex optimization

The structured feedback controller can be optimized by the frequency response data. The traditional feedback controller design with optimization [26–29] is based on the parametric model. Although the mathematical theory is clear and it can be extended to the structured controller design [30], it is hard to get a parametric model of the multivariable system with necessary and sufficient complexity in practice. To overcome the difficulty in the modeling process, the structured controller design using frequency response data [31–33] is developed. The approach can directly use the nonparametric model of the controlled system and the nonparametric model can be measured as frequency response data by the excitation experiments. The challenge in data-based design is the convex formulation of the optimization problem because the non-convex optimization problem is not monotonically converging and it could take a long time for the optimization calculation. Fig. 1.12 shows the concept of sequential linearization using concave-convex procedure [34]. In the concave-convex procedure, the non-convex functions  $f(x) - g(x)$  consisting of the difference between the convex functions  $f(x)$  and  $g(x)$  can be solved by the sequential linearization of  $g(x)$  and iterative convex optimization. The sequential linearization



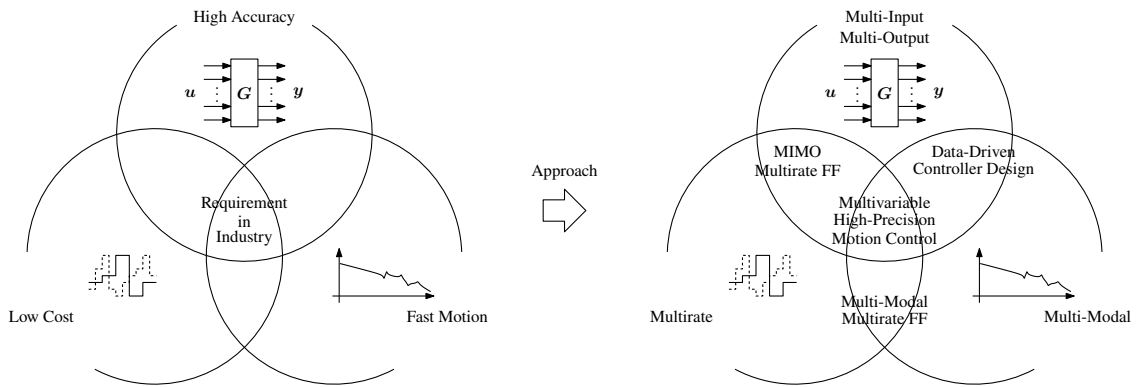


Fig. 1.13: Framework of the dissertation.

method using the concave-convex procedure has an advantage in monotonic convergence to a saddle point or a local optimum and suits controller design in industrial applications.

## 1.4 Contributions

The goal of the dissertation is as follows.

**Goal :** *Develop a framework for multivariable high-precision motion control combining model-based and data-based approaches that is suitable for mechatronic systems in industrial applications.*

The key to achieving the goal is to consider the redundancy of the multivariable systems in the controller design. The framework of the dissertation is shown in Fig. 1.13. There are several redundancies such as multirate sampling, multi-modal dynamics, and multi-input multi-output interactions. The redundancy should be effectively used to improve the control performance, and the optimization of these redundancies should be intuitive and tuning-friendly for industrial applicability. The challenges in the dissertation consist of two parts.

**Challenge (model-based aspect) :** *The dynamics of the multivariable controlled system should be considered as a model structure with respect to the limitations of sampled-data characteristics and multi-modal flexibility, and the control approach should be successfully implemented in physically intuitive tuning parameters for industrial applicability.*

**Challenge (data-based aspect) :** *The tuning parameters of the multivariable controllers should be tuned by the intuitive process or data-driven optimization to avoid too much effort in the tuning process when the controllers are implemented in industrial mechatronic systems.*

To overcome these challenges toward the goal, the contributions of the dissertations are presented. The framework of multivariable high-precision motion control can be divided into three categories that are “multirate feedforward control in multivariable motion systems”, “fixed-structure sampled-data feedforward and learning control”, and “feedback controller design using frequency response data”.

## Multirate feedforward control in multivariable motion systems

The contributions of multirate feedforward control in multivariable motion systems are presented in Part II which consists of Contributions M-1 and M-2.

**Contribution M-1 :** *The state trajectory generation method is extended to a general framework including non-minimum-phase and MIMO motion systems, and the redundancy of the multi-modal system is considered by the mode selection. It is the result of Chapter 2.*

**Contribution M-2 :** *The redundancy of multirate input sampling is analytically optimized by the state controllability of the generalized controllability indices. It is the result of Chapter 3.*

## Fixed-structure sampled-data feedforward and learning control

The contributions of fixed-structure sampled-data feedforward and learning control are presented in Part III which consists of Contributions M-3 and D-1.

**Contribution M-3 :** *The state tracking sampled-data feedforward controller is linearly parameterized and it enables intuitive tuning and ease for the extension to data-driven parameter updates. It is the result of Chapter 4.*

**Contribution D-1 :** *Iterative learning control with sampled-data basis functions is presented for MIMO systems and it enables the data-driven parameter update and interaction compensation of MIMO systems without the MIMO model. It is the result of Chapter 5.*

## Feedback controller design using frequency response data

The contributions of feedback controller design using frequency response data are presented in Part IV which consists of Contributions D-2 and D-3.

**Contribution D-2 :** *The feedback controller for disturbance rejection is designed by convex optimization considering the robust performance that includes model variations, stroke constraints, and actuator redundancies. It is the result of Chapter 6.*

**Contribution D-3 :** *The feedback controller for disturbance rejection is designed by convex optimization considering MIMO robust stability, and it is the first attempt to apply the high-gain filter to the actual industrial large-scale MIMO high-precision scan stage. It is the result of Chapter 7.*

## 1.5 Outline of the dissertation

The outline of the dissertation is shown in Fig. 1.14. In the dissertation, multivariable high-precision motion control with structured modeling and data-driven convex optimization is presented. In Chapter 2, multirate feedforward control is generalized to multi-modal motion systems. In Chapter 3, multirate feedforward control is generalized to MIMO motion systems. In Chapter 4, the linearly parameterized feedforward control with sampled-data differentiator is presented. In Chapter 5, the iterative learning control with MIMO sampled-data basis functions is presented. In Chapter 6, the frequency response data-based disturbance rejection with robust performance is presented. In Chapter 7, the frequency response data-based disturbance rejection with MIMO robust stability is presented. In Chapter 8, conclusions are presented.

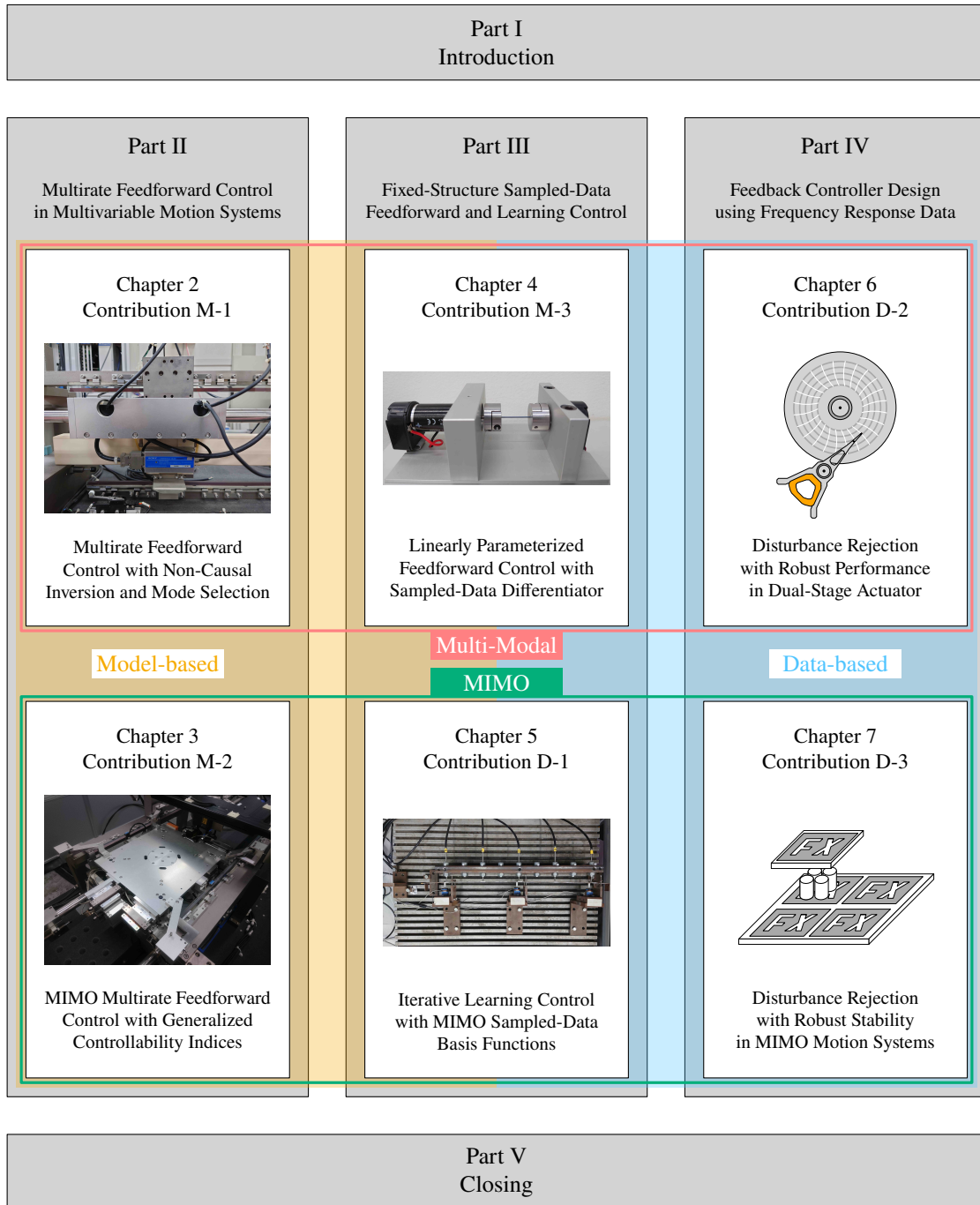


Fig. 1.14: Outline of the dissertation.



## **Part II**

# **Multirate Feedforward Control in Multivariable Motion Systems**



## Chapter 2

# Multirate Feedforward Control with Non-Causal Inversion and Mode Selection

Multirate feedforward control enables perfect tracking control for the desired state trajectory at every sample as the same number of the model order. The aim of this chapter is the comparison of perfect tracking control approaches for intersample performance in multi-modal motion systems. The multirate feedforward control has a trade-off between the number of states for perfect tracking control and the reference sampling frequency. To balance the trade-off, the states for the perfect tracking control can be selected by the mode decomposition. Intersample performance of each approach in a multi-modal motion system is compared in both frequency domain and time domain.

### 2.1 Introduction

Feedforward control based on exact model inversion enables perfect tracking control [35] for the model of the controlled system. The quality of the feedforward controller directly results in tracking performance in high-precision mechatronic systems such as wafer scanners [36], wire bonders [37], and ball-screw-driven stages [38]. In industrial applications, the system is controlled in discrete time but the tracking performance should be improved in continuous time.

The exact model inversion has a challenge when the model has nonminimum-phase zeros such as intrinsic and discretization zeros [19]. The single-rate stable inversion approach [39] generates the noncausal bounded feedforward input for the model with nonminimum-phase zeros and provides perfect output tracking for every sample. However, it cannot compensate for the zeros around  $-1$  that cause the oscillating input and deteriorate intersample performance when the relative degree of the model is more than 2 [19].

To improve intersample performance, the multirate feedforward control [20, 40] is presented. The multirate feedforward control provides perfect  $n$  states tracking for every  $n$  sample and prevents intersample oscillation. There is a trade-off in the multirate feedforward control between the number of states for perfect tracking control and the reference sampling frequency. To balance the trade-off, the multirate feedforward control approaches based on modal form with additive decomposition [41, 42] and multiplicative decomposition [43] are presented. Both approaches select the states for perfect tracking control and balance the trade-off to improve intersample performance.

Although several approaches are available to design the perfect tracking controller, the choice of the feedforward controller can be arbitrarily and there is no comparison in terms of intersample

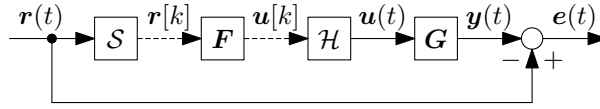


Fig. 2.1: Block diagram of tracking control. The continuous-time system  $G$  is controlled by the discrete-time controller  $F$  with sampler  $S$  and zero-order-hold  $\mathcal{H}$ . The objective is to minimize the continuous-time error  $e(t)$ .

performance for perfect tracking controllers. The aim of this chapter is the analysis of pre-existing perfect tracking controllers in both frequency domain and time domain and provides the guideline to design the feedforward controller to improve intersample performance. The main contributions of this chapter are as follows.

**Contribution 2.1 :** *Perfect tracking control approaches are described focusing on improving intersample performance in multi-modal motion systems.*

**Contribution 2.2 :** *Intersample performance of each approach is evaluated in both frequency domain and time domain.*

The theory is described in a general multi-input multi-output (MIMO) system and the verification is conducted in a single-input single-output (SISO) system.

The outline is as follows. In Section 2.2, the tracking problem for intersample performance is formulated. In Section 2.3, the desired state trajectory generation method is presented for SISO and MIMO systems. In Section 2.4, the multirate feedforward controller design methods with additive and multiplicative decomposition are presented. In Section 2.5, the intersample performance is validated in a multi-modal motion system. In Section 2.6, conclusions are presented.

## 2.2 Problem formulation

In this section, the problem to improve continuous-time tracking performance is formulated. The perfect tracking control methods based on the single-rate and multirate feedforward are described. From the trade-off of these two approaches, the requirements of the optimal perfect tracking controller design are presented.

### 2.2.1 Intersample performance in sampled-data control

The considered tracking control configuration is shown in Fig. 2.1, with input  $\mathbf{u} \in \mathbb{R}^{n_u \times 1}$ , output  $\mathbf{y} \in \mathbb{R}^{n_y \times 1}$ , reference  $\mathbf{r} \in \mathbb{R}^{n_y \times 1}$ , and error  $\mathbf{e} \in \mathbb{R}^{n_y \times 1}$ . In this chapter, the system is assumed to be square as  $n_u = n_y = m$ . The  $m$ -input  $m$ -output  $n^{\text{th}}$  order continuous-time linear time-invariant system  $\mathbf{G}_c \stackrel{s}{=} (\mathbf{A}_c, \mathbf{B}_c, \mathbf{C}_c, \mathbf{O})$  is given by

$$\dot{\mathbf{x}}(t) = \mathbf{A}_c \mathbf{x}(t) + \mathbf{B}_c \mathbf{u}(t), \quad (2.1)$$

$$\mathbf{y}(t) = \mathbf{C}_c \mathbf{x}(t), \quad (2.2)$$

where  $\mathbf{A}_c \in \mathbb{R}^{n \times n}$ ,  $\mathbf{B}_c \in \mathbb{R}^{n \times m}$ , and  $\mathbf{C}_c \in \mathbb{R}^{m \times n}$ . The discrete-time system  $\mathbf{H}_d$  of the continuous-time system  $\mathbf{H}_c$  discretized by sampler  $S$  and zero-order-hold  $\mathcal{H}$  in sampling time  $\delta$



is generally defined as

$$\mathbf{H}_c \stackrel{s}{=} \left[ \begin{array}{c|c} \mathbf{A}_c & \mathbf{B}_c \\ \hline \mathbf{C}_c & \mathbf{D}_c \end{array} \right], \quad (2.3)$$

$$\mathbf{H}_d \stackrel{z}{=} \mathcal{S}\mathbf{H}_c\mathcal{H} = \left[ \begin{array}{c|c} \mathbf{A}_d & \mathbf{B}_d \\ \hline \mathbf{C}_d & \mathbf{D}_d \end{array} \right] = \left[ \begin{array}{c|c} e^{\mathbf{A}_c\delta} & \mathbf{A}_c^{-1}(e^{\mathbf{A}_c\delta} - \mathbf{I})\mathbf{B}_c \\ \hline \mathbf{C}_c & \mathbf{D}_c \end{array} \right], \quad (2.4)$$

$$\mathbf{x}[k] = \mathbf{x}(k\delta). \quad (2.5)$$

The discrete-time system  $\mathbf{G}_d \stackrel{z}{=} (\mathbf{A}_d, \mathbf{B}_d, \mathbf{C}_d, \mathbf{O}) = \mathcal{S}\mathbf{G}_c\mathcal{H}$  is given by

$$\mathbf{x}[k+1] = \mathbf{A}_d\mathbf{x}[k] + \mathbf{B}_d\mathbf{u}[k], \quad (2.6)$$

$$\mathbf{y}[k] = \mathbf{C}_d\mathbf{x}[k]. \quad (2.7)$$

The control objective considered in this chapter is to minimize the continuous-time error  $\mathbf{e}(t)$  that includes both on-sample and intersample performance for the continuous-time reference  $\mathbf{r}(t)$  that is assumed to be known in advance.

## 2.2.2 Single-rate feedforward control based on discrete-time model inversion

The one-sample forward shifted system  $\tilde{\mathbf{G}}_d$  of  $\mathbf{G}_d$  from  $\mathbf{u}[k]$  to  $\mathbf{y}[k+1]$  is given by

$$\mathbf{x}[k+1] = \mathbf{A}_d\mathbf{x}[k] + \mathbf{B}_d\mathbf{u}[k], \quad (2.8)$$

$$\mathbf{y}[k+1] = \mathbf{C}_d\mathbf{A}_d\mathbf{x}[k] + \mathbf{C}_d\mathbf{B}_d\mathbf{u}[k]. \quad (2.9)$$

For the system  $\mathbf{H} = (\mathbf{A}, \mathbf{B}, \mathbf{C}, \mathbf{D})$  with nonsingular  $\mathbf{D}$ , the inverse system  $\mathbf{H}^{-1}$  is generally defined as

$$\mathbf{H}^{-1} = \left[ \begin{array}{c|c} \mathbf{A} - \mathbf{B}\mathbf{D}^{-1}\mathbf{C} & \mathbf{B}\mathbf{D}^{-1} \\ \hline -\mathbf{D}^{-1}\mathbf{C} & \mathbf{D}^{-1} \end{array} \right]. \quad (2.10)$$

By inverting  $\tilde{\mathbf{G}}_d$ , the input  $\mathbf{u}$  generated by the single-rate feedforward controller is given by

$$\mathbf{u}[k] = \tilde{\mathbf{G}}_d^{-1}\mathbf{r}[k+1], \quad (2.11)$$

where the single-rate feedforward controller  $\tilde{\mathbf{G}}_d^{-1}$  is given by

$$\tilde{\mathbf{G}}_d^{-1} = \left[ \begin{array}{c|c} \mathbf{A}_d - \mathbf{B}_d(\mathbf{C}_d\mathbf{B}_d)^{-1}\mathbf{C}_d\mathbf{A}_d & \mathbf{B}_d(\mathbf{C}_d\mathbf{B}_d)^{-1} \\ \hline -(\mathbf{C}_d\mathbf{B}_d)^{-1}\mathbf{C}_d\mathbf{A}_d & (\mathbf{C}_d\mathbf{B}_d)^{-1} \end{array} \right]. \quad (2.12)$$

When  $\tilde{\mathbf{G}}_d^{-1}$  has unstable poles, it can be decomposed as

$$\begin{bmatrix} \mathbf{x}_s[k+1] \\ \mathbf{x}_u[k+1] \end{bmatrix} = \begin{bmatrix} \mathbf{A}_s & \mathbf{O} \\ \mathbf{O} & \mathbf{A}_u \end{bmatrix} \begin{bmatrix} \mathbf{x}_s[k] \\ \mathbf{x}_u[k] \end{bmatrix} + \begin{bmatrix} \mathbf{B}_s \\ \mathbf{B}_u \end{bmatrix} \mathbf{r}[k+1], \quad (2.13)$$

$$\mathbf{u}[k] = \begin{bmatrix} \mathbf{C}_s & \mathbf{C}_u \end{bmatrix} \begin{bmatrix} \mathbf{x}_s[k] \\ \mathbf{x}_u[k] \end{bmatrix} + \mathbf{D}\mathbf{r}[k+1], \quad (2.14)$$

where  $|\lambda(\mathbf{A}_s)| \leq 1$  and  $|\lambda(\mathbf{A}_u)| > 1$ . The bounded feedforward input  $u$  is given by

$$\mathbf{u}[k] = \mathbf{C}_s \mathbf{x}_s[k] + \mathbf{C}_u \mathbf{x}_u[k] + \mathbf{D} \mathbf{r}[k+1] \quad (2.15)$$

where  $\mathbf{x}_s$  follows from solving

$$\mathbf{x}_s[k+1] = \mathbf{A}_s \mathbf{x}_s[k] + \mathbf{B}_s \mathbf{r}[k+1], \quad \mathbf{x}_s[-\infty] = \mathbf{0} \quad (2.16)$$

forward in time and  $\mathbf{x}_u$  follows from solving

$$\mathbf{x}_u[k+1] = \mathbf{A}_u \mathbf{x}_u[k] + \mathbf{B}_u \mathbf{r}[k+1], \quad \mathbf{x}_u[\infty] = \mathbf{0} \quad (2.17)$$

backward in time [39]. The generated feedforward input  $u$  provides perfect output tracking for every sample.

Note that although the feedforward input generated by the single-rate stable inversion approach is bounded, the oscillating poles around  $\lambda = -1$  cannot be compensated. The oscillating feedforward input can deteriorate intersample performance.

### 2.2.3 Multirate feedforward control for full-state tracking

To compensate for oscillating poles of the feedforward controller due to discretization, multirate feedforward control [20] based on perfect state tracking is presented.

The  $n$  samples lifted system  $\underline{\mathbf{H}}_d$  of  $\mathbf{H}_d \stackrel{z}{=} (\mathbf{A}_d, \mathbf{B}_d, \mathbf{C}_d, \mathbf{D}_d)$  is generally defined as

$$\underline{\mathbf{H}}_d \stackrel{z^n}{=} \mathcal{L}_n \mathbf{H}_d \mathcal{L}_n^{-1} = \left[ \begin{array}{c|ccc} \mathbf{A}_d & \mathbf{B}_d & & \\ \mathbf{C}_d & \mathbf{D}_d & & \end{array} \right] = \begin{bmatrix} \mathbf{A}_d^n & \mathbf{A}_d^{n-1} \mathbf{B}_d & \mathbf{A}_d^{n-2} \mathbf{B}_d & \cdots & \mathbf{A}_d \mathbf{B}_d & \mathbf{B}_d \\ \mathbf{C}_d & \mathbf{D}_d & \mathbf{O} & \cdots & \cdots & \mathbf{O} \\ \mathbf{C}_d \mathbf{A}_d & \mathbf{C}_d \mathbf{B}_d & \mathbf{D}_d & \ddots & & \vdots \\ \vdots & \vdots & \ddots & \ddots & \ddots & \vdots \\ \mathbf{C}_d \mathbf{A}_d^{n-2} & \mathbf{C}_d \mathbf{A}_d^{n-3} \mathbf{B}_d & \mathbf{C}_d \mathbf{A}_d^{n-4} \mathbf{B}_d & \ddots & \mathbf{D}_d & \mathbf{O} \\ \mathbf{C}_d \mathbf{A}_d^{n-1} & \mathbf{C}_d \mathbf{A}_d^{n-2} \mathbf{B}_d & \mathbf{C}_d \mathbf{A}_d^{n-3} \mathbf{B}_d & \cdots & \mathbf{C}_d \mathbf{B}_d & \mathbf{D}_d \end{bmatrix} \quad (2.18)$$

$$\underline{\mathbf{u}}[i_n] = \mathcal{L}_n \mathbf{u}[k] = \left[ \mathbf{u}[ni_n] \quad \cdots \quad \mathbf{u}[ni_n + (n-1)] \right]^T \in \mathbb{R}^{(m \times n)}, \quad (2.19)$$

$$\underline{\mathbf{y}}[i_n] = \mathcal{L}_n \mathbf{y}[k] = \left[ \mathbf{y}[ni_n] \quad \cdots \quad \mathbf{y}[ni_n + (n-1)] \right]^T \in \mathbb{R}^{(m \times n)}, \quad (2.20)$$

where  $\underline{\mathbf{u}}[i_n]$  and  $\underline{\mathbf{y}}[i_n]$  are column vectors, and  $\mathcal{L}_n$  is  $n$  samples lifting operator [15].

The  $N$  ( $\leq n$ ) samples lifted system of  $\mathbf{G}_d$  is given by

$$\underline{\mathbf{G}}_d \stackrel{z^N}{=} \mathcal{L}_N \mathbf{G}_d \mathcal{L}_N^{-1} = \left[ \begin{array}{c|c} \mathbf{A}_d & \mathbf{B}_d \\ \mathbf{C}_d & \mathbf{D}_d \end{array} \right]. \quad (2.21)$$

Note that the number of lifting samples is  $N = n$  in SISO systems but it is not the case in MIMO systems, see [44]. The desired state trajectory of  $\underline{\mathbf{G}}_d$  is given by the multirate sampler for every  $N$  sample  $\mathcal{S}_N$  that is defined as

$$\hat{\mathbf{x}}[i_N] = \mathcal{S}_N \hat{\mathbf{x}}(t) = \hat{\mathbf{x}}(i_N N \delta), \quad (2.22)$$

where  $\hat{\mathbf{x}}(t)$  is the desired state trajectory in continuous time. By inverting the state equation of  $\underline{\mathbf{G}}_d$ , the input  $u$  generated by the multirate feedforward controller is given by

$$\begin{aligned} \mathbf{u}[k] &= \mathcal{L}_N^{-1} \left( \underline{\mathbf{B}}_d^{-1} \hat{\mathbf{x}}[i_N + 1] - \underline{\mathbf{B}}_d^{-1} \underline{\mathbf{A}}_d \hat{\mathbf{x}}[i_N] \right) \\ &= \mathcal{L}_N^{-1} \underline{\mathbf{B}}_d^{-1} (\mathbf{I} - z^{-N} \underline{\mathbf{A}}_d) \hat{\mathbf{x}}[i_N + 1], \end{aligned} \quad (2.23)$$

where  $z$  is shift operator in sampling time  $\delta$ . The generated feedforward input  $\mathbf{u}$  provides perfect state tracking for every  $N$  sample and improves intersample performance.

Note that the desired state trajectory  $\hat{\mathbf{x}}$  is given by the reference and its derivatives in continuous time for the rigid body system without zeros in such as controllable canonical form. When the system has zeros, the desired state trajectory generation method is described in the next section. Although the multirate feedforward controller provides perfect state tracking for every  $N$  sample, the sampling time of the desired state trajectory is  $N\delta$ , and the higher  $N$  is, the lower the reference sampling frequency  $1/N\delta$  is.

## 2.2.4 Problem description

From these discussions, the optimal perfect tracking controller should be designed by considering the following requirements.

**Requirement 2.1 :** *Oscillating poles of the feedforward controller due to discretization is compensated by state tracking.*

**Requirement 2.2 :** *States for perfect tracking control are selected to make reference sampling frequency enough high.*

The state tracking can be provided by multirate feedforward control and the states can be selected based on the mode decomposition. In this chapter, two kinds of multirate feedforward controllers with mode selection in additive decomposition [41, 42] and multiplicative decomposition [43] are described and intersample performance is compared with pre-existing perfect tracking control approaches.

## 2.3 Desired state trajectory generation

In this section, the desired state trajectory methods are presented for the SISO and MIMO systems [45]. For the SISO system, the desired state trajectory is generated in controllable canonical form. For the MIMO system, the desired state trajectory is generated by the state transformation using the singular value decomposition of the input matrix. The bounded desired state trajectory is generated by the stable and unstable decomposition and the non-causal convolution with time axis reversal.

### 2.3.1 Desired state trajectory generation for SISO system

The single-input single-output continuous-time linear time-invariant  $n^{\text{th}}$  order system is given by

$$G_c(s) = \frac{B(s)}{A(s)} = \frac{b_m s^m + \cdots + b_1 s + b_0}{s^n + a_{n-1} s^{n-1} + \cdots + a_1 s + a_0}, \quad (2.24)$$

where  $n > m$  and  $b_0 \neq 0$ .  $G_c$  in controllable canonical form  $G_{c,ccf} \stackrel{s}{=} (\mathbf{A}_{c,ccf}, \mathbf{b}_{c,ccf}, \mathbf{c}_{c,ccf}, 0)$  is given by

$$\dot{\mathbf{x}}_{ccf}(t) = \mathbf{A}_{c,ccf} \mathbf{x}_{ccf}(t) + \mathbf{b}_{c,ccf} u(t), \quad (2.25)$$

$$y(t) = \mathbf{c}_{c,ccf} \mathbf{x}_{ccf}(t), \quad (2.26)$$

where

$$\left[ \begin{array}{c|c} \mathbf{A}_{c,ccf} & \mathbf{b}_{c,ccf} \\ \mathbf{c}_{c,ccf} & 0 \end{array} \right] = \left[ \begin{array}{cccc|c} 0 & 1 & & 0 & 0 \\ & \ddots & \ddots & & \vdots \\ 0 & & 0 & 1 & 0 \\ -a_0 & \cdots & \cdots & -a_{n-1} & 1 \\ \hline b_0 & \cdots & b_m & 0 & 0 \end{array} \right]. \quad (2.27)$$

The filter for the state trajectory generation is given by

$$\beta(t) = \mathcal{L}^{-1} [B(s)^{-1}], \quad (2.28)$$

where  $\mathcal{L}[\cdot]$  is the unilateral Laplace transform. The desired state trajectory in the controllable canonical form is given by

$$\hat{\mathbf{x}}_{ccf}(t) = \int_0^t \beta(t - \tau) \bar{\mathbf{r}}_n(\tau) d\tau, \quad (2.29)$$

where

$$\hat{\mathbf{x}}_{ccf}(t) = [\hat{x}_{ccf,0}(t) \ \cdots \ \hat{x}_{ccf,n-1}(t)]^T, \quad (2.30)$$

$$\bar{\mathbf{r}}_n(t) = \left[ 1 \ \cdots \ \frac{d^{n-1}}{dt^{n-1}} \right]^T r(t). \quad (2.31)$$

When  $B(s)^{-1}$  has unstable poles, it can be decomposed as

$$B(s)^{-1} = B_s^{-1}(s) + B_u^{-1}(s), \quad (2.32)$$

where all poles  $p_s \in \mathbb{C}$  of  $B_s^{-1}(s)$  are  $\text{Re}(p_s) \leq 0$  and all poles  $p_u \in \mathbb{C}$  of  $B_u^{-1}(s)$  are  $\text{Re}(p_u) > 0$ . The filters of stable and unstable parts for the state trajectory generation are given by

$$\beta_s(t) = \mathcal{L}^{-1} [B_s^{-1}(s)], \quad (2.33)$$

$$\beta_u(t) = \mathcal{L}^{-1} [B_u^{-1}(-s)]. \quad (2.34)$$

The stable and unstable parts of the desired state trajectory are given by

$$\hat{\mathbf{x}}_s(t) = \int_{-\infty}^t \beta_s(t - \tau) \bar{\mathbf{r}}_n(\tau) d\tau, \quad (2.35)$$

$$\hat{\mathbf{x}}_u(t) = \int_t^{\infty} \beta_u(t - \tau) \bar{\mathbf{r}}_n(\tau) d\tau, \quad (2.36)$$

and the bounded desired state trajectory in controllable canonical form  $\hat{\mathbf{x}}_{ccf}$  is given by

$$\hat{\mathbf{x}}_{ccf}(t) = \hat{\mathbf{x}}_s(t) + \hat{\mathbf{x}}_u(t). \quad (2.37)$$

The state transformation of the system  $H = (A, B, C, D)$  with the state transformation matrix  $T$  is generally defined as

$$\mathcal{T}(H, T) = \left[ \begin{array}{c|c} \mathbf{TA}T^{-1} & \mathbf{TB} \\ \hline \mathbf{CT}^{-1} & \mathbf{D} \end{array} \right]. \quad (2.38)$$

The state transformation matrix  $T_{ccf}^{-1}$  from the system in controllable canonical form  $G_{ccf}$  to the system  $G_c \stackrel{s}{=} (A_c, b_c, c_c, 0)$  with the states  $x$  is given by

$$T_{ccf}^{-1} = \begin{bmatrix} B_c & \cdots & A_c^{n-1}B_c \end{bmatrix} \begin{bmatrix} a_1 & \cdots & a_{n-1} & 1 \\ \vdots & \ddots & \ddots & \\ a_{n-1} & \ddots & & \\ 1 & & & \mathbf{O} \end{bmatrix}, \quad (2.39)$$

where

$$G_{c,ccf} = \mathcal{T}(G_c, T_{ccf}), \quad (2.40)$$

$$x_{ccf}(t) = T_{ccf}x(t). \quad (2.41)$$

### 2.3.2 Desired state trajectory generation for MIMO system

The  $m$ -input  $m$ -output  $n^{\text{th}}$  order continuous-time linear time-invariant system  $G_c \stackrel{s}{=} (A_c, B_c, C_c, \mathbf{O})$  is given by

$$\dot{x}(t) = A_c x(t) + B_c u(t), \quad (2.42)$$

$$y(t) = C_c x(t), \quad (2.43)$$

where  $A_c \in \mathbb{R}^{n \times n}$ ,  $B_c \in \mathbb{R}^{n \times m}$ , and  $C_c \in \mathbb{R}^{m \times n}$ . Singular Value Decomposition (SVD) of  $B_c$  is given by

$$B_c = U \Sigma V^H, \quad (2.44)$$

where  $U \in \mathbb{R}^{n \times n}$  and  $V \in \mathbb{R}^{m \times m}$  are unitary matrices so that  $U^{-1} = U^H$  and  $V^{-1} = V^H$ . The elements of  $\Sigma \in \mathbb{R}^{n \times m}$  are given by

$$\Sigma = \begin{bmatrix} \Delta \\ \mathbf{O} \end{bmatrix}, \quad (2.45)$$

$$\Delta = \text{diag}(\sigma_i) \quad (i = 1 \cdots m \in \mathbb{N}), \quad (2.46)$$

where  $\sigma_i$  ( $i = 1 \cdots m \in \mathbb{N}$ ) are the singular values of  $B$ .

The system  $G_{svd} \stackrel{s}{=} (A_{svd}, B_{svd}, C_{svd}, \mathbf{O}) = \mathcal{T}(G_c, U^H)$  with the states  $x_{svd} = U^H x$  is given by

$$\begin{bmatrix} W_u(s) & \Delta V^H \\ W_l(s) & \mathbf{O}_{(n-m) \times m} \\ C_{svd} & \mathbf{O}_{m \times m} \end{bmatrix} \begin{bmatrix} x_{svd}(s) \\ u(s) \end{bmatrix} = \begin{bmatrix} \mathbf{O}_{m \times m} \\ \mathbf{O}_{(n-m) \times m} \\ y(s) \end{bmatrix}, \quad (2.47)$$

where  $\mathbf{u}(s) = \mathcal{L}[\mathbf{u}(t)]$ ,  $\mathbf{x}(s) = \mathcal{L}[\mathbf{x}(t)]$ ,  $\mathbf{y}(s) = \mathcal{L}[\mathbf{y}(t)]$ ,  $\mathbf{W}_u(s) \in \mathbb{R}^{m \times n}$ ,  $\mathbf{W}_l(s) \in \mathbb{R}^{(n-m) \times n}$ , and the Rosenbrock system matrix  $\mathbf{\Pi}_{svd}(s)$  is given by

$$\mathbf{\Pi}_{svd}(s) = \begin{bmatrix} \mathbf{A}_{svd} - s\mathbf{I} & \mathbf{B}_{svd} \\ \mathbf{C}_{svd} & \mathbf{O} \end{bmatrix} = \begin{bmatrix} \mathbf{W}_u(s) & \Delta\mathbf{V}^H \\ \mathbf{W}_l(s) & \mathbf{O}_{(n-m) \times m} \\ \mathbf{C}_{svd} & \mathbf{O}_{m \times m} \end{bmatrix}. \quad (2.48)$$

The following theorem shows that  $\mathbf{W}_l(s)$  contains the property for the invariant zeros of the system.

**Theorem 2.1** (Identity of invariant zeros) : *Invariant zeros of  $\mathbf{G}_{svd}$  are the values when  $\mathbf{W}_l(s)$  is not full row rank.*

*Proof.* The invariant zero is defined as the value when the Rosenbrock system matrix is not full rank. It is assumed that  $\text{rank}(\Delta\mathbf{V}^H) = m$  and the upper  $m$  rows of  $\mathbf{\Pi}_{svd}(s)$  are full row rank. It is assumed that  $\text{rank}(\mathbf{C}_c) = m$  and  $\text{rank}(\mathbf{U}) = n$ . From Sylvester's rank inequality, for  $\mathbf{X} \in \mathbb{R}^{l \times n}$  and  $\mathbf{Y} \in \mathbb{R}^{n \times k}$  it generally follows

$$\text{rank}(\mathbf{X}) + \text{rank}(\mathbf{Y}) - n \leq \text{rank}(\mathbf{XY}). \quad (2.49)$$

Sylvester's rank inequality is applied to  $\mathbf{X}$  as  $\mathbf{C}_c$  and  $\mathbf{Y}$  as  $\mathbf{U}$ . It follows that  $\text{rank}(\mathbf{C}_{svd}) = \text{rank}(\mathbf{C}_c\mathbf{U}) = m$  and the lower  $m$  rows of  $\mathbf{\Pi}_{svd}(s)$  are full row rank. Therefore, the values when  $\mathbf{W}_l(s)$  is not full rank are the same as the values when the Rosenbrock system matrix is not full rank.  $\square$

From (2.47),

$$\begin{bmatrix} \mathbf{W}_l(s) \\ \mathbf{C}_{svd} \end{bmatrix} \mathbf{x}_{svd}(s) = \begin{bmatrix} \mathbf{O}_{(n-m) \times m} \\ \mathbf{y}(s) \end{bmatrix}, \quad (2.50)$$

and it follows that

$$\mathbf{x}_{svd}(s) = \begin{bmatrix} \mathbf{W}_l(s) \\ \mathbf{C}_{svd} \end{bmatrix}^{-1} \begin{bmatrix} \mathbf{O}_{(n-m) \times m} \\ \mathbf{y}(s) \end{bmatrix}. \quad (2.51)$$

Let the state transformation be

$$\mathbf{x}(s) = \mathbf{U}\mathbf{x}_{svd}(s) = \mathbf{U} \begin{bmatrix} \mathbf{W}_l(s) \\ \mathbf{C}_{svd} \end{bmatrix}^{-1} \begin{bmatrix} \mathbf{O}_{(n-m) \times m} \\ \mathbf{y}(s) \end{bmatrix}. \quad (2.52)$$

Let the inverse Laplace transform be  $\beta(t) = \mathcal{L}^{-1}[\mathbf{B}^{-1}(s)]$ , where

$$\mathbf{B}^{-1}(s) = \mathbf{U} \begin{bmatrix} \mathbf{W}_l(s) \\ \mathbf{C}_{svd} \end{bmatrix}^{-1}. \quad (2.53)$$

The desired state trajectory is given by

$$\hat{\mathbf{x}}(t) = \int_0^t \beta(t - \tau) \begin{bmatrix} \mathbf{O}_{(n-m) \times m} \\ \mathbf{r}(\tau) \end{bmatrix} d\tau. \quad (2.54)$$

When  $\mathbf{B}(s)^{-1}$  has unstable poles, it can be decomposed as

$$\mathbf{B}(s)^{-1} = \mathbf{B}_s^{-1}(s) + \mathbf{B}_u^{-1}(s), \quad (2.55)$$

where all poles  $p_s \in \mathbb{C}$  of  $\mathbf{B}_s^{-1}(s)$  are  $\text{Re}(p_s) \leq 0$  and all poles  $p_u \in \mathbb{C}$  of  $\mathbf{B}_u^{-1}(s)$  are  $\text{Re}(p_u) > 0$ . The filter matrices of stable and unstable parts for the state trajectory generation are given by

$$\beta_s(t) = \mathcal{L}^{-1} \left[ \mathbf{B}_s^{-1}(s) \right], \quad (2.56)$$

$$\beta_u(t) = \mathcal{L}^{-1} \left[ \mathbf{B}_u^{-1}(-s) \right]. \quad (2.57)$$

The stable and unstable parts of the desired state trajectory are given by

$$\hat{\mathbf{x}}_s(t) = \int_{-\infty}^t \beta_s(t - \tau) \begin{bmatrix} \mathbf{O}_{(n-m) \times m} \\ \mathbf{r}(\tau) \end{bmatrix} d\tau, \quad (2.58)$$

$$\hat{\mathbf{x}}_u(t) = \int_t^{\infty} \beta_u(t - \tau) \begin{bmatrix} \mathbf{O}_{(n-m) \times m} \\ \mathbf{r}(\tau) \end{bmatrix} d\tau, \quad (2.59)$$

and the bounded desired state trajectory  $\hat{\mathbf{x}}$  is given by

$$\hat{\mathbf{x}}(t) = \hat{\mathbf{x}}_s(t) + \hat{\mathbf{x}}_u(t). \quad (2.60)$$

Note that the unitary matrix  $\mathbf{U}$  that is used as the state transformation matrix is not unique in singular value decomposition but the desired state trajectory is generated uniquely for the desired state-space representation. The calculation of the singular value decomposition can be numerically ill-conditioned and the state-space representation should be properly formulated so that the state transformation matrix  $\mathbf{U}$  is not numerically ill-conditioned.

## 2.4 Multirate feedforward control with mode decomposition

In this section, the multirate feedforward control with mode decomposition is presented. First, the model of the multi-modal motion system is defined. Second, the multirate feedforward control with additive decomposition is described. Third, the multirate feedforward control with multiplicative decomposition is described. The intersample performance of these two approaches is verified in the next section.

### 2.4.1 Definition of multi-modal motion system

The  $m$ -input  $m$ -output continuous-time multi-modal motion system [46] is defined as

$$\mathbf{G}_c(s) = \sum_{k_m=1}^{n_m} \frac{\mathbf{c}_{k_m} \mathbf{b}_{k_m}}{s^2 + 2\zeta_{k_m} \omega_{k_m} s + \omega_{k_m}^2} = \sum_{k_m=1}^{n_m} \mathbf{G}_{c,mod,k_m}(s), \quad (2.61)$$

where  $\omega$  is the resonance angle frequency,  $\zeta$  is the damping coefficient, and  $n_m$  is the number of modes. The vectors  $\mathbf{b} \in \mathbb{R}^{1 \times m}$  and  $\mathbf{c} \in \mathbb{R}^{m \times 1}$  are associated with the inputs, the outputs, and the mode shapes.  $\mathbf{G}_c$  in modal form  $\mathbf{G}_{c,mod} \stackrel{s}{=} (\mathbf{A}_{c,mod}, \mathbf{B}_{c,mod}, \mathbf{C}_{c,mod}, \mathbf{O})$  is given by

$$\dot{\mathbf{x}}_{mod}(t) = \mathbf{A}_{c,mod} \mathbf{x}_{mod}(t) + \mathbf{B}_{c,mod} \mathbf{u}(t), \quad (2.62)$$

$$\mathbf{y}(t) = \mathbf{C}_{c,mod} \mathbf{x}_{mod}(t), \quad (2.63)$$

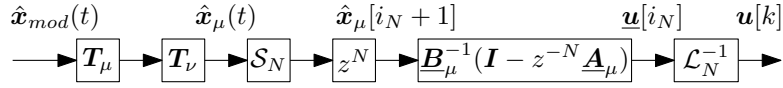


Fig. 2.2: Block diagram of multirate feedforward control with additive decomposition.

where

$$\left[ \begin{array}{c|c} \mathbf{A}_{c,mod} & \mathbf{B}_{c,mod} \\ \mathbf{C}_{c,mod} & \mathbf{O} \end{array} \right] = \left[ \begin{array}{ccc|c} \mathbf{A}_{c,mod,1} & & \mathbf{O} & \mathbf{B}_{c,mod,1} \\ & \ddots & & \vdots \\ \mathbf{O} & & \mathbf{A}_{c,mod,n_m} & \mathbf{B}_{c,mod,n_m} \\ \mathbf{C}_{c,mod,1} & \cdots & \mathbf{C}_{c,mod,n_m} & \mathbf{O} \end{array} \right], \quad (2.64)$$

$$\mathbf{x}_{mod}(t) = [\mathbf{x}_{mod,1}(t) \ \cdots \ \mathbf{x}_{mod,n_m}(t)]^\top, \quad (2.65)$$

and the subsystem  $\mathbf{G}_{c,mod,k_m} \stackrel{s}{=} (\mathbf{A}_{c,mod,k_m}, \mathbf{B}_{c,mod,k_m}, \mathbf{C}_{c,mod,k_m}, \mathbf{O})$  is given by

$$\left[ \begin{array}{c|c} \mathbf{A}_{c,mod,k_m} & \mathbf{B}_{c,mod,k_m} \\ \mathbf{C}_{c,mod,k_m} & \mathbf{O} \end{array} \right] = \left[ \begin{array}{cc|c} 0 & 1 & \mathbf{O} \\ -\omega_{k_m}^2 & -2\zeta_{k_m}\omega_{k_m} & \mathbf{b}_{k_m} \\ \mathbf{c}_{k_m} & \mathbf{O} & \mathbf{O} \end{array} \right]. \quad (2.66)$$

$$\mathbf{x}_{mod,k_m}(t) = [x_{mod,k_m,0}(t) \ x_{mod,k_m,1}(t)]^\top. \quad (2.67)$$

## 2.4.2 Multirate feedforward control with additive decomposition

The overview of multirate feedforward control with additive decomposition [41, 42] is shown in Fig. 2.2. The indices  $\mu$  of the selected modes are defined as

$$\mu = \{k_m | k_m \in 1, \dots, n_m\}, \quad (2.68)$$

and the order  $\nu$  of the selected modes is defined as

$$\nu = 2 \times \text{number}\{\mu\}. \quad (2.69)$$

The permutation matrix for the selected modes is defined as

$$\mathbf{T}_\mu = \begin{bmatrix} \mathbf{E}_\mu \\ \mathbf{E}_\times \end{bmatrix}, \quad (2.70)$$

where  $\mathbf{E}_\mu$  and  $\mathbf{E}_\times$  consist of standard basis vectors of selected and unselected modes, and the standard basis vectors of the mode  $k_m$  is defined as

$$\mathbf{E}_{k_m} = [\mathbf{O}_{2 \times 2(k_m-1)} \ \mathbf{I}_2 \ \mathbf{O}_{2 \times 2(n_m-k_m)}]. \quad (2.71)$$

The model reduction matrix extracting upper  $\nu$  states is defined as

$$\mathbf{T}_\nu = [\mathbf{I}_\nu \ \mathbf{O}_{\nu \times (n-\nu)}]. \quad (2.72)$$

The system of the selected modes  $\mathbf{G}_{c,\mu}$  is given by

$$\dot{\mathbf{x}}_\mu(t) = \mathbf{A}_{c,\mu} \mathbf{x}_\mu(t) + \mathbf{B}_{c,\mu} \mathbf{u}(t), \quad (2.73)$$

$$\mathbf{y}(t) = \mathbf{C}_{c,\mu} \mathbf{x}_\mu(t), \quad (2.74)$$



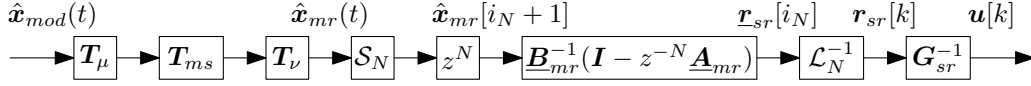


Fig. 2.3: Block diagram of multirate feedforward control with multiplicative decomposition.

where

$$\mathbf{x}_\mu(t) = \mathbf{T}_\nu \mathbf{T}_\mu \mathbf{x}_{mod}(t), \quad (2.75)$$

$$\mathbf{A}_{c,\mu} = \mathbf{T}_\nu \mathbf{T}_\mu \mathbf{A}_{c,mod} \mathbf{T}_\mu^{-1} \mathbf{T}_\nu^\top, \quad (2.76)$$

$$\mathbf{B}_{c,\mu} = \mathbf{T}_\nu \mathbf{T}_\mu \mathbf{B}_{c,mod}, \quad (2.77)$$

$$\mathbf{C}_{c,\mu} = \mathbf{C}_{c,mod} \mathbf{T}_\mu^{-1} \mathbf{T}_\nu^\top. \quad (2.78)$$

The discrete-time system of  $\mathbf{G}_{c,\mu}$  is given by

$$\mathbf{G}_{d,\mu} \stackrel{z}{=} \mathcal{S} \mathbf{G}_{c,\mu} \mathcal{H} = \left[ \begin{array}{c|c} \mathbf{A}_{d,\mu} & \mathbf{B}_{d,\mu} \\ \hline \mathbf{C}_{d,\mu} & \mathbf{O} \end{array} \right], \quad (2.79)$$

and the  $N$  ( $\leq \nu$ ) samples lifted system of  $\mathbf{G}_{d,\mu}$  is given by

$$\mathbf{G}_{d,\mu} \stackrel{z^N}{=} \mathcal{L}_N \mathbf{G}_{d,\mu} \mathcal{L}_N^{-1} = \left[ \begin{array}{c|c} \mathbf{A}_{d,\mu} & \mathbf{B}_{d,\mu} \\ \hline \mathbf{C}_{d,\mu} & \mathbf{D}_{d,\mu} \end{array} \right]. \quad (2.80)$$

Note that the number of lifting samples is  $N = \nu$  in SISO systems but it is not the case in MIMO systems, see [44]. By inverting the state equation of  $\mathbf{G}_{d,\mu}$ , the input  $\mathbf{u}$  generated by the multirate feedforward controller with additive decomposition is given by

$$\begin{aligned} \mathbf{u}[k] &= \mathcal{L}_N^{-1} \left( \mathbf{B}_{d,\mu}^{-1} \hat{\mathbf{x}}_\mu[i_N + 1] - \mathbf{B}_{d,\mu}^{-1} \mathbf{A}_{d,\mu} \hat{\mathbf{x}}_\mu[i_N] \right) \\ &= \mathcal{L}_N^{-1} \mathbf{B}_{d,\mu}^{-1} (\mathbf{I} - z^{-N} \mathbf{A}_{d,\mu}) \hat{\mathbf{x}}_\mu[i_N + 1], \end{aligned} \quad (2.81)$$

where  $\hat{\mathbf{x}}_\mu[i_N] = \mathcal{S}_N \mathbf{T}_\nu \mathbf{T}_\mu \hat{\mathbf{x}}_{mod}(t)$ . The generated feedforward input  $\mathbf{u}$  provides perfect state tracking for every  $N$  sample for the states corresponding to the selected modes  $\mu$ .

Note that although perfect state tracking for selected states does not guarantee perfect output tracking, it can provide better intersample performance because the desired state trajectory is generated by the model with full states, and the reference sampling frequency for selected  $\nu$  states becomes higher to  $1/N\delta$  where  $N \leq \nu \leq n$ .

### 2.4.3 Multirate feedforward control with multiplicative decomposition

The overview of multirate feedforward control with multiplicative decomposition [43] is shown in Fig. 2.3. The one-sample forward shifted system  $\tilde{\mathbf{G}}_{d,mod} \stackrel{z}{=} (\tilde{\mathbf{A}}_{d,mod}, \tilde{\mathbf{B}}_{d,mod}, \tilde{\mathbf{C}}_{d,mod}, \tilde{\mathbf{D}}_{d,mod})$  of the discrete-time system in modal form  $\mathbf{G}_{d,mod} \stackrel{z}{=} (\mathbf{A}_{d,mod}, \mathbf{B}_{d,mod}, \mathbf{C}_{d,mod}, \mathbf{O}) = \mathcal{S} \mathbf{G}_{c,mod} \mathcal{H}$  from  $\mathbf{u}[k]$  to  $\mathbf{y}[k + 1]$  is given by

$$\left[ \begin{array}{c|c} \tilde{\mathbf{A}}_{d,mod} & \tilde{\mathbf{B}}_{d,mod} \\ \hline \tilde{\mathbf{C}}_{d,mod} & \tilde{\mathbf{D}}_{d,mod} \end{array} \right] = \left[ \begin{array}{c|c} \mathbf{A}_{d,mod} & \mathbf{B}_{d,mod} \\ \hline \mathbf{C}_{d,mod} \mathbf{A}_{d,mod} & \mathbf{C}_{d,mod} \mathbf{B}_{d,mod} \end{array} \right]. \quad (2.82)$$

When  $\nu$  states corresponding to the modes  $\mu$  are selected,

$$\mathbf{\Pi} = \mathbf{S} \begin{bmatrix} \mathbf{I}_\nu & \mathbf{O}_{\nu \times (n-\nu)} \\ \mathbf{O}_{(n-\nu) \times \nu} & \mathbf{O}_{(n-\nu)} \end{bmatrix} \mathbf{S}^{-1} \quad (2.83)$$

is defined with full rank  $\mathbf{S} = [\mathbf{V} \ \mathbf{V}_\times]$ , where  $\mathbf{V} \in \mathbb{R}^{n \times \nu}$  and  $\mathbf{V}_\times \in \mathbb{R}^{n \times (n-\nu)}$  are a column space of an invariant subspace of  $\mathbf{A} = \tilde{\mathbf{A}}_{d,mod}$  and  $\mathbf{A}_\times = \tilde{\mathbf{A}}_{d,mod} - \tilde{\mathbf{B}}_{d,mod} \tilde{\mathbf{D}}_{d,mod}^{-1} \tilde{\mathbf{C}}_{d,mod}$  that correspond to the poles of  $\mathbf{G}_{mr}$  and the zeros of  $\mathbf{G}_{sr}$ . Then the state-space realizations are given by

$$\mathbf{G}_{mrf} \stackrel{z}{=} \left[ \begin{array}{c|c} \tilde{\mathbf{A}}_{d,mod} & \mathbf{\Pi} \tilde{\mathbf{B}}_{d,mod} \tilde{\mathbf{D}}_{d,mod}^{-1} \\ \hline \tilde{\mathbf{C}}_{d,mod} & \mathbf{I} \end{array} \right], \quad (2.84)$$

$$\mathbf{G}_{srf} \stackrel{z}{=} \left[ \begin{array}{c|c} \tilde{\mathbf{A}}_{d,mod} & \tilde{\mathbf{B}}_{d,mod} \\ \hline \tilde{\mathbf{C}}_{d,mod} (\mathbf{I} - \mathbf{\Pi}) & \tilde{\mathbf{D}}_{d,mod} \end{array} \right]. \quad (2.85)$$

Let the permutation matrix  $\mathbf{T}_\mu$  be such that

$$\mathcal{T}(\mathbf{G}_{mrf}, \mathbf{T}_\mu) \stackrel{z}{=} \left[ \begin{array}{cc|c} \mathbf{A}_{mr} & \mathbf{O} & \mathbf{B}_{mr} \\ \mathbf{O} & \mathbf{A}_{sr} & \mathbf{O} \\ \hline \mathbf{C}_{mr} & \mathbf{C}_{mrr} & \mathbf{I} \end{array} \right], \quad (2.86)$$

$$\mathcal{T}(\mathbf{G}_{srf}, \mathbf{T}_\mu) \stackrel{z}{=} \left[ \begin{array}{cc|c} \mathbf{A}_{mr} & \mathbf{O} & \mathbf{B}_{srr} \\ \mathbf{O} & \mathbf{A}_{sr} & \mathbf{B}_{sr} \\ \hline \mathbf{O} & \mathbf{C}_{sr} & \mathbf{D}_{sr} \end{array} \right]. \quad (2.87)$$

$\mathbf{G}_{mr}$  with states  $\mathbf{x}_{mr}$  and  $\mathbf{G}_{sr}$  with states  $\mathbf{x}_{sr}$  are given by

$$\mathbf{G}_{mr} \stackrel{z}{=} \left[ \begin{array}{c|c} \mathbf{A}_{mr} & \mathbf{B}_{mr} \\ \hline \mathbf{C}_{mr} & \mathbf{I} \end{array} \right], \quad (2.88)$$

$$\mathbf{G}_{sr} \stackrel{z}{=} \left[ \begin{array}{c|c} \mathbf{A}_{sr} & \mathbf{B}_{sr} \\ \hline \mathbf{C}_{sr} & \mathbf{D} \end{array} \right]. \quad (2.89)$$

The product of the system  $\mathbf{H}_1 = (\mathbf{A}_1, \mathbf{B}_1, \mathbf{C}_1, \mathbf{D}_1)$  and  $\mathbf{H}_2 = (\mathbf{A}_2, \mathbf{B}_2, \mathbf{C}_2, \mathbf{D}_2)$  is generally defined as

$$\mathbf{H}_1 \mathbf{H}_2 = \left[ \begin{array}{cc|c} \mathbf{A}_1 & \mathbf{B}_1 \mathbf{C}_2 & \mathbf{B}_1 \mathbf{D}_2 \\ \mathbf{O} & \mathbf{A}_2 & \mathbf{B}_2 \\ \hline \mathbf{C}_1 & \mathbf{D}_1 \mathbf{C}_2 & \mathbf{D}_1 \mathbf{D}_2 \end{array} \right]. \quad (2.90)$$

The state transformation matrix  $\mathbf{T}_{ms}$  is given by

$$\mathbf{T}_{ms} = \left[ \begin{array}{cc} \mathbf{I}_\nu & \mathbf{X} \\ \mathbf{O}_{\nu \times (n-\nu)} & \mathbf{I}_{(n-\nu)} \end{array} \right]^{-1}, \quad (2.91)$$

where  $\mathbf{X} \in \mathbb{R}^{\nu \times (n-\nu)}$  is the solution of the Sylvester equation

$$\mathbf{A}_{mr} \mathbf{X} - \mathbf{X} \mathbf{A}_{sr} = \mathbf{B}_{mr} \mathbf{C}_{sr}. \quad (2.92)$$

$\tilde{\mathbf{G}}_{ms} \stackrel{z}{=} (\tilde{\mathbf{A}}_{ms}, \tilde{\mathbf{B}}_{ms}, \tilde{\mathbf{C}}_{ms}, d) = \mathcal{T}(\tilde{\mathbf{G}}_{d,mod}, \mathbf{T}_{ms}\mathbf{T}_\mu) = \mathbf{G}_{mr}\mathbf{G}_{sr}$  is given by

$$\left[ \begin{array}{c|c} \tilde{\mathbf{A}}_{ms} & \tilde{\mathbf{B}}_{ms} \\ \hline \tilde{\mathbf{C}}_{ms} & \mathbf{D} \end{array} \right] = \left[ \begin{array}{cc|c} \mathbf{A}_{mr} & \mathbf{B}_{mr}\mathbf{C}_{sr} & \mathbf{B}_{mr}d \\ \mathbf{O} & \mathbf{A}_{sr} & \mathbf{B}_{sr} \\ \hline \mathbf{C}_{mr} & \mathbf{C}_{sr} & \mathbf{D} \end{array} \right]. \quad (2.93)$$

The  $N$  ( $\leq \nu$ ) samples lifted system of  $\mathbf{G}_{mr}$  is given by

$$\underline{\mathbf{G}}_{mr} \stackrel{z^N}{=} \mathcal{L}_N \mathbf{G}_{mr} \mathcal{L}_N^{-1} = \left[ \begin{array}{c|c} \underline{\mathbf{A}}_{mr} & \underline{\mathbf{B}}_{mr} \\ \hline \underline{\mathbf{C}}_{mr} & \mathbf{O} \end{array} \right]. \quad (2.94)$$

Note that the number of lifting samples is  $N = \nu$  in SISO systems but it is not the case in MIMO systems, see [44]. By inverting the state equation of  $\underline{\mathbf{G}}_{mr}$ , the reference for the single-rate inversion  $\mathbf{r}_{sr}$  is given by

$$\begin{aligned} \mathbf{r}_{sr}[k] &= \mathcal{L}_N^{-1} \left( \underline{\mathbf{B}}_{d,mr}^{-1} \hat{\mathbf{x}}_{mr}[i_N + 1] - \underline{\mathbf{B}}_{d,mr}^{-1} \underline{\mathbf{A}}_{d,mr} \hat{\mathbf{x}}_{mr}[i_N] \right) \\ &= \mathcal{L}_N^{-1} \underline{\mathbf{B}}_{d,mr}^{-1} (\mathbf{I} - z^{-N} \underline{\mathbf{A}}_{d,mr}) \hat{\mathbf{x}}_{mr}[i_N + 1], \end{aligned} \quad (2.95)$$

where  $\hat{\mathbf{x}}_{mr}[i_N] = \mathcal{S}_N \mathbf{T}_\nu \mathbf{T}_{ms} \mathbf{T}_\mu \hat{\mathbf{x}}_{mod}(t)$ . Then, the input  $u$  generated by the multirate feedforward controller with multiplicative decomposition is given by

$$\mathbf{u}[k] = \mathbf{G}_{sr}^{-1} \mathbf{r}_{sr}[k], \quad (2.96)$$

where

$$\mathbf{G}_{sr}^{-1} = \left[ \begin{array}{c|c} \mathbf{A}_{sr} - \mathbf{B}_{sr} \mathbf{D}_{sr}^{-1} \mathbf{C}_{sr} & \mathbf{B}_{sr} \mathbf{D}_{sr}^{-1} \\ \hline -\mathbf{D}_{sr}^{-1} \mathbf{C}_{sr} & \mathbf{D}_{sr}^{-1} \end{array} \right]. \quad (2.97)$$

Note that the one-sample backward shifted system of  $\tilde{\mathbf{G}}_{ms}$  is given by

$$\begin{aligned} \mathbf{G}_{ms} &= \mathcal{T}(\mathbf{G}_{d,mod}, \mathbf{T}_{ms}\mathbf{T}_\mu) = \left[ \begin{array}{c|c} \mathbf{A}_{ms} & \mathbf{B}_{ms} \\ \hline \mathbf{C}_{ms} & \mathbf{O} \end{array} \right] \\ &= \left[ \begin{array}{c|c} \tilde{\mathbf{A}}_{ms} & \tilde{\mathbf{B}}_{ms} \\ \hline \tilde{\mathbf{C}}_{ms} \mathbf{A}_{ms}^{-1} & \mathbf{O} \end{array} \right] = \left[ \begin{array}{cc|c} \mathbf{A}_{mr} & \mathbf{B}_{mr}\mathbf{C}_{sr} & \mathbf{B}_{mr}\mathbf{D} \\ \mathbf{O} & \mathbf{A}_{sr} & \mathbf{B}_{sr} \\ \hline \mathbf{C}_{mr}^* & \mathbf{D}_{mr}^* \mathbf{C}_{sr}^* & \mathbf{D}_{mr}^* \mathbf{D} \end{array} \right] \\ &= \left[ \begin{array}{c|c} \mathbf{A}_{mr} & \mathbf{B}_{mr} \\ \hline \mathbf{C}_{mr}^* & \mathbf{D}_{mr}^* \end{array} \right] \left[ \begin{array}{c|c} \mathbf{A}_{sr} & \mathbf{B}_{sr} \\ \hline \mathbf{C}_{sr}^* & \mathbf{D} \end{array} \right], \end{aligned} \quad (2.98)$$

where  $\mathbf{D}_{mr}^* \mathbf{D} = \mathbf{O}$  and the output is given by

$$\mathbf{y}[k] = \mathbf{C}_{mr}^* \mathbf{x}_{mr}[k] + \mathbf{D}_{mr}^* \mathbf{C}_{sr}^* \mathbf{x}_{sr}[k]. \quad (2.99)$$

It shows that the approach provides perfect output tracking for every  $N$  sample with  $\mathbf{D}_{mr}^* = \mathbf{O}$  because the multirate inversion provides perfect state tracking of  $\mathbf{x}_{mr}$  for every  $N$  sample. If the system is decomposed as  $\mathbf{D}_{mr}^* \neq \mathbf{O}$ , there is no perfect output tracking because perfect state tracking of  $\mathbf{x}_{sr}$  is not guaranteed. Therefore,  $\mathbf{V}$  and  $\mathbf{V}_\times$  should be selected such that  $\mathbf{D}_{mr}^* = \mathbf{O}$ .

Table 2.1: Comparison of 8 approaches.  $T_r$  is the reference sampling time.  $G_{c,mr}$  and  $G_{c,sr}$  are the continuous-time model for the multirate and single-rate inversion. Intersample performance is evaluated by the Root Mean Square of the tracking error  $e_{\text{RMS}} = \text{RMS}(e(t))$  with the sampling time  $\delta/20 = 0.5$  ms. The evaluations are conducted by the simulation of  $G_c$  without feedback control,  $\hat{G}$  without feedback control, and  $\hat{G}$  with feedback control, and by the experiment.

Case	Line	Approach	$T_r$	$G_{c,mr}$	$G_{c,sr}$	$G_c$ w/o FB	$\hat{G}$ w/o FB	$\hat{G}$ with FB	Experiment
1	—	Single-rate	$\delta$	-	$G_c$	9862 nm	16 811 nm	17 642 nm	27 152 nm
2	—	Multirate	$4\delta$	$G_c$	-	5174 nm	11 646 nm	12 406 nm	15 027 nm
3	—	Additive	$2\delta$	$G_1$	-	8199 nm	12 176 nm	13 397 nm	17 210 nm
4	—	Additive	$2\delta$	$G_2$	-	>1 mm	>1 mm	-	-
5	—	Multiplicative	$2\delta$	$N_1/D_1$	$N_2/D_2$	9309 nm	11 280 nm	12 510 nm	22 579 nm
6	—	Multiplicative	$2\delta$	$N_2/D_1$	$N_1/D_2$	8559 nm	14 547 nm	-	-
7	—	Multiplicative	$2\delta$	$N_1/D_2$	$N_2/D_1$	9309 nm	11 280 nm	-	-
8	—	Multiplicative	$2\delta$	$N_2/D_2$	$N_1/D_1$	8559 nm	14 547 nm	-	-

## 2.5 Application to multi-modal motion system

In this section, the intersample performance of the perfect tracking control approaches is validated in a multi-modal motion system. The intersample performance is evaluated in both frequency domain and time domain. The nominal and robust performance is verified in the simulation using the model without and with modeling error. The experimental validation is conducted with feedback controller.

### 2.5.1 Conditions

The validation is conducted in a single-input single-output multi-modal motion system in Fig. 2.4. The frequency response of the controlled system is shown in Fig. 2.5. For the verification of the modeling error, the high-order continuous-time model  $\hat{G}$  is given by

$$\begin{aligned} \hat{G}(s) &= \frac{2.44}{s^2} + \frac{1.1}{s^2 + 2 \times 0.024 \times (2\pi \times 30)s + (2\pi \times 30)^2} \\ &+ \frac{-2.44}{s^2 + 2 \times 0.038 \times (2\pi \times 89)s + (2\pi \times 89)^2} + \frac{-1.1}{s^2 + 2 \times 0.07 \times (2\pi \times 297)s + (2\pi \times 297)^2} \\ &= G_1(s) + G_2(s) + G_3(s) + G_4(s). \end{aligned} \quad (2.100)$$

For the controller design, a low-order continuous-time model  $G_c$  is given by

$$\begin{aligned} G_c(s) &= G_1(s) + G_2(s) = \frac{2.44}{s^2} + \frac{1.1}{s^2 + 2 \times 0.024 \times (2\pi \times 30)s + (2\pi \times 30)^2} \\ &= \frac{3.54}{s^2} \times \frac{s^2 + 2 \times 0.02 \times (2\pi \times 25)s + (2\pi \times 25)^2}{s^2 + 2 \times 0.024 \times (2\pi \times 30)s + (2\pi \times 30)^2} = \frac{N_1(s)}{D_1(s)} \times \frac{N_2(s)}{D_2(s)}. \end{aligned} \quad (2.101)$$

The controller is designed by the low-order continuous-time model  $G_c$  and the continuous-time performance is verified by the simulation in the low-order continuous-time model  $G_c$  without modeling error and the high-order continuous-time model  $\hat{G}$  with modeling error. The verification is conducted in both frequency domain and time domain. The sampling time of the controller is  $\delta = 10$  ms. The intersample performance is evaluated in the sampling time  $\delta/20 = 0.5$  ms. The compared 8 approaches are shown in Table 2.1.

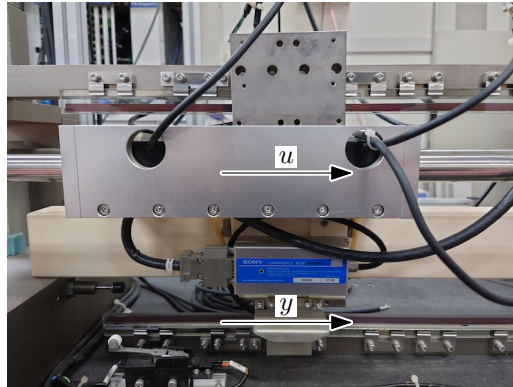


Fig. 2.4: High-precision positioning stage with input current  $u$  [A] generating force with linear motor and output displacement  $y$  [m] measured by linear encoder with 1 nm resolution.

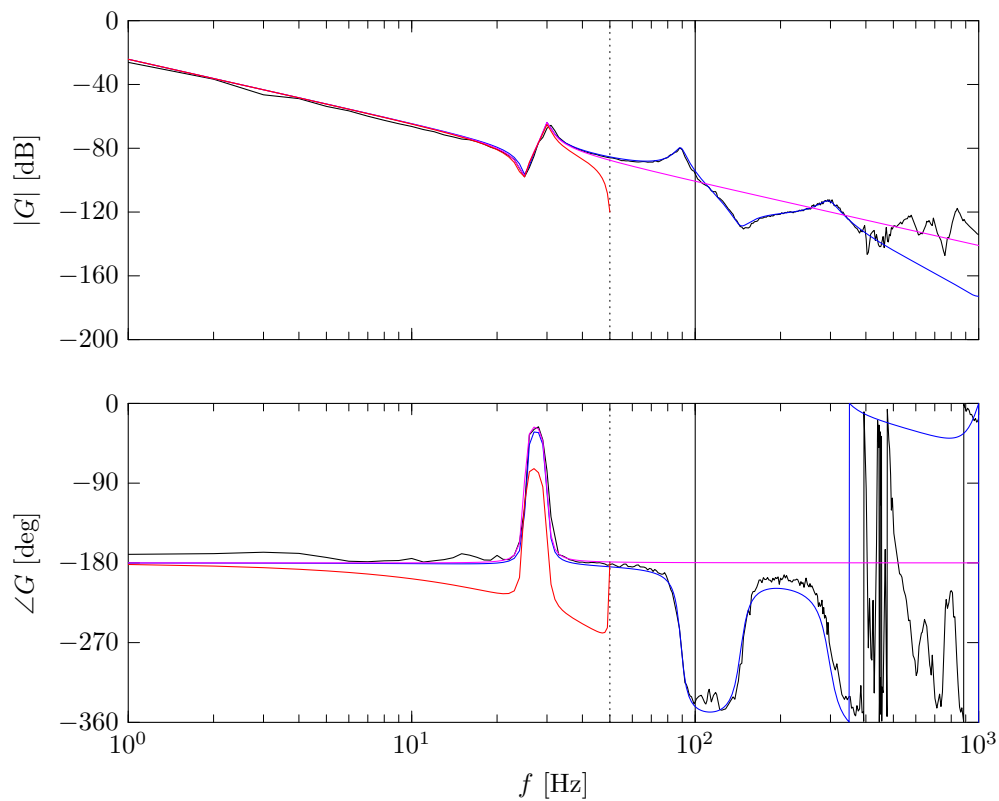


Fig. 2.5: Bode diagram of the controlled system: frequency response data (—), a high-order continuous-time model  $\hat{G}$  (—), a low-order continuous-time model  $G_c$  (—), and a low-order discrete-time model for controller design  $G_d$  (—). Vertical lines (---) and (—) show Nyquist frequency  $1/2\delta$  and sampling frequency  $1/\delta$ , respectively.

## 2.5.2 Frequency domain verification

In frequency domain verification, the intersample performance is verified by the performance frequency gain  $|E_r|$  [47–49] in the simulation that is the steady state continuous-time tracking error normalized by the step sine wave reference and is defined as

$$|E_r(j\omega)| = \frac{\text{RMS}(e_{j\omega}(t))}{\text{RMS}(r_{j\omega}(t))}, \quad (2.102)$$

where  $r_{j\omega}(t)$  can only contain a single frequency at each frequency and the intersample performance is evaluated in the sampling time  $\delta/20 = 0.5$  ms.

The performance frequency gain of the continuous-time tracking error in  $G_c$  without modeling error is shown in Fig. 2.6. It shows that Case 5 = Case 7 and Case 6 = Case 8 in the performance frequency gain. It is because the discretization only affects the dynamics of zeros, and the choice of the pole does not affect the performance. Case 4 makes a large error for the whole frequency range because it cannot compensate for rigid body dynamics. The approaches like Case 1, Case 6, and Case 8 that cannot compensate for oscillating poles of the feedforward controller due to discretization make large errors around Nyquist frequency. In low frequency,  $|E_r|$  is smaller in order of Case 1 < Case 5 = Case 7 < Case 2 < Case 3. From these analyses, Case 2 with multirate feedforward control for full-state tracking provides the best performance in steady state, and Case 2, Case 3, Case 5, and Case 7 are preferable approaches.

The performance frequency gain of the continuous-time tracking error in  $\hat{G}$  with modeling error is shown in Fig. 2.7. There is the same trend around Nyquist frequency compared to the simulation in  $G_c$  without modeling error. In low frequency,  $|E_r|$  is around the same performance in all approaches except Case 4. It is because the controller cannot compensate for the low-frequency compliance of the unmodeled high-frequency dynamics.

## 2.5.3 Time domain verification

In the time domain verification, the intersample performance is verified by the continuous-time tracking error in the simulation for the continuous-time reference trajectory shown in Fig. 2.8. The intersample performance is evaluated by Root Mean Square error  $e_{\text{RMS}} = \text{RMS}(e(t))$  in Table 2.1 with the sampling time  $\delta/20 = 0.5$  ms.

The time series error  $e(t)$  in  $G_c$  without modeling error is shown in Fig. 2.9. The result shows that Case 2 achieves the best performance because there is no modeling error between the controller and the controlled system and perfect tracking for all states provides smooth intersample behavior.

The time series error  $e(t)$  in  $\hat{G}$  with modeling error is shown in Fig. 2.10. The result shows that Case 5 and Case 7 achieve the best performance because the control input contains relatively low-frequency components compared to Case 2, and it does not excite the resonances of the unmodeled dynamics. The performance of Case 1, Case 6, and Case 8 is getting worse in  $\hat{G}$  because the oscillating feedforward input due to discretization excites the unmodeled high-frequency dynamics. From these analyses, multirate feedforward control with mode decomposition can provide better intersample performance in transient response than that of multirate feedforward control for full-state tracking.

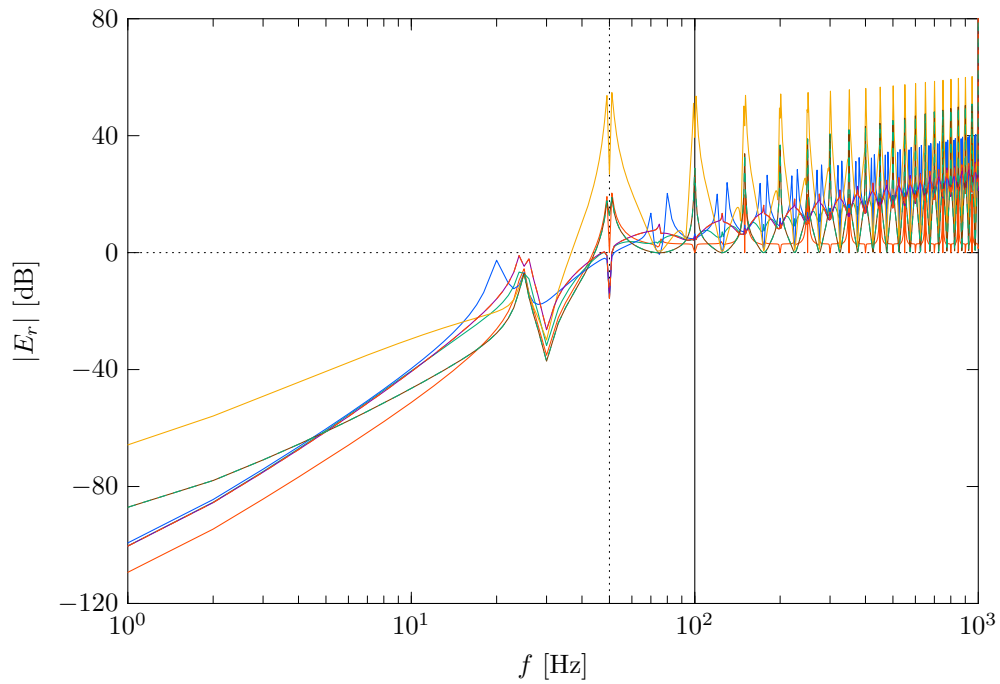


Fig. 2.6: Performance frequency gain of the continuous-time tracking error in  $G_c$ . Vertical lines (----) and (—) show Nyquist frequency  $1/2\delta$  and sampling frequency  $1/\delta$ , respectively.

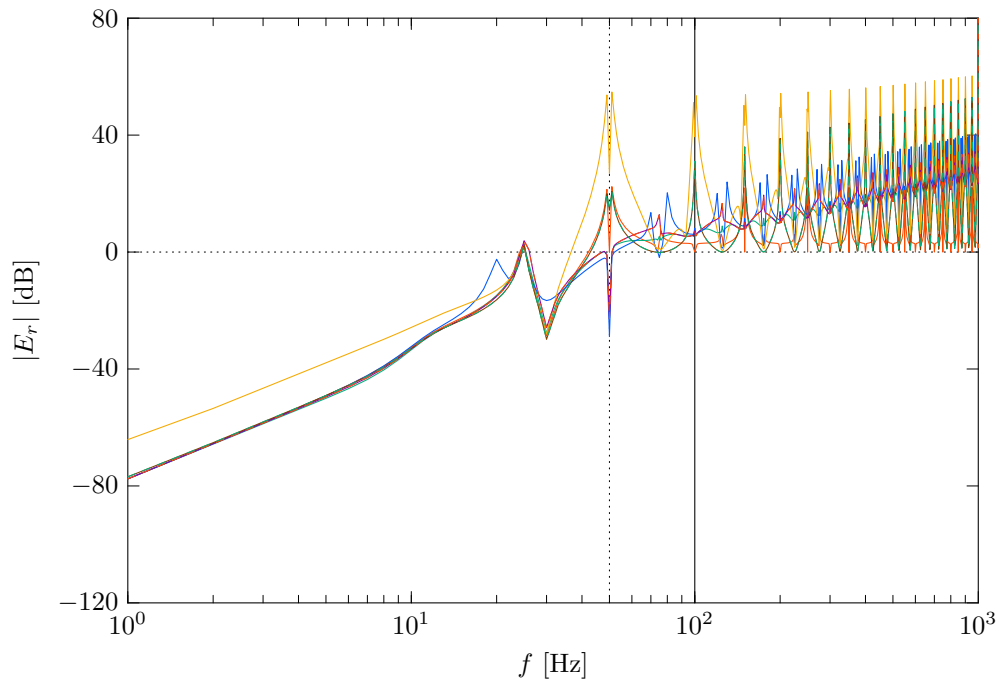


Fig. 2.7: Performance frequency gain of the continuous-time tracking error in  $\hat{G}$ . Vertical lines (----) and (—) show Nyquist frequency  $1/2\delta$  and sampling frequency  $1/\delta$ , respectively.

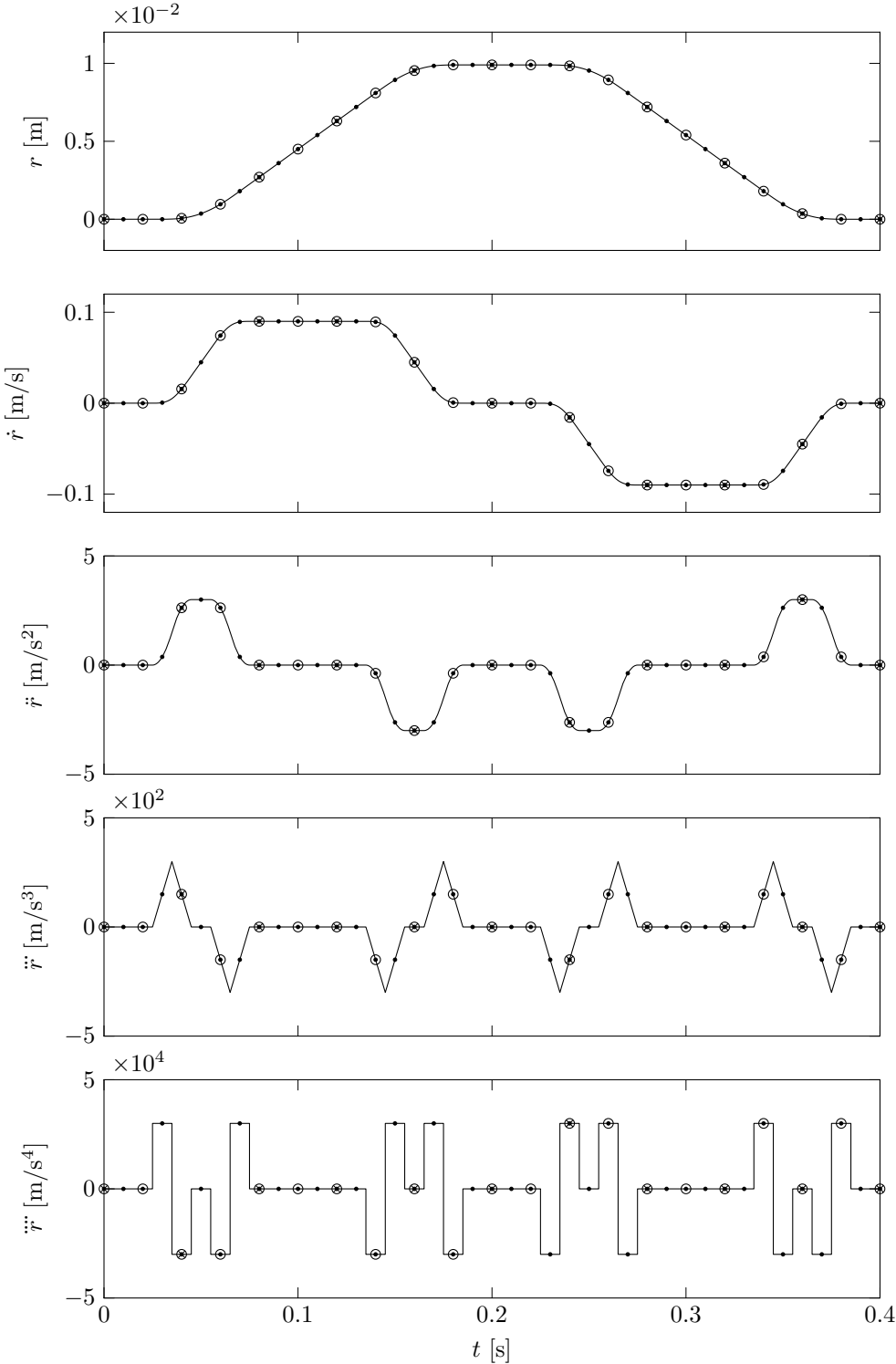


Fig. 2.8: Continuous-time 4<sup>th</sup> order polynomial trajectory reference  $r(t)$  and its derivatives. (•), (◦), and (×) show sampling points every  $\delta$ ,  $2\delta$ , and  $4\delta$ .



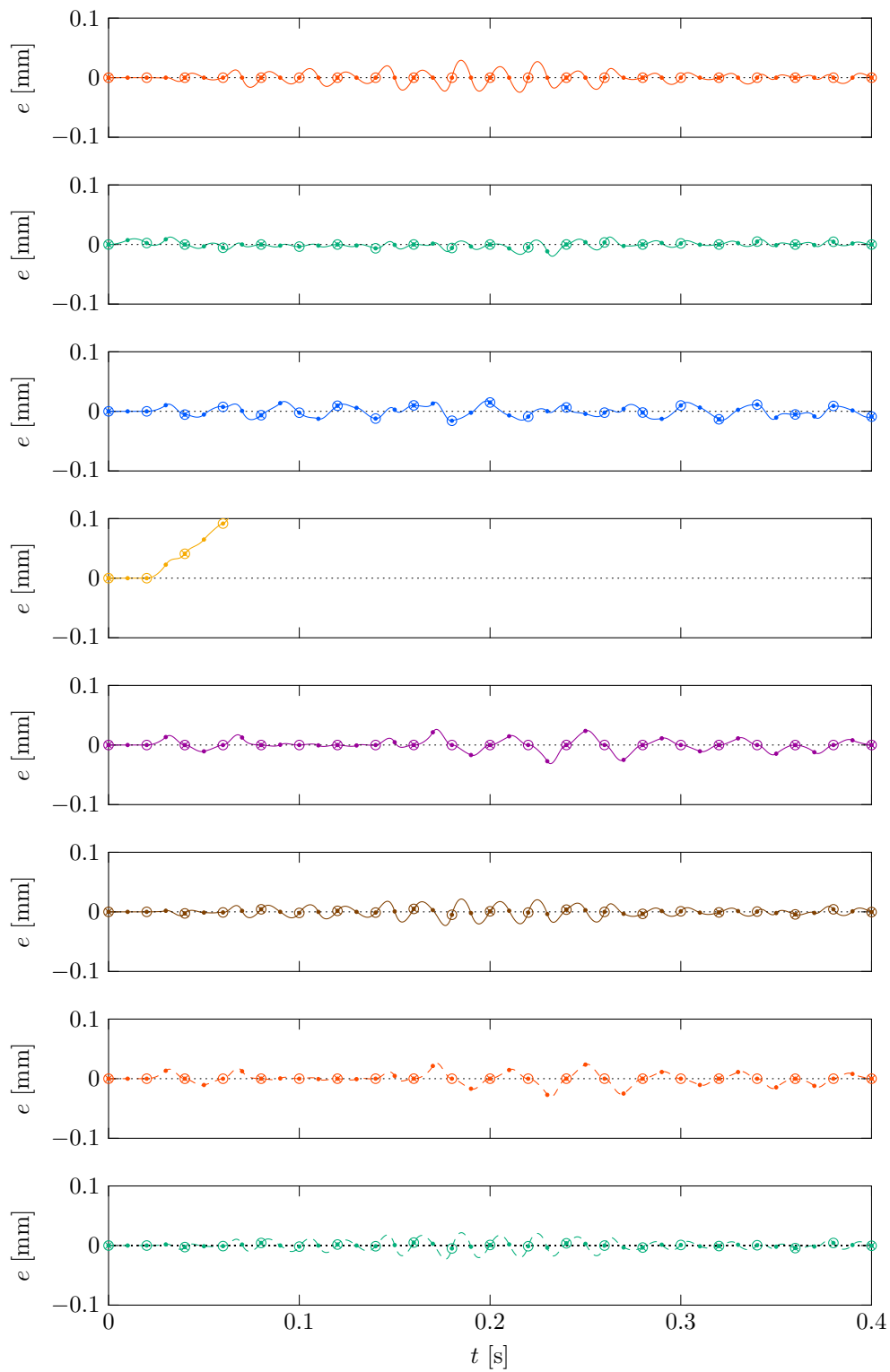


Fig. 2.9: Error  $e(t)$  in the simulation of  $G_c$  with sampling time  $\delta/20 = 0.5$  ms.  $(\bullet)$ ,  $(\circ)$ , and  $(\times)$  show sampling point every  $\delta$ ,  $2\delta$ , and  $4\delta$ .

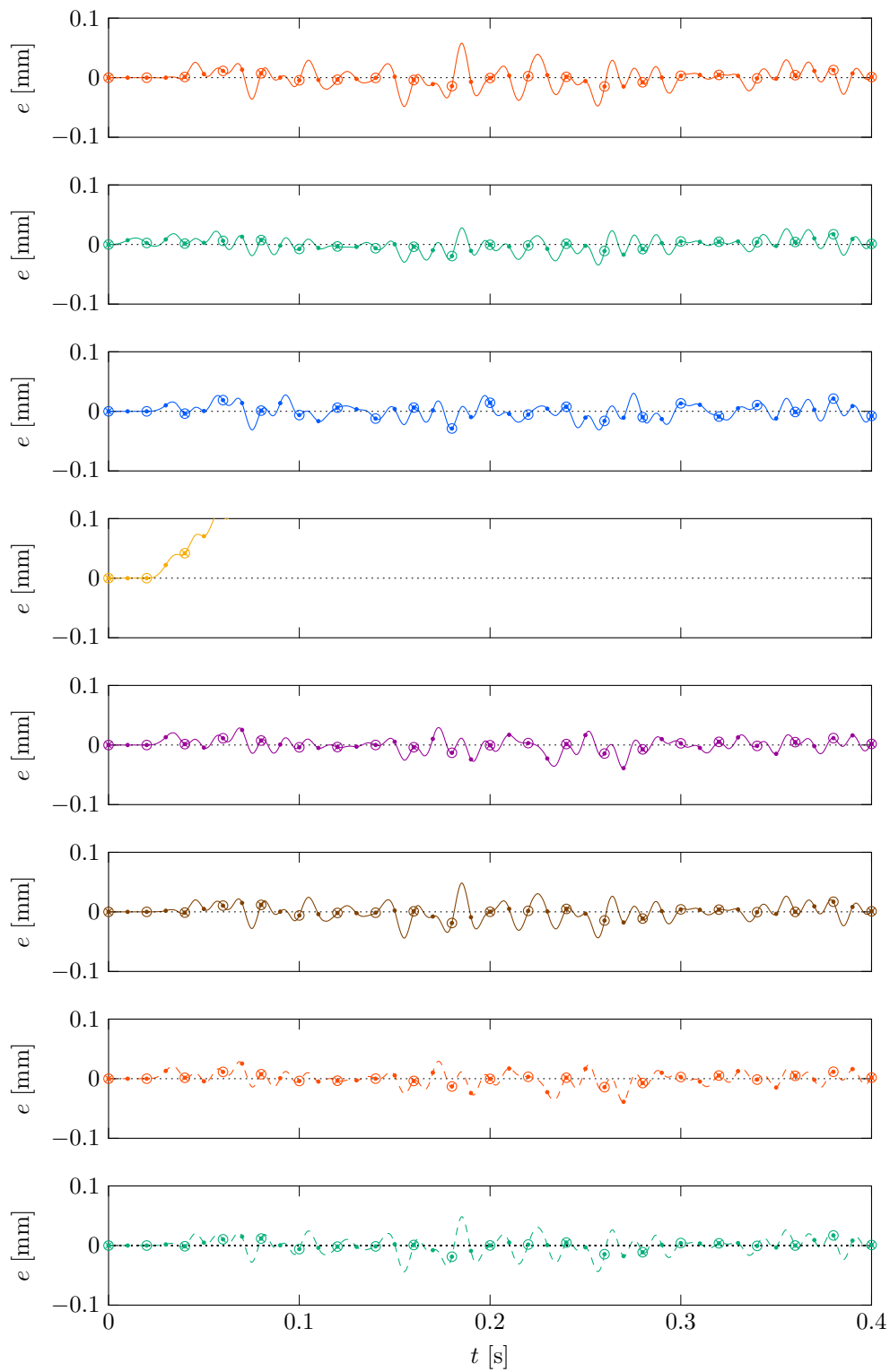


Fig. 2.10: Error  $e(t)$  in the simulation of  $\hat{G}$  with sampling time  $\delta/20 = 0.5$  ms.  $(*)$ ,  $(o)$ , and  $(x)$  show sampling point every  $\delta$ ,  $2\delta$ , and  $4\delta$ .

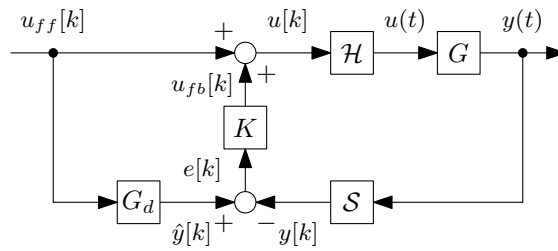


Fig. 2.11: Block diagram of the experimental validation.  $G$ ,  $G_d$ ,  $K$ ,  $S$  and  $\mathcal{H}$  denote a controlled system, a low-order discrete-time model for controller design, a feedback controller, sampler and zero-order-hold, respectively.

### 2.5.4 Experimental validation

From the result of the simulation verification, the experimental validation is conducted in Case 1, Case 2, Case 3, and Case 5 as shown in Table 2.1 with the same reference that is shown in Fig. 2.8. The overview of the experimental validation is shown in Fig. 2.11. A feedback controller  $K$  is used for stabilization and compensation for low-frequency modeling errors in the experimental validation. For the feedback controller, the PD controller is designed as 5 Hz bandwidth and 6 dB modulus margin. The simulation with the feedback controller and the quantization of the linear encoder is also conducted for the validation of the experimental results.

The time series error  $e(t)$  in the experiment is shown in Fig. 2.12. The result has a similar trend to the simulation in  $\hat{G}$  with feedback control. Note that due to experimental conditions such as model mismatches, the exact on-sample tracking is not provided. The intersample performance is evaluated by Root Mean Square error  $e_{\text{RMS}} = \text{RMS}(e(t))$  in Table 2.1 with the sampling time  $\delta/20 = 0.5$  ms. It shows that Case 2 with multirate feedforward control for full-state tracking provides the best performance in simulation and experiment with feedback control. The amplitude spectrum of error  $e(t)$  in the experiment is shown in Fig. 2.13. The result shows that Case 1 and Case 5 which contain single-rate filters have a large error in over sampling frequency because the frequency components of the feedforward input over sampling frequency excite the unmodeled high-frequency dynamics.

## 2.6 Conclusion

In this chapter, perfect tracking control approaches are described focusing on intersample performance in multi-modal motion systems. The model of the multi-modal motion system is decomposed into combinations of the states that can be selected for the perfect tracking control. The simulation verification and experimental validation in a multi-modal motion system show that state tracking should be used to compensate for the oscillating poles of the feedforward controller due to discretization. In summary, the feedforward controller to improve intersample performance should be designed with the following conditions.

- State tracking approach can compensate for oscillating poles of the feedforward controller due to discretization when the relative degree of the model is more than 2.
- For steady-state performance without modeling error, multirate feedforward control for full-state tracking provides the best performance.

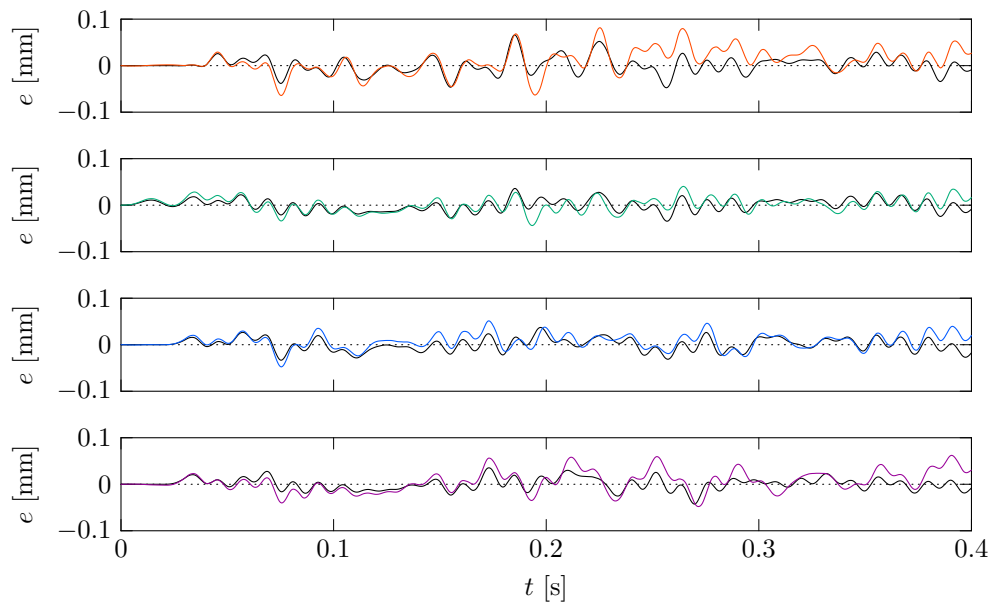


Fig. 2.12: Error  $e(t)$  in the experiment with sampling time  $\delta/20 = 0.5$  ms. The solid black line shows that in the simulation of  $\hat{G}$  with feedback control.

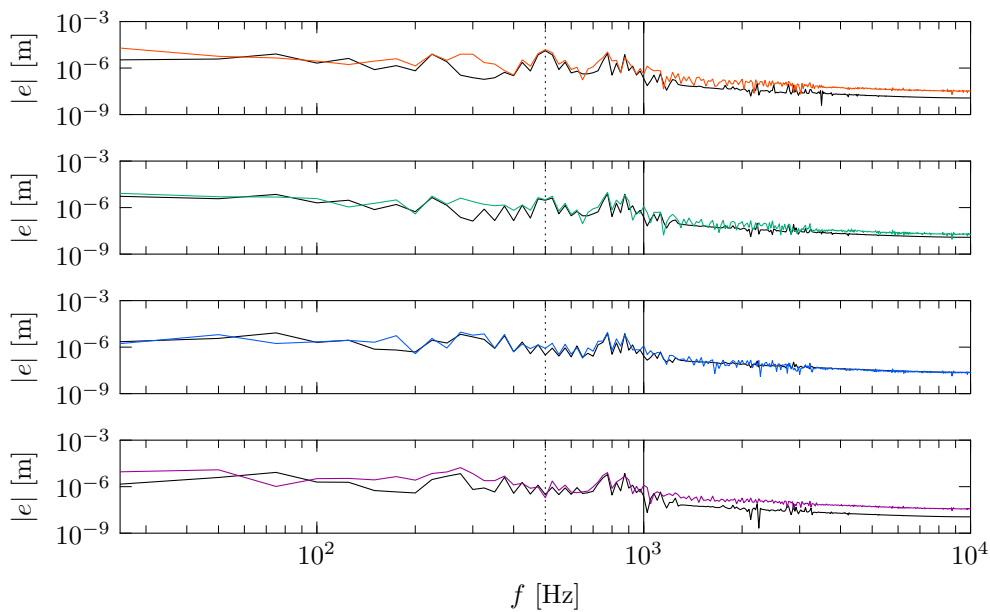


Fig. 2.13: Amplitude spectrum of error  $e(t)$  in the experiment with sampling time  $\delta/20 = 0.5$  ms. The solid black line shows that in the simulation of  $\hat{G}$  with feedback control. Vertical lines (----) and (—) show Nyquist frequency  $1/2\delta$  and sampling frequency  $1/\delta$ , respectively.

- Multirate feedforward control with mode decomposition can provide the best intersample performance in transient response depending on the frequency components of the reference and the unmodeled dynamics of the controlled system.

Ongoing research focuses on the optimal mode selection depending on the reference signal in higher-order motion systems.

# Chapter 3

## MIMO Multirate Feedforward Control with Generalized Controllability Indices

Inversion-based feedforward control is a basic method of tracking controls. The aim of this chapter is to design MIMO multirate feedforward controller that improves continuous-time tracking performance in MIMO LTI systems considering not only on-sample but also intersample behavior. Several types of MIMO multirate feedforward controllers are designed and evaluated in terms of the 2-norm of the control inputs. The approach is compared with a conventional MIMO single-rate feedforward controller in simulations. The interaction compensation is compared with a conventional SISO multirate feedforward controller in experiments. The approach improves the intersample behavior through the optimal selection of input multiplicities with MIMO multirate system inversion.

### 3.1 Introduction

Inversion-based feedforward controllers play an important role in the tracking control of many high-precision mechatronic systems, such as wafer and LCD scanners, and industrial robots [50]. For the demands of high-performance, high-speed, and flexible tasks, many high-precision mechatronic systems have multiple degree-of-freedom and are multi-input multi-output (MIMO) systems.

Many high-precision mechatronic systems are usually controlled by single-input single-output (SISO) controllers under the assumption that they are mechanically decoupled, and coupling problems between each axis can be ignored. Several high-precision mechatronic systems with severe coupling problem between each axis, such as a 6-degree-of-freedom high-precision positioning stage, are controlled with MIMO controllers, such as SISO controllers with a continuous-time pre-compensator [51], feedforward input shaping approach [52], and feedforward  $H_\infty$  approach [53]. However, these continuous-time controllers are usually discretized by Tustin transform for digital implementation. Therefore, the effect of discretization by sampler and zero-order-hold is not strictly considered and perfect tracking control cannot be achieved for a discrete-time model.

In high-precision positioning systems with multiple actuators and sensors, such as a 6-degree-of-freedom high-precision positioning stage, it is common that the number of actuators and sensors are imaginarily converted by coordinate transformation to the same number of degrees of freedom of motion [51]. In this framework, this chapter mainly focuses on MIMO linear-time-invariant (LTI) systems with an equal number of inputs and outputs. For the tracking control

of MIMO LTI systems, MIMO feedforward controllers are needed to achieve good tracking performance by considering the coupling problems and redundancy of MIMO LTI systems.

The continuous-time inversion-based approaches such as [54–56] can be used for continuous-time systems. However, practical tracking controllers are often implemented by digital systems for large flexibility and low-cost [15]. Therefore, the tracking control is conducted with digital control and has some limitations attributed to discretization. The main problem of the inversion-based feedforward controllers is the unstable discretized zeros, which are out of the unit circle on the  $z$  plane, of the controlled system discretized by a sampler and a holder. The inversion-based feedforward controllers are designed by the inverse of controlled systems and they have unstable poles due to the unstable zeros of the controlled systems.

To overcome the discretized unstable zero problems, several approximated inverse approaches are presented in the single-rate feedforward control, such as nonminimum-phase zeros ignore (NPZI) [57], zero phase error tracking control (ZPETC) [35] and zero magnitude error tracking controller (ZMETC) method [58]. However, these methods cannot achieve the exact tracking at sampling points because of the approximation.

An exact inverse approach, discrete-time stable inversion [39], is presented, but this method cannot cope with the discretized zeros around  $z = -1$  that become oscillating poles of the inversion-based feedforward controllers [59, 60]. It is noted that these single-rate feedforward control approaches can be extended to MIMO LTI systems [61, 62]. FIR filter tuning with a gradient approximation-based algorithm is presented for decoupling control of MIMO systems with a discrete-time controller [63]. However, this approach uses an optimization in the algorithm and it is not suitable when many kinds of references are used.

Based on these approaches in the single-rate feedforward control, a multirate control approach is presented [20]. Compared with the single-rate system, the multirate system has all zeros at  $z = 0$ . Therefore, the multirate feedforward controller has all poles at  $z = 0$ , and exact on-sample tracking can be achieved, and intersample behavior is also improved.

Although several multirate control approaches have been developed, the optimal design for redundancy of the multiple inputs in MIMO systems is not presented. Previous researches show that the multirate feedforward control approach can be extended from the SISO LTI systems to the MIMO LTI systems [48]. MIMO multirate feedforward controller is effective to reject cross-coupling effects compared with the basic pre-compensator approach [64]. The MIMO multirate feedforward controller can be designed for several kinds because of the redundancy of MIMO LTI systems and multirate sampling periods. In this chapter, a procedure of designing an optimal MIMO multirate feedforward controller is presented.

The main contributions of this chapter are as follows.

**Contribution 3.1 :** *The redundancy of multiple inputs in MIMO systems is optimized by evaluating the control input for the normalized state vector.*

**Contribution 3.2 :** *The performance improvement of the MIMO multirate feedforward controller considering the sampled-data dynamics is demonstrated by the comparison between the MIMO single-rate feedforward controller.*

**Contribution 3.3 :** *The performance improvement of the MIMO multirate feedforward controller considering the interaction compensation is demonstrated by the comparison between the SISO multirate feedforward controller.*

The outline is as follows. In Section 3.2, the problem of tracking with digital control is formulated. In Section 3.3, the conventional MIMO single-rate feedforward control approach and

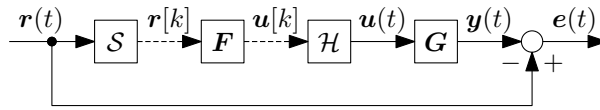


Fig. 3.1: Block diagram of tracking control. The continuous-time system  $G$  is controlled by the discrete-time controller  $F$  with sampler  $S$  and zero-order-hold  $\mathcal{H}$ . The objective is to minimize the continuous-time error  $e(t)$ .

its limitations are presented before introducing the proposed method. In Section 3.4, the proposed MIMO multirate feedforward control approach is presented. In Section 3.5, the advantages of the approach in the continuous-time tracking performance are demonstrated by application to a MIMO motion system in the simulation. In Section 3.6, the advantages of the approach in the interaction compensation are demonstrated by application to a MIMO motion system in the experiment. In Section 3.7, the conclusion of this chapter is presented.

## 3.2 Problem formulation

In this section, the control problem is formulated. The overview of tracking control is shown in Fig. 3.1.

### 3.2.1 Definition of multi-input multi-output system

The state equation and the output equation of an  $m$ -input  $m$ -output  $n^{\text{th}}$  order continuous-time linear time-invariant system  $G_c$  are given by

$$\dot{\mathbf{x}}(t) = \mathbf{A}_c \mathbf{x}(t) + \mathbf{B}_c \mathbf{u}(t), \quad (3.1)$$

$$\mathbf{y}(t) = \mathbf{C}_c \mathbf{x}(t), \quad (3.2)$$

$$\mathbf{B}_c = [\mathbf{b}_{c_1} \quad \cdots \quad \mathbf{b}_{c_m}], \quad \mathbf{C}_c = [\mathbf{c}_{c_1} \quad \cdots \quad \mathbf{c}_{c_m}]^T,$$

where the state variables are  $\mathbf{x}(t) \in \mathbb{R}^{n \times 1}$ , inputs are  $\mathbf{u}(t) \in \mathbb{R}^{m \times 1}$ , outputs are  $\mathbf{y}(t) \in \mathbb{R}^{m \times 1}$ , and the matrices are  $\mathbf{A}_c \in \mathbb{R}^{n \times n}$ ,  $\mathbf{B}_c \in \mathbb{R}^{n \times m}$ , and  $\mathbf{C}_c \in \mathbb{R}^{m \times n}$ . this chapter mainly focuses on the MIMO LTI systems that have the same number of inputs and outputs. This is a natural assumption for mechatronic systems to achieve both state controllability and hardware cost reduction.

### 3.2.2 Discretization and sampling periods

The discrete-time system  $G_d$  discretized by sampler and zero-order-hold with  $G_c$  and the generalized sampling period  $\delta$  is given by

$$\mathbf{x}[k+1] = \mathbf{A}_d \mathbf{x}[k] + \mathbf{B}_d \mathbf{u}[k], \quad (3.3)$$

$$\mathbf{y}[k] = \mathbf{C}_d \mathbf{x}[k], \quad (3.4)$$

where  $k \in \mathbb{Z}$ .  $\mathbf{A}_d$ ,  $\mathbf{B}_d$ , and  $\mathbf{C}_d$  are given by

$$\mathbf{A}_d = e^{\mathbf{A}_c \delta}, \quad \mathbf{B}_d = \int_0^\delta e^{\mathbf{A}_c \tau} \mathbf{B}_c d\tau, \quad \mathbf{C}_d = \mathbf{C}_c. \quad (3.5)$$

In the discrete-time system, three sampling periods exist,  $T_r$ ,  $T_y$ , and  $T_u$ , which represent the sampling periods of a reference  $r(t)$ , an output  $y(t)$ , and a control input  $u(t)$ , respectively. Three sampling periods  $T_r$ ,  $T_y$ , and  $T_u$  are the same in the single-rate system and are different in the multirate system.

### 3.2.3 Perfect tracking control and intersample behavior

In the problem of tracking control, the discrete-time controller  $F$  should be designed as  $G_d F = I$ , where  $G_d = S G_c \mathcal{H}$ , at every sampling point and achieves perfect tracking control.

The perfect tracking control is defined as follows [35].

**Definition 3.1 :** *The perfect tracking control is defined as a method with which the plant output perfectly tracks the desired trajectory with zero tracking error at every sampling point.*

It is important that the perfect tracking control only guarantees the tracking error on the discrete-time sampling points, but not in the continuous-time. In the problem of tracking control, the objective is to minimize the continuous-time error  $e(t)$ . Therefore, not only on-sample tracking error but also intersample tracking error should be considered in the design of the discrete-time controller  $F$ .

### 3.2.4 Problem description

In this chapter, the feedforward controller is designed with respect to the following requirements.

**Requirement 3.1 :** *The redundancy of the multiple inputs should be optimized in designing the MIMO multirate feedforward controller.*

**Requirement 3.2 :** *The sampled-data characteristics of the system discretized by sampler and zero-order-hold should be considered to improve the continuous-time tracking performance.*

**Requirement 3.3 :** *The coupling dynamics of the MIMO system should be compensated by the MIMO feedforward controller design.*

For comparison, two types of discrete-time controllers are described in this chapter, the first is a single-rate feedforward controller and the second is a multirate feedforward controller.

## 3.3 Single-rate feedforward control for multi-input multi-output system

The single-rate system  $G_s$  discretized by sampler and zero-order-hold with  $G_c$  and the sampling period  $\delta = T_u$  is given by

$$\mathbf{x}[k+1] = \mathbf{A}_s \mathbf{x}[k] + \mathbf{B}_s \mathbf{u}[k], \quad (3.6)$$

$$\mathbf{y}[k] = \mathbf{C}_s \mathbf{x}[k]. \quad (3.7)$$

From the state-space representation of the single-rate system  $G_s$ , control inputs  $\mathbf{u}_{ff}[k]$  of the single-rate feedforward controller  $F_{sr}$  for the reference of the desired output trajectory are given by

$$\mathbf{u}_{ff}[k] = \mathbf{F}_{sr} \mathbf{r}[k+1], \quad (3.8)$$



where  $F_{sr}$  is given by

$$F_{sr} = \left[ \begin{array}{c|c} \mathbf{A}_s - \mathbf{B}_s(\mathbf{C}_s\mathbf{B}_s)^{-1}\mathbf{C}_s\mathbf{A}_s & \mathbf{B}_s(\mathbf{C}_s\mathbf{B}_s)^{-1} \\ \hline -(\mathbf{C}_s\mathbf{B}_s)^{-1}\mathbf{C}_s\mathbf{A}_s & (\mathbf{C}_s\mathbf{B}_s)^{-1} \end{array} \right]. \quad (3.9)$$

There is exact tracking of the desired output trajectory  $\mathbf{r}$  at every sample in the systems with the single feedforward control.

However, the single-rate feedforward controller has a problem. It is known that a single-rate system discretized by sampler and zero-order-hold has discretized zeros depending on the relative degree of the continuous-time system [19]. The discretized zeros appear around  $z = -1$  on the real axis on the  $z$  plane. The single-rate feedforward controller is designed as the inverse of the single-rate system, and the zeros of the single-rate system become the poles of the single-rate feedforward controller. When the pole of the system is around  $z = -1$  of the  $z$  plane, the system becomes oscillated or diverged. Therefore, the single-rate feedforward controller has the problem that the generated control inputs may be oscillated or diverged. If the single-rate feedforward controller  $F_{sr}$  has unstable poles, a stable inversion approach or an approximated inverse approach is used, see details in [39, 62].

On the other hand, the multirate feedforward controller is designed so that all poles are at  $z = 0$  and the generated control inputs are not oscillated or diverged. In this chapter, a MIMO multirate feedforward controller is proposed to make the continuous-time error smaller than that of a MIMO single-rate feedforward controller.

## 3.4 Multirate feedforward control for multi-input multi-output system

In this section, the design method of the MIMO multirate feedforward controller is proposed for the tracking control of MIMO LTI systems. The multirate feedforward control has an advantage of intersample behavior compared with the single-rate feedforward control [39].

### 3.4.1 Design of input matrix from generalized controllability indices

The generalized controllability indices are defined as follows [48].

**Definition 3.2 :** The generalized controllability indices of  $\mathbf{A}_c \in \mathbb{R}^{n \times n}$  and  $\mathbf{B}_c = [\mathbf{b}_{c1}, \dots, \mathbf{b}_{cm}] \in \mathbb{R}^{n \times m}$  are defined as

$$\{\mathbf{b}_{c1}, \dots, \mathbf{b}_{cm}, \mathbf{A}_c\mathbf{b}_{c1}, \dots, \mathbf{A}_c\mathbf{b}_{cm}, \dots, \mathbf{A}_c^{n-1}\mathbf{b}_{cm}\}.$$

If  $(\mathbf{A}_c, \mathbf{B}_c)$  is a controllable pair,  $n$  linearly independent vectors be selected from the he generalized controllability indices.

The generalized controllability indices are the sets of the input multiplicities  $\sigma_l$ .

The input multiplicities  $\sigma_l$  is defined as follows [48].

**Definition 3.3 :** Input multiplicities  $\sigma_l$  are defined as the number of the input which comes from the same input in the same frame period  $T_f$ .

Setting  $\varphi$  as a set of  $n$  vectors selected from the generalized controllability indices,  $\sigma_l$  and  $N$  are defined by

$$\sigma_l = \text{number}\{k | \mathbf{A}_c^{k-1} \mathbf{b}_{cl} \in \varphi\}, \quad (3.10)$$

$$N = \max(\sigma_l), \quad (3.11)$$

where  $l \in \mathbb{N}$  is the index of the inputs. The plant order  $n$  is equal to the sum of the input multiplicities  $\sigma_l$  as

$$\sum_{l=1}^m \sigma_l = n. \quad (3.12)$$

In MIMO LTI systems,  $n$  vectors are selected from the generalized controllability indices, and the full row rank matrix  $\mathbf{B}$  can be designed for almost all discretized sampling periods<sup>1</sup>. Therefore, several types of multirate systems are designed according to the selection of input multiplicities.

From the selection of input multiplicities,  $T_{u_l}$ , which is the sampling period of  $l$ th input  $u_l$ , is defined by

$$T_{u_l} = \frac{N}{\sigma_l} T_u. \quad (3.13)$$

It is noted that the sampling period  $T_u$  is the smallest value of  $T_{u_l}$ .

A sampling period  $T_f$  is defined as the frame period which is the largest value between  $T_r$ ,  $T_y$ , and  $T_u$ . In this chapter, the frame period  $T_f$  of the multirate system is defined by

$$T_f = T_r = NT_y = NT_u. \quad (3.14)$$

The multirate system  $\mathbf{G}$  discretized by sampler and zero-order-hold with  $\mathbf{G}_c$  and the sampling period  $\delta = T_{u_l}$  is given by

$$\mathbf{x}[i+1] = \mathbf{A}\mathbf{x}[i] + \mathbf{B}\mathbf{u}[i], \quad (3.15)$$

$$\mathbf{y}[i] = \mathbf{C}\mathbf{x}[i], \quad (3.16)$$

where  $i \in \mathbb{Z}$ .  $\mathbf{A}$ ,  $\mathbf{B}$ ,  $\mathbf{x}[i]$ , and  $\mathbf{u}[i]$  are given by

$$\mathbf{A} = e^{\mathbf{A}_c T_f}, \quad (3.17)$$

$$\mathbf{B} = [\mathbf{B}_1 \quad \cdots \quad \mathbf{B}_l \quad \cdots \quad \mathbf{B}_m], \quad (3.18)$$

$$\mathbf{C} = \mathbf{C}_c, \quad (3.19)$$

$$\mathbf{x}[i] = \mathbf{x}(iT_f), \quad (3.20)$$

$$\begin{aligned} \mathbf{u}[i] &= [\mathbf{u}_1[i] \quad \cdots \quad \mathbf{u}_m[i]]^T \\ &= [u_{1_1}[i] \quad \cdots \quad u_{1_{\sigma_1}}[i] \quad u_{2_1}[i] \quad \cdots \quad u_{m_{\sigma_m}}[i]]^T, \end{aligned} \quad (3.21)$$

<sup>1</sup>This is possible because the controllability of a continuous-time system is not preserved in the discrete system only if the two poles  $\eta_i$  and  $\eta_j$  have the same real parts, and the discretizing sampling period  $T$  satisfies  $\eta_i = \eta_j + j \frac{2k\pi}{T}$  ( $k = \pm 1, \pm 2, \dots$ ); furthermore, it is limited to only several cases [65].

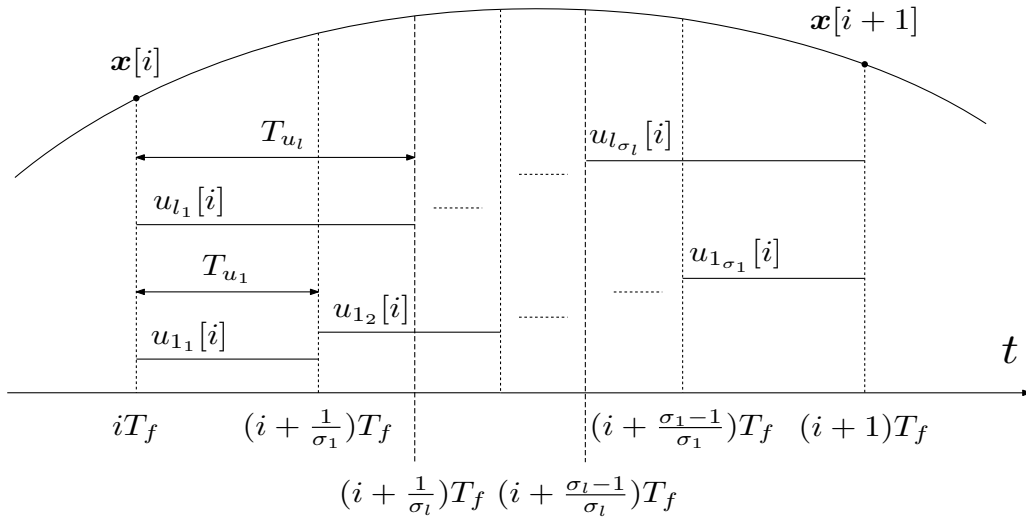


Fig. 3.2: MIMO multirate input control.

and  $B_l$ ,  $A_{s_l}$  and  $b_{s_l}$  are defined as

$$B_l = \begin{bmatrix} A_{s_l}^{\sigma_l-1} b_{s_l} & A_{s_l}^{\sigma_l-2} b_{s_l} & \cdots & A_{s_l} b_{s_l} & b_{s_l} \end{bmatrix}, \quad (3.22)$$

$$A_{s_l} = e^{A_c T_{u_l}}, \quad b_{s_l} = \int_0^{T_{u_l}} e^{A_c \tau} b_{c_l} d\tau. \quad (3.23)$$

The input matrix  $B$  in a multirate system is designed by the generalized controllability indices depending on the input multiplicities  $\sigma_l$ . It becomes a nonsingular square matrix because of the definition of the generalized controllability indices. The state and input of the multirate system are shown in Fig. 3.2. Note that the numerical condition of the MIMO multirate system is also improved compared with that of the SISO multirate system in the same order of the model because the maximum number of lifting samples is reduced.

### 3.4.2 Controller design and control input generation

From the state equation of the multirate system (3.15), control inputs  $u_{ff}[i]$  of the multirate feedforward controller  $F_{mr}$  for the reference of the desired state trajectory are given by

$$u_{ff}[i] = F_{mr} \hat{x}[i+1], \quad (3.24)$$

where  $F_{mr}$  and  $z^N$  is given by

$$F_{mr} = B^{-1} (I - z^{-N} A) = \left[ \begin{array}{c|c} \mathbf{O} & \mathbf{I} \\ \hline -B^{-1} A & B^{-1} \end{array} \right], \quad (3.25)$$

$$z^N = (e^{s T_u})^N = e^{s T_f}. \quad (3.26)$$

There is exact tracking of the desired state trajectory  $\hat{x}$  at every  $N$  sample in the model with the multirate feedforward control. It is noted that all poles of the multirate feedforward controller  $F_{mr}$  are  $z = 0$  because the state matrix of  $F_{mr}$  is  $\mathbf{O}$ , and smooth control input is generated

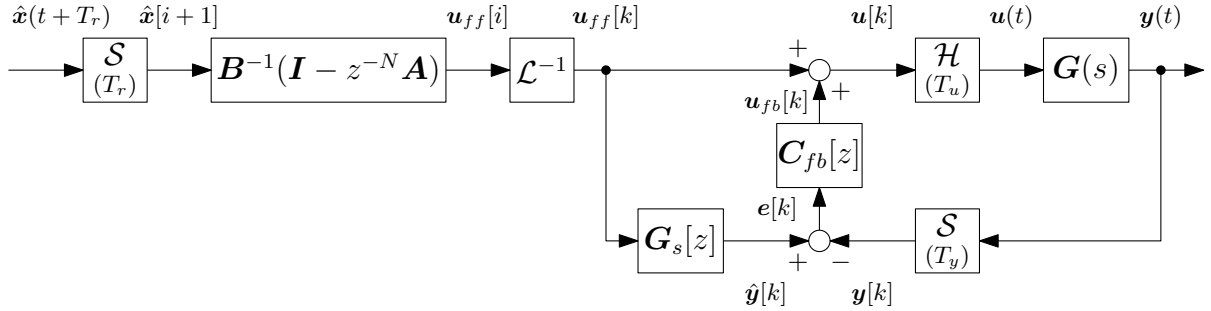


Fig. 3.3: Block diagram of MIMO multirate feedforward control.  $\mathcal{S}$ ,  $\mathcal{H}$ , and  $\mathcal{L}$  denote sampler, zero-order-hold, and lifting operator [15], respectively.

compared with the single-rate feedforward controller  $F_{sr}$ . For the details of the desired state trajectory generation, see [40,45]. A block diagram of the control system is shown in Fig. 3.3.  $\mathcal{L}$  is a discrete-time lifting operator [15].  $\mathcal{L}^{-1}$  outputs the elements of the  $N$ th dimensional vector  $u_{ff}[i]$ , which are inputs at every period  $T_f$ , in the order from 1 to  $\sigma_l$  by  $T_{u_l}$ .

### 3.4.3 Optimal selection of input multiplicities

Several types of multirate feedforward controllers can be designed depending on the multirate system  $G$  with the selection of input multiplicities  $\sigma_l$ . There is exact tracking of the desired state trajectory  $\hat{\mathbf{x}}$  at every  $N$  sample in the systems with all kinds of multirate feedforward controllers [64]. However, the control inputs and intersample behavior are different depending on the multirate system  $G$ . For the application of high-precision positioning control in mechatronic systems, continuous-time tracking error is preferred to be small, and also control input  $\mathbf{u}$  should be smaller because of the limitation of mechatronic systems. An approach of designing the optimal MIMO multirate feedforward controller is proposed to make 2-norm of control inputs smaller in the rest of this section.

From the state equation of a multirate system (3.15), the part in which the control input  $\mathbf{u}$  affects to the state  $\mathbf{x}$  is given by

$$B\mathbf{u}[i] = \mathbf{x}[i+1] - A\mathbf{x}[i]. \quad (3.27)$$

In the multirate feedforward control, there is exact tracking of the state  $\mathbf{x}[i]$  and  $\mathbf{x}[i+1]$ . The difference of the state  $\mathbf{v}[i]$  is defined as

$$\mathbf{v}[i] = \mathbf{x}[i+1] - A\mathbf{x}[i], \quad (3.28)$$

and the control input  $\mathbf{u}[i]$  is represented as

$$\mathbf{u}[i] = B^{-1}\mathbf{v}[i]. \quad (3.29)$$

The square of the 2-norm of the control input  $\|\mathbf{u}[i]\|_2^2 = u_1^2 + \dots + u_n^2$  is given by

$$\|\mathbf{u}[i]\|_2^2 = \mathbf{v}^T[i](B^{-1})^T B^{-1}\mathbf{v}[i], \quad (3.30)$$

and  $\|\mathbf{u}[i]\|_2^2$  becomes a quadratic form of  $\mathbf{v}[i]$ .

For the normalization of the difference of the state,  $\mathbf{v}[i]$  is defined as the unit sphere:

$$\|\mathbf{v}[i]\|_2^2 = v_1^2 + \cdots + v_n^2 = 1. \quad (3.31)$$

According to the relationship between the range of a quadratic form with the unit sphere and eigenvalues [66], the range of  $\|\mathbf{u}[i]\|_2^2$  is given by

$$\lambda_n \leq \|\mathbf{u}[i]\|_2^2 \leq \lambda_1 \quad (\lambda_n \leq \lambda_{(n-1)} \leq \cdots \leq \lambda_1), \quad (3.32)$$

where  $\lambda_i$  is the eigenvalue of  $(\mathbf{B}^{-1})^\top \mathbf{B}^{-1}$ .  $\lambda_{ci}$ , which is the eigenvalue of  $\mathbf{B}\mathbf{B}^\top$ , is the reciprocal of  $\lambda_i$  as

$$\lambda_{ci} = \frac{1}{\lambda_i}, \quad (3.33)$$

and the range of  $\|\mathbf{u}[i]\|_2^2$  given by

$$\frac{1}{\lambda_{cn}} \leq \|\mathbf{u}[i]\|_2^2 \leq \frac{1}{\lambda_{c1}} \quad (\lambda_{c1} \leq \lambda_{c2} \leq \cdots \leq \lambda_{cn}). \quad (3.34)$$

$\sigma_{ci}$ , which is the singular value of the input matrix  $\mathbf{B}$  is the square root of  $\lambda_{ci}$  as

$$\sigma_{ci}(\mathbf{B}) = \sqrt{\lambda_{ci}(\mathbf{B}\mathbf{B}^\top)}, \quad (3.35)$$

and the range of 2-norm of the control input  $\|\mathbf{u}[i]\|_2$  is given by

$$\frac{1}{\sigma_{cn}} \leq \|\mathbf{u}[i]\|_2 \leq \frac{1}{\sigma_{c1}} \quad (\sigma_{c1} \leq \sigma_{c2} \leq \cdots \leq \sigma_{cn}). \quad (3.36)$$

If 2-norm of the control input  $\|\mathbf{u}[i]\|_2$  is too large, it is not suitable for the limitation of the mechatronic systems. Making the upper bound of the 2-norm of control input  $\|\mathbf{u}[i]\|_2$  smaller is equal making the smallest singular value  $\sigma_{c1}(\mathbf{B})$  larger. From this consideration, the input multiplicity is selected so that the smallest singular value  $\sigma_{c1}(\mathbf{B})$  becomes the largest. Therefore, the optimal design of the MIMO multirate feedforward controller to make the maximum value of 2-norm of control inputs smaller is proposed. Note that this analysis is based on the normalized state vector and the physical meaning of the states depends on the estate-space representation. The input and output scaling and the state-space realization should be selected properly so that the normalized state vector represents the state values of the reference sets. The MIMO multirate feedforward controller cannot specify the band of the continuous-time error because it only guarantees the exact tracking of the desired state trajectory  $\hat{\mathbf{x}}$  at every frame period  $T_f$  in the model, but the intersample behavior becomes smoothly connected between the discrete sampling points in continuous time with the control inputs of the optimally designed controller. The analysis of the bound of the continuous-time error is an open issue.

### 3.4.4 Example of intersample behavior in different sets of input multiplicities

The optimal design of the MIMO multirate feedforward controller is validated with the example of a numerical simulation.

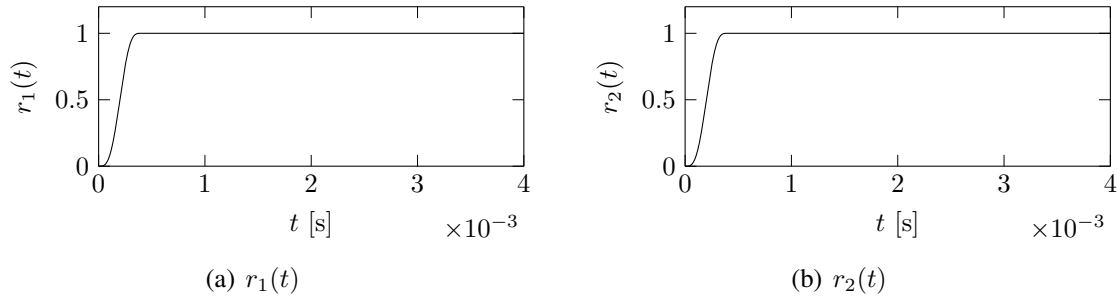


Fig. 3.4: Desired output trajectory  $\mathbf{r}(t) = [r_1(t) \ r_2(t)]^T$ : they are 7<sup>th</sup> order polynomials, respectively.

$$\begin{aligned}
 & (\sigma_1, \sigma_2) && 3T_u = T_f \\
 (3, 3) & \begin{array}{l} T_{u_1} = T_u \\ T_{u_2} = T_u \end{array} & \begin{array}{l} u_1 \\ u_2 \end{array} & \left| \begin{array}{ccc} 1 & 2 & 3 \\ 1 & 2 & 3 \end{array} \right| \\
 & & & \\
 (4, 2) & \begin{array}{l} T_{u_1} = T_u \\ T_{u_2} = 2T_u \end{array} & \begin{array}{l} u_1 \\ u_2 \end{array} & \left| \begin{array}{cccc} 1 & 2 & 3 & 4 \\ 1 & 2 & & \end{array} \right| \\
 & & & \\
 (6, 0) & \begin{array}{l} T_{u_1} = T_u \\ \text{not used} \end{array} & \begin{array}{l} u_1 \\ u_2 \end{array} & \left| \begin{array}{cccccc} 1 & 2 & 3 & 4 & 5 & 6 \\ \dots & \dots & \dots & \dots & \dots & \dots \end{array} \right|
 \end{aligned}$$

Fig. 3.5: Examples of multirate inputs. Two inputs  $u_1$  and  $u_2$  are generated according to the input multiplicities  $(\sigma_1, \sigma_2)$ . A control input with 0 input multiplicity is not in use.

The continuous-time system  $\mathbf{G}_c$  is defined as the transfer function matrix (3.37).

$$\mathbf{G}_c(s) = \frac{1}{\begin{bmatrix} s^6 + 8895s^5 + 3.979 \times 10^7 s^4 + 2.428 \times 10^9 s^3 + 9.099 \times 10^{12} s^2 + 4.382 \times 10^{13} s + 24 & & \\ \begin{array}{l} 4.702 \times 10^{10} s^2 + 2.294 \times 10^{11} s + 5.477 \times 10^{15} \\ 5.477 \times 10^{15} \end{array} & \begin{array}{l} 1.387 \times 10^8 s^2 + 1.233 \times 10^{12} s + 5.477 \times 10^{15} \\ 1220s^4 + 1.085 \times 10^7 s^3 + 4.835 \times 10^{10} s^2 + 1.462 \times 10^{12} s + 5.477 \times 10^{15} \end{array} & \end{bmatrix}} \quad (3.37)$$

The reference of the desired output trajectory  $\mathbf{r}$  is given by 7<sup>th</sup> order polynomials which change from 0 to 1 in 0 s to 0.4 ms for each output. The sampling period of the control input is set to  $T_u = 0.4$  ms. For the design of MIMO multirate feedforward controller, seven types of sets of input multiplicities are selected as

$$(\sigma_1, \sigma_2) = (0, 6), (1, 5), (2, 4), (3, 3), (4, 2), (5, 1), (6, 0). \quad (3.38)$$

The examples of multirate inputs are shown in Fig. 3.5.

The smallest singular value  $\sigma_{c1}(\mathbf{B})$  and the simulation results are shown in Table 3.1. From the procedure of designing the optimal MIMO multirate feedforward controller, the set of input multiplicities in which the smallest singular value  $\sigma_{c1}(\mathbf{B})$  is the largest is the optimal set of input multiplicities for the controlled system. The advantage of this procedure is that the optimal MIMO multirate feedforward controller is designed without numerical simulations. When the order of the system is high or the number of inputs and outputs is large, the number of the set of input

Table 3.1:  $\sigma_{c1}(\mathbf{B})$ , the smallest singular value of  $\mathbf{B}$ , and root mean square and maximum absolute value of control inputs  $\mathbf{u}$  and tracking errors  $\mathbf{e}$  depending on sets of input multiplicities  $(\sigma_1, \sigma_2)$ .

$(\sigma_1, \sigma_2)$	$\sigma_{c1}(\mathbf{B})$	RMS( $u_1$ )	MAX( $ u_1 $ )	RMS( $u_2$ )	MAX( $ u_2 $ )	RMS( $e_1$ )	MAX( $ e_1 $ )	RMS( $e_2$ )	MAX( $ e_2 $ )
(0, 6)	$1.86 \times 10^{-16}$	$0.00 \times 10^{00}$	$0.00 \times 10^{00}$	$9.81 \times 10^{04}$	$2.27 \times 10^{05}$	$4.48 \times 10^{-01}$	$9.94 \times 10^{-01}$	$7.34 \times 10^{00}$	$1.53 \times 10^{01}$
(1, 5)	$6.77 \times 10^{-13}$	$5.54 \times 10^{-12}$	$7.83 \times 10^{-12}$	$1.71 \times 10^{05}$	$4.27 \times 10^{05}$	$4.01 \times 10^{-01}$	$9.88 \times 10^{-01}$	$9.30 \times 10^{00}$	$2.47 \times 10^{01}$
(2, 4)	$8.09 \times 10^{-07}$	$2.24 \times 10^{-10}$	$5.01 \times 10^{-10}$	$3.95 \times 10^{05}$	$8.37 \times 10^{05}$	$3.28 \times 10^{-01}$	$9.70 \times 10^{-01}$	$1.40 \times 10^{01}$	$3.67 \times 10^{01}$
(3, 3)	$4.70 \times 10^{-07}$	$4.70 \times 10^{03}$	$1.48 \times 10^{04}$	$6.72 \times 10^{05}$	$1.73 \times 10^{06}$	$2.26 \times 10^{-01}$	$8.50 \times 10^{-01}$	$4.01 \times 10^{01}$	$1.28 \times 10^{02}$
(4, 2)	$1.54 \times 10^{-04}$	$2.06 \times 10^{03}$	$4.78 \times 10^{03}$	$8.12 \times 10^{02}$	$1.29 \times 10^{03}$	$2.77 \times 10^{-01}$	$9.20 \times 10^{-01}$	$3.09 \times 10^{-01}$	$8.99 \times 10^{-01}$
(5, 1)	$5.70 \times 10^{-07}$	$5.84 \times 10^{05}$	$1.51 \times 10^{06}$	$2.27 \times 10^{03}$	$3.21 \times 10^{03}$	$3.44 \times 10^{01}$	$1.01 \times 10^{02}$	$7.66 \times 10^{-01}$	$1.70 \times 10^{00}$
(6, 0)	$1.01 \times 10^{-06}$	$3.44 \times 10^{05}$	$7.45 \times 10^{05}$	$0.00 \times 10^{00}$	$0.00 \times 10^{00}$	$1.05 \times 10^{01}$	$2.58 \times 10^{01}$	$4.11 \times 10^{-01}$	$9.96 \times 10^{-01}$

multiplicities becomes enormous. Therefore, testing all sets with several references in numerical simulations spends a large amount of time, and the proposed design procedure is effective.

The validity of the procedure can be confirmed from the root mean square and the maximum absolute value of control inputs  $\mathbf{u}$  and tracking errors  $\mathbf{e}$  in Table 3.1. The trend is that control inputs  $\mathbf{u}$  and tracking errors  $\mathbf{e}$  become small when the smallest singular value  $\sigma_{c1}(\mathbf{B})$  is large. From Table 3.1, the optimal MIMO multirate feedforward controller is designed with the set of input multiplicities  $(\sigma_1, \sigma_2) = (4, 2)$  which makes the smallest singular value  $\sigma_{c1}(\mathbf{B})$  largest, and the root mean square of tracking errors  $\mathbf{e}$  are the smallest in all sets.

In summary, the proposed procedure is validated, and the optimal MIMO multirate feedforward controller can be designed with the set of input multiplicities which makes the smallest singular value  $\sigma_{c1}(\mathbf{B})$  largest, without spending time on numerical simulations.

## 3.5 Comparison for intersample behavior analysis

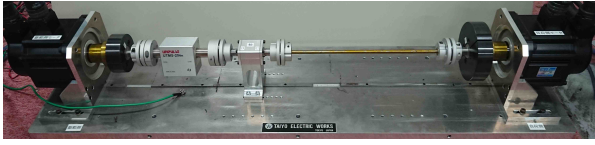
In this section, the tracking performance considering the intersample behavior of the optimal MIMO multirate feedforward controller is verified compared with that of a MIMO single-rate feedforward controller.

### 3.5.1 Modeling

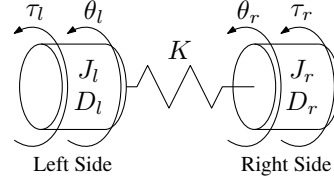
The approach is validated on the two-inertia system motor bench shown in Fig. 3.6(a). The two-inertia system motor bench has two motors on the left and right side and two motors are connected by the flexible shaft as shown in Fig. 3.6(b). The two-inertia system motor bench is used for theoretical and applicability validation. The two-inertia system motor bench has 20 bit/rev optical encoder for both sides which is enough high resolution for high-precision mechatronic systems.

In this chapter, the two-inertia system motor bench is modeled as a two-input two-output 4<sup>th</sup> order system. The block diagram of the system is shown in Fig. 3.7. The two inputs  $\mathbf{u}$  are the left and right side torque,  $\tau_l$  and  $\tau_r$ , and the outputs  $\mathbf{y}$  are the left and right side angle,  $\theta_l$  and  $\theta_r$ , respectively.

The Bode diagram of a frequency response function measurement of the system is shown in Fig. 3.8. The measurement is obtained through the identification experiment with a multisine input [67] from 1 Hz to 1250 Hz, and a sampling frequency is 2500 Hz. From the frequency response function measurement, the parameters of the two-inertia system motor bench are given as shown in Table 3.2 and the identified continuous-time system  $\mathbf{G}_c$  is given by the state-space



(a) Photograph of two-inertia system motor bench.



(b) Model of two-inertia system.

Fig. 3.6: Details of two-inertia system motor bench. In this chapter, the two-inertia system motor bench is modeled as a two-input two-output system. The two inputs are left side torque  $\tau_l$  and right side torque  $\tau_r$ , respectively. The two outputs are left side angle  $\theta_l$  and right side angle  $\theta_r$ , respectively.

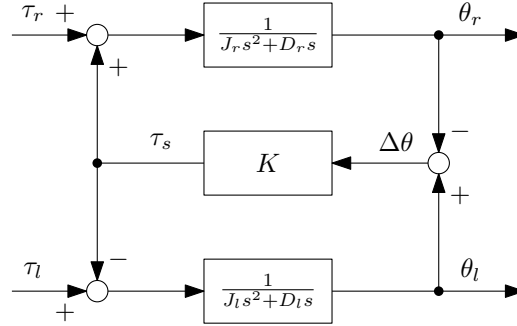


Fig. 3.7: Block diagram of two-inertia system.

Table 3.2: Parameters of two-inertia system motor bench.

$J_l$	$8.40 \times 10^{-4} \text{ kgm}^2$	$J_r$	$8.20 \times 10^{-4} \text{ kgm}^2$
$D_l$	$4.00 \times 10^{-3} \text{ Nms/rad}$	$D_r$	$4.00 \times 10^{-3} \text{ Nms/rad}$
$K$	$95.5 \text{ Nm/rad}$		

model with the state equation (3.39) and the output equation (3.40).

$$\frac{d}{dt} \begin{bmatrix} \theta_l(t) \\ \theta_r(t) \\ \dot{\theta}_l(t) \\ \dot{\theta}_r(t) \end{bmatrix} = \begin{bmatrix} 0 & 0 & 1 & 0 \\ 0 & 0 & 0 & 1 \\ -\frac{K}{J_l} & \frac{K}{J_l} & -\frac{D_l}{J_l} & 0 \\ \frac{K}{J_r} & -\frac{K}{J_r} & 0 & -\frac{D_r}{J_r} \end{bmatrix} \begin{bmatrix} \theta_l(t) \\ \theta_r(t) \\ \dot{\theta}_l(t) \\ \dot{\theta}_r(t) \end{bmatrix} + \begin{bmatrix} 0 & 0 \\ 0 & 0 \\ \frac{1}{J_l} & 0 \\ 0 & \frac{1}{J_r} \end{bmatrix} \begin{bmatrix} \tau_l(t) \\ \tau_r(t) \end{bmatrix} \quad (3.39)$$

$$\begin{bmatrix} \theta_l(t) \\ \theta_r(t) \end{bmatrix} = \begin{bmatrix} 1 & 0 & 0 & 0 \\ 0 & 1 & 0 & 0 \end{bmatrix} \begin{bmatrix} \theta_l(t) \\ \theta_r(t) \\ \dot{\theta}_l(t) \\ \dot{\theta}_r(t) \end{bmatrix} \quad (3.40)$$



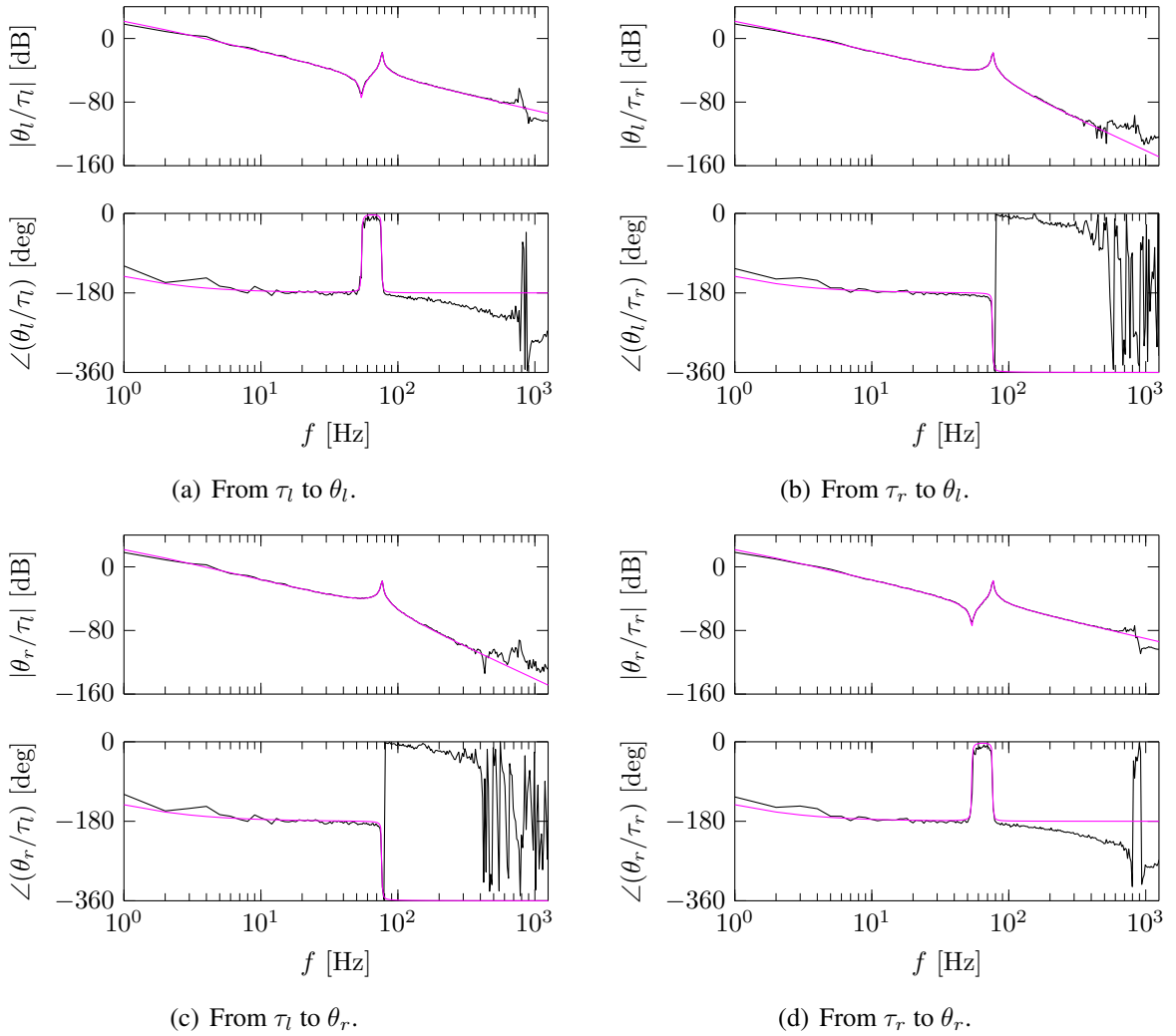


Fig. 3.8: Bode diagram of two-inertia system motor bench. The black line (—) is a frequency response measurement of the system and the magenta line (—) is the identified continuous-time model.

### 3.5.2 Conditions

The conventional MIMO single-rate feedforward controller  $\mathbf{F}_{sr}$  and the proposed MIMO multirate feedforward controller  $\mathbf{F}_{mr}$  are compared in the tracking control of the continuous-time system  $\mathbf{G}_c$ . With the proposed procedure, the optimal MIMO multirate feedforward controller is designed for  $\mathbf{G}_c$  with the set of input multiplicities  $(\sigma_1, \sigma_2) = (2, 2)$  which makes the smallest singular value  $\sigma_{c1}(\mathbf{B})$  largest. The poles and zeros of the feedforward controllers  $\mathbf{F}_{sr}$  and  $\mathbf{F}_{mr}$  are shown in Fig. 3.9. From Fig. 3.9(a), the conventional MIMO single-rate feedforward controller  $\mathbf{F}_{sr}$  has one pole around  $z = -1$  which leads to an oscillation, and from Fig. 3.9(b), the proposed MIMO multirate feedforward controller  $\mathbf{F}_{mr}$  has all poles on  $z = 0$ . The reference of the desired output trajectory  $\mathbf{r}$  is given by 7<sup>th</sup> order polynomials which change from 0 rad to 0.1 mrad in 0.8 ms to 2 ms for each output. The sampling period of the control input is set to  $T_u = 0.4$  ms. From these conditions, the reference signal is steep enough compared with  $T_u$ . In Fig. 3.3, the feedback controller is set to  $\mathbf{C}_{fb} = \mathbf{O}$  in the simulation.

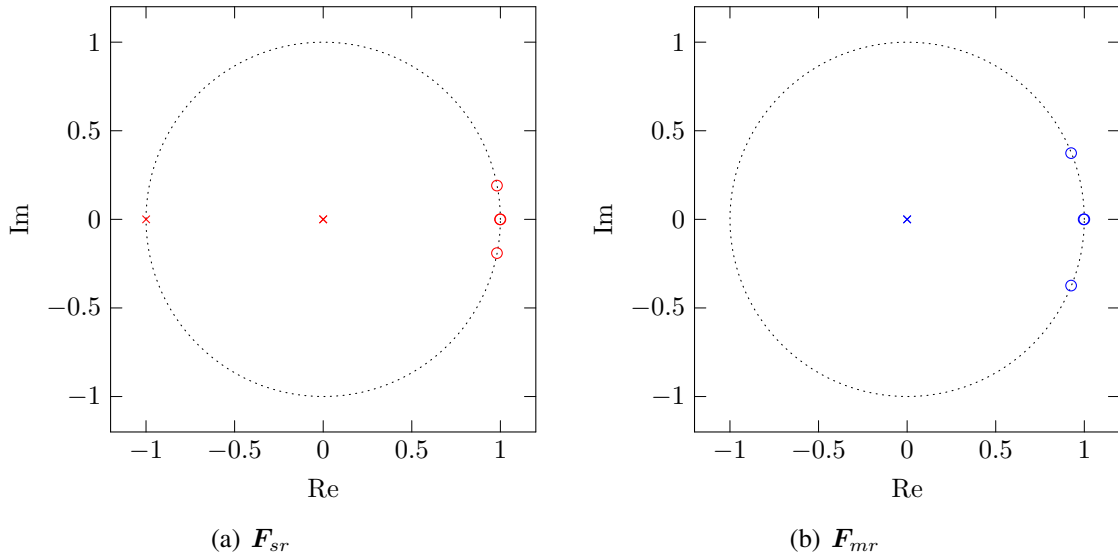


Fig. 3.9: Poles and zeros of multirate feedforward controller  $F_{mr}$  and single-rate feedforward controller  $F_{sr}$  with unit circle on  $z$  plane. ( $\times$ ) and ( $\circ$ ) are poles and zeros, respectively.

### 3.5.3 Simulation results

The simulation results are shown in Fig. 3.10. Fig. 3.10(a) and Fig. 3.10(b) show that the control inputs of the conventional MIMO single-rate feedforward controller  $F_{sr}$  oscillate and the proposed MIMO multirate feedforward controller  $F_{mr}$  generates the smooth control inputs. Fig. 3.10(c) and Fig. 3.10(d) show that the outputs of the single-rate feedforward controller are oscillated because of the oscillated control inputs, and the outputs of the multirate feedforward controller are settled after 2 s. Fig. 3.10(e) and Fig. 3.10(f) show that the continuous-time tracking error of the multirate feedforward controller is smaller than that of the single-rate feedforward controller, thus the effectiveness proposed method is verified.

MIMO multirate feedforward controller is used in the two-degree-of-freedom robust control with feedback controllers which reduce modeling error and disturbances. The role of the feedforward controller is to compensate for the tracking performance in the two-degree-of-freedom control scheme, and the simulation validations accurately verify it. In summary, the proposed optimal MIMO multirate feedforward controller outperforms the conventional MIMO single-rate feedforward controller in smooth control inputs and continuous-time tracking errors.

## 3.6 Application to MIMO motion system

In this section, the tracking performance considering the interaction compensation is validated by comparing the MIMO multirate feedforward controller and the SISO multirate feedforward controller in each axis.

### 3.6.1 Modeling

The approach is validated on the six-degrees-of-freedom (DOF) high-precision stage shown in Fig. 3.11(a). The six-DOF high-precision stage is supported by a six-DOF air-bearing gravity

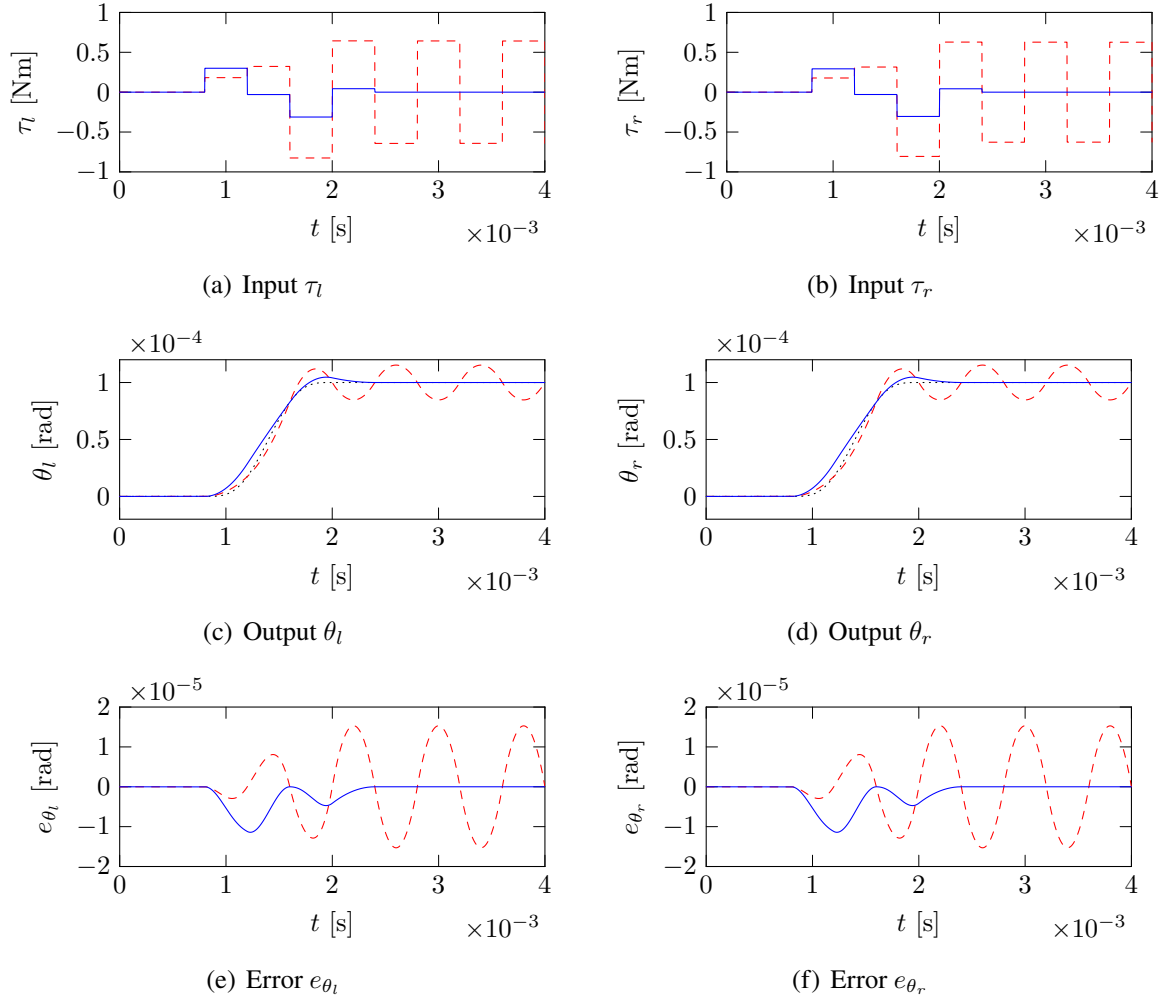


Fig. 3.10: Simulation results of multirate feedforward control (—), single-rate feedforward control (---), and 7<sup>th</sup> order polynomial reference (----).

canceller. In the experiment, the dual-input dual-output system with the translation  $x$  and the pitching  $\theta_y$  is considered as shown in Fig. 3.11(b).

In this chapter, the controlled system is modeled as a two-input two-output 4<sup>th</sup> order system. The block diagram of the system is shown in Fig. 3.12. The two inputs  $\mathbf{u}$  are the force and the torque,  $f_x$  and  $\tau_y$ , and the outputs  $\mathbf{y}$  are the translation and pitching,  $x$  and  $\theta_y$ , respectively. The multi-input multi-output rigid body mass-damper-spring model structure is given by

$$\frac{d}{dt} \begin{bmatrix} x(t) \\ \theta_y(t) \\ \dot{x}(t) \\ \dot{\theta}_y(t) \end{bmatrix} = \begin{bmatrix} \mathbf{O} & \mathbf{I} \\ -\mathbf{M}^{-1}\mathbf{K} & -\mathbf{M}^{-1}\mathbf{D} \end{bmatrix} \begin{bmatrix} x(t) \\ \theta_y(t) \\ \dot{x}(t) \\ \dot{\theta}_y(t) \end{bmatrix} + \begin{bmatrix} \mathbf{O} \\ \mathbf{M}^{-1} \end{bmatrix} \begin{bmatrix} f_x(t) \\ \tau_y(t) \end{bmatrix}, \quad (3.41)$$

$$\begin{bmatrix} x(t) \\ \theta_y(t) \end{bmatrix} = \begin{bmatrix} \mathbf{I} & \mathbf{O} \end{bmatrix} \begin{bmatrix} x(t) \\ \theta_y(t) \\ \dot{x}(t) \\ \dot{\theta}_y(t) \end{bmatrix}, \quad (3.42)$$

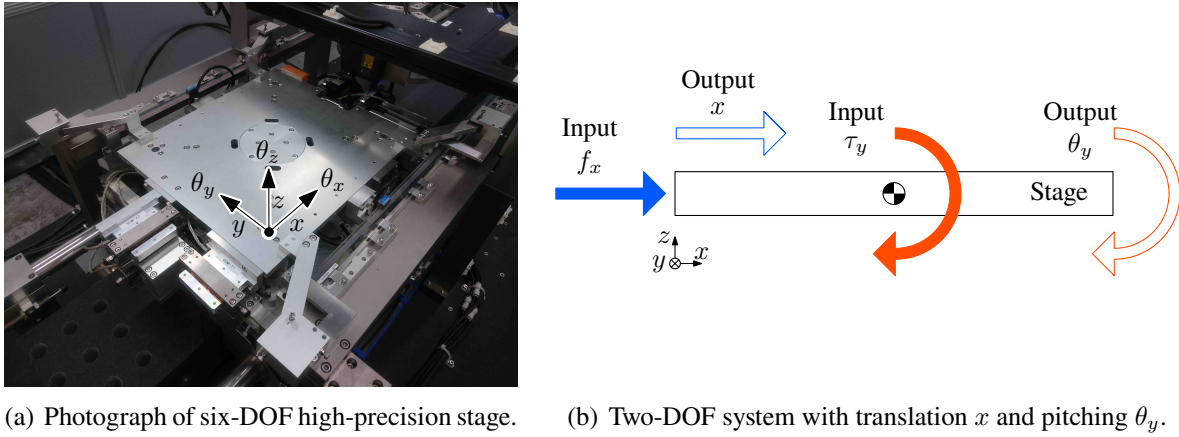


Fig. 3.11: Details of the six-DOF high-precision stage. In this chapter, the dual-input dual-output system with the translation  $x$  and the pitching  $\theta_y$  is considered.

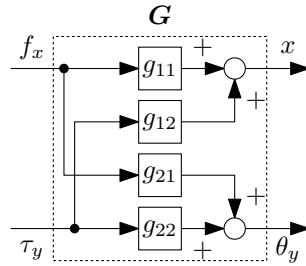


Fig. 3.12: Block diagram of the dual-input dual-output system with the translation  $x$  and the pitching  $\theta_y$ .

where

$$\mathbf{M} = \begin{bmatrix} m_{11} & m_{12} \\ m_{21} & m_{22} \end{bmatrix} \in \mathbb{R}^{2 \times 2}, \quad \mathbf{D} = \begin{bmatrix} d_{11} & d_{12} \\ d_{21} & d_{22} \end{bmatrix} \in \mathbb{R}^{2 \times 2}, \quad \mathbf{K} = \begin{bmatrix} k_{11} & k_{12} \\ k_{21} & k_{22} \end{bmatrix} \in \mathbb{R}^{2 \times 2}, \quad (3.43)$$

are mass, damper, and spring coefficient matrices from the equations of motion in the translation  $x$  and the pitching  $\theta_y$  that are given by

$$m_{11}\ddot{x}(t) + m_{12}\ddot{\theta}_y(t) + d_{11}\dot{x}(t) + d_{12}\dot{\theta}_y(t) + k_{11}x(t) + k_{12}\theta_y(t) = f_x(t), \quad (3.44)$$

$$m_{21}\ddot{x}(t) + m_{22}\ddot{\theta}_y(t) + d_{21}\dot{x}(t) + d_{22}\dot{\theta}_y(t) + k_{21}x(t) + k_{22}\theta_y(t) = \tau_y(t). \quad (3.45)$$

The Bode diagram of a frequency response function measurement of the system is shown in Fig. 3.13. The measurement is obtained through the identification experiment with a multisine input [67] from 1 Hz to 1000 Hz, and a sampling frequency is 2000 Hz. From the frequency response function measurement in Fig. 3.13, the continuous-time model with MIMO dynamics  $\mathbf{G}_c$  and without off-diagonal dynamics  $\tilde{\mathbf{G}}_c$  are identified. Note that the off-diagonal elements of  $\mathbf{M}$ ,  $\mathbf{D}$ , and  $\mathbf{K}$  in the continuous-time model without off-diagonal dynamics  $\tilde{\mathbf{G}}_c$  are zero, respectively.

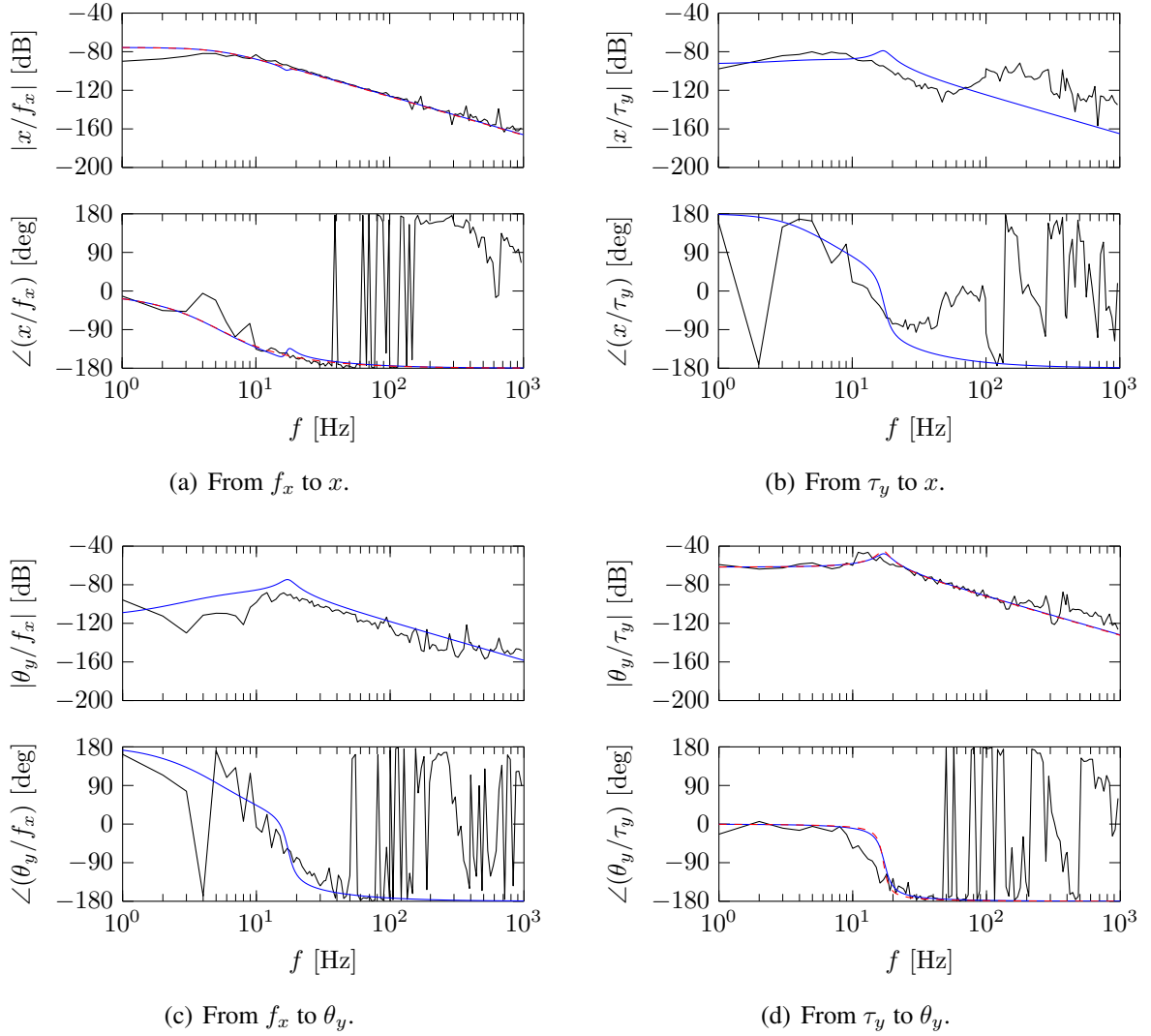


Fig. 3.13: Bode diagram of the dual-input dual-output system with the translation  $x$  and the pitching  $\theta_y$ : the frequency response function measurement of the system (—), the identified continuous-time model with MIMO dynamics  $\mathbf{G}_c$  (—) and without off-diagonal dynamics  $\tilde{\mathbf{G}}_c$  (--).

### 3.6.2 Conditions

The MIMO multirate feedforward controller based on the continuous-time model with MIMO dynamics  $\mathbf{G}_c$  and without off-diagonal dynamics  $\tilde{\mathbf{G}}_c$  are compared in the experiment. With the proposed procedure, the optimal MIMO multirate feedforward controller is designed for  $\mathbf{G}_c$  with the set of input multiplicities  $(\sigma_1, \sigma_2) = (2, 2)$  which makes the smallest singular value  $\sigma_{c1}(\mathbf{B})$  largest. The reference of the desired output trajectory  $\mathbf{r}$  is given by 7<sup>th</sup> order polynomials which change from 0 m to 0.1 mm in 0 s to 20 ms for  $x$  and zero constant reference for  $\theta_y$ . The sampling period of the control input is set to  $T_u = 0.2$  ms. In Fig. 3.3, the feedback controller  $\mathbf{C}_{fb}$  is designed as a PID controller with 20 Hz rigid body closed-loop bandwidth for six-DOFs in the experiment.

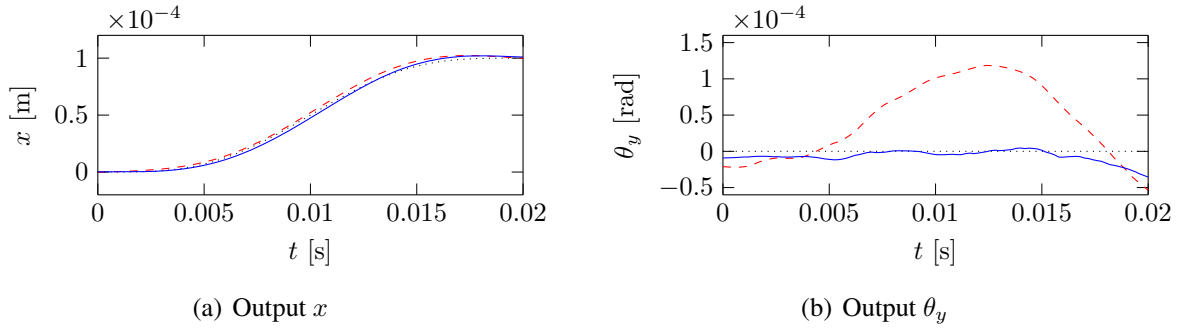


Fig. 3.14: Experimental results of MIMO multirate feedforward controller based on the continuous-time model with MIMO dynamics  $\mathbf{G}_c$  (—) and without off-diagonal dynamics  $\tilde{\mathbf{G}}_c$  (---), and the reference (----).

### 3.6.3 Experimental results

The experimental results are shown in Fig. 3.14. It shows that the error of  $x$  is almost the same in the MIMO multirate feedforward controller based on  $\mathbf{G}_c$  and  $\tilde{\mathbf{G}}_c$  because the reference of  $\theta_y$  is set to 0 rad for all time and there is not much interaction from  $\theta_y$  to  $x$ . However, the error of  $\theta_y$  is much smaller in the MIMO multirate feedforward controller based  $\mathbf{G}_c$  than the MIMO multirate feedforward controller based on  $\tilde{\mathbf{G}}_c$  because the MIMO multirate feedforward controller based  $\mathbf{G}_c$  can compensate to the interaction from  $\theta_y$  to  $x$ . These results show that the MIMO multirate feedforward controller based on the continuous-time model with MIMO dynamics  $\mathbf{G}_c$  that without off-diagonal dynamics  $\tilde{\mathbf{G}}_c$ , and the MIMO dynamics should be considered in the feedforward controller design.

## 3.7 Conclusion

The procedure of the optimal MIMO multirate feedforward controller design is proposed. The optimal MIMO multirate feedforward controller makes the upper bound of the 2-norm of control input  $\|\mathbf{u}[i]\|_2$  smaller, and as a result, the continuous-time tracking errors become smaller. The numerical simulation is conducted for the 6<sup>th</sup> order system, and the proposed procedure of the selection of input multiplicities is validated.

The continuous-time tracking errors of the proposed MIMO multirate feedforward controller  $\mathbf{F}_{mr}$  are compared with the conventional MIMO single-rate feedforward controller  $\mathbf{F}_{sr}$  in the simulation. Depending on the poles of each controller, the conventional single-rate controller generates oscillated control inputs and the proposed multirate controller generates smooth control inputs.

The interaction compensation performance is compared with the MIMO multirate feedforward controller based on the continuous-time model with MIMO dynamics and without off-diagonal dynamics in the experiment. The experimental results show that the MIMO multirate feedforward controller based on the continuous-time model with MIMO dynamics outperforms that without off-diagonal dynamics because of the interaction compensation.

As a result, continuous-time tracking errors of the MIMO multirate controller are better than that of the MIMO single-rate controller and that of the SISO multirate controller in the MIMO LTI system.

## **Part III**

# **Fixed-Structure Sampled-Data Feedforward and Learning Control**





# Chapter 4

## Linearly Parameterized Feedforward Control with Sampled-Data Differentiator

Sampled-data control requires both on-sample and intersample performance in high-precision mechatronic systems. The aim is to design a discrete-time linearly parameterized feedforward controller to improve both on-sample and intersample performance in a multi-modal motion system. The continuous-time performance is taken into account as state compatibility by a multirate zero-order-hold differentiator. The developed approach enables the linearly parameterized feedforward controller design for sampled-data systems with physically intuitive tuning parameters. The performance improvement is validated by comparing the developed approach with a conventional approach using a backward differentiator for a multi-modal motion system.

### 4.1 Introduction

Feedforward control is essential for reference tracking in industrial high-precision mechatronic systems such as semiconductor lithography systems [36] and high-speed scanners [68]. The feedforward controllers are usually implemented in digital hardware, and the parameter of the feedforward controller is first designed from the model of the controlled system, and secondly tuned by experimental data. For intuitive tuning of the feedforward controller, it is preferable that the feedforward controller is represented by the parameters with physical meaning.

The linearly parameterized feedforward control [69] has an advantage because the tuning process is physically intuitive. Model inversion based feedforward controllers such as zero phase error tracking control [70] are widely used to improve tracking performance. However, it is time-consuming to identify the model of the controlled system and hard to tune parameters manually.

The feedforward controller design for higher-order motion systems has a challenge because of the model complexity and it results in many non-intuitive parameters in the feedforward controller. Industrial mechatronic systems are modeled as the dominant rigid mode at a lower frequency and several flexible modes at a higher frequency due to limited mechanical stiffness [46]. The feedforward controller can be parameterized in physically intuitive using the modal characteristics.

The sampled-data characteristics should be considered in the feedforward controller design because of the limitation of the sampling frequency. The feedforward controllers are usually implemented in discrete time with the sampler and zero-order-hold [15]. Several related studies using the multirate feedforward control [20] are developed to improve intersample performance

by compensating for the oscillation of the Nyquist frequency.

Although several linearly parameterized feedforward control approaches exist, the on-sample performance is mainly discussed in conventional approaches and the sampled-data characteristics with sampler and zero-order-hold are not taken into account. The conventional linearly parameterized feedforward control is designed by using the backward differentiator [69] and it is not compatible with the states of the continuous-time motion system. The pre-existing state tracking approaches for both on-sample and intersample performance [43] need the model of the controlled system based on the system identification and they are not linearly parameterized in tuning parameters.

The main contribution of this chapter is the linearly parameterized feedforward control approach considering sampled-data characteristics to improve both on-sample and intersample performance in multi-modal motion systems. The contributions include:

**Contribution 4.1 :** *The multirate zero-order-hold differentiator is developed to design the discrete-time basis functions  $\Psi[k]$  that satisfy state compatibility for the continuous-time reference  $r(t)$ .*

**Contribution 4.2 :** *The linearly parameterized feedforward considering sampled-data characteristics is designed with a multirate zero-order-hold differentiator and both on-sample and intersample performance improvement is experimentally validated in a multi-modal motion system.*

The outline is as follows. In Section 4.2, the problem that is considered in this chapter is formulated. In Section 4.3, the design method of the feedforward controller using the multirate zero-order-hold differentiator is developed, constituting Contribution 4.1. In Section 4.4, the tracking performance of the approach is compared with that of the multirate feedforward in the simulation. In Section 4.5, the advantage of the approach is demonstrated in the experiment with a multi-modal motion system, constituting Contribution 4.2. In Section 4.6, conclusions are presented.

## 4.2 Problem formulation

In this section, the problem to improve continuous-time tracking performance is formulated. First, the requirements in this chapter are described. Second, the reference tracking problem is defined in intersample performance. Third, the low-order feedforward control approach is investigated for reference tracking in a multi-modal motion system. Fourth, the low-order feedforward control approach is implemented in discrete-time. Finally, the problem in the conventional approach is described.

### 4.2.1 Problem description

In this chapter, the feedforward controller is designed with respect to the following requirements:

**Requirement 4.1 :** *The feedforward controller is linearly parameterized with physical parameters for intuitive tuning.*

**Requirement 4.2 :** *The sampled-data characteristics with sampler and zero-order-hold are considered in the feedforward controller design.*

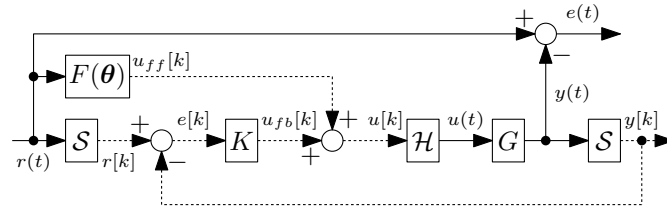


Fig. 4.1: Tracking control diagram. The continuous-time system  $G$  is controlled by the feedforward controller  $F(\theta)$  and the discrete-time feedback controller  $K$  with sampler  $\mathcal{S}$  and zero-order-hold  $\mathcal{H}$ . The objective is to minimize the continuous-time error  $e(t)$ . The solid and dotted lines denote the continuous-time and discrete-time signals, respectively.

**Requirement 4.3 :** *The designed feedforward controller can be applied to multi-modal motion systems.*

To improve both on-sample and intersample performance, the main problem in the feedforward control with acceleration and snap is the discrete-time basis function design that is compatible with the continuous-time reference  $r(t)$  considering sampled-data characteristics.

## 4.2.2 Reference tracking for intersample performance

The considered tracking control configuration is shown in Fig. 4.1, with reference  $r(t) \in \mathbb{R}$ , control input  $u(t) \in \mathbb{R}$ , and output  $y(t) \in \mathbb{R}$ . The continuous-time linear time-invariant system  $G(s)$  is controlled by the sampled-data controller that consists of feedforward controller  $F(\theta)$ , feedback controller  $K[z]$ , sampler  $\mathcal{S}$ , and zero-order-hold  $\mathcal{H}$ , where sampler and zero-order-hold are defined as follows.

**Definition 4.1 (Sampler) :** *The sampler  $\mathcal{S}$  with sampling time  $T_s$  is defined as*

$$\mathcal{S} : r(t) \mapsto r[k], \quad r[k] = r(kT_s). \quad (4.1)$$

**Definition 4.2 (Zero-order-hold) :** *The zero-order-hold  $\mathcal{H}$  with sampling time  $T_s$  is defined as*

$$\mathcal{H} : u[k] \mapsto u(t), \quad u(kT_s + \tau) = u[k], \quad \tau = [0, T_s). \quad (4.2)$$

The control objective in this chapter is to minimize the continuous-time error  $e(t)$ . Traditionally, the conventional discrete-time controller only focuses on the on-sample performance with the discrete-time error  $e[k]$ . To improve the continuous-time error  $e(t)$ , not only on-sample but also intersample performance should be considered.

## 4.2.3 Low-order feedforward for multi-modal motion system

The goal of the feedforward controller design is to extend the rigid mode behavior over a frequency range as high as possible. Note that the controlled system and the controllers are assumed to be the continuous-time system only in this subsection.

Industrial mechatronic systems consist of the dominant rigid mode at a lower frequency and several flexible modes at a higher frequency due to limited mechanical stiffness. The continuous-time single-input single-output multi-modal motion system is defined as

$$G_c(s) = \frac{1}{ms^2} + \sum_{i=1}^{n_{fl}} \frac{k_i}{m(s^2 + 2\zeta_i\omega_i s + \omega_i^2)}, \quad (4.3)$$

where  $m$  is the total mass of the system,  $n_{fl}$  is the number of the flexible modes. The resonance frequency, the damping coefficient, and the mode gain at the  $i^{\text{th}}$  mode are  $\omega_i$ ,  $\zeta_i$ , and  $k_i \in \{-1, 1\}$ , respectively.

To compensate for not only the rigid mode but also the flexible modes, the traditional acceleration feedforward is extended with the additional snap feedforward [71] and the ideal feedforward controller  $F^*(s)$  is defined as

$$F^*(s) = ms^2 + D^*(s)s^4, \quad (4.4)$$

where  $D^*(s)$  is the coefficient of the snap feedforward.

The objective of the feedforward  $F^*(s)$  is to minimize the closed-loop error given by

$$e(s) = S(s)r(s) - S(s)G_c(s)F^*(s)r(s), \quad (4.5)$$

where  $S(s)$  denotes the sensitivity function and is defined as

$$S(s) = (1 + G_c(s)K(s))^{-1}. \quad (4.6)$$

It results in  $F^*(s) = G_c^{-1}(s)$  and  $D^*(s)$  is given by

$$D^*(s) = G_c^{-1}(s) \frac{1}{s^4} - m \frac{1}{s^2}. \quad (4.7)$$

Assuming the reference trajectory in the mechatronic systems mainly contains low-frequency components, the low-frequency contribution of the snap feedforward is given by

$$\begin{aligned} D &= \lim_{s \rightarrow 0} D^*(s) = \lim_{s \rightarrow 0} \left( G_c^{-1}(s) \frac{1}{s^4} - m \frac{1}{s^2} \right) \\ &= \frac{-m \sum_{i=1}^{n_{fl}} k_i \prod_{j \neq i} \omega_j^2}{\prod_{i=1}^{n_{fl}} \omega_i^2}. \end{aligned} \quad (4.8)$$

Finally, the low-order feedforward controller with acceleration and snap is given by

$$F(s) = ms^2 + Ds^4, \quad (4.9)$$

where  $m$  and  $D$  are the tuning parameters in acceleration and snap.

#### 4.2.4 Feedforward implementation with basis functions

The feedforward controller design method is discussed above in continuous time. However, the controllers are implemented to digital hardware in discrete time. As a result, the continuous-time differentiator  $\frac{d}{dt}$  used in the feedforward controller is conventionally replaced by  $\xi$  which consists of the discrete-time differentiator and sampler  $S$ .

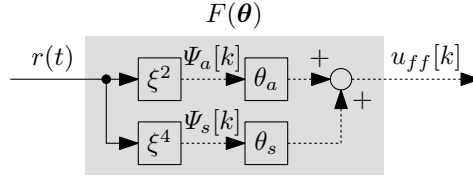


Fig. 4.2: Linearly parameterized feedforward with acceleration and snap.

The linearly parameterized feedforward with acceleration and snap is shown in Fig. 4.2. The feedforward controller  $F(\boldsymbol{\theta})$  from the continuous-time reference  $r(t)$  to design the discrete-time feedforward input  $u_{ff}[k]$  is defined as

$$F(\boldsymbol{\theta}) = \begin{bmatrix} \xi^2 & \xi^4 \end{bmatrix} \begin{bmatrix} \theta_a \\ \theta_s \end{bmatrix}, \quad (4.10)$$

where  $\boldsymbol{\theta} = [\theta_a \ \theta_s]^\top$  are the tuning parameters in acceleration and snap.

Finally, the discrete-time feedforward input  $u_{ff}[k]$  with acceleration and snap is given by

$$u_{ff}[k] = F(\boldsymbol{\theta})r(t) = \boldsymbol{\Psi}[k]\boldsymbol{\theta} = \begin{bmatrix} \Psi_a[k] & \Psi_s[k] \end{bmatrix} \begin{bmatrix} \theta_a \\ \theta_s \end{bmatrix}, \quad (4.11)$$

where  $\boldsymbol{\Psi}[k] = [\Psi_a[k] \ \Psi_s[k]] = [\xi^2 \ \xi^4] r(t)$  are the discrete-time basis functions that are correlated to the acceleration and snap of the continuous-time reference  $r(t)$ , respectively.

#### 4.2.5 Acceleration snap feedforward using backward differentiator

In the conventional approach [69], the discrete-time basis functions are designed by the continuous-time reference  $r(t)$  and the backward differentiator that is defined as follows.

**Definition 4.3** (Backward differentiator) : *The  $n^{\text{th}}$  order backward differentiator  $\xi_{bd}^n$  is given by*

$$\xi_{bd}^n = \begin{cases} \left( \frac{1-z^{-1}}{T_s} \right)^n z^{\frac{n}{2}} \mathcal{S} & (n : \text{even}) \\ \left( \frac{1-z^{-1}}{T_s} \right)^n \frac{1+z^{-1}}{2} z^{\frac{n+1}{2}} \mathcal{S} & (n : \text{odd}) \end{cases}, \quad (4.12)$$

where  $z$  is the discrete-time shift operator with sampling time  $T_s$  defined as  $z^n r[k] = r[k+n]$ .  $z^{\frac{n}{2}}$  denotes the phase compensation. When  $n$  is odd, the phase compensation consists of the half sample shift  $z^{\frac{1}{2}}$  that is a combination of one sample shift and the first order approximation of averaging the current and previous value [69].

The basis function design in acceleration and snap with backward differentiator is shown in Fig. 4.3 and the basis functions are given by

$$\begin{aligned} \boldsymbol{\Psi}_{bd}[k] &= \begin{bmatrix} \xi_{bd}^2 & \xi_{bd}^4 \end{bmatrix} r(t) \\ &= \begin{bmatrix} \left( \frac{1-z^{-1}}{T_s} \right)^2 z r[k] & \left( \frac{1-z^{-1}}{T_s} \right)^4 z^2 r[k] \end{bmatrix}, \end{aligned} \quad (4.13)$$

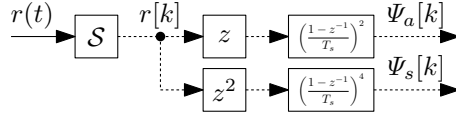


Fig. 4.3: Basis functions of acceleration and snap with a backward differentiator. The solid and dotted lines denote the continuous-time and discrete-time signals, respectively.

where  $r[k] = \mathcal{S}r(t)$ .

Finally, the discrete-time feedforward input  $u_{ff}[k]$  with backward differentiator is given by

$$u_{ff}[k] = \Psi_{bd}[k]\theta, \quad (4.14)$$

where  $\theta = [\theta_a \ \theta_s]^\top$  is the tuning parameter.

Although the on-sample performance is mainly discussed in the conventional approach using the backward differentiator, the sampled-data characteristics with sampler and zero-order-hold are not taken into account.

### 4.3 Structured feedforward using multirate zero-order-hold differentiator

In this section, the linearly parameterized feedforward controller design method considering sampled-data characteristics is presented. The improvement of both on-sample and intersample performance is based on the state compatibility in a sampled-data system with zero-order-hold and integrator. The basis functions are designed by the multirate zero-order-hold differentiator. The approach is applied to the low-order feedforward controller design with acceleration and snap for multi-modal motion systems. It results in Contribution 4.1.

#### 4.3.1 State compatibility in integrator with zero-order-hold

The continuous-time differentiator  $\frac{d}{dt}$  used in the feedforward controller should be replaced by the sampled-data differentiator  $\xi$  defined as follows.

**Definition 4.4** (Sampled-data differentiator) : *The  $n^{\text{th}}$  order sampled-data differentiator  $\xi^n$  with sampling time  $T_s$  is the conversion from the continuous-time signal  $r(t)$  to the discrete-time signal  $\Psi_n[k]$  that is correlated to the  $n^{\text{th}}$  order derivative of  $r(t)$  and defined as*

$$\Psi_n[k] = \xi^n r(t). \quad (4.15)$$

In the  $n$  samples lifted system, the exact state tracking can be achieved in every  $n$  sample using such as a minimum-time dead-beat control [72] and multirate feedforward control [20]. In such cases, the states in every  $n$  sample are given by the multirate sampler defined as follows.

**Definition 4.5** (Multirate sampler) : *The multirate sampler  $\mathcal{S}_n$  in every  $n$  sample with sampling time  $T_s$  is defined as*

$$\mathcal{S}_n : r(t) \mapsto r[i_n], \quad r[i_n] = r(knT_s). \quad (4.16)$$

The state-space representation of the continuous-time  $n^{\text{th}}$  order integrator in the controllable canonical form is given by

$$\left(\frac{1}{s}\right)^n = H_{nc} \stackrel{s}{=} \left[ \begin{array}{c|c} \mathbf{A}_{nc} & \mathbf{b}_{nc} \\ \mathbf{c}_{nc} & 0 \end{array} \right] = \left[ \begin{array}{cccc|c} 0 & 1 & 0 & 0 & 0 \\ 0 & \ddots & \ddots & 0 & \vdots \\ 0 & 0 & \ddots & 1 & 0 \\ 0 & 0 & 0 & 0 & 1 \\ \hline 1 & 0 & \cdots & 0 & 0 \end{array} \right], \quad (4.17)$$

where  $\mathbf{A}_{nc} \in \mathbb{R}^{n \times n}$ ,  $\mathbf{b}_{nc} \in \mathbb{R}^{n \times 1}$ , and  $\mathbf{c}_{nc} \in \mathbb{R}^{1 \times n}$ . To improve both on-sample and intersample performance in sampled-data systems with zero-order-hold and integrator, the basis functions used in the linearly parameterized feedforward controller should satisfy the state compatibility defined as follows.

**Definition 4.6** (State compatibility) : *The discrete-time signal  $\Psi_n[k]$  correlated to the  $n^{\text{th}}$  order derivative signal of the continuous-time signal  $r(t)$  satisfies state compatibility if the output through the system consisted of the continuous-time  $(n - m)^{\text{th}}$  order integrator  $H_{(n-m)c}$  and zero-order-hold  $\mathcal{H}$  is equal to the continuous-time  $m^{\text{th}}$  order derivative signal of  $r(t)$  in every  $n$  sample sampled by multirate sampler  $\mathcal{S}_n$  and defined as*

$$\mathcal{S}_n \frac{d^m}{dt^m} r(t) = \mathcal{S}_n H_{(n-m)c} \mathcal{H} \Psi_n[k], \quad (4.18)$$

where  $m = 0, 1, \dots, n - 1$ .

### 4.3.2 Multirate zero-order-hold differentiator for intersample performance

To improve the intersample performance in the discrete-time system, not only the output but also the states of the reference trajectory are considered. The multirate zero-order-hold differentiator is designed by the inverse of the continuous-time integrator discretized by sampler and zero-order-hold to satisfy the state compatibility. In this chapter, it is assumed that the continuous-time reference  $r(t)$  is  $\mathcal{C}^{n-1}$  class and differentiable at least  $n - 1$  times.

To satisfy the  $n$  states compatibility in  $n$  every sample, the lifted signal is considered using the lifted operator defined as follows.

**Definition 4.7** (Lifting operator) : *The lifting operator  $\mathcal{L}_n$  in every  $n$  sample is defined as*

$$\mathcal{L}_n : u[k] \mapsto \underline{u}[i_n], \quad (4.19)$$

where

$$\underline{u}[i_n] = \left[ u[ni_n] \quad u[ni_n + 1] \quad \cdots \quad u[ni_n + (n - 1)] \right]^T \in \mathbb{R}^n. \quad (4.20)$$

The  $n$  sample lifted system is defined as follows.

**Definition 4.8** (Lifted system) : *Consider a discrete-time system  $H_d \stackrel{z}{=} \mathbf{C}_d(z\mathbf{I} - \mathbf{A}_d)^{-1} \mathbf{B}_d + \mathbf{D}_d$ . The relation between the input and the output in the  $n$  sample lifted system of  $H_d$  is given by*

$$\underline{y}[i_n] = \mathcal{L}_n y[k] = (\mathcal{L}_n H_d \mathcal{L}_n^{-1})(\mathcal{L}_n u[k]) = \underline{H}_d \underline{u}[i_n], \quad (4.21)$$

where

$$\underline{y}[i_n] = [y[ni_n] \quad y[ni_n + 1] \quad \cdots \quad y[ni_n + (n - 1)]]^T \in \mathbb{R}^n, \quad (4.22)$$

and the lifted system  $\underline{H}_d$  is defined as

$$\begin{aligned} \underline{H}_d \stackrel{z^n}{=} \mathcal{L}_n H_d \mathcal{L}_n^{-1} &= \left[ \begin{array}{c|c} \underline{\mathbf{A}}_d & \underline{\mathbf{B}}_d \\ \hline \underline{\mathbf{C}}_d & \underline{\mathbf{D}}_d \end{array} \right] \\ &= \begin{bmatrix} \mathbf{A}_d^n & \mathbf{A}_d^{n-1} \mathbf{B}_d & \mathbf{A}_d^{n-2} \mathbf{B}_d & \cdots & \mathbf{A}_d \mathbf{B}_d & \mathbf{B}_d \\ \hline \mathbf{C}_d & \mathbf{D}_d & \mathbf{O} & \cdots & \cdots & \mathbf{O} \\ \mathbf{C}_d \mathbf{A}_d & \mathbf{C}_d \mathbf{B}_d & \mathbf{D}_d & \ddots & & \vdots \\ \vdots & \vdots & \ddots & \ddots & \ddots & \vdots \\ \mathbf{C}_d \mathbf{A}_d^{n-2} & \mathbf{C}_d \mathbf{A}_d^{n-3} \mathbf{B}_d & \mathbf{C}_d \mathbf{A}_d^{n-4} \mathbf{B}_d & \ddots & \mathbf{D}_d & \mathbf{O} \\ \mathbf{C}_d \mathbf{A}_d^{n-1} & \mathbf{C}_d \mathbf{A}_d^{n-2} \mathbf{B}_d & \mathbf{C}_d \mathbf{A}_d^{n-3} \mathbf{B}_d & \cdots & \mathbf{C}_d \mathbf{B}_d & \mathbf{D}_d \end{bmatrix}. \end{aligned} \quad (4.23)$$

Considering the states in discrete-time, the  $n^{\text{th}}$  order integrator discretized by sampler and zero-order-hold is given by

$$\begin{aligned} H_{nd} \stackrel{z}{=} \mathcal{S} H_{nc} \mathcal{H} &= \left[ \begin{array}{c|c} \mathbf{A}_{nd} & \mathbf{b}_{nd} \\ \hline \mathbf{c}_{nd} & 0 \end{array} \right] \\ &= \left[ \begin{array}{c|c} e^{\mathbf{A}_{nc} T_s} & \mathbf{A}_{nc}^{-1} (e^{\mathbf{A}_{nc} T_s} - \mathbf{I}) \mathbf{b}_{nc} \\ \hline \mathbf{c}_{nc} & 0 \end{array} \right]. \end{aligned} \quad (4.24)$$

To design the inverse of the continuous-time integrator discretized by sampler and zero-order-hold, the  $n$  sample lifted  $n^{\text{th}}$  order integrator is given by

$$\underline{H}_{nd} \stackrel{z^n}{=} \mathcal{L}_n H_{nd} \mathcal{L}_n^{-1} = \left[ \begin{array}{c|c} \underline{\mathbf{A}}_{nd} & \underline{\mathbf{B}}_{nd} \\ \hline \underline{\mathbf{C}}_{nd} & \underline{\mathbf{D}}_{nd} \end{array} \right], \quad (4.25)$$

and in state-space representation defined as

$$\mathbf{x}_n[i_n + 1] = \underline{\mathbf{A}}_{nd} \mathbf{x}_n[i_n] + \underline{\mathbf{B}}_{nd} \underline{u}[i_n] \quad (4.26)$$

$$\underline{y}[i_n] = \underline{\mathbf{C}}_{nd} \mathbf{x}_n[i_n] + \underline{\mathbf{D}}_{nd} \underline{u}[i_n] \quad (4.27)$$

where

$$\mathbf{x}_n[i_n] = [x_0[i_n] \quad x_1[i_n] \quad \cdots \quad x_{n-1}[i_n]]^T \in \mathbb{R}^n. \quad (4.28)$$

Satisfying the state compatibility, the relationship between the reference and the states is given by

$$\bar{r}_n[i_n] = \mathbf{x}_n[i_n], \quad (4.29)$$

where

$$\begin{aligned} \bar{r}_n[i_n] &= \mathcal{S}_n \left[ 1 \quad \frac{d}{dt} \quad \cdots \quad \frac{d^{n-1}}{dt^{n-1}} \right]^T r(t) \\ &= [r_0[i_n] \quad r_1[i_n] \quad \cdots \quad r_{n-1}[i_n]]^T \in \mathbb{R}^n. \end{aligned} \quad (4.30)$$

From the discussions above, the multirate zero-order-hold differentiator is given as follows.



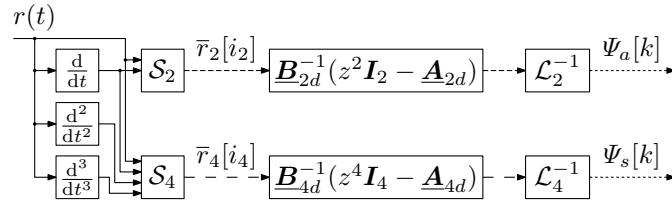


Fig. 4.4: Basis functions of acceleration and snap using multirate zero-order-hold differentiator. The solid line denotes the continuous-time signal. The dotted, high-frequency dashed and low-frequency dashed lines denote the discrete-time signal sampled by  $T_s$ ,  $2T_s$ , and  $4T_s$ , respectively.

**Theorem 4.1** (Multirate zero-order-hold differentiator) : From (4.26) and (4.29), considering the inverse of the continuous-time  $n^{\text{th}}$  order integrator discretized by sampler and zero-order-hold using the multirate feedforward control [20], the  $n^{\text{th}}$  order multirate zero-order-hold differentiator that satisfies the state compatibility is given by

$$\xi_{mr}^n = \mathcal{L}_n^{-1} \underline{\mathbf{B}}_{nd}^{-1} (z^n \mathbf{I}_n - \underline{\mathbf{A}}_{nd}) \mathcal{S}_n \begin{bmatrix} 1 & \frac{d}{dt} & \cdots & \frac{d^{n-1}}{dt^{n-1}} \end{bmatrix}^T. \quad (4.31)$$

*Proof.* See Definition 4.6 and [20]. □

### 4.3.3 Acceleration snap feedforward using multirate zero-order-hold differentiator

To design the feedforward controller with acceleration and snap, the lifted systems of the double integrator and the 4<sup>th</sup> integrator discretized by zero-order-hold are given by

$$\underline{H}_{2d} \stackrel{z^2}{=} \mathcal{L}_2 \mathcal{S} H_{2c} \mathcal{H} \mathcal{L}_2^{-1} = \left[ \begin{array}{c|c} \underline{\mathbf{A}}_{2d} & \underline{\mathbf{B}}_{2d} \\ \hline \underline{\mathbf{C}}_{2d} & \underline{\mathbf{D}}_{2d} \end{array} \right], \quad (4.32)$$

$$\underline{H}_{4d} \stackrel{z^4}{=} \mathcal{L}_4 \mathcal{S} H_{4c} \mathcal{H} \mathcal{L}_4^{-1} = \left[ \begin{array}{c|c} \underline{\mathbf{A}}_{4d} & \underline{\mathbf{B}}_{4d} \\ \hline \underline{\mathbf{C}}_{4d} & \underline{\mathbf{D}}_{4d} \end{array} \right], \quad (4.33)$$

where the continuous-time double integrator  $H_{2c}$  and 4<sup>th</sup> integrator  $H_{4c}$  are represented in controllable canonical form, respectively.

The basis function design using multirate zero-order-hold differentiator is shown in Fig. 4.4 and the basis functions are given by

$$\begin{aligned} \underline{\Psi}_{mr}[k] &= \begin{bmatrix} \xi_{mr}^2 & \xi_{mr}^4 \end{bmatrix} r(t) \\ &= \begin{bmatrix} \mathcal{L}_2^{-1} \underline{\mathbf{B}}_{2d}^{-1} (z^2 \mathbf{I}_2 - \underline{\mathbf{A}}_{2d}) \bar{r}_2[i_2] \\ \mathcal{L}_4^{-1} \underline{\mathbf{B}}_{4d}^{-1} (z^4 \mathbf{I}_4 - \underline{\mathbf{A}}_{4d}) \bar{r}_4[i_4] \end{bmatrix}^T. \end{aligned} \quad (4.34)$$

Finally, the discrete-time feedforward input  $u_{ff}[k]$  using the multirate zero-order-hold differentiator is given by

$$u_{ff}[k] = \underline{\Psi}_{mr}[k] \boldsymbol{\theta}, \quad (4.35)$$

where  $\boldsymbol{\theta} = \begin{bmatrix} \theta_a & \theta_s \end{bmatrix}^T$  is the tuning parameter.

## 4.4 Comparison with multirate feedforward control

In this section, the comparison between the linearly parameterized feedforward (LPFF) and the multirate feedforward (MRFF) [20] is conducted via simulations in a mass-damper-spring motion system and a mass-spring-mass motion system.

### 4.4.1 Conditions

The continuous-time reference  $r(t)$  is the 4<sup>th</sup> order polynomial trajectory shown in Fig. 4.5. The sampling time of the discrete-time controller is  $T_s = 5$  ms. The continuous-time output  $y(t)$  is obtained by higher sampling frequency in every 0.5 ms only for evaluation of the continuous-time error  $e(t)$ . The continuous-time error  $e(t)$  is compared using the linearly parameterized feedforward with model parameters, the linearly parameterized feedforward with tuning  $\min\|e[k]\|_2$ , and the multirate feedforward with model parameters. The simulation is conducted in an open loop without a feedback controller.

### 4.4.2 Controller design for mass-damper-spring motion system

The model  $G_2$  of the mass-damper-spring motion system is given by

$$G_2(s) = \frac{1}{ms^2 + bs + k}, \quad (4.36)$$

where  $m = 4 \times 10^{-4}$ ,  $b = 8 \times 10^{-2}$ , and  $k = 4$ .

In the linearly parameterized feedforward, the basis functions are given by

$$\Psi[k] = \begin{bmatrix} 1 & \xi_{mr}^1 & \xi_{mr}^2 \end{bmatrix} r(t), \quad (4.37)$$

and the tuning parameters are given by

$$\theta = \begin{bmatrix} k & b & m \end{bmatrix}^T. \quad (4.38)$$

The multirate feedforward provides perfect state tracking at every 2 sample for the second order model.

### 4.4.3 Controller design for mass-spring-mass motion system

The model  $G_4$  of the mass-spring-mass motion system is given by

$$G_4(s) = \frac{1}{\frac{m_1 m_2}{k} s^4 + (m_1 + m_2) s^2}, \quad (4.39)$$

where  $m_1 = m_2 = 2 \times 10^{-4}$  and  $k = 20$ .

In the linearly parameterized feedforward, the basis functions are given by

$$\Psi[k] = \begin{bmatrix} \xi_{mr}^2 & \xi_{mr}^4 \end{bmatrix} r(t), \quad (4.40)$$

and the tuning parameters are given by

$$\theta = \begin{bmatrix} m_1 + m_2 & \frac{m_1 m_2}{k} \end{bmatrix}^T. \quad (4.41)$$

The multirate feedforward provides perfect state tracking at every 4 sample for the 4<sup>th</sup> order model.

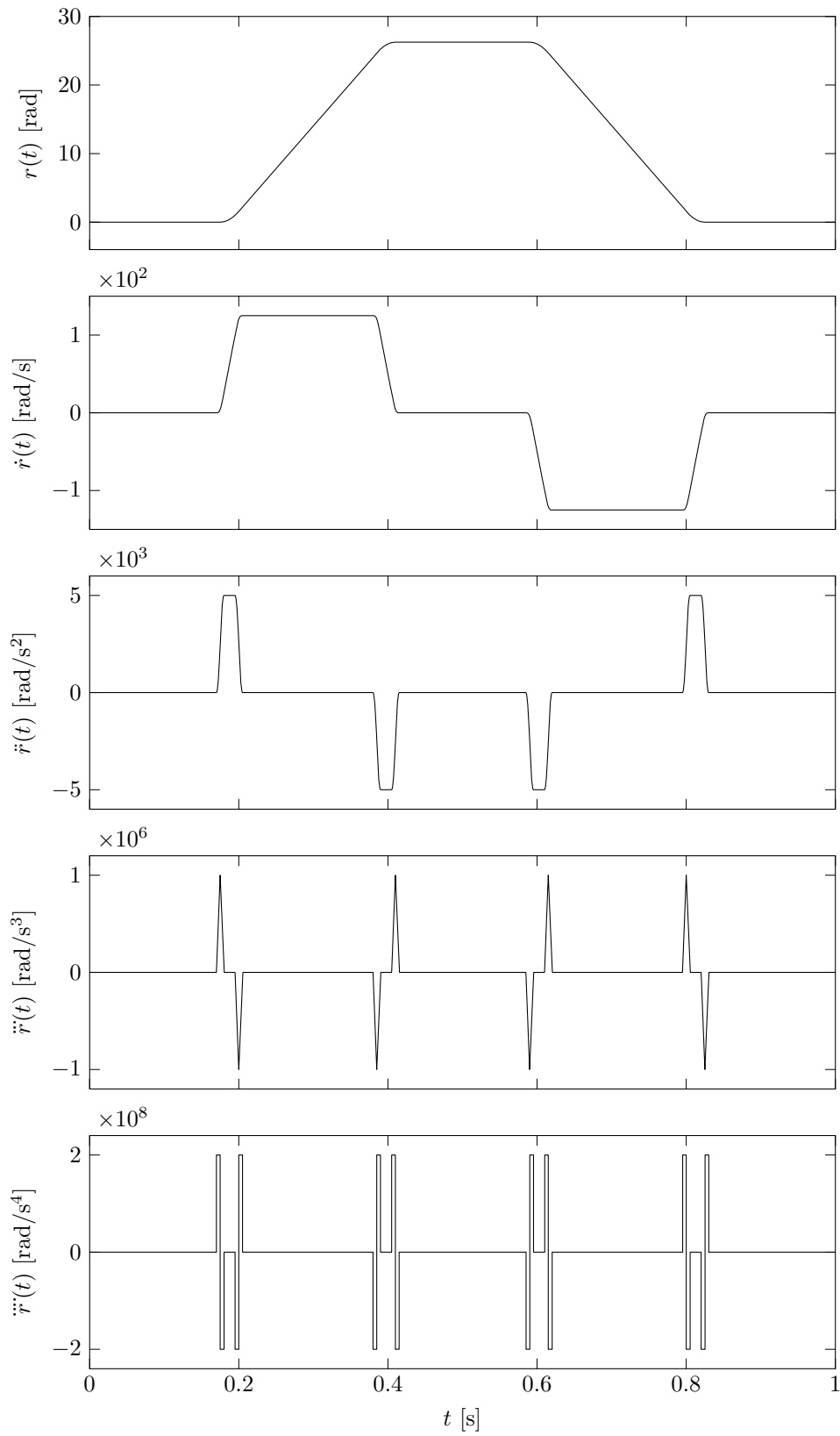


Fig. 4.5: Continuous-time 4<sup>th</sup> order polynomial trajectory reference  $r(t)$  and its derivatives.

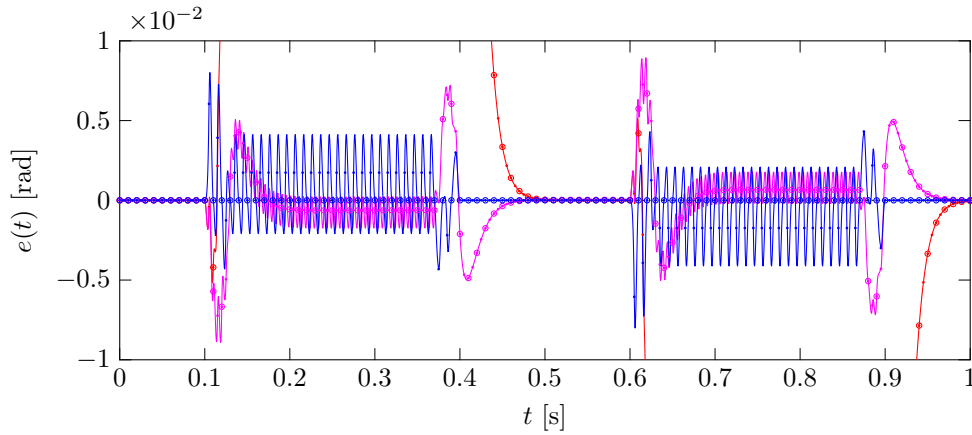


Fig. 4.6: Simulation results of tracking error  $e(t)$  in mass-damper-spring motion system  $G_2$  using linearly parameterized feedforward with model parameters (—), linearly parameterized feedforward with tuning  $\min\|e[k]\|_2$  (—), multirate feedforward with model parameters (—). (•) and (◦) show sampling point every  $T_s$  and  $2T_s$ .

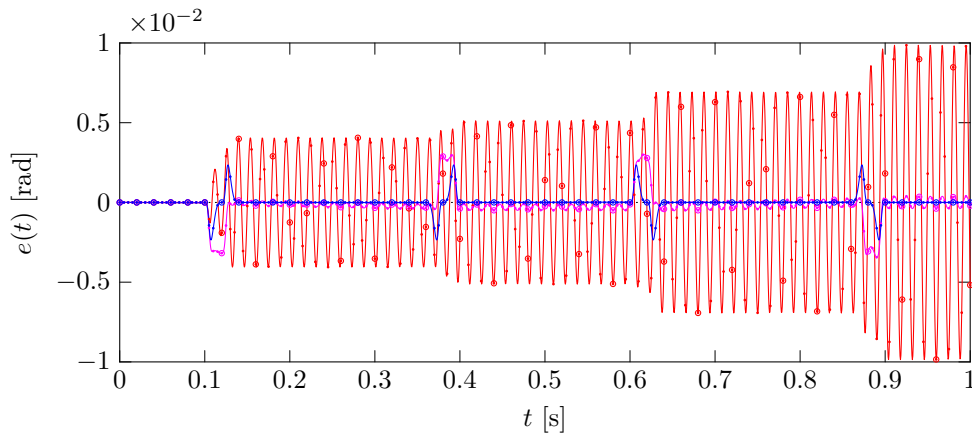


Fig. 4.7: Simulation results of tracking error  $e(t)$  in mass-spring-mass motion system  $G_4$  using linearly parameterized feedforward with model parameters (—), linearly parameterized feedforward with tuning  $\min\|e[k]\|_2$  (—), multirate feedforward with model parameters (—). (•) and (◦) show sampling point every  $T_s$  and  $4T_s$ .

#### 4.4.4 Comparison

The tracking errors of simulations in the mass-damper-spring motion system are shown in Fig. 4.6. It shows that the linearly parameterized feedforward with the model parameter makes a large error at constant velocity regions because of the mismatch between the feedforward model and the discretized model of the controlled system. After tuning as  $\min\|e[k]\|_2$ , the linearly parameterized feedforward provides a smaller error than that of the multirate feedforward.

The tracking errors of simulations in the mass-damper-spring motion system are shown in Fig. 4.7. It shows that the linearly parameterized feedforward with the model parameter makes a large oscillating error because of the mismatch of the resonance frequency between the feedforward model and the discretized model of the controlled system. The large oscillating error

Table 4.1: Root Mean Square error  $\text{RMS}(e(t))$  in simulation.

$\text{RMS}(e(t))$ [rad]	$G_2$	$G_4$
LPFF with model parameters	$1.78 \times 10^{-1}$	$4.14 \times 10^{-3}$
LPFF with tuning $\min\ e[k]\ _2$	$2.20 \times 10^{-3}$	$8.35 \times 10^{-4}$
MRFF with model parameters	$1.81 \times 10^{-3}$	$4.65 \times 10^{-4}$

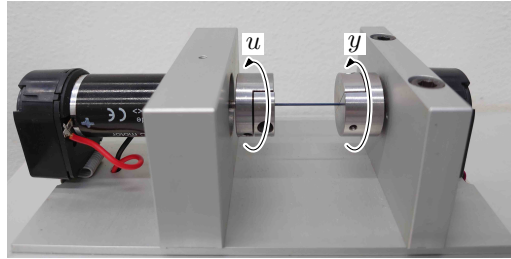


Fig. 4.8: Experimental setup of a two-inertia system connected via a flexible shaft. The motor on the left side is used as an input  $u$  and the encoder on the right side is used as an output  $y$ , respectively.

is improved in the linearly parameterized feedforward with tuning as  $\min\|e[k]\|_2$ .

The Root Mean Square (RMS) of the tracking errors in simulations is shown in Table 4.1. It shows that the tracking error of the linearly parameterized feedforward with tuning as  $\min\|e[k]\|_2$  is around the same scale as that of the multirate feedforward. As a result, the linearly parameterized feedforward can provide around the same performance as the multirate feedforward through a tuning process using the experimental data.

## 4.5 Application to multi-modal motion system

In this section, the approach in Section 4.3 is applied to a multi-modal motion system. The experimental results demonstrate performance improvement in both rigid and flexible modes. It results in Contribution 4.2.

### 4.5.1 Setup

The experimental setup of the two-inertia system is shown in Fig. 4.8. The system is modeled as the multi-modal representation and given by

$$G_c(s) = G_{rb}(s) + G_{fl}(s) \quad (4.42)$$

$$= \frac{1}{ms^2} + \frac{k}{m(s^2 + 2\zeta\omega s + \omega^2)}, \quad (4.43)$$

where  $m = 0.0004$ ,  $k = -1$ ,  $\zeta = 0.01$ , and  $\omega = 2\pi \times 54$  rad/s.

The frequency response data, the continuous-time model  $G_c$ , and the discrete-time model  $G_d$  are shown in Fig. 4.9. Note that these models are not directly used for the feedforward controller design but only used for the physical analysis.

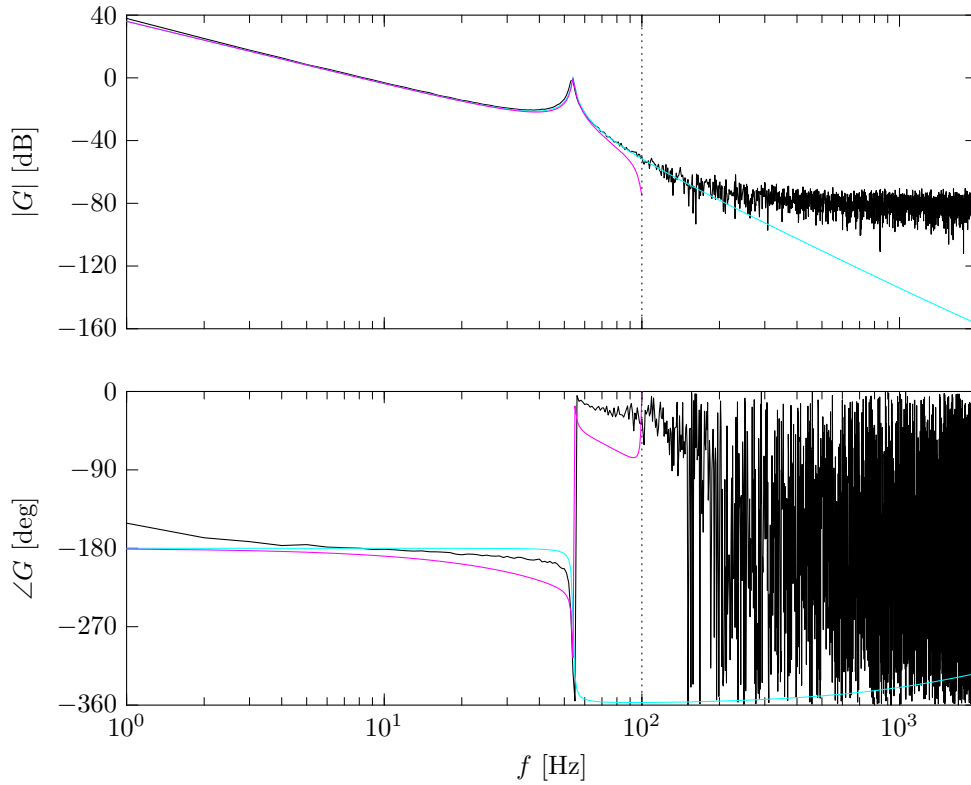


Fig. 4.9: Bode diagram of experimental setup: frequency response data (—), continuous-time model  $G_c$  (—), and discrete-time model  $G_d$  (—). Nyquist frequency is shown in a black dotted line (---).

## 4.5.2 Conditions

The continuous-time reference  $r(t)$  is the 4<sup>th</sup> order polynomial trajectory shown in Fig. 4.5. The sampling time of the discrete-time controller is  $T_s = 5$  ms. The continuous-time output  $y(t)$  is obtained by higher sampling frequency in every 0.25 ms only for evaluation of the continuous-time error  $e(t)$ . The approach using the multirate zero-order-hold differentiator  $\xi_{mr}$  is compared to that using the backward differentiator  $\xi_{bd}$ . The feedforward controller with acceleration and snap is used in the experiment. The same viscous friction compensation with the basis function  $\dot{r}[k] = \mathcal{S} \frac{d}{dt} r(t)$  is used in each method. The tuning parameters are optimized by the norm-optimal iterative learning control with several iterative experiments [73].

## 4.5.3 Experimental validation

The continuous-time error  $e(t)$  in the experimental result is shown in Fig. 4.10. The tracking performance using the multirate zero-order-hold differentiator is improved in two points compared to that using the backward differentiator. First, the acceleration feedforward compensates for rigid dynamics correctly and the error during acceleration and deceleration periods of the reference becomes smaller. Second, the snap feedforward compensates flexible dynamics correctly and the error because of the mechanical resonance becomes smaller. The results demonstrate that the feedforward using the multirate zero-order-hold differentiator outperforms that using the backward differentiator in both rigid and flexible modes.

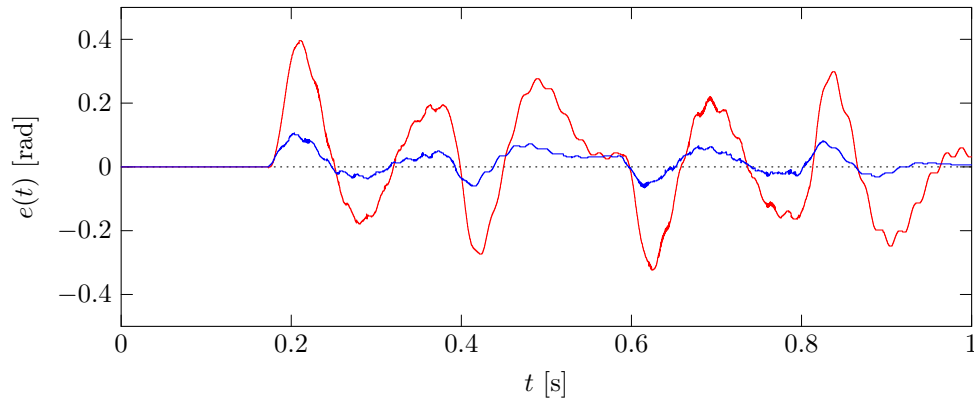


Fig. 4.10: Tracking error  $e(t)$  in experiment with  $\Psi = [\dot{r}, \Psi_a, \Psi_s]$ : using backward differentiator (—) and multirate zero-order-hold differentiator (—). The feedforward using the multirate zero-order-hold differentiator outperforms that using the backward differentiator in both rigid and flexible modes.

## 4.6 Conclusion

The low-order feedforward control approach considering the sampled-data characteristics is developed to improve both on-sample and intersample performance for reference tracking in multi-modal motion systems. The feedforward controller is linearly parameterized and the basis functions are designed using the multirate zero-order-hold differentiator for the state compatibility to the continuous-time reference. Application to the multi-modal motion system demonstrates a significant improvement in tracking performance compared to the conventional approach in the experiment. Ongoing research focuses on learning the tuning parameters from the experimental data, rational basis functions considering the sampled-data characteristics, and extension to the multi-input multi-output systems.





# Chapter 5

## Iterative Learning Control with MIMO Sampled-Data Basis Functions

Increasing performance requirements in high-precision motion systems lead to a situation where both multivariable and sampled-data implementation aspects need to be addressed. The aim is to develop a design framework for a multi-input multi-output feedforward controller to improve continuous-time tracking performance through learning. The sampled-data feedforward controller is designed with physically interpretable parameters using a multirate zero-order-hold differentiator. The developed approach enables interaction compensation for multi-input multi-output systems and the feedforward parameters are updated through learning. The performance improvement is experimentally validated in a multi-input multi-output motion system compared to a conventional diagonal feedforward controller.

### 5.1 Introduction

Feedforward control is essential in increasing performance requirements for motion control in industrial mechatronic systems such as semiconductor lithography systems [63, 74], wire bonders [37], machine tools [38, 75], printers [50], atomic force microscopies [76], magnetic bearings [77], and industrial robots [78]. Iterative learning control (ILC) is one of the algorithms to update the feedforward controller by the error data of the previous iteration, and the error is reduced through each iteration. It is beneficial that the feedforward controller consists of physically intuitive parameters to enable manual tuning in an industrial implementing process after learning from experimental data.

Sampled-data feedforward control improves the continuous-time tracking performance of high-precision motion systems where the sampling frequency is not sufficiently high compared to the motion profile [15]. In industrial control applications, the controlled system is discretized by sampler and zero-order-hold and these characteristics should be considered in feedforward controller design to improve not only on-sample but also intersample performance. State tracking feedforward control [20, 43] and ILC [79] with multirate inversion can improve the continuous-time tracking performance in sampled-data systems. These controllers enable on-sample state tracking and it leads to physically natural intersample behavior.

Physical interpretability and intuitive tuning of the feedforward controller are achieved by physical analysis of the model structure for the controlled system [80, 81]. From these analyses, the feedforward controller can be parameterized with tuning parameters and basis functions [69].

Basis functions typically consist of a reference signal and its derivatives [69] and nonlinear functions such as friction compensation [38]. This structure enables low-complexity parameterization and tuning parameters can have a physical meaning depending on the structure of the basis functions.

Although important contributions have been made to improve the performance and intuitiveness of feedforward control, the sampled-data characteristics with sampler and zero-order-hold are not taken into account in the basis function design, and the structure of multi-input multi-output (MIMO) feedforward control is not discussed in the context of intuitive tuning and leaning from experimental data. The aim of this chapter is to design the MIMO feedforward controller to improve the continuous-time tracking performance through learning. Compared to conventional approaches, the developed basis function design considers the sampled-data characteristics. In this chapter, the feedforward controller is parameterized with basis functions for MIMO motion systems and it enables physical interpretation of the feedforward controller parameters and analytic solution of data-driven parameter tuning.

The main contribution of this chapter is fixed-structure feedforward considering sampled-data characteristics and interactions in MIMO motion systems. The contributions include:

**Contribution 5.1 :** *Discrete-time basis functions are designed for continuous-time reference considering sampled-data characteristics.*

**Contribution 5.2 :** *ILC with basis functions is formulated considering the dynamics and interaction of MIMO motion systems.*

**Contribution 5.3 :** *The developed approach is experimentally validated in a MIMO motion system.*

The outline is as follows. In Section 5.2, the problem that is considered in this chapter is formulated. In Section 5.3, the basis function design considering continuous-time performance is described, constituting Contribution 5.1. In Section 5.4, ILC with basis functions is formulated in MIMO motion systems, constituting Contribution 5.2. In Section 5.5, the performance improvement with interaction compensation is experimentally validated, constituting Contribution 5.3. In Section 5.6, conclusions are presented.

## 5.2 Problem formulation

In this section, the problem to improve continuous-time tracking performance in MIMO motion systems is formulated. First, the reference tracking problem is defined in continuous time. Second, interaction compensation is investigated for reference tracking in MIMO motion systems. Finally, the problems in this chapter are described.

### 5.2.1 Continuous-time performance in sampled-data control

The considered tracking control configuration in a  $n_u$ -input  $n_y$ -output continuous-time linear time-invariant system  $G$  is shown in Fig. 5.1, with reference  $r(t) \in \mathbb{R}^{n_y}$ , control input  $u(t) \in \mathbb{R}^{n_u}$ , and output  $y(t) \in \mathbb{R}^{n_y}$ .

The system is controlled by the sampled-data controller that consists of feedforward controller  $F(\theta)$ , feedback controller  $K$ , sampler  $S$ , and zero-order-hold  $\mathcal{H}$ , where sampler and zero-order-hold are defined as follows.

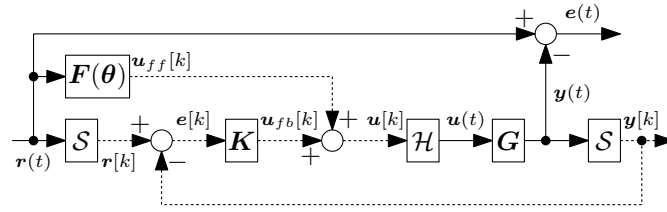


Fig. 5.1: Tracking control diagram. The continuous-time system  $\mathbf{G}$  is controlled by the feedforward controller  $\mathbf{F}(\theta)$  and the discrete-time feedback controller  $\mathbf{K}$  with sampler  $\mathcal{S}$  and zero-order-hold  $\mathcal{H}$ . The objective is to minimize the continuous-time error  $e(t)$ . The solid and dotted lines denote the continuous-time and discrete-time signals, respectively.

**Definition 5.1** (Sampler) : *The sampler  $\mathcal{S}$  with sampling time  $T_s$  is defined as*

$$\mathcal{S} : \mathbf{r}(t) \mapsto \mathbf{r}[k], \quad \mathbf{r}[k] = \mathbf{r}(kT_s). \quad (5.1)$$

**Definition 5.2** (Zero-order-hold) : *The zero-order-hold  $\mathcal{H}$  with sampling time  $T_s$  is defined as*

$$\mathcal{H} : \mathbf{u}[k] \mapsto \mathbf{u}(t), \quad \mathbf{u}(kT_s + \tau) = \mathbf{u}[k], \quad \tau = [0, T_s). \quad (5.2)$$

The control objective in this chapter is to minimize the continuous-time error  $e(t)$ . Traditionally, the conventional discrete-time controller only focuses on the on-sample performance with the discrete-time error  $e[k]$ . To improve the continuous-time error  $e(t)$ , not only on-sample but also intersample performance should be considered.

## 5.2.2 Decoupling control for interaction compensation

In the motion control of MIMO motion systems, the static decoupling is applied by the input decoupling matrix  $\mathbf{T}_u$  and the output decoupling matrix  $\mathbf{T}_y$ . The decoupled system  $\mathbf{T}_y \mathbf{G} \mathbf{T}_u$  should be square and diagonally dominant. In many cases, the single-input single-output (SISO) controller is designed after the static decoupling. Even if the system is statically decoupled, the off-diagonal terms still remain and it results in interaction between inputs and outputs [63].

In this chapter, the feedforward controller is designed considering both diagonal and off-diagonal dynamics to compensate for interaction through learning from data with less modeling effort of the MIMO motion system.

## 5.2.3 Problem description

In this chapter, the controller design problem is with respect to the following requirements:

**Requirement 5.1** : *The sampled-data characteristic should be considered in the discrete-time basis functions to improve continuous-time performance.*

**Requirement 5.2** : *The basis functions should be parameterized with physically interpretable parameters considering the dynamics and interaction of MIMO motion systems.*

Requirement 5.1 is dealt with in Section 5.3 and it results in Contribution 5.1. Requirement 5.2 is dealt with in Section 5.4 and it results in Contribution 5.2.

### 5.3 Basis function design using multirate zero-order-hold differentiator

In this section, the basis function design using a sampled-data differentiator is presented. First, the conventional approach using a backward differentiator is analyzed in sampled-data control. Second, the idea of state compatibility is defined to improve intersample performance. Third, the multirate zero-order-hold differentiator is developed to design the sampled-data basis functions that satisfy state compatibility. Finally, continuous-time performance improvement is shown in a single-mass motion system example. It results in Contribution 5.1.

#### 5.3.1 Challenge in sampled-data basis function design

The continuous-time feedforward controller can be parameterized using the reference signals  $r$  and its derivatives. It results in the combination with the tuning parameters  $\theta$  and the continuous-time basis functions that consist of a continuous-time differentiator  $\frac{d}{dt}$ . For example, the continuous-time acceleration feedforward controller  $F(\theta)$  can be designed for a single-mass motion system  $G(s) = \frac{1}{ms^2}$  as  $F(\theta) = \theta \frac{d^2}{dt^2}$ . In this example, the basis function is  $\Psi = \frac{d^2}{dt^2} r(t)$  and the tuning parameter is  $\theta = m$ . However, in industrial mechatronic systems, the motion controllers are typically implemented in discrete time. Therefore, to design the discrete-time basis function  $\Psi$ , the continuous-time differentiator  $\frac{d}{dt}$  should be replaced by the sampled-data differentiator  $\xi$  defined as follows.

**Definition 5.3** (Sampled-data differentiator) : *The  $n^{\text{th}}$  order sampled-data differentiator  $\xi^n$  with sampling time  $T_s$  is the conversion from the continuous-time signal  $r(t)$  to the discrete-time signal  $\Psi_n[k]$  that is compatible with the  $n^{\text{th}}$  order derivative of  $r(t)$  and defined as*

$$\Psi_n[k] = \xi^n r(t). \quad (5.3)$$

In the conventional approach [69], the discrete-time basis functions are designed by the continuous-time reference  $r(t)$  and the backward differentiator defined as follows.

**Definition 5.4** (Backward differentiator) : *The  $n^{\text{th}}$  order backward differentiator  $\xi_{bd}^n$  is given by*

$$\xi_{bd}^n = \begin{cases} \left( \frac{1 - z^{-1}}{T_s} \right)^n z^{\frac{n}{2}} \mathcal{S} & (n : \text{even}) \\ \left( \frac{1 - z^{-1}}{T_s} \right)^n \frac{1 + z^{-1}}{2} z^{\frac{n+1}{2}} \mathcal{S} & (n : \text{odd}) \end{cases}, \quad (5.4)$$

where  $z$  is the discrete-time shift operator with sampling time  $T_s$  defined as  $z^n r[k] = r[k + n]$ .  $z^{\frac{n}{2}}$  denotes the phase compensation. When  $n$  is odd, the phase compensation consists of the half sample shift  $z^{\frac{1}{2}}$  that is a combination of one sample shift and the first order approximation of averaging the current and previous value [69].

The backward differentiator does not take into account the effects of sampler and zero-order-hold, the performance deteriorates when the sampling frequency is not sufficiently high.

### 5.3.2 State compatibility for intersample performance

The sampled-data characteristics can be taken into account by the state tracking control framework [20, 43, 79]. In the  $n$  samples lifted system, the exact state tracking can be achieved in every  $n$  sample using such as a minimum-time dead-beat control [72] and multirate feedforward control [20]. In such cases, the states in every  $n$  sample are given by the multirate sampler defined as follows.

**Definition 5.5** (Multirate sampler) : *The multirate sampler  $\mathcal{S}_n$  in every  $n$  sample with sampling time  $T_s$  is defined as*

$$\mathcal{S}_n : r(t) \mapsto r[i_n], \quad r[i_n] = r(i_n n T_s). \quad (5.5)$$

The state-space representation of the continuous-time  $n^{\text{th}}$  order integrator in the controllable canonical form is given by

$$\left(\frac{1}{s}\right)^n = H_{nc} \stackrel{s}{=} \left[ \begin{array}{c|c} \mathbf{A}_{nc} & \mathbf{b}_{nc} \\ \mathbf{c}_{nc} & 0 \end{array} \right] = \left[ \begin{array}{cccc|c} 0 & 1 & 0 & 0 & 0 \\ 0 & \ddots & \ddots & 0 & \vdots \\ 0 & 0 & \ddots & 1 & 0 \\ 0 & 0 & 0 & 0 & 1 \\ \hline 1 & 0 & \cdots & 0 & 0 \end{array} \right], \quad (5.6)$$

where  $\mathbf{A}_{nc} \in \mathbb{R}^{n \times n}$ ,  $\mathbf{b}_{nc} \in \mathbb{R}^{n \times 1}$ , and  $\mathbf{c}_{nc} \in \mathbb{R}^{1 \times n}$ . To improve both on-sample and intersample performance in sampled-data systems with zero-order-hold and integrators, the basis functions should satisfy the state compatibility defined as follows.

**Definition 5.6** (State compatibility) : *The discrete-time signal  $\Psi_n[k]$ , which is compatible with the  $n^{\text{th}}$  order derivative signal of the continuous-time signal  $r(t)$ , satisfies state compatibility if the output through the system, that consists of the continuous-time  $(n - m)^{\text{th}}$  order integrator  $H_{(n-m)c}$  and zero-order-hold  $\mathcal{H}$ , is equal to the continuous-time  $m^{\text{th}}$  order derivative signal of  $r(t)$  in every  $n$  sample sampled by multirate sampler  $\mathcal{S}_n$  and defined as*

$$\mathcal{S}_n \frac{d^m}{dt^m} r(t) = \mathcal{S}_n H_{(n-m)c} \mathcal{H} \Psi_n[k], \quad (5.7)$$

where  $m = 0, 1, \dots, n - 1$ .

The sampled-data differentiator that satisfies the state compatibility should be designed to enable the feedforward parameterization with basis functions to improve continuous-time performance.

### 5.3.3 Multirate zero-order-hold differentiator with state compatibility

To improve the intersample performance in the discrete-time system, not only the output but also the states of the reference trajectory are considered. The multirate zero-order-hold differentiator is designed by the inverse of the continuous-time integrator discretized by sampler and zero-order-hold to satisfy the state compatibility. In this chapter, the reference is assumed to be sufficiently smooth and satisfies the following assumption:

**Assumption 5.1** (Smoothness of reference) : *The continuous-time reference  $r(t)$  for  $n$  states tracking is  $C^{n-1}$  class and differentiable at least  $n - 1$  times.*

To satisfy the  $n$  states compatibility in every  $n$  sample, the lifted signal is considered using the lifting operator defined as follows.

**Definition 5.7** (Lifting operator) : *The lifting operator  $\mathcal{L}_n$  in every  $n$  sample is defined as*

$$\mathcal{L}_n : u[k] \mapsto \underline{u}[i_n], \quad (5.8)$$

where

$$\underline{u}[i_n] = [u[ni_n] \quad u[ni_n + 1] \quad \cdots \quad u[ni_n + (n - 1)]]^T \in \mathbb{R}^n. \quad (5.9)$$

The  $n$  samples lifted system is defined as follows.

**Definition 5.8** (Lifted system) : *Consider a discrete-time system  $H_d \stackrel{z}{=} C_d(z\mathbf{I} - \mathbf{A}_d)^{-1}\mathbf{B}_d + \mathbf{D}_d$ . The relation between the input and the output in the  $n$  samples lifted system of  $H_d$  is given by*

$$\underline{y}[i_n] = \mathcal{L}_n y[k] = (\mathcal{L}_n H_d \mathcal{L}_n^{-1})(\mathcal{L}_n u[k]) = \underline{H}_d \underline{u}[i_n], \quad (5.10)$$

where

$$\underline{y}[i_n] = [y[ni_n] \quad y[ni_n + 1] \quad \cdots \quad y[ni_n + (n - 1)]]^T \in \mathbb{R}^n, \quad (5.11)$$

and the lifted system  $\underline{H}_d$  is defined as

$$\begin{aligned} \underline{H}_d \stackrel{z^n}{=} \mathcal{L}_n H_d \mathcal{L}_n^{-1} &= \left[ \begin{array}{c|ccc} \mathbf{A}_d & \mathbf{B}_d & & \\ \hline \mathbf{C}_d & \mathbf{D}_d & & \end{array} \right] \\ &= \left[ \begin{array}{c|cccc} \mathbf{A}_d^n & \mathbf{A}_d^{n-1}\mathbf{B}_d & \mathbf{A}_d^{n-2}\mathbf{B}_d & \cdots & \mathbf{A}_d\mathbf{B}_d & \mathbf{B}_d \\ \hline \mathbf{C}_d & \mathbf{D}_d & \mathbf{O} & \cdots & \cdots & \mathbf{O} \\ \mathbf{C}_d\mathbf{A}_d & \mathbf{C}_d\mathbf{B}_d & \mathbf{D}_d & \ddots & & \vdots \\ \vdots & \vdots & \ddots & \ddots & \ddots & \vdots \\ \mathbf{C}_d\mathbf{A}_d^{n-2} & \mathbf{C}_d\mathbf{A}_d^{n-3}\mathbf{B}_d & \mathbf{C}_d\mathbf{A}_d^{n-4}\mathbf{B}_d & \ddots & \mathbf{D}_d & \mathbf{O} \\ \mathbf{C}_d\mathbf{A}_d^{n-1} & \mathbf{C}_d\mathbf{A}_d^{n-2}\mathbf{B}_d & \mathbf{C}_d\mathbf{A}_d^{n-3}\mathbf{B}_d & \cdots & \mathbf{C}_d\mathbf{B}_d & \mathbf{D}_d \end{array} \right]. \quad (5.12) \end{aligned}$$

Considering the states in discrete-time, the  $n^{\text{th}}$  order integrator discretized by sampler and zero-order-hold is given by

$$\begin{aligned} H_{nd} \stackrel{z}{=} \mathcal{S}H_{nc}\mathcal{H} &= \left[ \begin{array}{c|c} \mathbf{A}_{nd} & \mathbf{b}_{nd} \\ \hline \mathbf{c}_{nd} & 0 \end{array} \right] \\ &= \left[ \begin{array}{c|c} e^{\mathbf{A}_{nc}T_s} & \mathbf{A}_{nc}^{-1}(e^{\mathbf{A}_{nc}T_s} - \mathbf{I})\mathbf{b}_{nc} \\ \hline \mathbf{c}_{nc} & 0 \end{array} \right]. \quad (5.13) \end{aligned}$$

To design the inverse of the  $n^{\text{th}}$  order integrator discretized by sampler and zero-order-hold, the  $n$  samples lifted system is given by

$$\underline{H}_{nd} \stackrel{z^n}{=} \mathcal{L}_n H_{nd} \mathcal{L}_n^{-1} = \left[ \begin{array}{c|c} \mathbf{A}_{nd} & \mathbf{B}_{nd} \\ \hline \mathbf{C}_{nd} & \mathbf{D}_{nd} \end{array} \right], \quad (5.14)$$

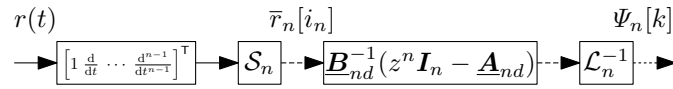


Fig. 5.2: Block diagram of basis function design using multirate zero-order-hold differentiator. The dotted and dashed lines denote the discrete-time signal sampled by  $T_s$  and  $nT_s$ , respectively.

and in state-space representation defined as

$$\mathbf{x}_n[i_n + 1] = \underline{\mathbf{A}}_{nd}\mathbf{x}_n[i_n] + \underline{\mathbf{B}}_{nd}\underline{u}[i_n] \quad (5.15)$$

$$\underline{y}[i_n] = \underline{\mathbf{C}}_{nd}\mathbf{x}_n[i_n] + \underline{\mathbf{D}}_{nd}\underline{u}[i_n] \quad (5.16)$$

where

$$\mathbf{x}_n[i_n] = [x_0[i_n] \quad x_1[i_n] \quad \cdots \quad x_{n-1}[i_n]]^T \in \mathbb{R}^n. \quad (5.17)$$

Satisfying the state compatibility, the relationship between the reference and the states is given by

$$\bar{r}_n[i_n] = \mathbf{x}_n[i_n], \quad (5.18)$$

where

$$\begin{aligned} \bar{r}_n[i_n] &= \mathcal{S}_n \left[ 1 \quad \frac{d}{dt} \quad \cdots \quad \frac{d^{n-1}}{dt^{n-1}} \right]^T r(t) \\ &= [r_0[i_n] \quad r_1[i_n] \quad \cdots \quad r_{n-1}[i_n]]^T \in \mathbb{R}^n. \end{aligned} \quad (5.19)$$

From the discussions above, the multirate zero-order-hold differentiator is given as follows.

**Theorem 5.1** (Multirate zero-order-hold differentiator) : *From (5.15) and (5.18), considering the inverse of the state equation in the continuous-time  $n^{\text{th}}$  order integrator discretized by sampler and zero-order-hold using the multirate feedforward control [20], the  $n^{\text{th}}$  order multirate zero-order-hold differentiator  $\xi_{mr}^n$  that satisfies the state compatibility is given by*

$$\xi_{mr}^n = \mathcal{L}_n^{-1} \underline{\mathbf{B}}_{nd}^{-1} (z^n \mathbf{I}_n - \underline{\mathbf{A}}_{nd}) \mathcal{S}_n \left[ 1 \quad \frac{d}{dt} \quad \cdots \quad \frac{d^{n-1}}{dt^{n-1}} \right]^T. \quad (5.20)$$

*Proof.* See Definition 5.6 and [20]. □

The basis function design procedure using multirate zero-order-hold differentiator is shown in Fig. 5.2.

### 5.3.4 Example in continuous-time performance improvement

The continuous-time performance improvement can be shown clearly in a single-mass motion system example. The controlled system is given as  $G(s) = \frac{1}{ms^2}$  where  $m = 1$  kg is the mass of the rigid body. The reference is the fourth order polynomial trajectory as shown at the top of Fig. 5.3. The sampling time is set to  $T_s = 10$  ms.

The center of Fig. 5.3 shows control inputs with the acceleration feedforward using the backward differentiator  $u[k] = m\xi_{bd}^2 r(t)$  [N] and that using the multirate zero-order-hold differentiator  $u[k] = m\xi_{mr}^2 r(t)$  [N].

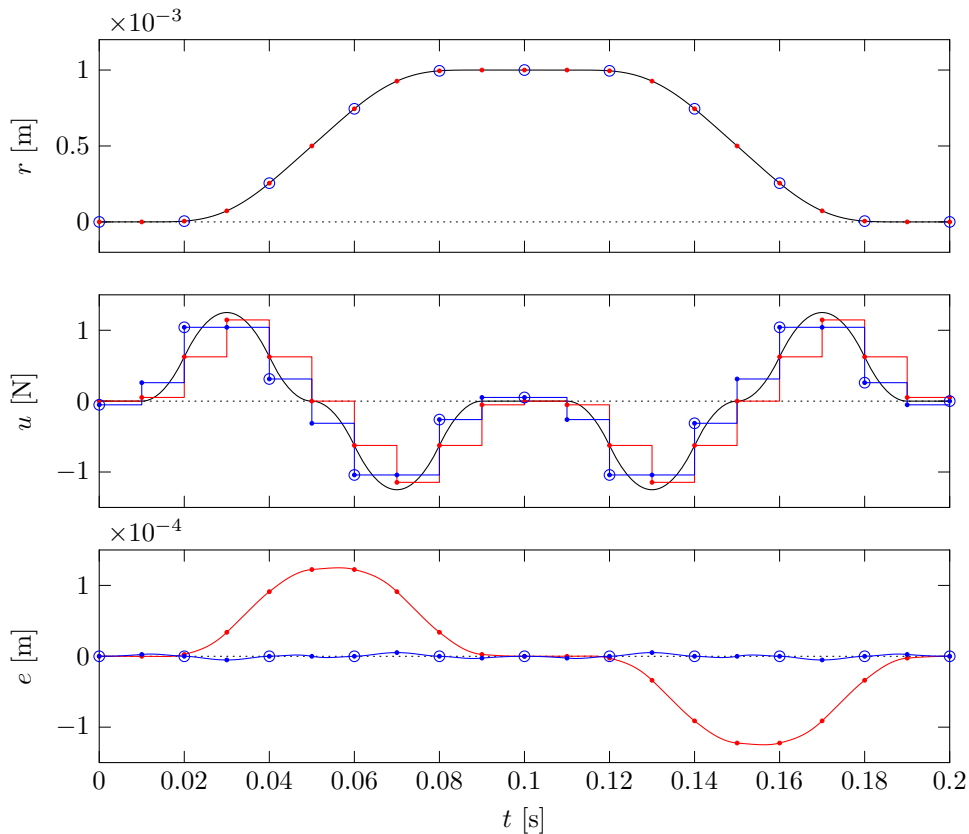


Fig. 5.3: Simulation results of the open-loop tracking in a single-mass motion system with acceleration feedforward using the backward differentiator (—) and that using the multirate zero-order-hold differentiator (—). Top: fourth order reference (—). Center: control inputs and a continuous-time acceleration profile (—). Bottom: tracking errors. The multirate zero-order-hold differentiator considers the sampled-data characteristics with sampler and zero-order-hold, and it results in a smaller error than the backward differentiator. (•) and (◦) show the sampling points every  $T_s$  and  $2T_s$ .

The bottom of Fig. 5.3 shows the comparison of the open-loop tracking errors. It shows that the acceleration feedforward using a multirate zero-order-hold differentiator outperforms that of the backward differentiator because of the state compatibility which compensates for the controlled system discretized by sampler and zero-order-hold.

## 5.4 Iterative learning control with MIMO structured basis functions

In this section, the feedforward parameterization and the parameter updating framework using ILC with basis functions are presented. The structured feedforward parameterization for MIMO motion systems is formulated with physically intuitive parameters. Parameter update through learning is described with the monotonic convergence condition in MIMO motion systems. It results in Contribution 5.2.



### 5.4.1 MIMO structured low-order feedforward parameterization

The dynamics of mechatronic systems are typically dominated by mechanics assuming that electronics are much faster than mechanics. This results in a situation where rigid modes are dominating the lower frequency and there are several flexible modes at a higher frequency due to limited mechanical stiffness. The  $n_u$ -input  $n_y$ -output continuous-time multi-modal motion system [46] is defined as

$$\begin{aligned} \mathbf{G}_c(s) &= \mathbf{G}_r(s) + \mathbf{G}_f(s) \\ &= \underbrace{\sum_{k_r=1}^{n_r} \frac{\mathbf{c}_{k_r} \mathbf{b}_{k_r}}{(s^2 + 2\zeta_{k_r} \omega_{k_r} s + \omega_{k_r}^2)}}_{\text{rigid modes}} + \underbrace{\sum_{k_f=1}^{n_f} \frac{\mathbf{c}_{k_f} \mathbf{b}_{k_f}}{(s^2 + 2\zeta_{k_f} \omega_{k_f} s + \omega_{k_f}^2)}}_{\text{flexible modes}}, \end{aligned} \quad (5.21)$$

where  $n_r \in \mathbb{N}_+$  and  $n_f \in \mathbb{N}_+$  are the number of rigid and flexible modes,  $\omega \in \mathbb{R}_+$  and  $\zeta \in \mathbb{R}_+$  are the resonance angular frequency and the damping coefficient. The vectors  $\mathbf{b} \in \mathbb{R}^{1 \times n_u}$  and  $\mathbf{c} \in \mathbb{R}^{n_y \times 1}$  are associated with the inputs, the outputs, and the mode shapes. In this chapter, the system is assumed to be square as  $n_y = n_u$ .

To compensate for not only the rigid modes but also the flexible modes in MIMO motion systems, the traditional rigid body feedforward is extended with the additional snap feedforward [80] and the ideal feedforward controller  $\mathbf{F}^*(s)$  is defined as

$$\mathbf{F}^*(s) = \mathbf{G}_r^{-1}(s) + \mathbf{D}^*(s)s^4, \quad (5.22)$$

where  $\mathbf{D}^*(s)$  is the coefficient of the snap feedforward aiming to compensate for the compliance of the flexible modes.

The objective of the feedforward controller  $\mathbf{F}^*(s)$  is to minimize the closed-loop error given by

$$\mathbf{e}(s) = \mathbf{S}(s)\mathbf{r}(s) - \mathbf{S}(s)\mathbf{G}_c(s)\mathbf{F}^*(s)\mathbf{r}(s), \quad (5.23)$$

where  $\mathbf{S}(s)$  denotes the sensitivity function matrix and is defined as

$$\mathbf{S}(s) = (\mathbf{I} + \mathbf{G}_c(s)\mathbf{K}_c(s))^{-1}. \quad (5.24)$$

It results in  $\mathbf{F}^*(s) = \mathbf{G}_c^{-1}(s)$  and  $\mathbf{D}^*(s)$  is given by

$$\mathbf{D}^*(s) = \frac{1}{s^4}(\mathbf{G}_c^{-1}(s) - \mathbf{G}_r^{-1}(s)). \quad (5.25)$$

Assuming the reference trajectory in the mechatronic systems mainly contains the low-frequency components and the resonance frequencies of the rigid modes are enough smaller than that of flexible modes approximated to  $\omega_{k_r} \simeq 0$ , the compliance that corresponds to the low-frequency behavior of the flexible modes is given by

$$\begin{aligned} \mathbf{D} &= \lim_{s \rightarrow 0} \mathbf{D}^*(s) = \lim_{s \rightarrow 0} \left\{ \frac{1}{s^4} (\mathbf{G}_c^{-1}(s) - \mathbf{G}_r^{-1}(s)) \right\} \\ &= - \left( \sum_{k_r=1}^{n_r} \mathbf{c}_{k_r} \mathbf{b}_{k_r} \right)^{-1} \left( \sum_{k_f=1}^{n_f} \frac{\mathbf{c}_{k_f} \mathbf{b}_{k_f}}{\omega_{k_f}^2} \right) \left( \sum_{k_r=1}^{n_r} \mathbf{c}_{k_r} \mathbf{b}_{k_r} \right)^{-1}. \end{aligned} \quad (5.26)$$

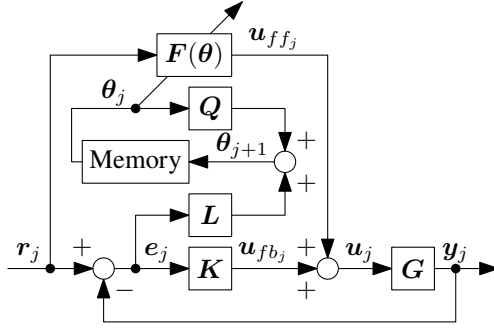


Fig. 5.4: Block diagram of iterative learning control with basis functions.

Hence, the low-order feedforward controller for MIMO motion systems is parameterized as

$$\mathbf{F}(\boldsymbol{\theta}) = \underbrace{\boldsymbol{\Theta}_p + \boldsymbol{\Theta}_v \frac{d}{dt} + \boldsymbol{\Theta}_a \frac{d^2}{dt^2}}_{\text{rigid body compensation}} + \underbrace{\boldsymbol{\Theta}_s \frac{d^4}{dt^4}}_{\text{compliance compensation}}, \quad (5.27)$$

where  $\boldsymbol{\Theta}_p, \boldsymbol{\Theta}_v, \boldsymbol{\Theta}_a, \boldsymbol{\Theta}_s \in \mathbb{R}^{n_u \times n_y}$  are the parameter matrices of the feedforward controller corresponding to the position, velocity, acceleration and snap basis functions. Finally, the continuous-time differentiator  $\frac{d}{dt}$  is replaced by the sampled-data differentiator  $\xi$ , and the fixed-structure sampled-data feedforward controller for MIMO motion systems is given by

$$\mathbf{F}(\boldsymbol{\theta}) = \boldsymbol{\Theta}_p + \boldsymbol{\Theta}_v \xi + \boldsymbol{\Theta}_a \xi^2 + \boldsymbol{\Theta}_s \xi^4. \quad (5.28)$$

Note that this feedforward parameterization includes the pole dynamics of the rigid mode and the compliance of pole and zero dynamics in flexible modes. The dynamics of the discretization zeros are included in the sampled-data differentiator.

### 5.4.2 Norm-optimal ILC with basis functions

Achieving higher performance and ease of tuning for the MIMO feedforward controller, ILC with basis functions is implemented. The controller structure is shown in Fig. 5.4. To update feedforward parameters through learning, the optimization criterion from the present studies [73, 81] is defined as follows.

**Definition 5.9** (Norm-optimal MIMO ILC with basis functions) : *The optimization criterion for norm-optimal ILC with basis functions is given by*

$$\mathcal{J}(\boldsymbol{\theta}_{j+1}) = \|\mathbf{e}_{j+1}\|_{\mathbf{W}_e} + \|\mathbf{u}_{ffj+1}\|_{\mathbf{W}_{ff}} + \|\mathbf{u}_{ffj+1} - \mathbf{u}_{ffj}\|_{\mathbf{W}_{\Delta ff}}, \quad (5.29)$$

where the weighting matrices are  $\mathbf{W}_e \succ 0$ ,  $\mathbf{W}_{ff}, \mathbf{W}_{\Delta ff} \succeq 0$ , the parameters of the feedforward controller are  $\boldsymbol{\theta}_j \in \mathbb{R}^{n_\theta}$ , and the feedforward input in next iteration is  $\mathbf{u}_{ffj+1} = \mathbf{F}(\boldsymbol{\theta}_{j+1})\mathbf{r}$ .

Here, the weighting matrices  $\mathbf{W}_e, \mathbf{W}_{ff}, \mathbf{W}_{\Delta ff}$  correspond to optimal performance, robustness for model uncertainty, and robustness for trial varying disturbances, respectively.

The error in trial  $j + 1$  is given by

$$\mathbf{e}_{j+1} = \mathbf{S}\mathbf{r} - \mathbf{S}\mathbf{G}\mathbf{u}_{ffj+1} \quad (5.30)$$

$$= \mathbf{e}_j - \mathbf{S}\mathbf{G}(\mathbf{u}_{ffj+1} - \mathbf{u}_{ffj}), \quad (5.31)$$

where  $\mathbf{S} = (\mathbf{I} + \mathbf{G}\mathbf{K})^{-1}$ .

The feedforward parameter update is given by

$$\boldsymbol{\theta}_{j+1}^* = \arg \min_{\boldsymbol{\theta}_{j+1}} \mathcal{J}(\boldsymbol{\theta}_{j+1}). \quad (5.32)$$

When the feedforward input is linearly parameterized in parameters  $\boldsymbol{\theta}_{j+1}$  and basis functions  $\boldsymbol{\Psi}$  and defined as

$$\mathbf{u}_{ffj+1} = \mathbf{F}(\boldsymbol{\theta}_{j+1})\mathbf{r} = \boldsymbol{\Psi}\boldsymbol{\theta}_{j+1}, \quad (5.33)$$

the optimization criterion (5.29) is quadratic in  $\boldsymbol{\theta}_{j+1}$  from (5.31), and an analytic solution to (5.32) exists [73, 81]. From basis functions  $\boldsymbol{\Psi} = \frac{\partial}{\partial \boldsymbol{\theta}_j} \mathbf{F}(\boldsymbol{\theta}_j)\mathbf{r} \in \mathbb{R}^{n_u \times n_\theta}$  and weighting matrices  $\mathbf{W}_e$ ,  $\mathbf{W}_{ff}$ ,  $\mathbf{W}_{\Delta ff}$ , the analytic solution to (5.32) for parameter update is given by

$$\boldsymbol{\theta}_{j+1} = \mathbf{Q}\boldsymbol{\theta}_j + \mathbf{L}e_j, \quad (5.34)$$

where the learning filters  $\mathbf{Q}$  and  $\mathbf{L}$  are given by

$$\mathbf{Q} = (\boldsymbol{\Psi}^\top((\mathbf{S}\mathbf{G})^\top \mathbf{W}_e(\mathbf{S}\mathbf{G}) + \mathbf{W}_{ff} + \mathbf{W}_{\Delta ff})\boldsymbol{\Psi})^{-1}\boldsymbol{\Psi}^\top((\mathbf{S}\mathbf{G})^\top \mathbf{W}_e(\mathbf{S}\mathbf{G}) + \mathbf{W}_{\Delta ff})\boldsymbol{\Psi}, \quad (5.35)$$

$$\mathbf{L} = (\boldsymbol{\Psi}^\top((\mathbf{S}\mathbf{G})^\top \mathbf{W}_e(\mathbf{S}\mathbf{G}) + \mathbf{W}_{ff} + \mathbf{W}_{\Delta ff})\boldsymbol{\Psi})^{-1}\boldsymbol{\Psi}^\top(\mathbf{S}\mathbf{G})^\top \mathbf{W}_e. \quad (5.36)$$

From (5.30), (5.33), and (5.34), parameter update is given by

$$\boldsymbol{\theta}_{j+1} = (\mathbf{Q} - \mathbf{L}\mathbf{S}\mathbf{G}\boldsymbol{\Psi})\boldsymbol{\theta}_j + \mathbf{L}\mathbf{S}\mathbf{r}, \quad (5.37)$$

and parameter update in (5.37) leads to monotonic convergence of  $\|\mathbf{u}_{ffj}\|$  if provided weighting matrices  $\mathbf{W}_e$ ,  $\mathbf{W}_{ff}$ ,  $\mathbf{W}_{\Delta ff}$  are selected properly as satisfying following conditions:

$$\begin{aligned} \bar{\sigma}(\mathbf{Q} - \mathbf{L}\mathbf{S}\mathbf{G}\boldsymbol{\Psi}) &< 1 \Leftrightarrow \\ \bar{\sigma}((\boldsymbol{\Psi}^\top((\mathbf{S}\mathbf{G})^\top \mathbf{W}_e(\mathbf{S}\mathbf{G}) + \mathbf{W}_{ff} + \mathbf{W}_{\Delta ff})\boldsymbol{\Psi})^{-1}\boldsymbol{\Psi}^\top \mathbf{W}_{\Delta ff}\boldsymbol{\Psi}) &< 1, \end{aligned} \quad (5.38)$$

where  $\bar{\sigma}(\cdot)$  is the maximum singular value of the matrix.

## 5.5 Application to MIMO motion system

In this section, the developed approach combining Section 5.3 and Section 5.4 is applied to a MIMO motion system. The results demonstrate the performance improvement with interaction compensation in both the simulation and the experiment. It results in Contribution 5.3.

### 5.5.1 Motion system

The MIMO motion system that consists of a suspended beam is shown in Fig. 5.5. After the static decoupling, the controlled system  $\mathbf{G}$  is given in translation and rotation motions with dual-inputs  $(F_y, T_z)$  and dual-outputs  $(y, R_z)$ . The frequency response data, the continuous-time model  $\mathbf{G}_c$  with the higher-order dynamics for the simulation and the discrete-time model  $\mathbf{G}_d$  with the only diagonal rigid dynamics for parameter update are shown in Fig. 5.6. The continuous-time reference of the translation  $y$  is the 4<sup>th</sup> order polynomial trajectory as shown in Fig. 5.7, and that of the rotation  $R_z$  is set to 0 rad for all time. The sampling frequency of the discrete-time controller is  $F_s = 128$  Hz and the sampling time is  $T_s = 1/F_s$ . The continuous-time outputs  $y$  and  $R_z$  are also measured in higher sampling frequency 1024 Hz only for evaluation of the continuous-time errors  $e(t)$ . The feedback controller  $\mathbf{K}$  is designed diagonally with a PD controller and a notch filter as a 5 Hz closed-loop bandwidth and a 6 dB modulus margin.

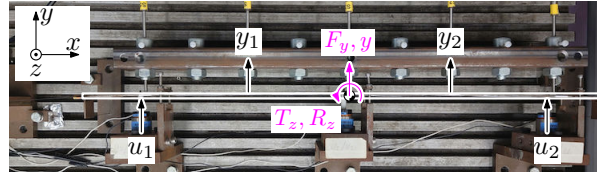


Fig. 5.5: Top view of the experimental setup. The system consists of the suspended beam with actuation through actuators ( $u_1, u_2$ ) and position measurement through sensors ( $y_1, y_2$ ) in a horizontal direction.

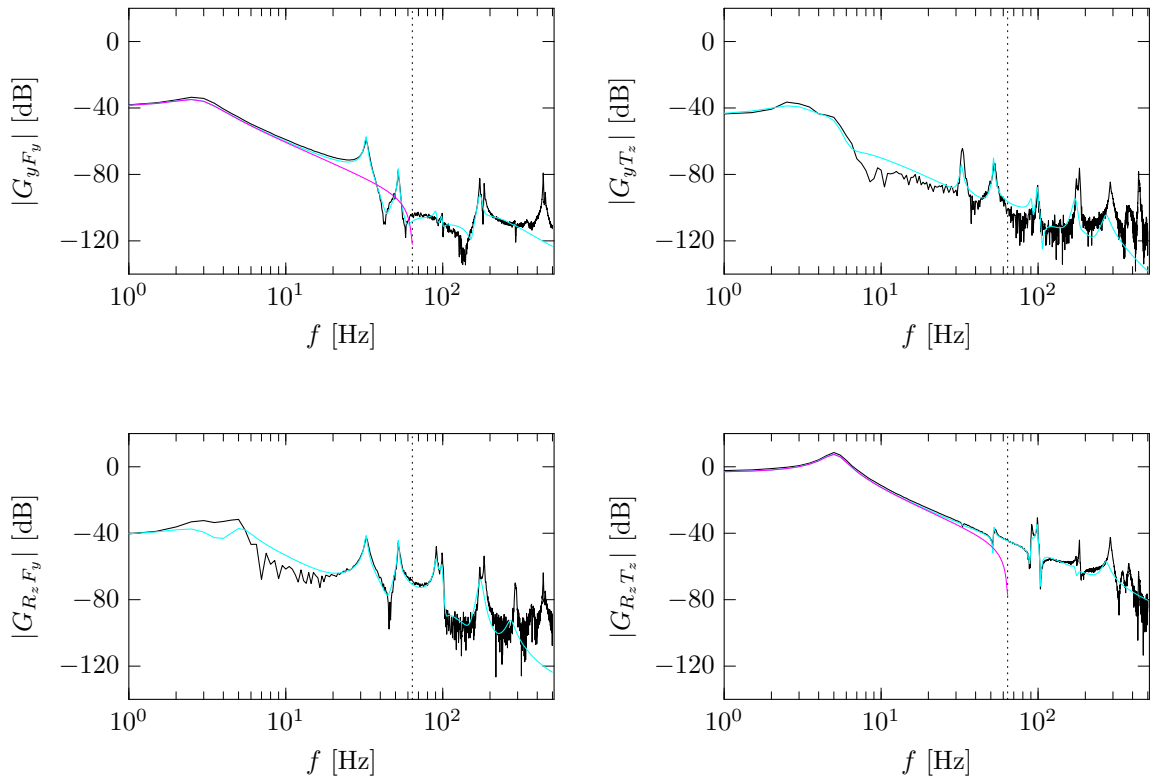


Fig. 5.6: Bode magnitude plot of the experimental setup: frequency response data (—), continuous-time model  $G_c$  (—) with the higher-order dynamics for the simulation, and discrete-time model  $G_d$  (—) with the only diagonal rigid dynamics for parameter update. Nyquist frequency of the controller is shown in a black dotted line (---).

## 5.5.2 Basis function design

From Section 5.4, the low-order feedforward controller for a MIMO motion system is parameterized as

$$\begin{aligned}
 \mathbf{F}(\boldsymbol{\theta}) = & \begin{bmatrix} \theta_{p11} & \theta_{p12} \\ \theta_{p21} & \theta_{p22} \end{bmatrix} \begin{bmatrix} 1 \\ 1 \end{bmatrix} + \begin{bmatrix} \theta_{v11} & \theta_{v12} \\ \theta_{v21} & \theta_{v22} \end{bmatrix} \begin{bmatrix} \xi \\ \xi \end{bmatrix} \\
 & + \begin{bmatrix} \theta_{a11} & \theta_{a12} \\ \theta_{a21} & \theta_{a22} \end{bmatrix} \begin{bmatrix} \xi^2 \\ \xi^2 \end{bmatrix} + \begin{bmatrix} \theta_{s11} & \theta_{s12} \\ \theta_{s21} & \theta_{s22} \end{bmatrix} \begin{bmatrix} \xi^4 \\ \xi^4 \end{bmatrix}, \quad (5.39)
 \end{aligned}$$

where the multirate zero-order-hold differentiator  $\xi_{mr}$  presented in Section 5.3 is used as a sampled-data differentiator  $\xi$ . The basis functions of each output are defined as

$$\Psi_y = \begin{bmatrix} r_y & \xi r_y & \xi^2 r_y & \xi^4 r_y \end{bmatrix}, \quad (5.40)$$

$$\Psi_{R_z} = \begin{bmatrix} r_{R_z} & \xi r_{R_z} & \xi^2 r_{R_z} & \xi^4 r_{R_z} \end{bmatrix}, \quad (5.41)$$

and the tuning parameter vectors are defined as

$$\begin{aligned} \theta_{11} &= [\theta_{p11} & \theta_{v11} & \theta_{a11} & \theta_{s11}], & \theta_{12} &= [\theta_{p12} & \theta_{v12} & \theta_{a12} & \theta_{s12}], \\ \theta_{21} &= [\theta_{p21} & \theta_{v21} & \theta_{a21} & \theta_{s21}], & \theta_{22} &= [\theta_{p22} & \theta_{v22} & \theta_{a22} & \theta_{s22}]. \end{aligned} \quad (5.42)$$

In the conventional approach, only the diagonal terms of the feedforward controller are considered. The feedforward input in the conventional approach is parameterized as

$$\mathbf{u}_{ff} = \mathbf{F}(\boldsymbol{\theta})\mathbf{r} = \Psi\boldsymbol{\theta} = \begin{bmatrix} \Psi_y & \mathbf{0} \\ \mathbf{0} & \Psi_{R_z} \end{bmatrix} [\boldsymbol{\theta}_{11} \quad \boldsymbol{\theta}_{22}]^\top. \quad (5.43)$$

In the developed approach, not only the diagonal terms but also the off-diagonal terms of the feedforward controller are taken into account. The off-diagonal terms also can be obtained for interaction compensation through learning even if there is only a diagonal model. The feedforward input in the developed approach is parameterized as

$$\begin{aligned} \mathbf{u}_{ff} &= \mathbf{F}(\boldsymbol{\theta})\mathbf{r} = \Psi\boldsymbol{\theta} \\ &= \begin{bmatrix} \Psi_y & \Psi_{R_z} & \mathbf{0} & \mathbf{0} \\ \mathbf{0} & \mathbf{0} & \Psi_y & \Psi_{R_z} \end{bmatrix} [\boldsymbol{\theta}_{11} \quad \boldsymbol{\theta}_{12} \quad \boldsymbol{\theta}_{21} \quad \boldsymbol{\theta}_{22}]^\top. \end{aligned} \quad (5.44)$$

In both the simulation and the experiment, the weighting matrices are set to  $\mathbf{W}_e = \mathbf{I}$  and  $\mathbf{W}_{ff} = \mathbf{W}_{\Delta ff} = \mathbf{O}$  in both the conventional and developed approaches.

### 5.5.3 Simulation results

The continuous-time errors in the simulations after 20 iterations are shown in Fig. 5.8. It shows that the rotation error  $e_{R_z}$  in the conventional approach is improved by the developed approach due to interaction compensation about factor 100. The translation error  $e_y$  is also improved but the interaction effect is not serious in the translation  $y$  because the reference of the rotation  $R_z$  is set to 0 rad for all time.

### 5.5.4 Experimental results

The continuous-time errors in the experiments after 20 iterations are shown in Fig. 5.9. It shows that the rotation error  $e_{R_z}$  in the conventional approach is improved by the developed approach due to interaction compensation also in the experiment about factor 10. The errors  $e_y$  and  $e_{R_z}$  show a similar trend in both the simulation and experimental results. Note that the scales of the errors in simulation and experiment are different about factor 10 in translation  $y$  and about factor 5 in rotation  $R_z$  because of the dynamics not included in the simulation model, measurement noise, and quantization of the sensors and actuators.

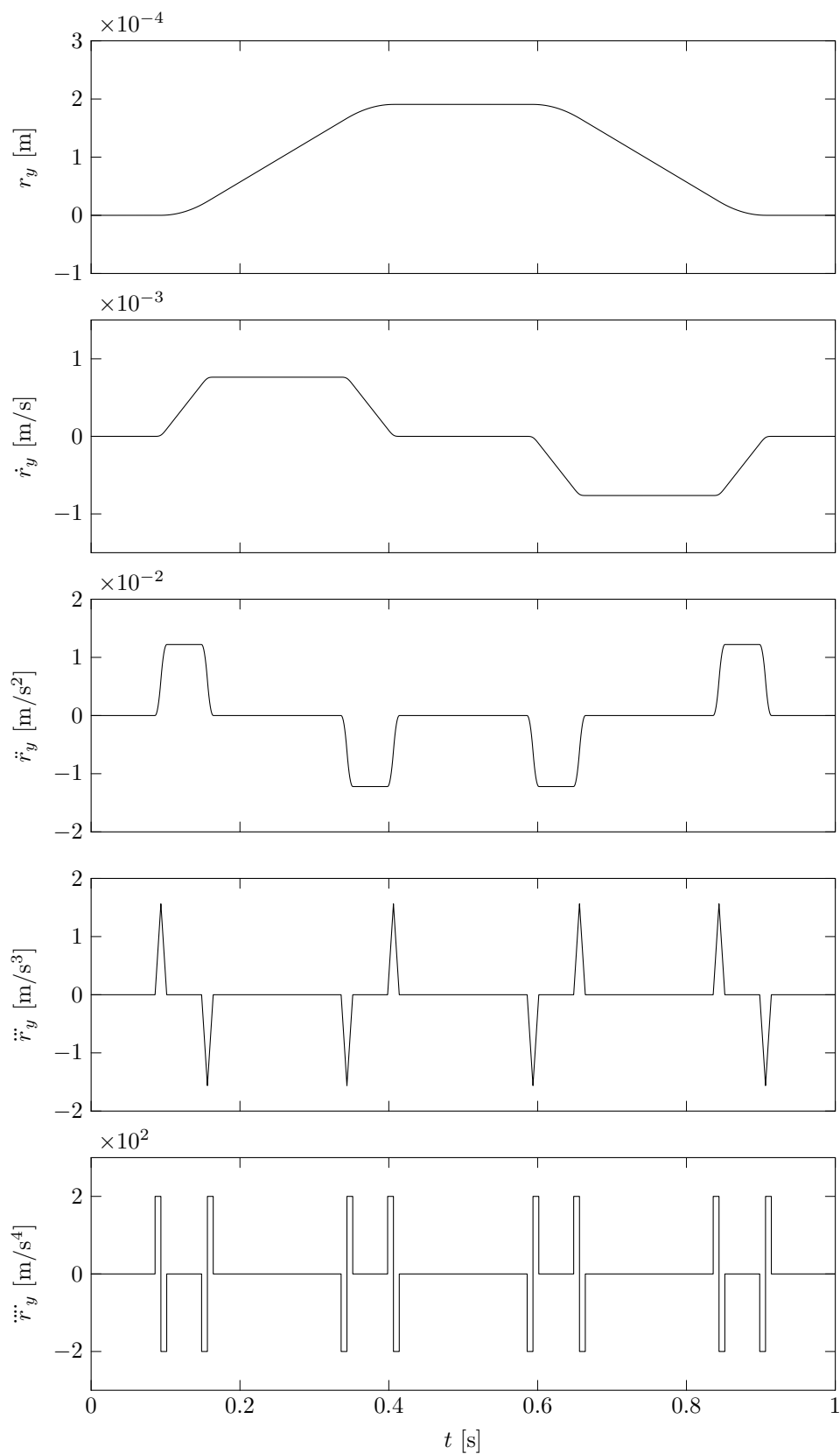


Fig. 5.7: Reference of  $y$ : continuous-time 4<sup>th</sup> order polynomial trajectory and its derivatives. Reference of  $R_z$  is set to 0 rad for all time.

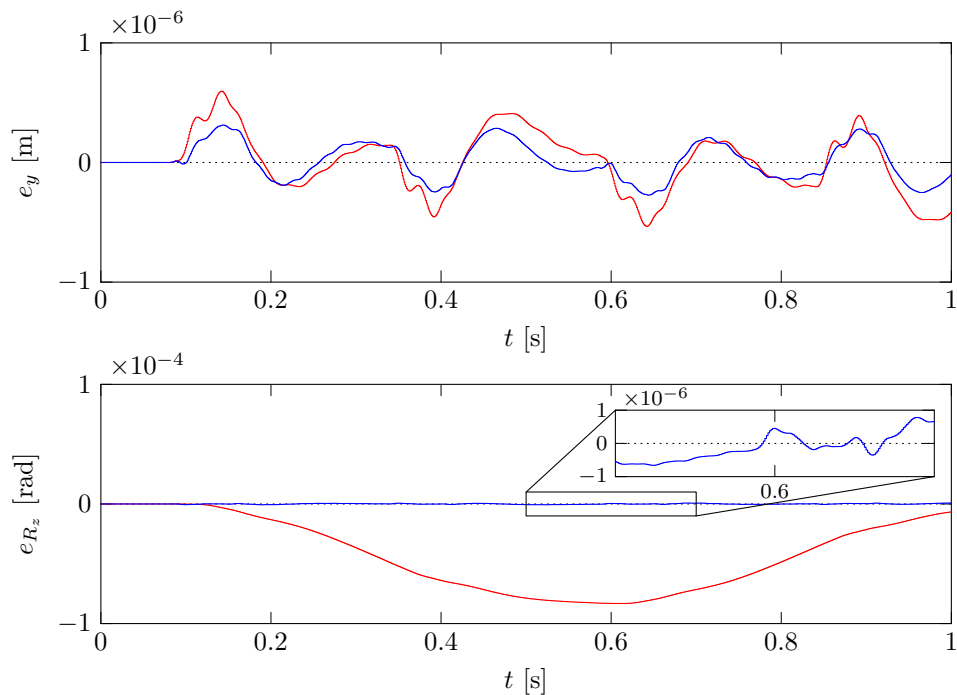


Fig. 5.8: Tracking error  $e(t)$  in simulation: without (—) and with (—) interaction compensation. Rotation error  $e_{R_z}$  is improved about factor 100.

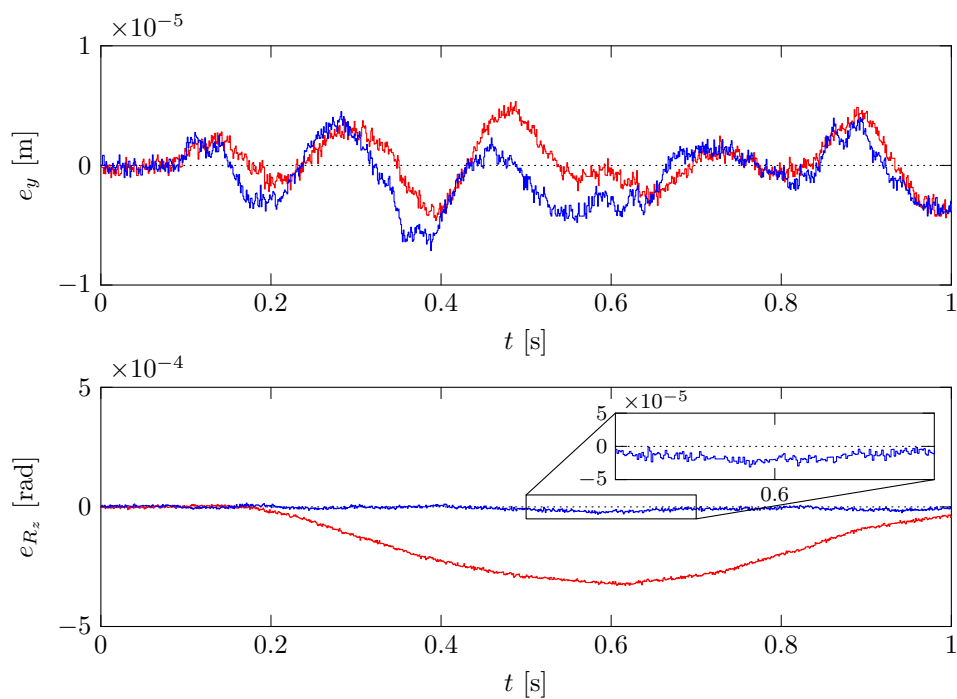


Fig. 5.9: Tracking error  $e(t)$  in experiment: without (—) and with (—) interaction compensation. Rotation error  $e_{R_z}$  is improved about factor 10.

## **5.6 Conclusion**

Fixed-structure feedforward control considering sampled-data characteristics and interactions in MIMO motion systems is developed. The feedforward inputs parameterized by MIMO sampled-data basis functions and physically intuitive tuning parameters are updated through learning. Application to the MIMO motion system demonstrates a significant improvement in tracking performance with interaction compensation compared to the conventional diagonal approach in both the simulation and the experiment even if the parameters are updated with the diagonal model of the controlled system. Ongoing research focuses on ILC with rational sampled-data basis functions and basis function design with higher-order dynamics.



## **Part IV**

# **Feedback Controller Design using Frequency Response Data**



# Chapter 6

## Disturbance Rejection with Robust Performance in Dual-Stage Actuator

Disturbance rejection of a Hard Disk Drive (HDD) enables a large amount of data storage in a recent information society. The aim is to design a feedback controller which rejects disturbances at multiple frequencies in HDDs. The disturbance rejection is achieved using resonant filters which have a large peak at disturbance frequencies. The developed approach enables the convex optimization of resonant filters with phase stabilization and stroke limitation using frequency response data of a controlled system. The disturbance rejection performance of the optimized resonant filters is validated in a dual-stage actuator HDD benchmark problem.

### 6.1 Introduction

Increasing demand for storage capacity of data servers in a recent information society leads to the importance of the track-following performance in a Hard Disk Drive (HDD) [82]. To improve the track-following performance, the feedback controller should be designed to reject disturbances in HDDs.

Model-based approaches are traditionally developed such as using adaptive control [83–86], resonant filter [87], repetitive control [88, 89], Youla–Kucera parameterization [90], disturbance observer [91], and coupling controller [92]. They basically need a modeling process of a controlled system that makes it difficult to consider model variations of mass-produced HDDs. These approaches also need a heuristic tuning process. Data-based approaches are also developed to recover disadvantages of model-based approaches such as using  $H_\infty$  and  $H_2$  robust control [93, 94]. These approaches only consider the gain stabilization and it can result in a conservative controller design. Hardware constraints such as maximum strokes also should be considered for actual implementation.

Although important contributions have been made to design feedback controllers for disturbance rejection in HDDs, phase stabilization and stroke limitation are not considered in the optimization of feedback controllers. In this chapter, the developed approach enables the structured multiple resonant filter design considering phase stabilization and stroke limitation.

The main contributions of this chapter are as follows.

**Contribution 6.1 :** *Resonant filters for a dual-input single-output system are designed by iterative convex optimization.*



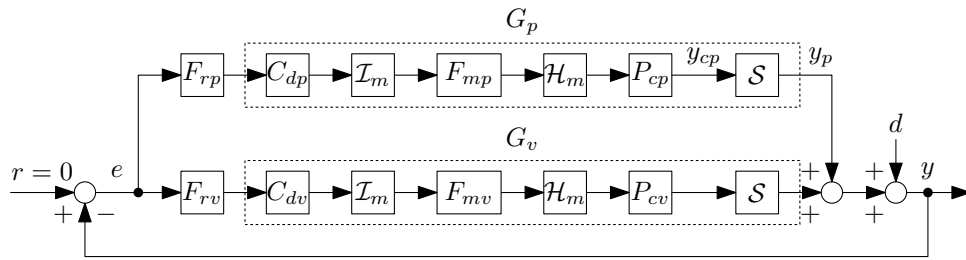
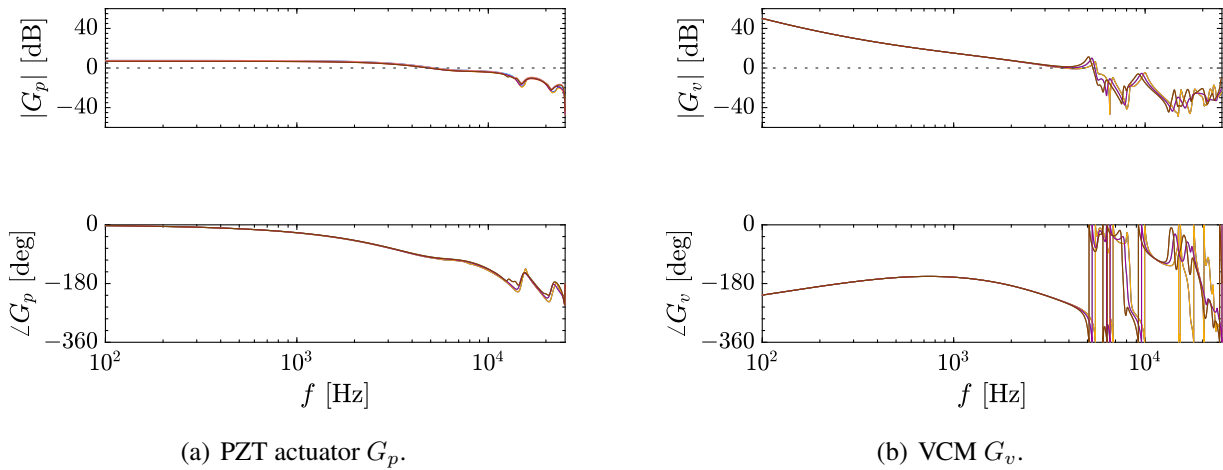


Fig. 6.2: Block diagram of a hard disk drive with a dual-stage actuator.



(a) PZT actuator  $G_p$ .

(b) VCM  $G_v$ .

Fig. 6.3: Frequency responses of given open-loop systems.

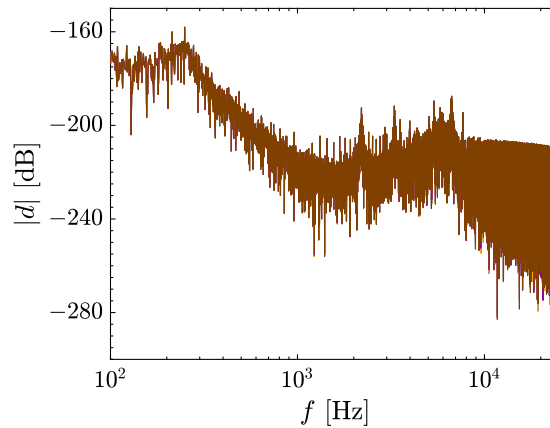


Fig. 6.4: Amplitude spectrum of output disturbances.

In this chapter, the reference signal is  $r = 0$  in all time and the objective is designing the resonant filters  $F_{rp}$  and  $F_{rv}$  for each actuator in addition to given open-loop controlled system  $G_p$  and  $G_v$  to minimize the worst case of track-following error against to the output disturbance  $d$ .

From these conditions, the data-based feedback controller design method should be presented with respect to the following requirements.

**Requirement 6.1 :** *The feedback controller is represented in structured parameterization and the parameters can be designed by convex optimization using frequency response data.*

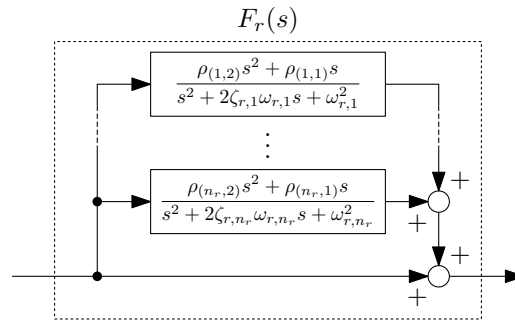


Fig. 6.5: Block diagram of resonant filters.

**Requirement 6.2 :** *The feedback controller satisfies robust stability and robust performance by considering the model variation of the controlled system.*

**Requirement 6.3 :** *The feedback controller can be applied to a dual-stage actuator HDD with respect to hardware restrictions.*

Considering these requirements, the design method of multiple resonant filters using convex optimization is presented in this chapter.

## 6.3 Convex optimization of multiple resonant filters

In this section, the optimization method of multiple resonant filters for a dual-stage actuator HDD is formulated. The structure of the designed resonant filters is presented. The optimization problem that directly uses frequency response data is formulated with conditions of robust stability, robust performance, and hardware constraints. The optimization problem is solved by iterative convex optimization with sequential linearization.

### 6.3.1 Structure of designed resonant filters

To improve the track-following performance, disturbances can be rejected by the resonant filters [87] that have the same resonance frequency as the disturbance frequencies because of the internal model principle. In this chapter, multiple resonant filters are designed in disturbance frequencies to improve the track-following performance.

The block diagram of the designed resonant filters with multiple resonance frequencies is shown in Fig. 6.5. The resonant filter in each actuator is defined as



maximum value with the given feedback controller. For robust stability, the vector locus with resonant filters must be on the same side against  $(-1, j0)$  and at the outside of the modulus margin. From these conditions, the optimization problem is formulated as follows.

$$\underset{\boldsymbol{\rho}}{\text{minimize}} \quad \max_{\forall k_c, \forall k_f} |e_{k_c}(j\omega_{k_f})| \quad (6.4a)$$

subject to  
 $\forall k_c, \forall k_f$

$$|y_{p,k_c}(j\omega_{k_f})| \leq y_{p,\max} \quad (6.4b)$$

$$w_s(j\omega_{k_f}) |S_{k_c}(j\omega_{k_f}, \boldsymbol{\rho})| \leq 1 \quad (6.4c)$$

$$-\frac{\pi}{2} \leq \angle(1 + L_{k_c}(j\omega_{k_f}, \boldsymbol{\rho})) - \angle(1 + G_{k_c}(j\omega_{k_f})) \leq \frac{\pi}{2}, \quad (6.4d)$$

where  $w_s$  is the weighting of the sensitivity function and

$$G_{k_c}(j\omega_r) = G_{p,k_c}(j\omega_{k_f}) + G_{v,k_c}(j\omega_{k_f}), \quad (6.5)$$

$$L_{k_c}(j\omega_{k_f}, \boldsymbol{\rho}) = L_{p,k_c}(j\omega_{k_f}, \boldsymbol{\rho}_p) + L_{v,k_c}(j\omega_{k_f}, \boldsymbol{\rho}_v), \quad (6.6)$$

$$L_{p,k_c}(j\omega_{k_f}, \boldsymbol{\rho}_p) = G_{p,k_c}(j\omega_{k_f}) F_{rp}(j\omega_{k_f}, \boldsymbol{\rho}_p), \quad (6.7)$$

$$L_{v,k_c}(j\omega_{k_f}, \boldsymbol{\rho}_v) = G_{v,k_c}(j\omega_{k_f}) F_{rv}(j\omega_{k_f}, \boldsymbol{\rho}_v), \quad (6.8)$$

$$S_{k_c}(j\omega_{k_f}, \boldsymbol{\rho}) = \frac{1}{1 + L_{k_c}(j\omega_{k_f}, \boldsymbol{\rho})}. \quad (6.9)$$

### 6.3.3 Convex optimization using sequential linearization

In (6.4a), the objective function can be equivalently given by

$$\begin{aligned} \underset{\boldsymbol{\rho}}{\text{minimize}} \quad \max_{\forall k_c, \forall k_f} |e_{k_c}(j\omega_{k_f})| &\Leftrightarrow \underset{\boldsymbol{\rho}}{\text{maximize}} \quad \min_{\forall k_c, \forall k_f} \frac{1}{|e_{k_c}(j\omega_{k_f})|} \\ &\Leftrightarrow \underset{\boldsymbol{\rho}}{\text{minimize}} \quad - \left( \min_{\forall k_c, \forall k_f} \left| \frac{1}{d_{k_c}(j\omega_{k_f})} (1 + L_{k_c}(j\omega_{k_f}, \boldsymbol{\rho})) \right| \right), \end{aligned} \quad (6.10)$$

where the error frequency response data is given by

$$e_{k_c}(j\omega_{k_f}) = S_{k_c}(j\omega_{k_f}, \boldsymbol{\rho}) d_{k_c}(j\omega_{k_f}). \quad (6.11)$$

In (6.4b), the amplitude spectrum of the output of the PZT actuator is evaluated as

$$|y_{p,k_c}(j\omega_{k_f})| = \left| \frac{L_{p,k_c}(j\omega_{k_f}, \boldsymbol{\rho}_p) d_{k_c}(j\omega_{k_f})}{1 + L_{k_c}(j\omega_{k_f}, \boldsymbol{\rho})} \right|, \quad (6.12)$$

and the maximum value with the given feedback controller is given by

$$y_{p,\max} = \max_{\forall k_c, \forall k_f} \left| \frac{G_{p,k_c}(j\omega_{k_f}) d_{k_c}(j\omega_{k_f})}{1 + G_{k_c}(j\omega_{k_f})} \right|. \quad (6.13)$$



In (6.4d), the angle of the vector locus is evaluated by atan2 function using the real and imaginary part of the vector locus. From these analyses, the optimization problem is given by (6.14).

$$\underset{\boldsymbol{\rho}}{\text{minimize}} \quad -\gamma \quad (6.14a)$$

subject to  
 $\forall k_c, \forall k_f$

$$\gamma - \left| \frac{1}{d_{k_c}(j\omega_{k_f})} (1 + L_{k_c}(j\omega_{k_f}, \boldsymbol{\rho})) \right| \leq 0 \quad (6.14b)$$

$$\frac{|d_{k_c}(j\omega_{k_f})|}{y_{p,\max}} \left| L_{p,k_c}(j\omega_{k_f}, \boldsymbol{\rho}_p) \right| - \left| 1 + L_{k_c}(j\omega_{k_f}, \boldsymbol{\rho}) \right| \leq 0 \quad (6.14c)$$

$$w_s(j\omega_{k_f}) - \left| 1 + L_{k_c}(j\omega_{k_f}, \boldsymbol{\rho}) \right| \leq 0 \quad (6.14d)$$

$$\mp \text{atan2} \left( \frac{\text{Im}(1 + L_{k_c}(j\omega_{k_f}, \boldsymbol{\rho}))}{\text{Re}(1 + L_{k_c}(j\omega_{k_f}, \boldsymbol{\rho}))} \right) \pm \text{atan2} \left( \frac{\text{Im}(1 + G_{k_c}(j\omega_{k_f}))}{\text{Re}(1 + G_{k_c}(j\omega_{k_f}))} \right) - \frac{\pi}{2} \leq 0 \quad \text{when} \quad \pm \text{Re}(1 + G_{k_c}(j\omega_{k_f})) \geq 0 \quad (6.14e)$$

$$\pm \text{atan2} \left( \frac{\text{Im}(1 + L_{k_c}(j\omega_{k_f}, \boldsymbol{\rho}))}{\text{Re}(1 + L_{k_c}(j\omega_{k_f}, \boldsymbol{\rho}))} \right) \mp \text{atan2} \left( \frac{\text{Im}(1 + G_{k_c}(j\omega_{k_f}))}{\text{Re}(1 + G_{k_c}(j\omega_{k_f}))} \right) - \frac{\pi}{2} \leq 0 \quad \text{when} \quad \pm \text{Re}(1 + G_{k_c}(j\omega_{k_f})) \geq 0 \quad (6.14f)$$

The optimization problem (6.14) is nonlinear and non-convex. Using sequential linearization, the optimization problem can be calculated by the iterative convex optimization and is given by (6.15).

$$\underset{\boldsymbol{\rho}_{k_i}}{\text{minimize}} \quad -\gamma \quad (6.15a)$$

subject to  
 $\forall k_c, \forall k_f$

$$\gamma - \text{Re} \left( \frac{\left( \frac{1}{d_{k_c}(j\omega_{k_f})} (1 + L_{k_c}(j\omega_{k_f}, \boldsymbol{\rho}_{k_i-1})) \right)^*}{\left| \frac{1}{d_{k_c}(j\omega_{k_f})} (1 + L_{k_c}(j\omega_{k_f}, \boldsymbol{\rho}_{k_i-1}) \right|} \left( \frac{1}{d_{k_c}(j\omega_{k_f})} (1 + L_{k_c}(j\omega_{k_f}, \boldsymbol{\rho}_{k_i})) \right) \right) \leq 0 \quad (6.15b)$$

$$\frac{|d_{k_c}(j\omega_{k_f})|}{y_{p,\max}} \text{Re} \left( \frac{(L_{p,k_c}(j\omega_{k_f}, \boldsymbol{\rho}_{p,k_i-1}))^*}{|L_{p,k_c}(j\omega_{k_f}, \boldsymbol{\rho}_{p,k_i-1})|} (L_{p,k_c}(j\omega_{k_f}, \boldsymbol{\rho}_{p,k_i})) \right) - \text{Re} \left( \frac{(1 + L_{k_c}(j\omega_{k_f}, \boldsymbol{\rho}_{k_i-1}))^*}{|1 + L_{k_c}(j\omega_{k_f}, \boldsymbol{\rho}_{k_i-1})|} (1 + L_{k_c}(j\omega_{k_f}, \boldsymbol{\rho}_{k_i})) \right) \leq 0 \quad (6.15c)$$

$$w_s(j\omega_{k_f}) - \text{Re} \left( \frac{(1 + L_{k_c}(j\omega_{k_f}, \boldsymbol{\rho}_{k_i-1}))^*}{|1 + L_{k_c}(j\omega_{k_f}, \boldsymbol{\rho}_{k_i-1})|} (1 + L_{k_c}(j\omega_{k_f}, \boldsymbol{\rho}_{k_i})) \right) \leq 0 \quad (6.15d)$$

$$\mp \left( \text{atan2} \left( \frac{\text{Im}(1 + L_{k_c,k_i-1}(j\omega_{k_f}, \boldsymbol{\rho}))}{\text{Re}(1 + L_{k_c,k_i-1}(j\omega_{k_f}, \boldsymbol{\rho}))} \right) + \frac{\text{Re}(1 + L_{k_c,k_i-1}(j\omega_{k_f}, \boldsymbol{\rho})) \text{Im}(1 + L_{k_c,k_i}(j\omega_{k_f}, \boldsymbol{\rho})) - \text{Im}(1 + L_{k_c,k_i-1}(j\omega_{k_f}, \boldsymbol{\rho})) \text{Re}(1 + L_{k_c,k_i}(j\omega_{k_f}, \boldsymbol{\rho}))}{|1 + L_{k_c,k_i-1}(j\omega_{k_f}, \boldsymbol{\rho})|^2} \right) \pm \text{atan2} \left( \frac{\text{Im}(1 + G_{k_c}(j\omega_{k_f}))}{\text{Re}(1 + G_{k_c}(j\omega_{k_f}))} \right) - \frac{\pi}{2} \leq 0$$

$$\text{when} \quad \pm \text{Re}(1 + G_{k_c}(j\omega_{k_f})) \geq 0 \quad (6.15e)$$

$$\pm \left( \text{atan2} \left( \frac{\text{Im}(1 + L_{k_c,k_i-1}(j\omega_{k_f}, \boldsymbol{\rho}))}{\text{Re}(1 + L_{k_c,k_i-1}(j\omega_{k_f}, \boldsymbol{\rho}))} \right) + \frac{\text{Re}(1 + L_{k_c,k_i-1}(j\omega_{k_f}, \boldsymbol{\rho})) \text{Im}(1 + L_{k_c,k_i}(j\omega_{k_f}, \boldsymbol{\rho})) - \text{Im}(1 + L_{k_c,k_i-1}(j\omega_{k_f}, \boldsymbol{\rho})) \text{Re}(1 + L_{k_c,k_i}(j\omega_{k_f}, \boldsymbol{\rho}))}{|1 + L_{k_c,k_i-1}(j\omega_{k_f}, \boldsymbol{\rho})|^2} \right) \mp \text{atan2} \left( \frac{\text{Im}(1 + G_{k_c}(j\omega_{k_f}))}{\text{Re}(1 + G_{k_c}(j\omega_{k_f}))} \right) - \frac{\pi}{2} \leq 0$$

$$\text{when} \quad \pm \text{Re}(1 + G_{k_c}(j\omega_{k_f})) \geq 0 \quad (6.15f)$$

## 6.4 Application to dual-stage actuator hard disk drive

In this section, the verification of disturbance rejection performance is conducted in a dual-stage actuator HDD benchmark problem. The result shows that the resonant filters are optimized with the conditions of robust stability, robust performance, and hardware constraints. The track-following performance with designed resonant filters outperforms that without resonant filters.

### 6.4.1 Conditions

The frequency response data is used from 100 Hz to Nyquist frequency  $F_s/2 = 1/2T_s = 25.2$  kHz. The frequency response data is arranged at linearly even intervals in every 1 Hz and the number of data points is  $n_f = 25101$ . Nyquist diagram, sensitivity function, amplitude spectrum of  $e$ , and amplitude spectrum of  $y_p$  without resonant filters are shown in Fig. 6.7(a), Fig. 6.8(a), Fig. 6.9(a), Fig. 6.10(a), and Fig. 6.11(a). From Fig. 6.7(a), the resonant filters are designed at eight frequencies with vertical black dotted lines, and the dumping coefficients of all resonant filters are set to  $\zeta_r = 0.05$ . For the initial condition, all tuning parameters are set to  $\rho = 0$  and  $F_{rp} = F_{rv} = 1$ . In the robust stability condition, the modulus margin is set to  $1/w_s = 6$  dB.

### 6.4.2 Optimization results

The optimization of the resonant filter design is conducted by YALMIP [96] and Mosek [97] until the improvement of the objective function from the previous iteration becomes less than 0.1%. Nyquist diagram, sensitivity function, amplitude spectrum of  $e$ , and amplitude spectrum of  $y_p$  with resonant filters are shown in Fig. 6.7(b), Fig. 6.8(b), Fig. 6.9(b), Fig. 6.10(b), and Fig. 6.11(b). The optimization result shows that the resonant filters are designed with conditions of robust stability, robust performance, and hardware constraints in 9 cases of the controlled system.

The comparison of the inverse disturbance spectrum  $|1/d|$  and the sensitivity function without and with resonant filters are shown in Fig. 6.12. It shows that the sensitivity function with resonant filters is reshaped as following the inverse disturbance spectrum and the resonant filters contain the model of the disturbance.

### 6.4.3 Simulation results

The time domain simulation is conducted in a dual-stage actuator HDD benchmark problem without and with resonant filters in 9 cases of the controlled system. The time series of the head position in the simulation are shown in Fig. 6.13. Fig. 6.14(a) shows the track-following performance. It shows that the tracking errors with resonant filters are smaller than those without resonant filters in all 9 cases. Fig. 6.14(b) shows the maximum stroke in a PZT actuator. It shows that the maximum stroke values with resonant filters are almost the same as those without resonant filters and both controlled systems satisfy the stroke limitation. As a result, the controlled system with resonant filters outperforms that without resonant filters.

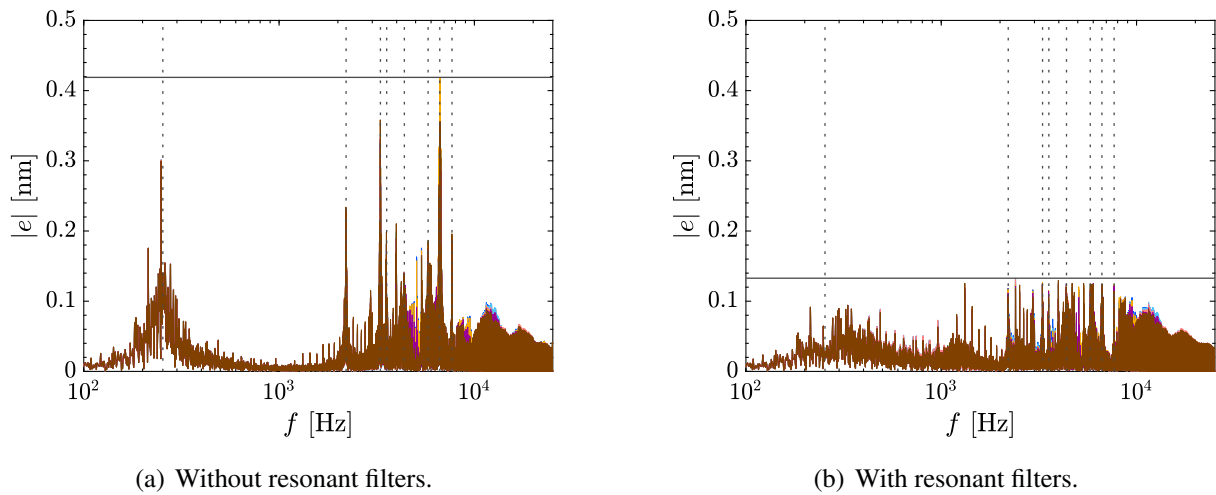


Fig. 6.7: Amplitude spectrum of  $e$ .

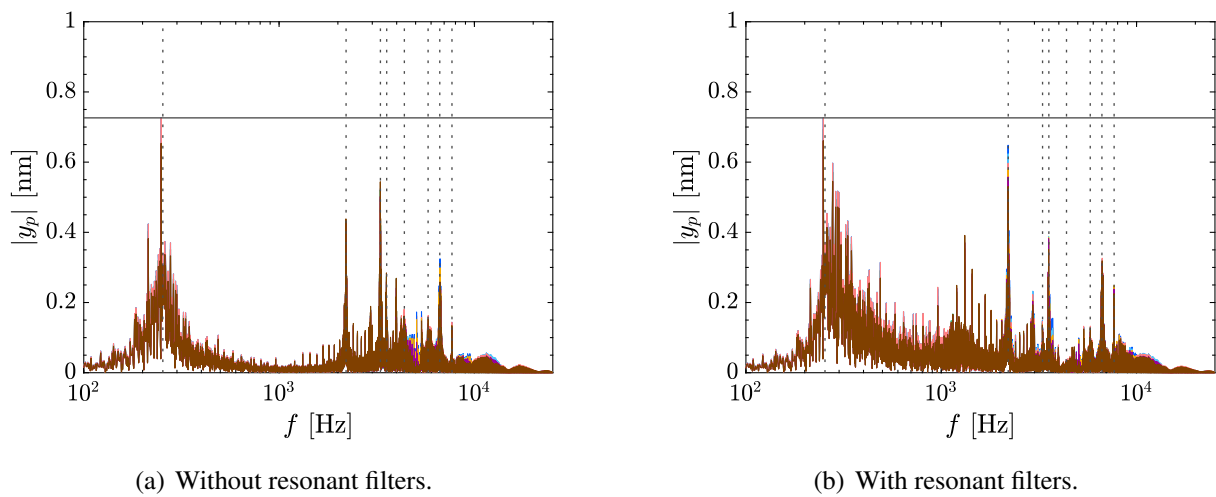


Fig. 6.8: Amplitude spectrum of  $y_p$ .

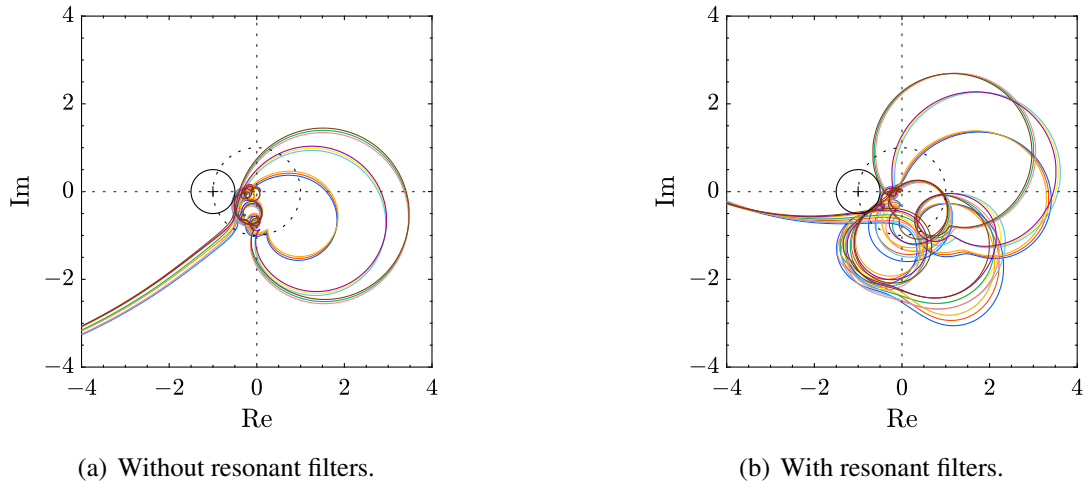


Fig. 6.9: Nyquist diagram (around the origin).

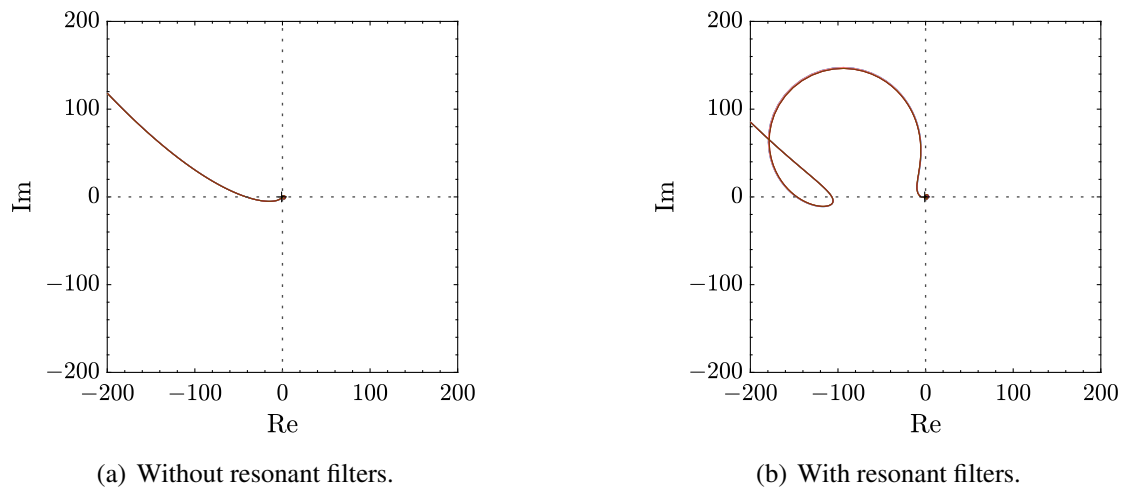


Fig. 6.10: Nyquist diagram (wide view).

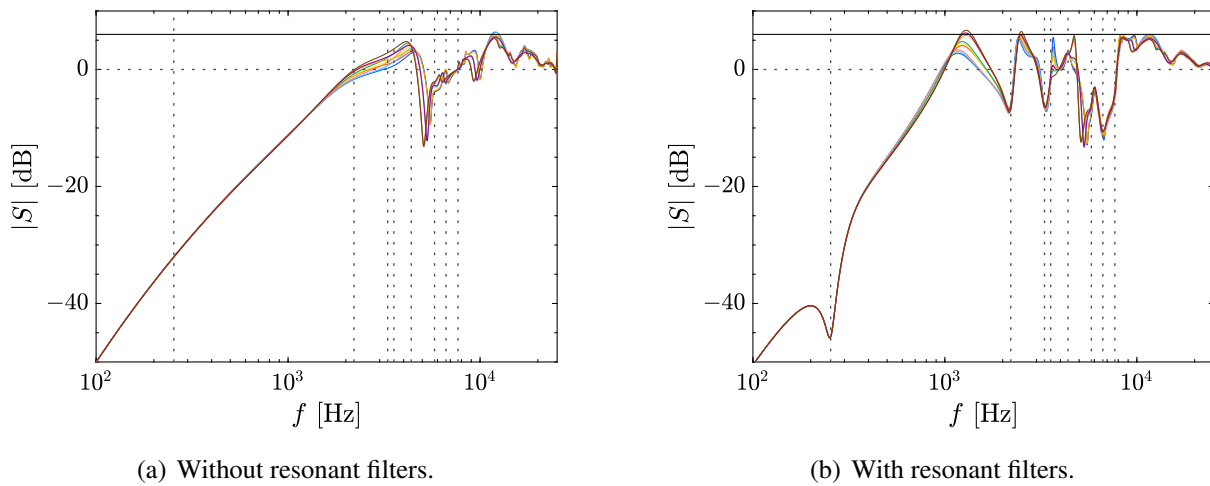


Fig. 6.11: Sensitivity function.

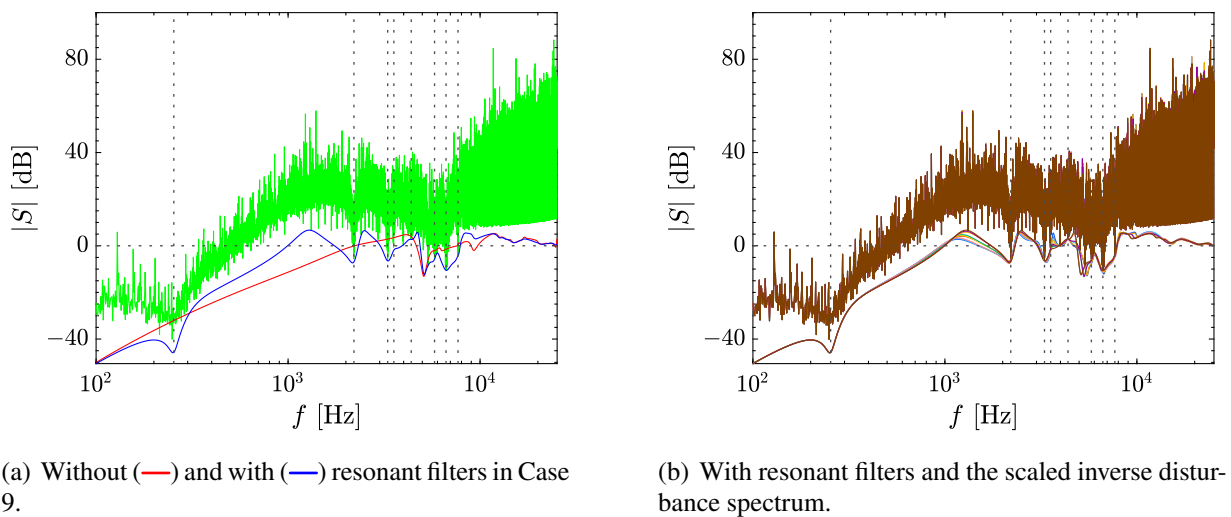


Fig. 6.12: Scaled inverse disturbance spectrum and sensitivity function.

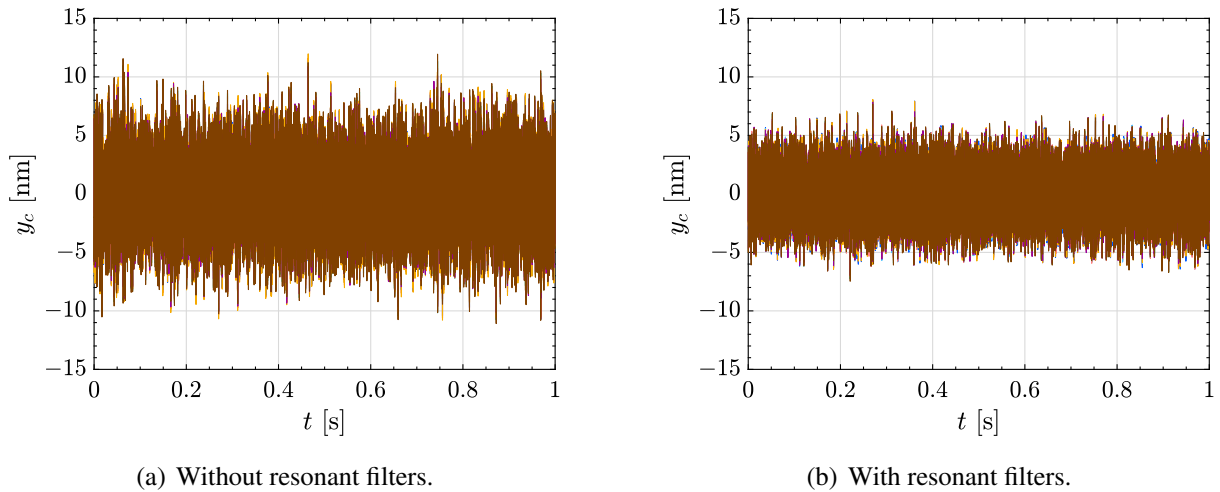


Fig. 6.13: Time series of the head position in the simulation.

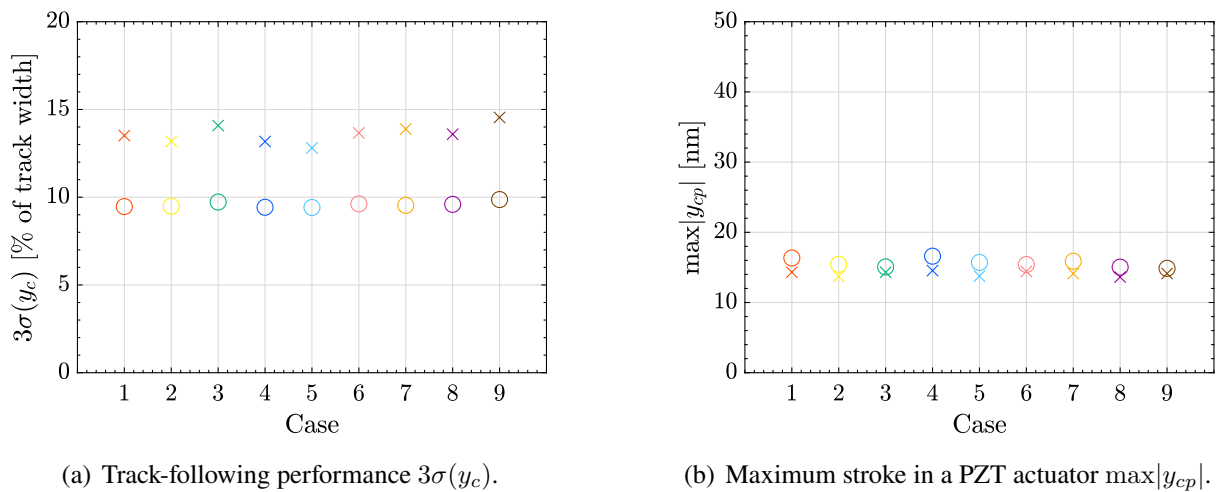


Fig. 6.14: Simulation results without and with resonant filters. (x) and (o) denote without and with optimized resonant filters.

## **6.5 Conclusion**

In this chapter, the design method of optimal resonant filters is developed to improve track-following performance in a dual-stage actuator HDD. The resonant filters with structured parameterization are optimized by iterative convex optimization directly using the frequency response data of the controlled system. Robust stability, robust performance, and hardware constraints are considered for the optimization calculation in 9 cases of the controlled system. The disturbance rejection performance of the optimized resonant filters is validated in a dual-stage actuator HDD benchmark problem. Ongoing researches focus on the usage of both frequency domain and time domain data, designing other feedback controllers simultaneously, and the optimal design of multirate filters.





# Chapter 7

## Disturbance Rejection with Robust Stability in MIMO Motion Systems

A large-scale high-precision scan stage is important equipment in the industrial productions of micro-fabrication such as flat panel display (FPD) lithography systems. Designing controllers for multi-input multi-output (MIMO) systems is time-consuming and needs experience because of the interaction between each axis and many controller tuning parameters. The aim of this chapter is to develop a peak filter design method based on frequency response data to reduce repetitive disturbance. This data-based approach does not use the model and only uses the frequency response data of the controlled system and the disturbance spectrum calculated from the scanning error data (Contribution 7.1). The peak filter is designed by convex optimization and satisfies robust stability conditions for six-degree-of-freedom systems (Contribution 7.2). The control performance of the designed peak filter is experimentally demonstrated with an industrial large-scale MIMO high-precision scan stage in reducing the scanning error of the main stroke of the translation along the  $x$ -axis (Contribution 7.3).

### 7.1 Introduction

Large-scale high-precision scan stages have an important role in industries such as manufacturing semiconductors and flat panel displays (FPD). To improve throughput and product quality, fast and precise positioning control is required, and these specifications become severe year by year because of the growing need for TVs, PCs, and smartphones [50].

The large-scale scan stage has several challenges in position control such as low resonant modes because of the low stiffness and many disturbances because of the wide scan range [98]. The large-scale scan stage is typically controlled with two-degree-of-freedom (DOF) control with a feedforward controller for reference tracking such as a perfect tracking control based on a multirate feedforward control [20, 44] and a feedback controller for disturbance rejection. In the scan region, the reference trajectory of the high-precision scan stage is with constant velocity without acceleration, and the feedback controller plays a major role in tracking control performance.

Classical scan stages move along  $(x, y, \theta_z)$ -axes, and the interaction between each axis is ignored, and a single-input single-output (SISO) decentralized control is commonly employed. However, in these applications, the high-precision scan stages are supported by the magnetic force or air pressure and moving in 6-DOF with  $(x, y, \theta_z, z, \theta_x, \theta_y)$ -axes to reduce disturbances by the

friction and the vibration from the ground and to improve tracking performance, and they become multi-input multi-output (MIMO) systems [51, 64, 99, 100]. The controller design of the MIMO systems has several challenges such as stability analysis in a coupled system between each axis, modeling of MIMO systems, and enormous tuning parameters of the controllers. Especially, improving the tuning method of the controller parameters is important for the cost of time and effort of on-site control engineers.

Based on these challenges in designing the feedback controller, several data-based controller design approaches with an optimization method are proposed, such as genetic algorithm [101], Nelder-Mead method [102], particle swarm optimization [103], loop shaping method [104], bundle method [105, 106], sequential linearization method [107–110] using concave-convex procedure [34].

Among these methods, the sequential linearization method using the concave-convex procedure has an advantage in monotonic convergence to a saddle point or a local optimum and suits for controller design. Other methods also need the parametric model of the controlled system. Precise modeling is difficult when the system is complicated such as MIMO systems.

In this chapter, the sequential linearization method using the concave-convex procedure is used with the frequency response data of the controlled system and disturbance spectrum to design the optimal feedback controller.

The disturbance spectrum during the scanning motion with constant velocity has a repetitive characteristic such as motor cogging and has a large amplitude in a certain frequency.

The repetitive control approaches are presented to reject the periodic disturbances [89, 111, 112]. They reject the disturbance on not only main disturbance frequency but also harmonic ones. The experimental setup in this chapter does not have a characteristic of harmonic disturbance frequencies, and the repetitive control approaches are not suitable for it.

Previous researches show that repetitive disturbance can be effectively rejected by a peak filter, which is the same as an inverse notch filter in other literature, with the same resonance frequency, and it is applied in several industrial products such as hard disk drives [87]. However, in the application of the high-precision scan stage, the repetitive disturbance rejection by a peak filter has not been reported in the literature.

Since the peak filter has a large gain at a certain frequency, it may easily deteriorate the closed-loop stability due to the interaction. Moreover, the combination of the controller parameter can blow up in such a multi-axis system. Hence, the heuristic tuning approach depends on experiences and efforts, and it is not the optimal solution. To address this problem, the frequency response data-based peak filter design method considering both the SISO robust stability condition and the MIMO stability condition is proposed in this chapter.

The optimal disturbance filter design method is also presented [113]. However, the peak filter is designed with a nonlinear optimization procedure that is not with convex optimization. The convergence of the nonlinear optimization procedure is not monotonic and it could take a long time for the optimization. Therefore, the data-based peak filter design method with convex optimization suitable to industrial applications is proposed in this chapter.

The proposed peak filter design method has an advantage in convex optimization without parametric modeling. The control performance of the designed peak filter is experimentally demonstrated with an industrial large-scale MIMO high-precision scan stage in reducing the scanning error of the main stroke of the translation along the  $x$ -axis. This chapter consists of mainly these three following contributions:

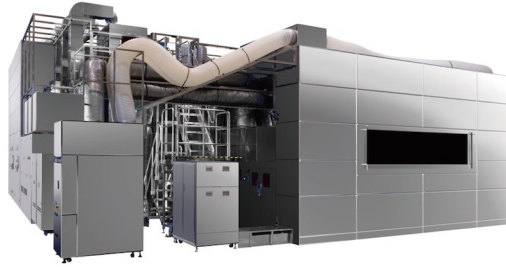


Fig. 7.1: Experimental setup of FPD lithography system [1].

**Contribution 7.1 :** *The optimization problem of data-based peak filter design for the MIMO system is formulated.*

**Contribution 7.2 :** *The data-based peak filter design method with convex optimization is presented.*

**Contribution 7.3 :** *The designed peak filter is validated in the experiment with the industrial large-scale MIMO high-precision scan stage.*

## 7.2 Problem formulation

In this section, the control problem is formulated.

### 7.2.1 MIMO high-precision scan stage

The experimental setup is shown in Fig. 7.1.

The experiment is conducted with the MIMO high-precision scan stage in the FPD lithography system which is 6-DOFs with six-inputs  $(f_x, f_y, \tau_z, f_z, \tau_x, \tau_y)$  and six-outputs  $(x, y, \theta_z, z, \theta_x, \theta_y)$ .

The 6-DOFs stage is floating by the air bearing to cancel the gravity and frictions and is actuated by voice coil motors and linear motors [99]. The positions and angles of the stage are measured by laser displacement sensors and linear encoders.

The frequency response of the experimental setup is shown in Fig. 7.2.

The main stroke of the scan stage is the translation along the  $x$ -axis. The scan trajectory of translation along the  $x$ -axis is shown in Fig. 7.3. The scan stage moves with constant velocity through four scan regions at the same scanning procedure. The same controllers are used through four scan regions at the same scanning procedure.

### 7.2.2 Disturbance rejection with peak filter

Previous researches in high-precision positioning systems such as a hard disk drive show that a repetitive disturbance that has a large spectrum in a specific frequency is rejected by a peak filter that has the same resonance frequency [87] due to the internal model principle [114]. The transfer function of the peak filter is given by

$$F_{\text{Peak}}(j\omega, \rho, \eta) = \frac{s^2 + 2\rho\omega s + \omega^2}{s^2 + 2\eta\omega s + \omega^2} = \frac{F_n(j\omega, \rho)}{F_d(j\omega, \eta)}$$

$$(0 \leq \eta < \rho \leq 1), \quad (7.1)$$

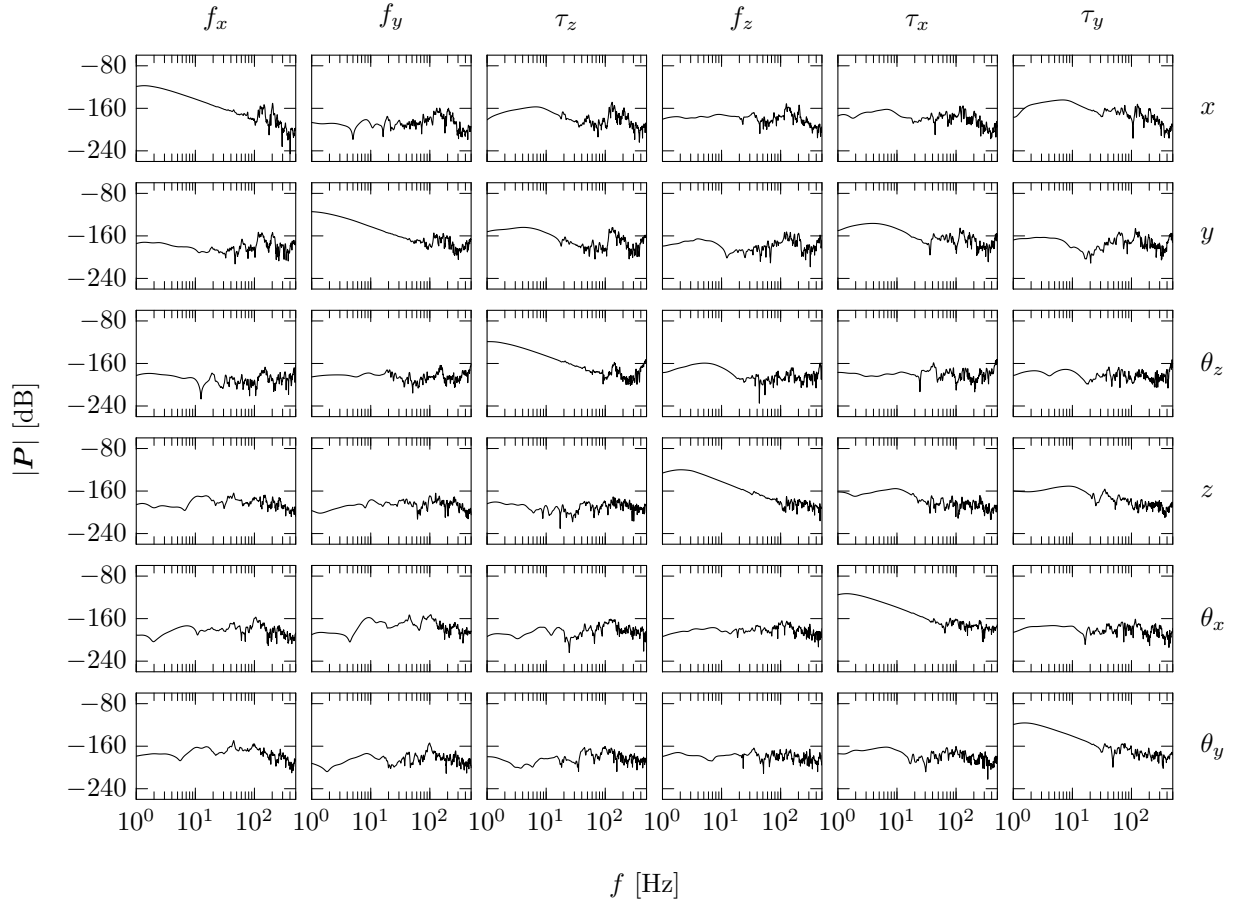


Fig. 7.2: Bode magnitude plot of 6-DOF experimental setup.

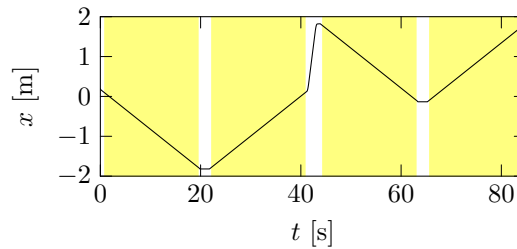


Fig. 7.3: Scan trajectory of translation along the  $x$ -axis. The scan stage moves through four scan regions (■) at the same scanning procedure. The scanning velocity of translation along the  $x$ -axis is set to 0.1 m/s.

where the resonance frequency is  $\omega \in \mathbb{R}$ , the damping coefficients are  $\rho \in \mathbb{R}$  and  $\eta \in \mathbb{R}$ , and  $\rho$  must be larger than  $\eta$  in the peak filter. It is noted that it becomes a notch filter when  $\rho$  is smaller than  $\eta$ .

The scan stage moves with constant velocity in the scan region and has several repetitive disturbances such as cogging. Therefore, the repetitive disturbance rejection approach with peak filter is applied to the MIMO high-precision scan stage. This approach has not been commonly used in the MIMO high-precision scan stage because the MIMO system high-gained by peak filter easily becomes unstable due to the interaction between each axis. In this chapter, the peak

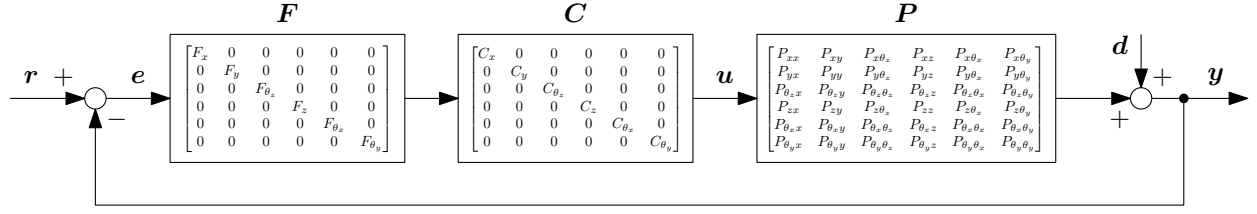


Fig. 7.4: Block diagram of 6-DOF controlled system.

filter is designed with SISO robust stability condition and MIMO stability condition not to make the controlled system unstable.

### 7.2.3 Details of controlled system

The block diagram of the 6-DOF controlled system is shown in Fig. 7.4. The 6-DOF controlled system  $P$  is given by frequency response data, as shown in Fig. 7.2. The 6-DOF experimental setup is decoupled by the mechanical design and the thrust distribution.

The diagonal term in the frequency range less than about 10 Hz is modeled as a second-order rigid body system in each axis. The feedback controllers are conventionally designed with the model of the second-order rigid body systems in only diagonal terms for ease of the on-site final tuning process. In the proposed method, the peak filter can be designed with convex optimization using the frequency response data of the controlled system without the mathematical modeling of the large-scale MIMO high-precision scan stage.

The fixed diagonal feedback controller  $C$  that consists of PID controllers, disturbance observers, phase lead filters, and notch filters is given beforehand. The diagonal peak filter  $F$  is designed with a proposed data-based design method.

The 6-DOF controlled system  $P$ , the fixed diagonal feedback controller  $C$ , and the diagonal peak filter  $F$  are defined as

$$P(j\omega_k) = P_{lm}(j\omega_k), \quad (7.2)$$

$$C(j\omega_k) = \begin{cases} C_l(j\omega_k) & (l = m) \\ 0 & (l \neq m) \end{cases}, \quad (7.3)$$

$$F(j\omega_k, \rho, \eta) = \begin{cases} \frac{F_{n_l}(j\omega_k, \rho_l)}{F_{d_l}(j\omega_k, \eta_l)} & (l = m) \\ 0 & (l \neq m) \end{cases}, \quad (7.4)$$

where  $(l, m) \in \{x, y, \theta_z, z, \theta_x, \theta_y\}$  denotes the index of the 6-DOFs and the subscript  $k$  represents the frequency point of the frequency response data. The damping coefficients  $\rho$  and  $\eta$  of the peak filter are defined as

$$\rho = [\rho_x \ \cdots \ \rho_{\theta_y}]^T, \quad (7.5)$$

$$\eta = [\eta_x \ \cdots \ \eta_{\theta_y}]^T. \quad (7.6)$$

### 7.2.4 Problem description and outline

In this chapter, the data-based peak filter design method is presented for the industrial large-scale MIMO high-precision scan stage with respect to the following requirements:

**Requirement 7.1 :** *The diagonal peak filter is designed with the fixed diagonal feedback controller and FRF data of the 6-DOF controlled system.*

**Requirement 7.2 :** *The optimization problem is convex.*

**Requirement 7.3 :** *The scanning error of the translation along the  $x$ -axis which is the main stroke of the scan stage should be reduced in the experiment.*

As is outlined in Section 7.1, pre-existing approaches fail to meet all requirements: the approaches with loop shaping method [104] and bundle method [105, 106] do not satisfy Requirement 7.1; the approaches with genetic algorithm [101], Nelder-Mead method [102], and particle swarm optimization [103] do not satisfy Requirement 7.2; the approach with sequential linearization method [107–109] using concave-convex procedure [34] does not satisfy Requirement 7.3. In summary, only the proposed approach satisfies the structured, diagonal, and convex optimized characteristics compared with other preexisting approaches.

In Section 7.3, the proposed data-based peak filter design method is presented that attains Requirement 7.1 through the weighting function of the sensitivity function with estimated disturbance spectrum, the SISO robust stability condition, and the MIMO stability condition, constituting Contribution 7.1. The convex optimization problem is formulated that attains Requirement 7.2 through sequential linearization method [107–109] using concave-convex procedure [34], constituting Contribution 7.2. In Section 7.4, the benefit of the approach that attains Requirement 7.3 is demonstrated through the experiment with the industrial large-scale MIMO high-precision scan stage, constituting Contribution 7.3. In Section 7.5, conclusions are presented.

## 7.3 Convex optimization of rational peak filter

In this section, the data-based peak filter design method is formulated as a convex optimization problem. The proposed method is formulated to design the peak filters for the MIMO controlled system in each axis, independently.

### 7.3.1 Weighting for sensitivity function using disturbance spectrum

As shown in Fig. 7.4, a sensitivity function  $\mathbf{S}$  is a transfer function from the output disturbance  $\mathbf{d}$  to the tracking error  $\mathbf{e}$ . The sensitive function  $\mathbf{S}$  in Fig. 7.4 is given by

$$\begin{aligned}\mathbf{S}(j\omega_k) &= (\mathbf{I} + \mathbf{P}(j\omega_k)\mathbf{C}(j\omega_k)\mathbf{F}(j\omega_k))^{-1} \\ &= S_{lm}(j\omega_k),\end{aligned}\quad (7.7)$$

and the output disturbance  $\mathbf{d}$  and the tracking error  $\mathbf{e}$  are also given by

$$\mathbf{d}(j\omega_k) = \begin{bmatrix} d_x(j\omega_k) & \cdots & d_{\theta_y}(j\omega_k) \end{bmatrix}^T, \quad (7.8)$$

$$\mathbf{e}(j\omega_k) = \begin{bmatrix} e_x(j\omega_k) & \cdots & e_{\theta_y}(j\omega_k) \end{bmatrix}^T. \quad (7.9)$$

The output disturbance  $\mathbf{d}$  does not deteriorate the tracking error  $\mathbf{e}$  within the frequency in which the gain of the sensitivity function  $\mathbf{S}$  is low. Therefore, the weighting function of the sensitivity function is designed from the disturbance spectrum of the scanning motion.

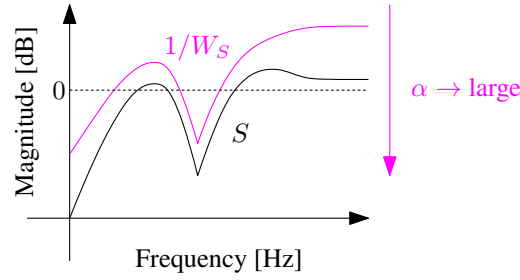


Fig. 7.5: Sensitivity function with disturbance spectrum weighting function.

The output disturbance spectrum estimated from the tracking error of the scanning motion is given by

$$\mathbf{d}(j\omega_k) = \mathbf{S}^{-1}(j\omega_k)\mathbf{e}(j\omega_k). \quad (7.10)$$

The weighting function of the sensitivity function using the output disturbance spectrum [115] is given by

$$\mathbf{W}_S(j\omega_k) = [W_{S_x}(j\omega_k) \ \cdots \ W_{S_{\theta_y}}(j\omega_k)]^T, \quad (7.11)$$

where

$$|W_{S_l}(j\omega_k)| = \alpha_l |d_l(j\omega_k)|, \quad (7.12)$$

and  $\alpha_l$  is a scaling parameter.

The feedback controller is designed to satisfy the condition of the sensitivity function as

$$|S_{ll}(j\omega_k)W_{S_l}(j\omega_k)| \leq 1. \quad (7.13)$$

As shown in Fig. 7.5, when the scaling parameter  $\alpha_l$  becomes large,  $1/W_{S_l}$  goes down. Therefore, the effective disturbance rejection is achieved when the condition (7.13) is satisfied in a larger scaling parameter  $\alpha_l$ .

### 7.3.2 SISO robust stability condition with circle condition

In this chapter, the stability condition of the controlled system is analyzed by the Nyquist stability theorem. The SISO robust stability condition is considered with the circle condition calculated from the gain margin  $g_m$  and the phase margin  $\Phi_m$  [116].

The center  $(-\sigma, 0j)$  and radius  $r_m$  of a circle condition on the Nyquist diagram is given by

$$\sigma = \frac{g_m^2 - 1}{2g_m(g_m \cos \Phi_m - 1)}, \quad (7.14)$$

$$r_m = \frac{(g_m - 1)^2 + 2g_m(1 - \cos \Phi_m)}{2g_m(g_m \cos \Phi_m - 1)}. \quad (7.15)$$

As shown in Fig. 7.6, when the controller is stable and the open-loop frequency response does not cross the circle condition on the Nyquist diagram, the controller satisfies the SISO robust stability condition for the gain margin  $g_m$  and the phase margin  $\Phi_m$ .

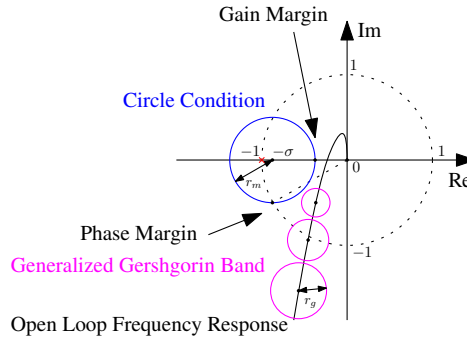


Fig. 7.6: Circle condition of gain margin, phase margin and generalized Gershgorin bands.

### 7.3.3 MIMO stability condition with generalized Gershgorin bands

The MIMO controlled system may become unstable due to the interaction between each axis even if the SISO controlled system in each axis is stable. The MIMO stability condition is considered in the Direct Nyquist Array (DNA) method with generalized Gershgorin bands [117–119].

In the DNA method, the interaction index  $\lambda(j\omega_k | \mathbf{P})$  of the controlled system  $\mathbf{P}$  is defined as a maximum eigenvalue of  $\mathbf{M}(j\omega_k | \mathbf{P})$ , where the matrix  $\mathbf{M}(j\omega_k | \mathbf{P})$  is given by

$$\mathbf{M}(j\omega_k | \mathbf{P}) = \begin{cases} 0 & (l = m) \\ \left| \frac{P_{lm}(j\omega_k)}{P_{mm}(j\omega_k)} \right| & (l \neq m) \end{cases}. \quad (7.16)$$

The radius  $r_{gl}$  of the generalized Gershgorin bands is given by

$$r_{gl}(j\omega_k) = \lambda(j\omega_k) \left| \frac{P_{ll}(j\omega_k) C_l(j\omega_k) F_{n_l}(j\omega_k, \rho)}{F_{d_l}(j\omega_k, \eta)} \right|. \quad (7.17)$$

The open-loop frequency response of each axis may move within the radius at each frequency point on the Nyquist diagram when MIMO systems have an interaction between each axis. As shown in Fig. 7.6, when the controller is stable and the generalized Gershgorin bands do not include the point of  $(-1, 0j)$  on the Nyquist diagram, the controlled system satisfies a MIMO stability condition with the interaction between each axis.



### 7.3.4 Optimization problem formulation

The optimization problem to design a peak filter with a disturbance spectrum, a SISO robust stability condition, and a MIMO stability condition is formulated from (7.18) to (7.22).

$$\underset{\rho_l, \eta_l}{\text{maximize}} \quad \alpha_l \quad (7.18)$$

subject to

$$|W_{S_l}(j\omega_k)| - \left| \frac{P_{ll}(j\omega_k)C_l(j\omega_k)F_{n_l}(j\omega_k, \rho_l)}{F_{d_l}(j\omega_k, \eta_l)} + 1 \right| \leq 0 \quad (7.19)$$

$$r_m - \left| \frac{P_{ll}(j\omega_k)C_l(j\omega_k)F_{n_l}(j\omega_k, \rho_l)}{F_{d_l}(j\omega_k, \eta_l)} + \sigma \right| \leq 0 \quad (7.20)$$

$$r_{g_l}(j\omega_k) - \left| \frac{P_{ll}(j\omega_k)C_l(j\omega_k)F_{n_l}(j\omega_k, \rho_l)}{F_{d_l}(j\omega_k, \eta_l)} + 1 \right| \leq 0 \quad (7.21)$$

$$0 \leq \beta\eta_l \leq \rho_l \leq 1 \quad (\beta > 1) \quad (7.22)$$

### 7.3.5 Concave-convex procedure

There are two challenges in solving this optimization problem with convex optimization. First, the peak filter has tuning parameters not only in the numerator but also in the denominator. Second, the constraints of the formulated optimization problem are non-convex functions because of the difference of the convex functions. To solve these challenges, a sequential linearization method using concave-convex procedure [34] with tuning parameters in both the numerator and the denominator [120] is applied to this optimization problem.

First, the denominator  $|F_{d_l}(j\omega_k, \eta)|$  is multiplied on both sides of the constraints, as shown in (7.23), (7.24), and (7.25).

$$|W_{S_l}(j\omega_k)F_{d_l}(j\omega_k, \eta_l)| - |P_{ll}(j\omega_k)C_l(j\omega_k)F_{n_l}(j\omega_k, \rho_l) + F_{d_l}(j\omega_k, \eta_l)| \leq 0 \quad (7.23)$$

$$r_m|F_{d_l}(j\omega_k, \eta_l)| - |P_{ll}(j\omega_k)C_l(j\omega_k)F_{n_l}(j\omega_k, \rho_l) + \sigma F_{d_l}(j\omega_k, \eta_l)| \leq 0 \quad (7.24)$$

$$r_{g_l}(j\omega_k)|F_{d_l}(j\omega_k, \eta_l)| - |P_{ll}(j\omega_k)C_l(j\omega_k)F_{n_l}(j\omega_k, \rho_l) + F_{d_l}(j\omega_k, \eta_l)| \leq 0 \quad (7.25)$$

Second, a first-order approximation of the difference term of the constraints is calculated, as shown in (7.26), (7.27), and (7.28).

$$|W_{S_l}(j\omega_k)F_{d_l}(j\omega_k, \eta_l)| - \text{Re} \left( \frac{(P_{ll}(j\omega_k)C_l(j\omega_k)F_{n_l}(j\omega_k, \rho_{l_{i-1}}) + F_{d_l}(j\omega_k, \eta_{l_{i-1}}))^*}{|P_{ll}(j\omega_k)C_l(j\omega_k)F_{n_l}(j\omega_k, \rho_{l_{i-1}}) + F_{d_l}(j\omega_k, \eta_{l_{i-1}})|} (P_{ll}(j\omega_k)C_l(j\omega_k)F_{n_l}(j\omega_k, \rho_l) + F_{d_l}(j\omega_k, \eta_l)) \right) \leq 0 \quad (7.26)$$

$$r_m|F_{d_l}(j\omega_k, \eta_l)| - \text{Re} \left( \frac{(P_{ll}(j\omega_k)C_l(j\omega_k)F_{n_l}(j\omega_k, \rho_{l_{i-1}}) + \sigma F_{d_l}(j\omega_k, \eta_{l_{i-1}}))^*}{|P_{ll}(j\omega_k)C_l(j\omega_k)F_{n_l}(j\omega_k, \rho_{l_{i-1}}) + \sigma F_{d_l}(j\omega_k, \eta_{l_{i-1}})|} (P_{ll}(j\omega_k)C_l(j\omega_k)F_{n_l}(j\omega_k, \rho_l) + \sigma F_{d_l}(j\omega_k, \eta_l)) \right) \leq 0 \quad (7.27)$$

$$r_{g_l}(j\omega_k)|F_{d_l}(j\omega_k, \eta_l)| - \text{Re} \left( \frac{(P_{ll}(j\omega_k)C_l(j\omega_k)F_{n_l}(j\omega_k, \rho_{l_{i-1}}) + F_{d_l}(j\omega_k, \eta_{l_{i-1}}))^*}{|P_{ll}(j\omega_k)C_l(j\omega_k)F_{n_l}(j\omega_k, \rho_{l_{i-1}}) + F_{d_l}(j\omega_k, \eta_{l_{i-1}})|} (P_{ll}(j\omega_k)C_l(j\omega_k)F_{n_l}(j\omega_k, \rho_l) + F_{d_l}(j\omega_k, \eta_l)) \right) \leq 0 \quad (7.28)$$

From these two procedures, the constraints of the optimization problem become convex in the current operating point. It is noted that  $\rho_{l_{i-1}}$  and  $\eta_{l_{i-1}}$  are the values of the optimization result in the previous iteration, and this optimization problem can be solved as a convex optimization problem with iterative calculations. In this chapter, a dichotomy method is used for an iterative calculation algorithm.

## 7.4 Application to MIMO high-precision scan stage

In this section, experimental validation is conducted. The aim of this chapter is to develop a peak filter design method based on frequency response data. The control performance of the designed peak filter is experimentally demonstrated with an industrial large-scale MIMO high-precision scan stage in reducing the scanning error of the main stroke of the translation along the  $x$ -axis.

### 7.4.1 Experimental setup

The experimental setup is shown in Fig. 7.1. In this setup, the MIMO high-precision scan stage moves with the constant velocity through four scan regions at the same scanning procedure as shown in Fig. 7.3. In this chapter, the scanning velocity of translation along the  $x$ -axis is set to 0.1 m/s. The frequency response of the 6-DOF experimental setup, as shown in Fig. 7.2, and the scanning error data are collected by pre-experiment and used for the peak filter design.

### 7.4.2 Optimization conditions

The peak filter is designed by convex optimization with the frequency response of the 6-DOF experimental setup and the scanning error data. The number of frequency response data points is set to 1000, and they are arranged at logarithmically even intervals in the range from 1 Hz to 500 Hz. The error spectrum and disturbance spectrum are averaged in four scan regions to consider four scan regions with the same designed peak filter.

The flowchart of the proposed peak filter design method is shown in Fig. 7.7. In this chapter, only one peak filter is designed in translation along the  $x$ -axis which is the main stroke of the scan stage, and the peak filters in other axes are set to 1. The frequency response data of  $C_x$  that is a fixed feedback controller along the  $x$ -axis consisting of PID controller, disturbance observer, phase lead filter, and notch filter is shown in Fig. 7.8.

The resonance frequency of the peak filter in translation along the  $x$ -axis is set to a constant frequency  $\omega_x = 41.1$  rad/s ( $f_x = \omega_x/2\pi = 6.54$  Hz) in which the power spectra of the scanning error is the maximum. From the difference of the disturbance spectrum at the peak and peripheral frequency, the gain of the peak filter should be larger than 6 dB ( $\approx 2$ ). Therefore, the minimum gain of the peak filter is set to  $\beta = 6$  dB ( $\approx 2$ ) in the parameter constraints (7.22). The initial value of each parameter is set to  $\rho_x^{\text{ini}} = 1 \times 10^{-2}$  and  $\eta_x^{\text{ini}} = 1 \times 10^{-3}$ , respectively. It is noted that the initial condition is set to be a feasible solution. Note that when the initial condition is not a feasible solution, there are several considerations that are making the gain of the peak filter smaller, making the gain and phase margin smaller, and redesigning the static decoupling to make interaction smaller.

The gain margin and the phase margin in the SISO robust stability condition are set to  $g_m = 4$  dB and  $\Phi_m = 20$  deg, respectively. This condition is satisfied in the controlled system without peak filter.

In the MIMO stability condition, the generalized Gershgorin bands are considered only in the frequency range  $f_c/2 \leq f < 2f_c$ , when  $f_c$  is the gain cross over frequency of the open-loop transfer function without using the peak filter. The MIMO stability condition with the generalized Gershgorin bands is a sufficient condition, and the controlled system should not be designed too conservatively. Therefore, only this frequency range in which the stability condition is most

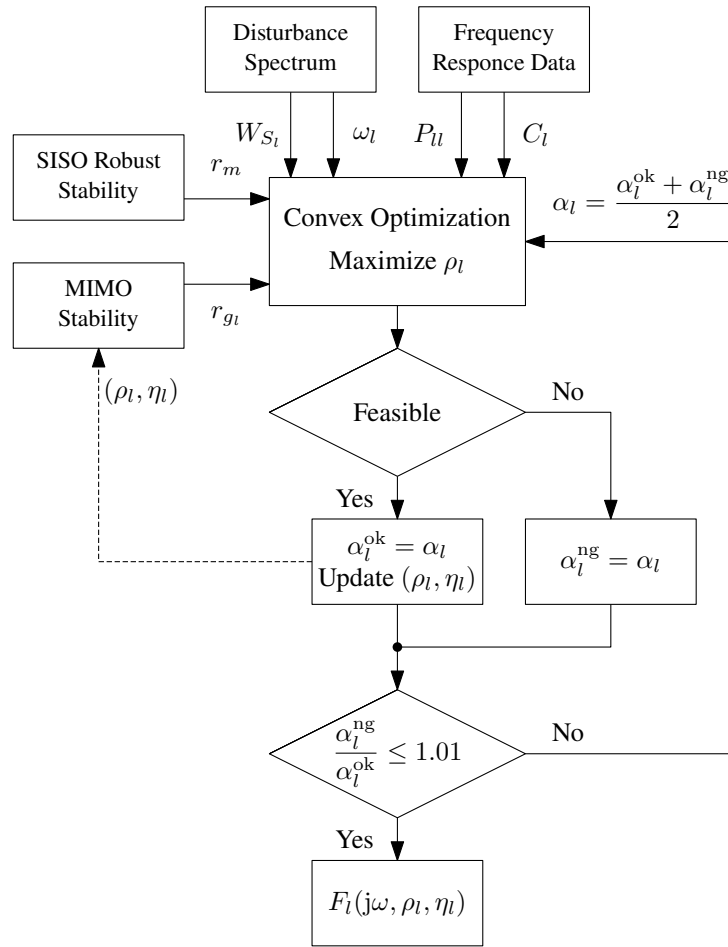


Fig. 7.7: Flowchart of proposed peak filter design method.

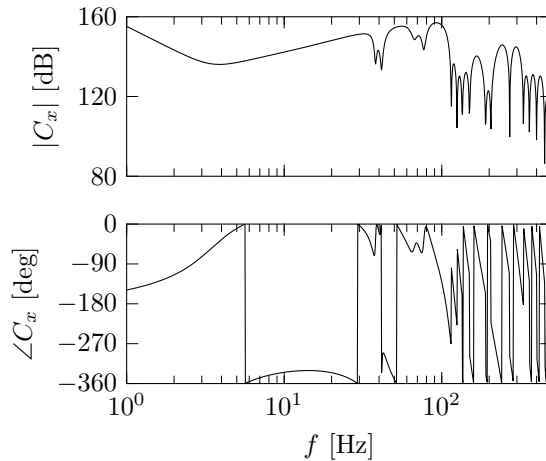


Fig. 7.8: Frequency response data of  $C_x$  that is fixed feedback controller along  $x$ -axis consisting of PID controller, disturbance observer, phase lead filter, and notch filter.

affected is considered in the MIMO stability condition. In other frequencies, the interference index is set to  $\lambda(j\omega_k) = 0$ .

The dichotomy method is used to solve the convex optimization problem with a sequential

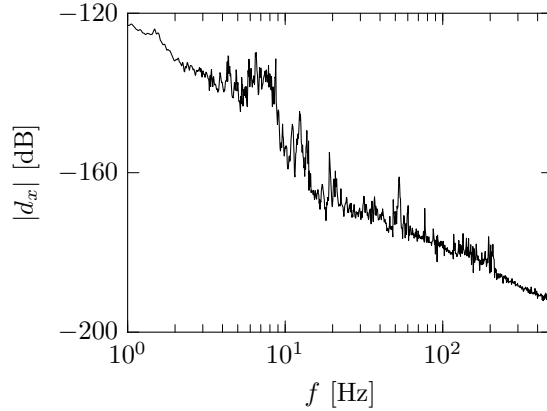


Fig. 7.9: Output disturbance spectrum along  $x$ -axis used for weighting function of sensitivity function with scaling parameter  $\alpha_x$ .

linearization method using the concave-convex procedure. The output disturbance spectrum along the  $x$ -axis used for the weighting function of the sensitivity function with the scaling parameter  $\alpha_x$  is shown in Fig. 7.9. The main reason for the disturbance in the frequency range from 5 Hz to 10 Hz is the vibrations from a coarse stage and a ground transmitted through the gravity canceller.

The objective function  $\alpha_x$  is searched in the range of  $\alpha_x^{\min} = 1 \times 10^5$  and  $\alpha_x^{\max} = 1 \times 10^7$ . The sensitivity function without peak filter and the weighting functions with the initial conditions are shown in Fig. 7.10. The Nyquist diagram without peak filter is shown in Fig. 7.11(a). The Nyquist diagram with the initial peak filter is shown in Fig. 7.11(b).

In the proposed peak filter design method, a parametric model of the controlled system and the given controller are not needed, and the frequency response data of them are enough for designing the peak filter.

The iterative optimization by the dichotomy method is repeated until  $\frac{\alpha_x^{\text{ng}}}{\alpha_x^{\text{ok}}} \leq 1.01$ , where  $\alpha_x^{\text{ok}}$  and  $\alpha_x^{\text{ng}}$  are defined as the values of  $\alpha_x$  in the feasible and infeasible solutions, respectively. The optimization calculation searches the feasible set of the parameter with larger  $\rho$  in the current operating point to design a peak filter with a wider resonance peak. The optimization problem is calculated by YALMIP [96] and Mosek [97].

### 7.4.3 Optimization results

By the optimization calculation, the values of the objective function and the optimal peak filter are given by  $\alpha_x^{\text{opt}} = 1482520$ ,  $\rho_x^{\text{opt}} = 0.02325$ , and  $\eta_x^{\text{opt}} = 0.011653$ , respectively.

The sensitivity function and the weighting function with the initial and the optimal peak filter are shown in Fig. 7.10. It is confirmed that the controller gain at the frequency of the maximum error spectrum becomes high due to using the peak filter, and the gain of the sensitivity function becomes low.

The Nyquist diagram with the optimal peak filter is shown in Fig. 7.11(c). It is confirmed that the designed controller satisfies both the SISO robust stability condition and the MIMO stability condition.

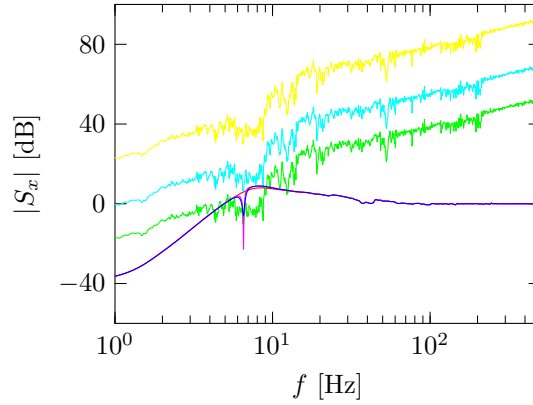


Fig. 7.10: Sensitivity function without (—), with initial (—), and with optimal (—) peak filter and weighting function with  $\alpha_x^{\min}$  (—),  $\alpha_x^{\max}$  (—), and  $\alpha_x^{\text{opt}}$  (—) of translation along the  $x$ -axis.

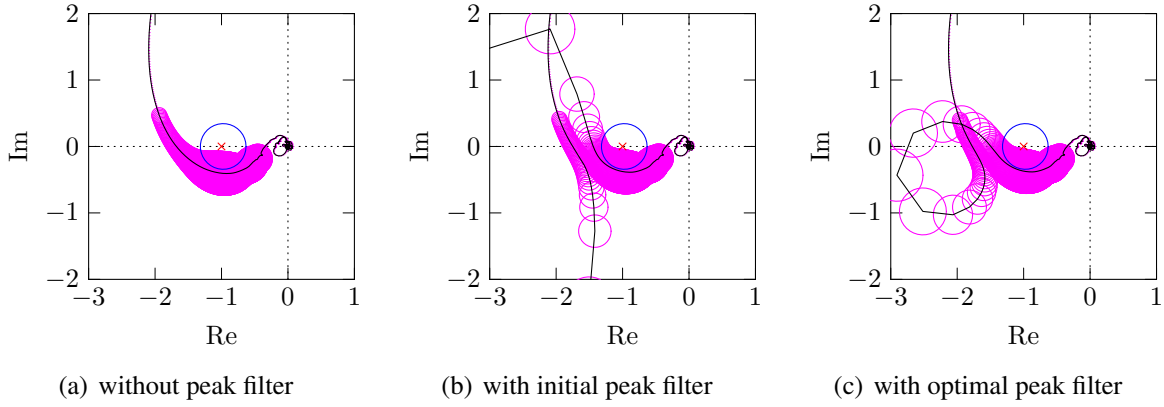


Fig. 7.11: Nyquist diagram of translation along the  $x$ -axis.

#### 7.4.4 Simulation evaluation

The simulation evaluation is conducted before the experiment.

The error with the peak filter  $e^w(j\omega_k)$  is calculated from the sensitivity function with and without the peak filter,  $S^w(j\omega_k)$  and  $S(j\omega_k)$ , and the error without the peak filter  $e(j\omega_k)$  as follows.

$$\begin{aligned} e^w(j\omega_k) &= S^w(j\omega_k) S^{-1}(j\omega_k) e(j\omega_k) \\ &= (\mathbf{I} + \mathbf{P}(j\omega_k) \mathbf{C}(j\omega_k) \mathbf{F}(j\omega_k, \boldsymbol{\rho}, \boldsymbol{\eta}))^{-1} \\ &\quad (\mathbf{I} + \mathbf{P}(j\omega_k) \mathbf{C}(j\omega_k)) e(j\omega_k). \end{aligned} \quad (7.29)$$

The time series of the simulated scanning errors of translation along the  $x$ -axis in four scan regions are calculated by inverse Fourier transform as shown in Fig. 7.12. The unit “[count]” means the resolution of the measurement sensor in the setup. From the simulation results, the optimized peak filter outperforms the without and with the initial peak filters.

#### 7.4.5 Experimental results

The experimental validation is conducted without and with the peak filter. In conventional methods, the peak filter cannot be designed with convex optimization using the frequency response

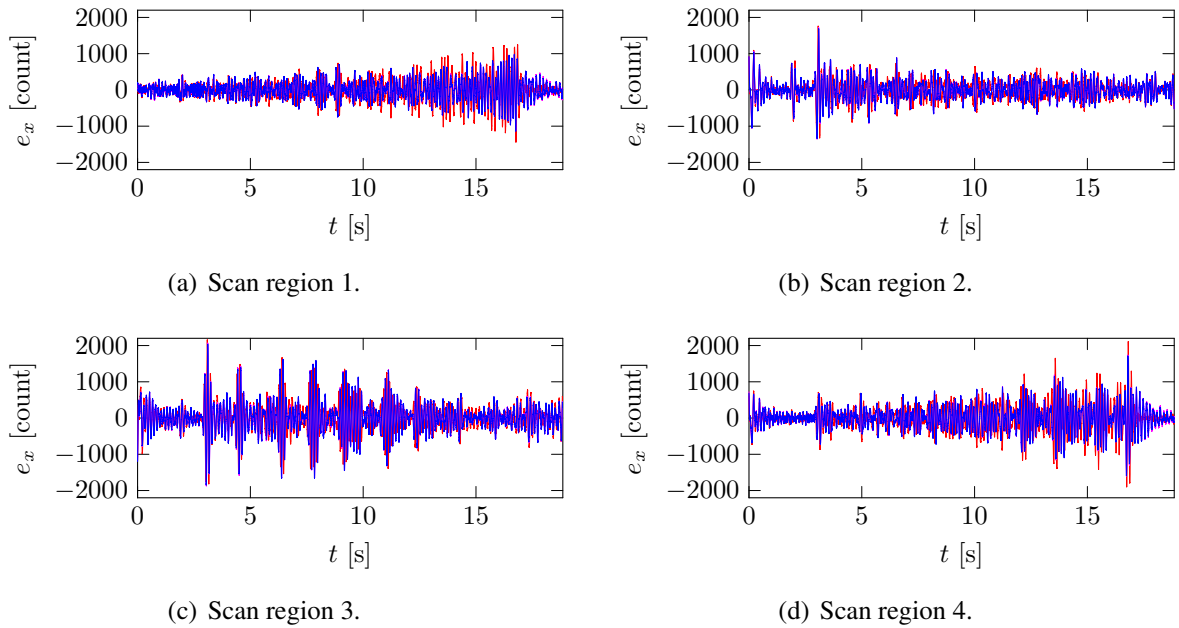


Fig. 7.12: Simulated position error of translation along the  $x$ -axis in four scan regions. No peak filter is used in w/o (—), one peak filter of translation along the  $x$ -axis with initial condition is used in (—), and one peak filter of translation along the  $x$ -axis with optimized condition is used in w/ (—). Errors in one peak filter of translation along the  $x$ -axis with initial and optimized conditions are overlapped but a little improved in the optimized condition.

data of the controlled system, not using the model of the controlled system. Therefore, the feedback controller without peak filter is used as the conventional method in the experimental validation.

The time series of the scanning errors of translation along the  $x$ -axis in four scan regions are shown in Fig. 7.13. The amplitude spectra of the scanning errors of translation along the  $x$ -axis in four scan regions are also shown in Fig. 7.14.

The scanning error is effectively reduced in scan region 1 and 4, as shown in Fig. 7.13(a) and Fig. 7.13(d). The disturbance around 6.54 Hz is effectively rejected by the peak filter and the scanning error is also reduced, as shown in Fig. 7.14(a) and Fig. 7.14(d). From this result, the effectiveness of the peak filter in disturbance rejection is validated.

On the other hand, the scanning error is not dramatically changed in scan regions 2 and 3, as shown in Fig. 7.13(b) and Fig. 7.13(c). This is because the frequency of the peak amplitude of the scanning error spectra in scan region 2 and 3 is around 7.5 Hz, and the disturbance in this frequency range can not be effectively rejected by the designed peak filter with the resonance frequency  $f_x = 6.54$  Hz.

The Root Mean Square (RMS) errors of a total of four scan regions in 6-DOFs ( $x, y, \theta_z, z, \theta_x, \theta_y$ ) are shown in Fig. 7.15. Fig. 7.15(a) shows that the RMS error in translation along the  $x$ -axis that is the main stroke of the scan stage is reduced. It means that the average scan quality is improved and the effectiveness of the designed peak filter is validated. It is also noteworthy that the RMS errors in ( $y, \theta_z, z$ )-axes are also improved. It is because the interaction of the disturbance from the  $x$ -axis is reduced by the peak filter. On the other hand, the RMS errors in ( $\theta_x, \theta_y$ )-axes are increased. It is because the interaction of the control input from the  $x$ -axis is increased by the

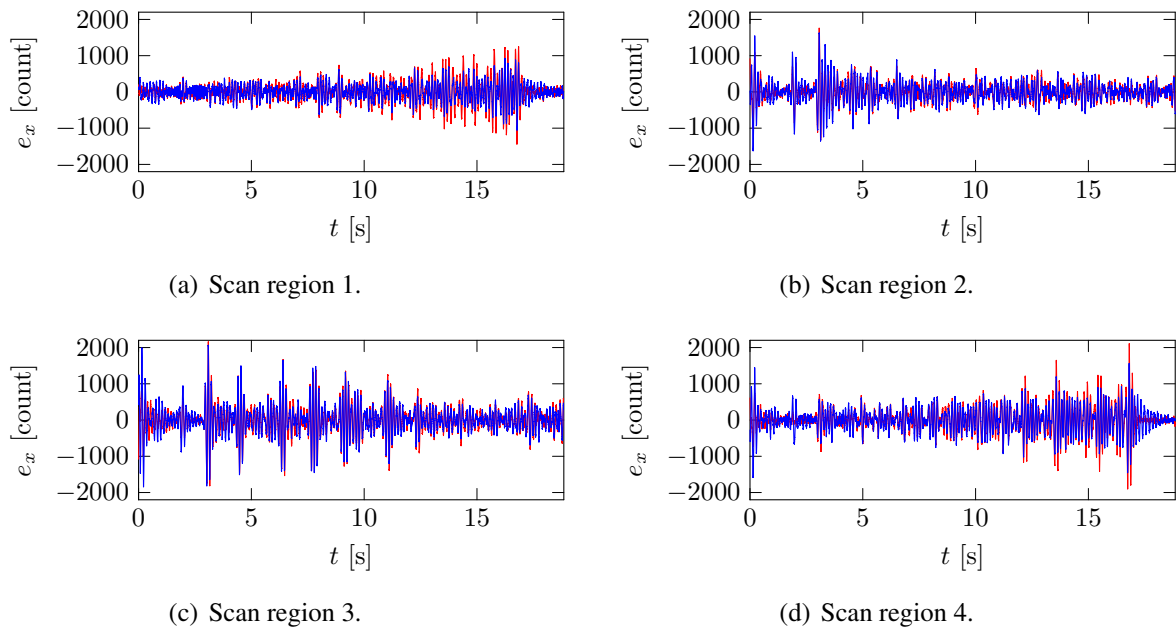


Fig. 7.13: Position error of translation along the  $x$ -axis in four scan regions. No peak filter is used in w/o (—) and one peak filter of translation along the  $x$ -axis is used in w/ (—).

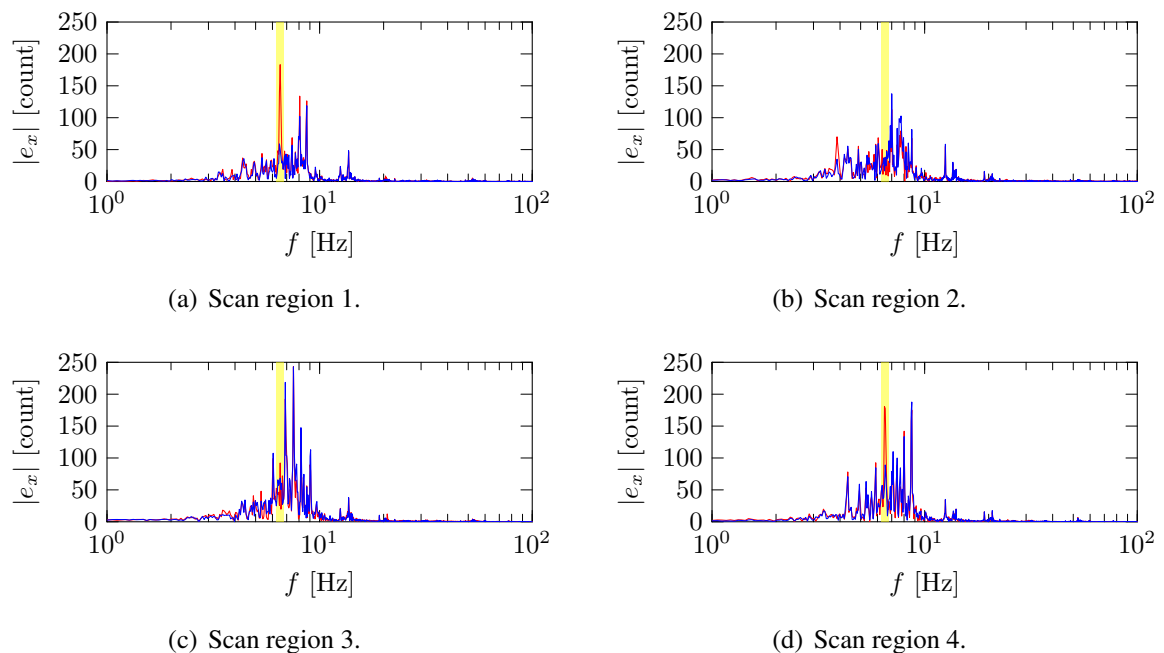


Fig. 7.14: Amplitude spectrum of position error of translation along the  $x$ -axis in four scan regions. No peak filter is used in w/o (—) and one peak filter of translation along the  $x$ -axis with optimized condition is used in w/ (—). The frequency range around the resonance frequency of the designed peak filter (6.54 Hz) is highlighted (■).

feedback controller high-gained by the peak filter. From these discussions, the peak filter has the advantage to reject the disturbance and to reduce the scanning error in the MIMO high-precision

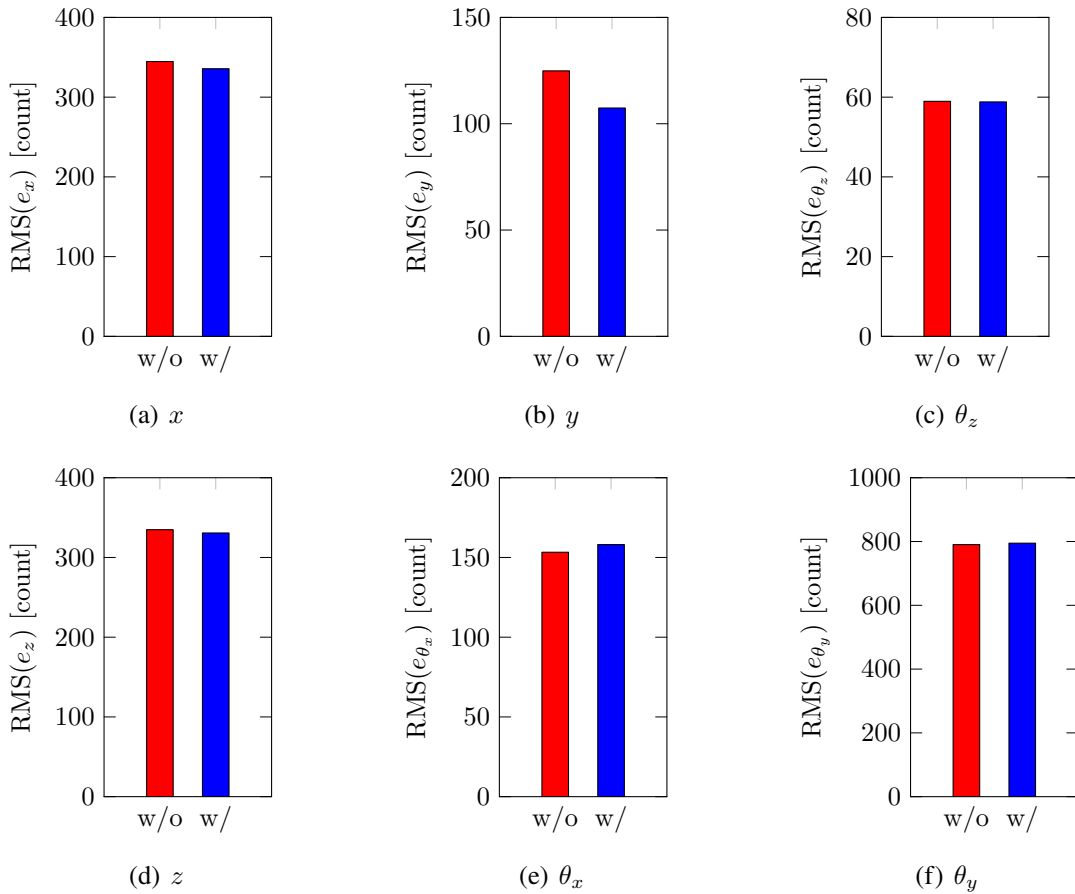


Fig. 7.15: Root Mean Square (RMS) errors of a total of four scan regions in 6-DOFs ( $x, y, \theta_z, z, \theta_x, \theta_y$ ). No peak filter is used in w/o (red bar ■) and one peak filter of translation along the  $x$ -axis with optimized condition is used in w/ (blue bar ■).

scan stage.

In this chapter, the feedback controller is designed diagonally as a setup restriction and human friendliness for manual tuning in the industrial final introduction process. In this case, the coupling effect cannot be completely suppressed by the feedback controller because of not enough degree of freedom. Therefore, the disturbance rejection performance of the main scan  $x$ -axis is mainly concerned, and only the MIMO stability condition is comprised in the peak filter design. Several decoupling control techniques are also proposed from both sides of the linear and the nonlinear control approach [121, 122]. The physical and mathematical analysis of the coupling effect by the designed peak filter and decoupling controller design is ongoing study.

Further improvement is possible with additional peak filters in the  $x$ -axis or other axes. The proposed peak filter design method can be applied to other axes with the MIMO stability condition. However, MIMO robust performance improvement is not guaranteed. Therefore, the decoupling controller also should be designed at the same time as the designed peak filters in multi-axes. It also should be concerned that the additional stability margin is needed to design the additional peak filters because of the phase lag after the resonance frequency. To deal with this problem, the phase compensator should be designed simultaneously as the peak filter, or all controllers should be optimized at once.



## **7.5 Conclusion**

The frequency response data-based peak filter design in this chapter enables reducing tracking errors in the scanning motion. The main underlying idea of this chapter is the combination of the frequency response data-based design approach with convex optimization and the robust design method of the MIMO controlled systems.

The effectiveness of the designed peak filter is demonstrated in the experiment with the industrial large-scale MIMO high-precision scan stage. The disturbance spectrum of the maximum error frequency is effectively rejected by the designed peak filter, and as a result, it is confirmed that the scanning error spectrum of that frequency is reduced.



**Part V**  
**Closing**



# Chapter 8

## Conclusion

In the dissertation, multivariable high-precision motion control with structured modeling and data-driven convex optimization is presented. The approaches consider the dynamics of multivariable systems such as multi-modal dynamics and multi-input multi-output (MIMO) interactions to achieve high-precision tracking performance. The structured parameterization of the controller enables an intuitive tuning process. In addition, the controllers can be designed by data-driven convex optimization to overcome the difficulty of tuning many controller parameters. The approaches are applied to actual setups such as a precision positioning stage, a two-inertia motor bench, a suspended beam, a hard disk drive, and an industrial scan stage. The effectiveness of the approaches is validated through simulations and experiments.

In Part I, Chapter 1 clarifies the requirements in the industrial application of mechatronics systems to achieve higher performance. The performance requirements for advanced motion control in industrial mechatronics systems are increasing year by year. It is necessary to design a controller considering the multivariable dynamics. High control performance can be achieved by effectively utilizing redundancy in multivariable systems such as combining the advantages of model-based and data-based controller design. From these backgrounds, the goal of the dissertation is that “develop a framework for multivariable high-precision motion control combining model-based and data-based approaches that is suitable for mechatronic systems in industrial applications”. In the first half of the dissertation (Chapter 2, 3, 4, and 5), the state tracking control approaches based on multirate feedforward control are used for multi-modal systems and MIMO systems to improve the continuous-time tracking performance. In the latter half of the dissertation (Chapter 4, 5, 6, and 7), the structured controllers are optimized by data-driven convex optimization to avoid the time-consuming tuning process in multivariable systems and the tuning parameters are interpretable by physically intuitive meaning.

In Part II, the multirate feedforward control is extended to multi-modeal systems and MIMO systems to improve the continuous-time tracking performance by effectively using the redundancy of the multivariable systems. In Chapter 2, multirate feedforward control is generally presented in multi-modal motion systems. The state trajectory generation is generalized to non-minimum-phase and MIMO motion systems. The redundancy of the multi-modal system is considered by the mode selection to improve the continuous-time tracking performance. The effectiveness of the approach is validated in a high-precision positioning stage with multiple resonant modes. It constitutes Contribution M-1. In Chapter 3, multirate feedforward control is generally presented in MIMO motion systems. The challenge in multirate feedforward control for MIMO systems is that there is redundancy in how to select sampling periods for multiple inputs. The redundancy of

multirate input sampling is analytically optimized by the state controllability of the generalized controllability indices. The effectiveness of the approach is validated in a two-inertia system motor bench for intersample performance and in a 6-DOF high-precision positioning stage for interaction compensation. It constitutes Contribution M-2.

In Part III, the sampled-data feedforward control based on state tracking is extended to structured parameterization and data-driven convex optimization. In Chapter 4, the state tracking sampled-data feedforward control is presented in linearly parameterized feedforward control. The linear parameterization enables intuitive tuning and ease for the extension to data-driven parameter updates. The conventional multirate feedforward controllers are designed as the inverse of the model. It is difficult to update the controller parameters intuitively by using experimental data. Therefore, to enable the data-driven tuning of the sampled-data feedforward controller based on state tracking, the feedforward controller is linearly parameterized by basis functions corresponding to the reference and the physically intuitive tuning parameters. The basis functions are designed by sampled-data differentiator considering zero-order-hold dynamics to improve intersample performance. The effectiveness of the approach is validated in a two-inertia system motor bench compared to the conventional basis function design that does not consider the zero-order-hold dynamics. It constitutes Contribution M-3. In Chapter 5, the state tracking sampled-data feedforward control that is presented in Chapter 4 is extended to an iterative learning control for MIMO motion systems. It enables the data-driven parameter update and interaction compensation of MIMO systems without the MIMO model. The MIMO feedforward controller is parameterized by physically intuitive basis functions and tuning parameters as a fixed structure based on low-frequency error dynamics of MIMO multi-modal systems. The tuning parameters of the controller are updated by iterative learning control using experimental data and a diagonal rigid body model to minimize errors. The effectiveness of the approach is validated in a suspended beam compared to the conventional feedforward controller that does not consider MIMO interaction. It constitutes Contribution D-1.

In Part IV, the feedback controller design using frequency response data and convex optimization for disturbance rejection in multivariable motion systems is presented. In Chapter 6 the frequency response data-based disturbance rejection is presented with robust performance in the system with model variations. In the conventional data-driven feedback controller design, there is a challenge that the improvement of the error is directly formulated as an objective function. To improve the disturbance rejection performance, it is necessary to design a feedback controller that can deal with the variations of models and disturbances. The approach formulates resonant filters corresponding to multiple disturbance frequencies in structured linear parameterization. The frequency response data is directly used for the controller design problem that is solved by an iterative convex optimization using sequential linearization. The multiple resonant filters enable disturbance rejection in several frequencies and the controller is optimized considering the model variations to minimize the error. The effectiveness of the approach is validated in a dual-stage actuator hard disk drive benchmark problem. It constitutes Contribution D-2. In Chapter 7, the frequency response data-based disturbance rejection is presented with robust stability in MIMO systems. The feedback controller design in MIMO systems has a challenge because MIMO systems have an interaction that can deteriorate robust stability and the parametric model identification of the MIMO systems is difficult and time-consuming. The disturbance rejection at a specific frequency is difficult to ensure robust stability in actual implementation because the gain of the controller becomes high at that frequency. Therefore, the approach formulates the robust controller design problem that directly uses the frequency response data considering

the interaction of the MIMO system. The feedback controller is designed by an iterative convex optimization using sequential linearization. The effectiveness of the approach is validated in the experiment and it is the first attempt to apply the high-gain controller to the actual industrial large-scale MIMO high-precision scan stage. It constitutes Contribution D-3.

In conclusion, the dissertation constructs a general framework of multivariable high-precision motion control with structured modeling and data-driven convex optimization for industrial applications. The developed approaches are theoretically novel and the engineering applicability is successfully demonstrated in simulation and experimental validation including the implementation in commercial products. The dissertation contributes to both the academic and industrial fields, and its importance will continue to increase in the future. These facts show that the dissertation makes a major breakthrough in control engineering about performance improvement and practical applicability for industrial applications.





# Bibliography

- [1] Nikon, “FPD Lithography Systems FX-103SH/103S,” 2019. [Online]. Available: [https://www.nikon.com/products/fpd/lineup/pdf/FX-103SH\\_103S\\_e.pdf](https://www.nikon.com/products/fpd/lineup/pdf/FX-103SH_103S_e.pdf)
- [2] ASML, “EUV lithography systems,” 2022. [Online]. Available: <https://www.asml.com/en/products/euv-lithography-systems>
- [3] G. E. Moore, “Cramming More Components Onto Integrated Circuits,” *Electronics*, vol. 38, no. 8, 1965.
- [4] DMG MORI, “NVX Series,” 2022. [Online]. Available: <https://us.dmgmori.com/products/machines/milling/vertical-milling/nvx>
- [5] YASKAWA, “Industrial Robots,” 2022. [Online]. Available: <https://www.yaskawa-global.com/product/robotics>
- [6] Canon, “Arizona 550 GT,” 2012. [Online]. Available: [https://en.canon-cna.com/for\\_work/products/large\\_format\\_printers/displaygraphics/oce\\_arizona\\_550\\_gt](https://en.canon-cna.com/for_work/products/large_format_printers/displaygraphics/oce_arizona_550_gt)
- [7] TOSHIBA, “High-Reliability FC-MAMR Nearline HDD with a Capacity of 18 TB,” 2021. [Online]. Available: [https://toshiba.semicon-storage.com/content/dam/toshiba-ss-v3/master/en/storage/technology-center/20210304\\_nearlinehdd\\_18tb\\_e\\_low.pdf](https://toshiba.semicon-storage.com/content/dam/toshiba-ss-v3/master/en/storage/technology-center/20210304_nearlinehdd_18tb_e_low.pdf)
- [8] Daikin, “AIR CONDITIONING & REFRIGERATION,” 2022. [Online]. Available: <https://www.daikin.com/products/ac>
- [9] S. Yamada, T. Beauduin, H. Fujimoto, T. Kanou, and E. Katsuyama, “Active Model-Based Suppression of Secondary Ride for Electric Vehicles With In-Wheel Motors,” *IEEE/ASME Transactions on Mechatronics*, pp. 1–10, 2022. [Online]. Available: <https://ieeexplore.ieee.org/document/9827602/>
- [10] S. Noguchi, M. Mae, and H. Fujimoto, “Quasi Multirate Feedforward Current Control toward Nyquist Frequency of PWM for SPMSM,” *IEEJ Journal of Industry Applications*, vol. 10, no. 4, p. 20004635, jul 2021. [Online]. Available: [https://www.jstage.jst.go.jp/article/ieejjia/10/4/10\\_20004635/\\_article](https://www.jstage.jst.go.jp/article/ieejjia/10/4/10_20004635/_article)
- [11] Y. Inagaki, M. Mae, O. Shimizu, S. Nagai, H. Fujimoto, T. Miyajima, Y. Yasuda, and A. Yamagiwa, “Effect of Harmonic Current Suppression on Iron Loss of IPMSM Using Repetitive Perfect Tracking Control,” *IEEJ Journal of Industry Applications*, p. 21005712, 2021. [Online]. Available: [https://www.jstage.jst.go.jp/article/ieejjia/advpub/0/advpub\\_21005712/\\_article](https://www.jstage.jst.go.jp/article/ieejjia/advpub/0/advpub_21005712/_article)

- [12] T. Suzuki, M. Mae, T. Takeuchi, H. Fujimoto, and E. Katsuyama, “Model-based Filter Design for Triple Skyhook Control of In-Wheel Motor Vehicles for Ride Comfort,” *IEEE Journal of Industry Applications*, vol. 10, no. 3, pp. 310–316, may 2021. [Online]. Available: [https://www.jstage.jst.go.jp/article/ieejia/10/3/10\\_20004677/\\_article](https://www.jstage.jst.go.jp/article/ieejia/10/3/10_20004677/_article)
- [13] G. F. Franklin, J. Powell, and A. Emami-Naeini, *Feedback Control of Dynamic Systems*, 7th ed. Addison-Wesley, 2014.
- [14] S. Skogestad and I. Postlethwaite, *Multivariable Feedback Control*, 2nd ed. John Wiley & Sons, Ltd, 2005.
- [15] T. Chen and B. A. Francis, *Optimal Sampled-Data Control Systems*. London: Springer London, 1995. [Online]. Available: <http://link.springer.com/10.1007/978-1-4471-3037-6>
- [16] J. M. Maciejowski, *Predictive Control with Constraints*. London: Pearson Education Limited, Prentice Hall, 2002.
- [17] S. Hara, J.-i. Imura, K. Tsumura, T. Ishizaki, and T. Sadamoto, “Glocal (global/local) control synthesis for hierarchical networked systems,” in *2015 IEEE Conference on Control Applications (CCA)*. IEEE, sep 2015, pp. 107–112. [Online]. Available: <https://ieeexplore.ieee.org/document/7320618>
- [18] S. Hara, T. Iwasaki, and Y. Hori, “Robust stability analysis for LTI systems with generalized frequency variables and its application to gene regulatory networks,” *Automatica*, vol. 105, pp. 96–106, jul 2019. [Online]. Available: <https://linkinghub.elsevier.com/retrieve/pii/S0005109819301402>
- [19] K. Åström, P. Hagander, and J. Sternby, “Zeros of sampled systems,” *Automatica*, vol. 20, no. 1, pp. 31–38, jan 1984. [Online]. Available: <https://linkinghub.elsevier.com/retrieve/pii/0005109884900621>
- [20] H. Fujimoto, Y. Hori, and A. Kawamura, “Perfect tracking control based on multirate feedforward control with generalized sampling periods,” *IEEE Transactions on Industrial Electronics*, vol. 48, no. 3, pp. 636–644, jun 2001. [Online]. Available: <http://ieeexplore.ieee.org/document/925591/>
- [21] S. Boyd and L. Vandenberghe, *Convex Optimization*. Cambridge University Press, 2004. [Online]. Available: [https://web.stanford.edu/~boyd/cvxbook/bv\\_cvxbook.pdf](https://web.stanford.edu/~boyd/cvxbook/bv_cvxbook.pdf)
- [22] S. Arimoto, S. Kawamura, and F. Miyazaki, “Bettering operation of Robots by learning,” *Journal of Robotic Systems*, vol. 1, no. 2, pp. 123–140, 1984. [Online]. Available: <https://onlinelibrary.wiley.com/doi/10.1002/rob.4620010203>
- [23] D. Bristow, M. Tharayil, and A. Alleyne, “A survey of iterative learning control,” *IEEE Control Systems*, vol. 26, no. 3, pp. 96–114, jun 2006. [Online]. Available: <https://ieeexplore.ieee.org/document/1636313/>
- [24] M. Phan and J. Frueh, “Learning control for trajectory tracking using basis functions,” in *Proceedings of 35th IEEE Conference on Decision and Control*, vol. 3, no. December. IEEE, 1996, pp. 2490–2492. [Online]. Available: <http://ieeexplore.ieee.org/document/573465/>

- [25] J. van de Wijdeven and O. Bosgra, "Using basis functions in iterative learning control: analysis and design theory," *International Journal of Control*, vol. 83, no. 4, pp. 661–675, apr 2010. [Online]. Available: <https://www.tandfonline.com/doi/full/10.1080/00207170903334805>
- [26] J. Doyle, "Analysis of feedback systems with structured uncertainties," *IEE Proceedings D Control Theory and Applications*, vol. 129, no. 6, p. 242, 1982. [Online]. Available: <https://digital-library.theiet.org/content/journals/10.1049/ip-d.1982.0053>
- [27] M. Safonov, "Stability margins of diagonally perturbed multivariable feedback systems," *IEE Proceedings D Control Theory and Applications*, vol. 129, no. 6, p. 251, 1982. [Online]. Available: <https://digital-library.theiet.org/content/journals/10.1049/ip-d.1982.0054>
- [28] J. Doyle, K. Glover, P. Khargonekar, and B. Francis, "State-space solutions to standard  $H_2$  and  $H_\infty$  control problems," *IEEE Transactions on Automatic Control*, vol. 34, no. 8, pp. 831–847, 1989. [Online]. Available: <http://ieeexplore.ieee.org/document/29425/>
- [29] J. Doyle, "Robust and optimal control," in *Proceedings of 35th IEEE Conference on Decision and Control*, vol. 2, no. 11. IEEE, nov 1997, pp. 1595–1598. [Online]. Available: <http://ieeexplore.ieee.org/document/572756/>
- [30] P. Apkarian and D. Noll, "Structured  $H_\infty$ -control of infinite-dimensional systems," *International Journal of Robust and Nonlinear Control*, vol. 28, no. 9, pp. 3212–3238, jun 2018. [Online]. Available: <http://doi.wiley.com/10.1002/rnc.4073>
- [31] A. Karimi, G. Galdos, and R. Longchamp, "Robust fixed-order  $H_\infty$  controller design for spectral models by convex optimization," in *2008 47th IEEE Conference on Decision and Control*. IEEE, dec 2008, pp. 921–926. [Online]. Available: <https://ieeexplore.ieee.org/document/4739130/>
- [32] S. Boyd, M. Hast, and K. J. Åström, "MIMO PID tuning via iterated LMI restriction," *International Journal of Robust and Nonlinear Control*, vol. 26, no. 8, pp. 1718–1731, may 2016. [Online]. Available: <https://onlinelibrary.wiley.com/doi/10.1002/rnc.3376>
- [33] K. Yubai, "Development of data-based controller synthesis by convex optimization," *Electronics and Communications in Japan*, vol. 102, no. 7, pp. 27–31, jul 2019. [Online]. Available: <https://onlinelibrary.wiley.com/doi/abs/10.1002/ecj.12180>
- [34] A. L. Yuille and A. Rangarajan, "The Concave-Convex Procedure," *Neural Computation*, vol. 15, no. 4, pp. 915–936, apr 2003. [Online]. Available: <http://www.mitpressjournals.org/doi/10.1162/08997660360581958>
- [35] M. Tomizuka, "Zero Phase Error Tracking Algorithm for Digital Control," *Journal of Dynamic Systems, Measurement, and Control*, vol. 109, no. 1, p. 65, 1987. [Online]. Available: <http://dynamicsystems.asmedigitalcollection.asme.org/article.aspx?articleid=1403902>
- [36] M. Steinbuch, T. Oomen, and H. Vermeulen, "Motion Control, Mechatronics Design, and Moore's Law," *IEEJ Journal of Industry Applications*, vol. 2, no. 4, p. 21006010,

2021. [Online]. Available: [https://www.jstage.jst.go.jp/article/ieejia/advpub/0/advpub\\_21006010/\\_article](https://www.jstage.jst.go.jp/article/ieejia/advpub/0/advpub_21006010/_article)
- [37] M. Poot, J. Portegies, N. Mooren, M. van Haren, M. van Meer, and T. Oomen, “Gaussian Processes for Advanced Motion Control,” *IEEJ Journal of Industry Applications*, no. 41, p. 21011492, 2022. [Online]. Available: [https://www.jstage.jst.go.jp/article/ieejia/advpub/0/advpub\\_21011492/\\_article](https://www.jstage.jst.go.jp/article/ieejia/advpub/0/advpub_21011492/_article)
- [38] T. Hayashi, H. Fujimoto, Y. Isaoka, and Y. Terada, “Projection-based Iterative Learning Control for Ball-screw-driven Stage with Consideration of Rolling Friction Compensation,” *IEEJ Journal of Industry Applications*, vol. 9, no. 2, pp. 132–139, mar 2020. [Online]. Available: [https://www.jstage.jst.go.jp/article/ieejia/9/2/9\\_132/\\_article](https://www.jstage.jst.go.jp/article/ieejia/9/2/9_132/_article)
- [39] J. van Zundert and T. Oomen, “On inversion-based approaches for feedforward and ILC,” *Mechatronics*, vol. 50, no. November 2016, pp. 282–291, apr 2018. [Online]. Available: <https://linkinghub.elsevier.com/retrieve/pii/S0957415817301368>
- [40] W. Ohnishi, T. Beauduin, and H. Fujimoto, “Preactuated Multirate Feedforward Control for Independent Stable Inversion of Unstable Intrinsic and Discretization Zeros,” *IEEE/ASME Transactions on Mechatronics*, vol. 24, no. 2, pp. 863–871, apr 2019. [Online]. Available: <https://ieeexplore.ieee.org/document/8629944/>
- [41] W. Ohnishi and H. Fujimoto, “Multirate Feedforward Control Based on Modal Form,” in *2018 IEEE Conference on Control Technology and Applications (CCTA)*, no. 2. IEEE, aug 2018, pp. 1120–1125. [Online]. Available: <https://ieeexplore.ieee.org/document/8511087/>
- [42] M. Mae, W. Ohnishi, and H. Fujimoto, “Multirate Feedforward Control based on Modal Form with Mode Selection Applied to Multi-Modal High-Precision Positioning Stage,” in *2021 IEEE International Conference on Mechatronics (ICM)*. IEEE, mar 2021, pp. 1–6. [Online]. Available: <https://ieeexplore.ieee.org/document/9385685/>
- [43] J. van Zundert, W. Ohnishi, H. Fujimoto, and T. Oomen, “Improving Intersample Behavior in Discrete-Time System Inversion: With Application to LTI and LPTV Systems,” *IEEE/ASME Transactions on Mechatronics*, vol. 25, no. 1, pp. 55–65, feb 2020. [Online]. Available: <https://ieeexplore.ieee.org/document/8902055/>
- [44] M. Mae, W. Ohnishi, and H. Fujimoto, “MIMO multirate feedforward controller design with selection of input multiplicities and intersample behavior analysis,” *Mechatronics*, vol. 71, no. February, p. 102442, nov 2020. [Online]. Available: <https://linkinghub.elsevier.com/retrieve/pii/S0957415820301112>
- [45] M. Mae, W. Ohnishi, and H. Fujimoto, “State Trajectory Generation for MIMO Multirate Feedforward using Singular Value Decomposition and Time Axis Reversal,” in *2019 American Control Conference (ACC)*, vol. 2019-July. IEEE, jul 2019, pp. 5693–5698. [Online]. Available: <https://ieeexplore.ieee.org/document/8815067/>
- [46] W. K. Gawronski, *Advanced Structural Dynamics and Active Control of Structures*. New York: Springer, 2004.

- [47] O. Lindgarde and B. Lennartson, "Performance and robust frequency response for multirate sampled-data systems," in *Proceedings of the 1997 American Control Conference (Cat. No.97CH36041)*, vol. 6, no. June. IEEE, 1997, pp. 3877–3881 vol.6. [Online]. Available: <http://ieeexplore.ieee.org/document/609611/>
- [48] H. Fujimoto, "General Framework of Multirate Sampling Control and Applications to Motion Control Systems," *Doctoral Dissertation*, 2000.
- [49] T. Oomen, M. van de Wal, and O. Bosgra, "Design framework for high-performance optimal sampled-data control with application to a wafer stage," *International Journal of Control*, vol. 80, no. 6, pp. 919–934, jun 2007. [Online]. Available: <http://www.tandfonline.com/doi/abs/10.1080/00207170701216329>
- [50] T. Oomen, "Advanced Motion Control for Precision Mechatronics: Control, Identification, and Learning of Complex Systems," *IEEJ Journal of Industry Applications*, vol. 7, no. 2, pp. 127–140, 2018. [Online]. Available: [https://www.jstage.jst.go.jp/article/ieejia/7/2/7\\_127/\\_article](https://www.jstage.jst.go.jp/article/ieejia/7/2/7_127/_article)
- [51] H. Butler, "Position Control in Lithographic Equipment [Applications of Control]," *IEEE Control Systems*, vol. 31, no. 5, pp. 28–47, oct 2011. [Online]. Available: <https://ieeexplore.ieee.org/document/6021296/>
- [52] Y. Al Hamidi and M. Rakotondrabe, "Multi-Mode Vibration Suppression in MIMO Systems by Extending the Zero Placement Input Shaping Technique: Applications to a 3-DOF Piezoelectric Tube Actuator," *Actuators*, vol. 5, no. 2, p. 13, apr 2016. [Online]. Available: <http://www.mdpi.com/2076-0825/5/2/13>
- [53] D. Habineza, M. Zouari, Y. Le Gorrec, and M. Rakotondrabe, "Multivariable Compensation of Hysteresis, Creep, Badly Damped Vibration, and Cross Couplings in Multiaxes Piezoelectric Actuators," *IEEE Transactions on Automation Science and Engineering*, vol. 15, no. 4, pp. 1639–1653, oct 2018. [Online]. Available: <https://ieeexplore.ieee.org/document/8207642/>
- [54] L. Hunt, G. Meyer, and R. Su, "Noncausal inverses for linear systems," *IEEE Transactions on Automatic Control*, vol. 41, no. 4, pp. 608–611, apr 1996. [Online]. Available: <http://ieeexplore.ieee.org/document/489285/>
- [55] S. Devasia, Degang Chen, and B. Paden, "Nonlinear inversion-based output tracking," *IEEE Transactions on Automatic Control*, vol. 41, no. 7, pp. 930–942, jul 1996. [Online]. Available: <http://ieeexplore.ieee.org/document/508898/>
- [56] T. Sogo, "On the equivalence between stable inversion for nonminimum phase systems and reciprocal transfer functions defined by the two-sided Laplace transform," *Automatica*, vol. 46, no. 1, pp. 122–126, jan 2010. [Online]. Available: <https://linkinghub.elsevier.com/retrieve/pii/S0005109809004695>
- [57] J. Butterworth, L. Pao, and D. Abramovitch, "Analysis and comparison of three discrete-time feedforward model-inverse control techniques for nonminimum-phase systems," *Mechatronics*, vol. 22, no. 5, pp. 577–587, aug 2012. [Online]. Available: <https://linkinghub.elsevier.com/retrieve/pii/S0957415812000311>

- [58] J. Wen and B. Potsaid, "An experimental study of a high performance motion control system," in *Proceedings of the 2004 American Control Conference*, vol. 6. IEEE, 2004, pp. 5158–5163. [Online]. Available: <https://ieeexplore.ieee.org/document/1384671/>
- [59] K. L. Moore, S. Bhattacharyya, and M. Dahleh, "Capabilities and limitations of multirate control schemes," *Automatica*, vol. 29, no. 4, pp. 941–951, jul 1993. [Online]. Available: <http://linkinghub.elsevier.com/retrieve/pii/000510989390098E>
- [60] T. Sogo and M. Joo, "Design of Compensators to Relocate Sampling Zeros of Digital Control Systems for DC Motors," *SICE Journal of Control, Measurement, and System Integration*, vol. 5, no. 5, pp. 283–289, 2012. [Online]. Available: <http://japanlinkcenter.org/DN/JST.JSTAGE/jcmsi/5.283?lang=en&from=CrossRef&type=abstract>
- [61] K. George, M. Verhaegen, and J. M. a. Scherpen, "Stable Inversion of MIMO Linear Discrete Time Non-Minimum Phase Systems," in *Proceedings of the 7th Mediterranean Conference on Control and Automation*, 1999, pp. 267–281.
- [62] L. Blanken and T. Oomen, "Multivariable Iterative Learning Control Design Procedures: From Decentralized to Centralized, Illustrated on an Industrial Printer," *IEEE Transactions on Control Systems Technology*, pp. 1–8, 2019. [Online]. Available: <https://ieeexplore.ieee.org/document/8684767/>
- [63] M. Heertjes, D. Hennekens, and M. Steinbuch, "MIMO feed-forward design in wafer scanners using a gradient approximation-based algorithm," *Control Engineering Practice*, vol. 18, no. 5, pp. 495–506, may 2010. [Online]. Available: <https://linkinghub.elsevier.com/retrieve/pii/S0967066110000146>
- [64] M. Mae, W. Ohnishi, H. Fujimoto, and Y. Hori, "Perfect Tracking Control Considering Generalized Controllability Indices and Application for High-Precision Stage in Translation and Pitching," *IEEJ Journal of Industry Applications*, vol. 8, no. 2, pp. 263–270, mar 2019. [Online]. Available: [https://www.jstage.jst.go.jp/article/ieejjia/8/2/8\\_263/\\_article](https://www.jstage.jst.go.jp/article/ieejjia/8/2/8_263/_article)
- [65] R. Kalman, "On the general theory of control systems," *IFAC Proceedings Volumes*, vol. 1, no. 1, pp. 491–502, aug 1960. [Online]. Available: <https://linkinghub.elsevier.com/retrieve/pii/S1474667017700948>
- [66] S. Lang, *Linear Algebra*, 3rd ed. Springer, 1987.
- [67] R. Pintelon, P. Guillaume, Y. Rolain, J. Schoukens, and H. Van Hamme, "Parametric identification of transfer functions in the frequency domain—a survey," *IEEE Transactions on Automatic Control*, vol. 39, no. 11, pp. 2245–2260, 1994. [Online]. Available: <http://ieeexplore.ieee.org/document/333769/>
- [68] S. Ito, S. Troppmair, F. Cigarini, and G. Schitter, "High-speed Scanner with Nanometer Resolution Using a Hybrid Reluctance Force Actuator," *IEEJ Journal of Industry Applications*, vol. 8, no. 2, pp. 170–176, mar 2019. [Online]. Available: [https://www.jstage.jst.go.jp/article/ieejjia/8/2/8\\_170/\\_article](https://www.jstage.jst.go.jp/article/ieejjia/8/2/8_170/_article)

- [69] P. Lambrechts, M. Boerlage, and M. Steinbuch, "Trajectory planning and feedforward design for electromechanical motion systems," *Control Engineering Practice*, vol. 13, no. 2, pp. 145–157, feb 2005. [Online]. Available: <https://linkinghub.elsevier.com/retrieve/pii/S0967066104000462>
- [70] M. Tomizuka and L. Sun, "Simplified Realization of Zero Phase Error Tracking," *Journal of Dynamic Systems, Measurement, and Control*, vol. 143, no. 3, pp. 1–6, mar 2021. [Online]. Available: <https://asmedigitalcollection.asme.org/dynamicsystems/article/doi/10.1115/1.4049391/1092400/Simplified-Realization-of-Zero-Phase-Error>
- [71] M. Boerlage, R. Tousain, and M. Steinbuch, "Jerk derivative feedforward control for motion systems," in *Proceedings of the 2004 American Control Conference*, vol. 5. IEEE, 2004, pp. 4843–4848 vol.5. [Online]. Available: <https://ieeexplore.ieee.org/document/1384080/>
- [72] G. C. Goodwin, S. F. Graebe, and M. E. Salgado, *Control System Design*. Prentice Hall, 2000.
- [73] J. Bolder, T. Oomen, S. Koekebakker, and M. Steinbuch, "Using iterative learning control with basis functions to compensate medium deformation in a wide-format inkjet printer," *Mechatronics*, vol. 24, no. 8, pp. 944–953, dec 2014. [Online]. Available: <https://linkinghub.elsevier.com/retrieve/pii/S0957415814000993>
- [74] Q. Zhu, F. Song, J.-X. Xu, and Y. Liu, "An Internal Model Based Iterative Learning Control for Wafer Scanner Systems," *IEEE/ASME Transactions on Mechatronics*, vol. 24, no. 5, pp. 2073–2084, oct 2019. [Online]. Available: <https://ieeexplore.ieee.org/document/8769933/>
- [75] J. Li, Y. Wang, Y. Li, and W. Luo, "Reference Trajectory Modification Based on Spatial Iterative Learning for Contour Control of Two-Axis NC Systems," *IEEE/ASME Transactions on Mechatronics*, vol. 25, no. 3, pp. 1266–1275, jun 2020. [Online]. Available: <https://ieeexplore.ieee.org/document/8994097/>
- [76] N. Nikooienejad, M. Maroufi, and S. O. R. Moheimani, "Iterative Learning Control for Video-Rate Atomic Force Microscopy," *IEEE/ASME Transactions on Mechatronics*, vol. 26, no. 4, pp. 2127–2138, aug 2021. [Online]. Available: <https://ieeexplore.ieee.org/document/9234107/>
- [77] C.-W. Chen, S. Rai, and T.-C. Tsao, "Iterative Learning of Dynamic Inverse Filters for Feedforward Tracking Control," *IEEE/ASME Transactions on Mechatronics*, vol. 25, no. 1, pp. 349–359, feb 2020. [Online]. Available: <https://ieeexplore.ieee.org/document/8890676/>
- [78] C. Wang, M. Zheng, Z. Wang, C. Peng, and M. Tomizuka, "Robust Iterative Learning Control for Vibration Suppression of Industrial Robot Manipulators," *Journal of Dynamic Systems, Measurement, and Control*, vol. 140, no. 1, pp. 1–9, jan 2018. [Online]. Available: <https://asmedigitalcollection.asme.org/dynamicsystems/article/doi/10.1115/1.4037265/371525/Robust-Iterative-Learning-Control-for-Vibration>
- [79] W. Ohnishi, N. Strijbosch, and T. Oomen, "Multirate State Tracking for Improving Intersample Behavior in Iterative Learning Control," in *2021 IEEE International*

- Conference on Mechatronics (ICM)*, no. 2. IEEE, mar 2021, pp. 01–06. [Online]. Available: <https://ieeexplore.ieee.org/document/9385661/>
- [80] M. Boerlage, “MIMO jerk derivative feedforward for motion systems,” in *2006 American Control Conference*, vol. 2006. IEEE, 2006, p. 6 pp. [Online]. Available: <http://ieeexplore.ieee.org/document/1657326/>
- [81] S. H. van der Meulen, R. L. Tousain, and O. H. Bosgra, “Fixed Structure Feedforward Controller Design Exploiting Iterative Trials: Application to a Wafer Stage and a Desktop Printer,” *Journal of Dynamic Systems, Measurement, and Control*, vol. 130, no. 5, pp. 0510061–05100616, sep 2008. [Online]. Available: <https://asmedigitalcollection.asme.org/dynamicsystems/article/doi/10.1115/1.2957626/466539/Fixed-Structure-Feedforward-Controller-Design>
- [82] T. Atsumi, “Emerging Technology for Head-Positioning System in HDDs,” *IEEJ Journal of Industry Applications*, vol. 5, no. 2, pp. 117–122, 2016. [Online]. Available: [https://www.jstage.jst.go.jp/article/ieejjia/5/2/5\\_117/\\_article](https://www.jstage.jst.go.jp/article/ieejjia/5/2/5_117/_article)
- [83] K. Ohno and T. Hara, “Adaptive resonant mode compensation for hard disk drives,” *IEEE Transactions on Industrial Electronics*, vol. 53, no. 2, pp. 624–630, apr 2006. [Online]. Available: <http://ieeexplore.ieee.org/document/1614146/>
- [84] N. O. Pérez-Arancibia, T.-C. Tsao, and J. S. Gibson, “A new method for synthesizing multiple-period adaptive–repetitive controllers and its application to the control of hard disk drives,” *Automatica*, vol. 46, no. 7, pp. 1186–1195, jul 2010. [Online]. Available: <http://dx.doi.org/10.1016/j.automatica.2010.04.007>
- [85] B. Shahsavari, E. Keikha, Fu Zhang, and R. Horowitz, “Adaptive Repetitive Control Design With Online Secondary Path Modeling and Application to Bit-Patterned Media Recording,” *IEEE Transactions on Magnetics*, vol. 51, no. 4, pp. 1–8, apr 2015. [Online]. Available: <http://ieeexplore.ieee.org/document/7109979/>
- [86] L. Sun, T. Jiang, and X. Chen, “Adaptive Loop Shaping for Wideband Disturbances Attenuation in Precision Information Storage Systems,” *IEEE Transactions on Magnetics*, vol. 53, no. 5, pp. 1–13, may 2017. [Online]. Available: <http://ieeexplore.ieee.org/document/7820197/>
- [87] T. Atsumi, A. Okuyama, and M. Kobayashi, “Track-Following Control Using Resonant Filter in Hard Disk Drives,” *IEEE/ASME Transactions on Mechatronics*, vol. 12, no. 4, pp. 472–479, aug 2007. [Online]. Available: <http://ieeexplore.ieee.org/document/4291569/>
- [88] H. Fujimoto, “RRO Compensation of Hard Disk Drives With Multirate Repetitive Perfect Tracking Control,” *IEEE Transactions on Industrial Electronics*, vol. 56, no. 10, pp. 3825–3831, oct 2009. [Online]. Available: <http://ieeexplore.ieee.org/document/4804798/>
- [89] X. Chen and M. Tomizuka, “New Repetitive Control With Improved Steady-State Performance and Accelerated Transient,” *IEEE Transactions on Control Systems Technology*, vol. 22, no. 2, pp. 664–675, mar 2014. [Online]. Available: <http://ieeexplore.ieee.org/document/6508823/>



- [90] X. Chen and M. Tomizuka, “Discrete-Time Reduced-Complexity Youla Parameterization for Dual-Input Single-Output Systems,” *IEEE Transactions on Control Systems Technology*, vol. 24, no. 1, pp. 302–309, jan 2016. [Online]. Available: <http://ieeexplore.ieee.org/document/7102697/>
- [91] M. Zheng, S. Zhou, and M. Tomizuka, “A design methodology for disturbance observer with application to precision motion control: An H-infinity based approach,” in *2017 American Control Conference (ACC)*. IEEE, may 2017, pp. 3524–3529. [Online]. Available: <https://ieeexplore.ieee.org/document/7963492/>
- [92] S. Yabui, T. Atsumi, and T. Inoue, “Coupling Controller Design for MISO System of Head Positioning Control Systems in HDDs,” *IEEE Transactions on Magnetics*, vol. 56, no. 5, pp. 1–9, may 2020. [Online]. Available: <https://ieeexplore.ieee.org/document/9025239/>
- [93] S. Bashash and S. Shariat, “Performance enhancement of hard disk drives through data-driven control design and population clustering,” *Precision Engineering*, vol. 56, no. November 2018, pp. 267–279, mar 2019. [Online]. Available: <https://linkinghub.elsevier.com/retrieve/pii/S0141635918305877>
- [94] N. Potu Surya Prakash and R. Horowitz, “Data-Driven Robust Feedback Control Design for Multi-Actuator Hard Disk Drives,” in *2nd IFAC Modeling, Estimation and Control Conference*, 2022.
- [95] T. Atsumi, “Magnetic-head positioning control system in HDDs,” 2022. [Online]. Available: <https://jp.mathworks.com/matlabcentral/fileexchange/111515>
- [96] J. Lofberg, “YALMIP : a toolbox for modeling and optimization in MATLAB,” in *2004 IEEE International Conference on Robotics and Automation (IEEE Cat. No.04CH37508)*. IEEE, 2004, pp. 284–289. [Online]. Available: <http://ieeexplore.ieee.org/document/1393890/>
- [97] Mosek, “MOSEK 9.3,” 2021. [Online]. Available: <https://www.mosek.com>
- [98] K. Sakata, H. Asaumi, K. Hirachi, K. Saiki, and H. Fujimoto, “Self Resonance Cancellation Techniques for a Two-Mass System and Its Application to a Large-Scale Stage,” *IEEJ Journal of Industry Applications*, vol. 3, no. 6, pp. 455–462, 2014. [Online]. Available: [https://www.jstage.jst.go.jp/article/ieejjia/3/6/3\\_455/\\_article](https://www.jstage.jst.go.jp/article/ieejjia/3/6/3_455/_article)
- [99] W. Ohnishi, H. Fujimoto, K. Sakata, K. Suzuki, and K. Saiki, “Design and control of 6-DOF high-precision scan stage with gravity canceller,” in *2014 American Control Conference*. IEEE, jun 2014, pp. 997–1002. [Online]. Available: <http://ieeexplore.ieee.org/document/6859023/>
- [100] N. Dirx, J. van de Wijdeven, and T. Oomen, “Frequency Response Function identification for multivariable motion control: Optimal experiment design with element-wise constraints,” *Mechatronics*, vol. 71, no. June, p. 102440, nov 2020. [Online]. Available: <https://linkinghub.elsevier.com/retrieve/pii/S0957415820301100>
- [101] K. Tang, Kim Fung Man, Guanrong Chen, and S. Kwong, “An optimal fuzzy PID controller,” *IEEE Transactions on Industrial Electronics*, vol. 48, no. 4, pp. 757–765, 2001. [Online]. Available: <http://ieeexplore.ieee.org/document/937407/>

- [102] S. Lee, N. Marsolan, T. Sun, S. Lee, and B. Kilian, "Application of Self-Optimizing Controllers to Variable Time-Delay Processes," in *Proceedings of the 1985 American Control Conference*, 1985, pp. 1275–1280.
- [103] Z.-L. Gaing, "A Particle Swarm Optimization Approach for Optimum Design of PID Controller in AVR System," *IEEE Transactions on Energy Conversion*, vol. 19, no. 2, pp. 384–391, jun 2004. [Online]. Available: <http://ieeexplore.ieee.org/document/1300705/>
- [104] A. Karimi and G. Galdos, "Fixed-order  $H_\infty$  controller design for nonparametric models by convex optimization," *Automatica*, vol. 46, no. 8, pp. 1388–1394, aug 2010. [Online]. Available: <https://linkinghub.elsevier.com/retrieve/pii/S0005109810002256>
- [105] T. M. T. Do and T. Artieres, "Regularized bundle methods for convex and non-convex risks," *Journal of Machine Learning Research*, vol. 13, pp. 3539–3583, 2012.
- [106] R. Kitayoshi and H. Fujimoto, "Automatic adjustment method of controller structure and parameter based on Structured  $H_\infty$  control," in *IECON 2019 - 45th Annual Conference of the IEEE Industrial Electronics Society*, 2019, pp. 3111–3116.
- [107] M. Hast, K. Astrom, B. Bernhardsson, and S. Boyd, "PID design by convex-concave optimization," in *2013 European Control Conference (ECC)*. IEEE, jul 2013, pp. 4460–4465. [Online]. Available: <https://ieeexplore.ieee.org/document/6669312/>
- [108] S. Shinoda, K. Yubai, D. Yashiro, and J. Hirai, "Multivariable Controller Design Achieving Diagonal Dominance Using Frequency Response Data," *Electronics and Communications in Japan*, vol. 100, no. 10, pp. 12–23, oct 2017. [Online]. Available: <https://onlinelibrary.wiley.com/doi/10.1002/ecj.11970>
- [109] W. Ohnishi, "Data-based feedback controller tuning utilizing collocated and non-collocated sensors," *IFAC-PapersOnLine*, vol. 52, no. 15, pp. 157–162, 2019. [Online]. Available: <https://linkinghub.elsevier.com/retrieve/pii/S2405896319316568>
- [110] M. Mae, W. Ohnishi, H. Fujimoto, K. Sakata, and A. Hara, "Peak Filter Tuning based on Disturbance Spectrum for MIMO High-Precision Scan Stage," *IFAC-PapersOnLine*, vol. 53, no. 2, pp. 8413–8418, 2020. [Online]. Available: <https://linkinghub.elsevier.com/retrieve/pii/S240589632032173X>
- [111] H. Fujimoto and Y. Hori, "Vibration suppression and optimal repetitive disturbance rejection control in semi-Nyquist frequency region using multirate sampling control," in *Proceedings of the 39th IEEE Conference on Decision and Control (Cat. No.00CH37187)*, vol. 4. IEEE, 2000, pp. 3745–3750. [Online]. Available: <http://ieeexplore.ieee.org/document/912292/>
- [112] H. Fujimoto and T. Takemura, "High-Precision Control of Ball-Screw-Driven Stage Based on Repetitive Control Using  $n$ -Times Learning Filter," *IEEE Transactions on Industrial Electronics*, vol. 61, no. 7, pp. 3694–3703, jul 2014. [Online]. Available: <https://ieeexplore.ieee.org/document/6661341/>
- [113] J. Zheng, G. Guo, Y. Wang, and W. Wong, "Optimal Narrow-Band Disturbance Filter for PZT-Actuated Head Positioning Control on a Spinstand," *IEEE Transactions*

- on *Magnetics*, vol. 42, no. 11, pp. 3745–3751, nov 2006. [Online]. Available: <http://ieeexplore.ieee.org/document/1715685/>
- [114] B. A. Francis and W. M. Wonham, “The internal model principle for linear multivariable regulators,” *Applied Mathematics & Optimization*, vol. 2, no. 2, pp. 170–194, jun 1975. [Online]. Available: <http://link.springer.com/10.1007/BF01447855>
- [115] T. Atsumi and W. C. Messner, “Optimization of Head-Positioning Control in a Hard Disk Drive Using the RNode Plot,” *IEEE Transactions on Industrial Electronics*, vol. 59, no. 1, pp. 521–529, jan 2012. [Online]. Available: <http://ieeexplore.ieee.org/document/5751673/>
- [116] Y. Maeda and M. Iwasaki, “Circle Condition-Based Feedback Controller Design for Fast and Precise Positioning,” *IEEE Transactions on Industrial Electronics*, vol. 61, no. 2, pp. 1113–1122, feb 2014. [Online]. Available: <http://ieeexplore.ieee.org/document/6494628/>
- [117] H. Rosenbrock, “Design of multivariable control systems using the inverse Nyquist array,” *Proceedings of the Institution of Electrical Engineers*, vol. 116, no. 11, p. 1929, 1969. [Online]. Available: <https://digital-library.theiet.org/content/journals/10.1049/piee.1969.0354>
- [118] M. Araki and O. Nwokah, “Bounds for closed-loop transfer functions of multivariable systems,” *IEEE Transactions on Automatic Control*, vol. 20, no. 5, pp. 666–670, oct 1975. [Online]. Available: <http://ieeexplore.ieee.org/document/1101051/>
- [119] N. Sebe, “Diagonal dominance and integrity,” in *Proceedings of 35th IEEE Conference on Decision and Control*, vol. 2, no. December. IEEE, 1996, pp. 1904–1909. [Online]. Available: <http://ieeexplore.ieee.org/document/572854/>
- [120] K. Nakamura, K. Yubai, D. Yashiro, and S. Komada, “Fully Parameterized Controller Design Method for High Control Bandwidth Using Frequency Response Data Sets,” in *The 3rd IEEJ international workshop on Sensing, Actuation, Motion Control, and Optimization (SAMCON 2017)*, 2017.
- [121] W. Ohnishi, H. Fujimoto, K. Sakata, K. Suzuki, and K. Saiki, “Decoupling Control Method for High-Precision Stages using Multiple Actuators considering the Misalignment among the Actuation Point, Center of Gravity, and Center of Rotation,” *IEEJ Journal of Industry Applications*, vol. 5, no. 2, pp. 141–147, 2016. [Online]. Available: [https://www.jstage.jst.go.jp/article/ieejjia/5/2/5\\_141/\\_article](https://www.jstage.jst.go.jp/article/ieejjia/5/2/5_141/_article)
- [122] W. R. Abdul-Adheem and I. K. Ibraheem, “Decoupled control scheme for output tracking of a general industrial nonlinear MIMO system using improved active disturbance rejection scheme,” *Alexandria Engineering Journal*, vol. 58, no. 4, pp. 1145–1156, dec 2019. [Online]. Available: <https://linkinghub.elsevier.com/retrieve/pii/S1110016819301024>



# Publications

## Journal Articles (peer-reviewed)

1. Masahiro Mae, Max van Haren, Koen Classens, Wataru Ohnishi, Tom Oomen, Hiroshi Fujimoto, “Fixed-structure sampled-data feedforward control for multivariable motion systems”, *submitted*.
2. Masahiro Mae, Wataru Ohnishi, Hiroshi Fujimoto, Koichi Sakata, “Multi-Axis Resonant Filter Design using Frequency Response Data applied to Industrial Scan Stage”, *submitted*.
3. Masahiro Mae, Wataru Ohnishi, Hiroshi Fujimoto, “Multirate feedforward control with mode decomposition for intersample performance in multivariable motion systems”, *submitted*.
4. Masahiro Mae, Wataru Ohnishi, Hiroshi Fujimoto, Koichi Sakata, Atsushi Hara, “Frequency response data-based peak filter design applied to MIMO large-scale high-precision scan stage”, *Mechatronics*, vol.83, pp.102733, May 2022.
5. Masahiro Mae, Wataru Ohnishi, Hiroshi Fujimoto, “MIMO multirate feedforward controller design with selection of input multiplicities and intersample behavior analysis”, *Mechatronics*, vol.71, pp.102442, November 2020.
6. Masahiro Mae, Wataru Ohnishi, Hiroshi Fujimoto, Yoichi Hori, “Perfect Tracking Control Considering Generalized Controllability Indices and Application for High-Precision Stage in Translation and Pitching”, *IEEJ Journal of Industry Applications*, vol.8, no.2, pp.263-270, March 2019.

## Co-authored Journal Articles (peer-reviewed)

1. Yuhiro Inagaki, Masahiro Mae, Osamu Shimizu, Sakahisa Nagai, Hiroshi Fujimoto, Takayuki Miyajima, Yoshiki Yasuda, Akio Yamagiwa, “Effect of Harmonic Current Suppression on Iron Loss of IPMSM Using Repetitive Perfect Tracking Control”, *IEEJ Journal of Industry Applications*, vol.11, no.2, pp.317-326, March 2022.
2. Shona Noguchi, Masahiro Mae, Hiroshi Fujimoto, “Quasi Multirate Feedforward Current Control toward Nyquist Frequency of PWM for SPMSM”, *IEEJ Journal of Industry Applications*, vol.10, no.4, pp.428-435, April 2021.

3. Tomonori Suzuki, Masahiro Mae, Takuma Takeuchi, Hiroshi Fujimoto, Etsuo Katsuyama, “Model-based Filter Design for Triple Skyhook Control of In-Wheel Motor Vehicles for Ride Comfort”, IEEJ Journal of Industry Applications, vol.10, no.3, pp.310-316, February 2021.

## Conference Proceedings (peer-reviewed)

1. Masahiro Mae, Wataru Ohnishi, Hiroshi Fujimoto, “Frequency Response Data-based Resonant Filter Design considering Phase Stabilization and Stroke Limitation applied to Dual-Stage Actuator Hard Disk Drives”, The 22nd IFAC World Congress, Yokohama, Japan, July 2023, *accepted*.
2. Masahiro Mae, Wataru Ohnishi, Hiroshi Fujimoto, “Review on Multirate Feedforward Control with Mode Decomposition for Intersample Performance in Multi-Modal Motion Systems”, The 9th IEEJ International Workshop on Sensing, Actuation, Motion Control, and Optimization, Nanjing, China, March 2023, *accepted*.
3. Masahiro Mae, Max van Haren, Wataru Ohnishi, Tom Oomen, Hiroshi Fujimoto, “Feedforward with Acceleration and Snap using Sampled-Data Differentiator for a Multi-Modal Motion System”, The 2nd Modeling, Estimation and Control Conference, MoBT6.4, Jersey City, USA, October 2022.
4. Masahiro Mae, Wataru Ohnishi, Hiroshi Fujimoto, Koichi Sakata, “Frequency Response Data-based Multiple Peak Filter Design Applied to High-Precision Stage in Translation and Pitching”, IEEE 17th International Conference on Advanced Motion Control, No.36, Padova, Italy, February 2022.
5. Masahiro Mae, Wataru Ohnishi, Hiroshi Fujimoto, “Multirate Feedforward Control based on Modal Form with Mode Selection Applied to Multi-Modal High-Precision Positioning Stage”, International Conference on Mechatronics 2021, SS7-4.2, Chiba, Japan, March 2021.
6. Masahiro Mae, Wataru Ohnishi, Hiroshi Fujimoto, Koichi Sakata, Atsushi Hara, “Peak Filter Tuning based on Disturbance Spectrum for MIMO High-Precision Scan Stage”, The 21st IFAC World Congress, Berlin, Germany, July 2020.
7. Masahiro Mae, Wataru Ohnishi, Hiroshi Fujimoto, “Intersample Behavior Analysis of MIMO Multirate Feedforward Control depending on Selection of Input Multiplicities”, The 8th IFAC Symposium on Mechatronic Systems, pp.566-571, Vienna, Austria, September 2019.
8. Masahiro Mae, Wataru Ohnishi, Hiroshi Fujimoto, “State Trajectory Generation for MIMO Multirate Feedforward using Singular Value Decomposition and Time Axis Reversal”, 2019 American Control Conference, pp.5693-5698, Philadelphia, USA, July 2019.
9. Masahiro Mae, Hiroshi Fujimoto, “State Trajectory Generation of MIMO Multirate Feedforward for Perfect Tracking Control in High-Precision Stage”, The 44th Annual Conference of the IEEE Industrial Electronics Society, pp.4612-4617, Washington D.C., USA, October 2018.

10. Masahiro Mae, Wataru Ohnishi, Hiroshi Fujimoto, Yoichi Hori, “Perfect Tracking Control of Dual-Input Dual-Output System for High-Precision Stage in Translation and Pitching Motion”, The 4th IEEJ International Workshop on Sensing, Actuation, Motion Control, and Optimization, TT6-5, Tokyo, Japan, March 2018.

## **Co-authored Conference Proceedings (peer-reviewed)**

1. Yuhiro Inagaki, Masahiro Mae, Osamu Shimizu, Sakahisa Nagai, Hiroshi Fujimoto, Takayuki Miyajima, Yoshiki Yasuda, Akio Yamagiwa, “Effect of Harmonic Current Control of IPMSMs by Repetitive Perfect Tracking Control on Torque Ripple and Iron Loss”, The 8th IEEJ International Workshop on Sensing, Actuation, Motion Control, and Optimization, P2.7, pp.379-384, Saitama, Japan, March 2022.
2. Yuhiro Inagaki, Masahiro Mae, Osamu Shimizu, Sakahisa Nagai, Hiroshi Fujimoto, Takayuki Miyajima, Yoshiki Yasuda, Akio Yamagiwa, “Basic Study on Effect of Repetitive Perfect Tracking Control on Iron Loss of IPMSM”, The 7th IEEJ International Workshop on Sensing, Actuation, Motion Control, and Optimization, P1-8, pp.296-301, Chiba, Japan, March 2021.
3. Shona Noguchi, Masahiro Mae, Hiroshi Fujimoto, “High-Bandwidth Current Control of PMSM Based on Quasi Multirate Feedforward Control”, The 6th IEEJ International Workshop on Sensing, Actuation, Motion Control, and Optimization, P-9, Tokyo, Japan, March 2020.

## **Conference Presentations**

1. Masahiro Mae, Wataru Ohnishi, Hiroshi Fujimoto, Koichi Sakata, Atsushi Hara, “Frequency Response Data-based Peak Filter Design Applied to MIMO Large-Scale High-Precision Scan Stage”, The 9th IFAC Symposium on Mechatronic Systems, No. 181, Los Angeles, USA, September 2022.
2. Masahiro Mae, Max van Haren, Wataru Ohnishi, Tom Oomen, Hiroshi Fujimoto, “Improving Intersample Performance with Linearly Parameterized Feedforward using Sampled-Data Differentiator”, The 9th IFAC Symposium on Mechatronic Systems, No. 180, Los Angeles, USA, September 2022.
3. Masahiro Mae, Max van Haren, Wataru Ohnishi, Tom Oomen, Hiroshi Fujimoto, “Flexible learning with prior knowledge: iterative learning control with sampled-data characterized basis functions”, Benelux Meeting on Systems and Control 2022, WeE04-5, Brussels, Belgium, July 2022.
4. Masahiro Mae, Max van Haren, Wataru Ohnishi, Tom Oomen, Hiroshi Fujimoto, “Feedforward of Sampled-Data System for High-Precision Motion Control using Basis Functions with ZOH Differentiator”, 2022 American Control Conference, ThCP.3, Atlanta, USA, June 2022.

5. Yuhiro Inagaki, Masahiro Mae, Osamu Shimizu, Sakahisa Nagai, Hiroshi Fujimoto, Takayuki Miyajima, Yoshiki Yasuda, Akio Yamagiwa, “Effect of Harmonic Current Suppression on Iron Loss of IPMSM Using Repetitive Perfect Tracking Control”, 2022 International Power Electronics Conference, 16C1-2, Himeji, Japan, May 2022.
6. Tomonori Suzuki, Masahiro Mae, Takuma Takeuchi, Hiroshi Fujimoto, Etsuo Katsuyama, “Model-based Filter Design for Triple Skyhook Control of In-Wheel Motor Vehicles for Ride Comfort”, The 7th IEEJ International Workshop on Sensing, Actuation, Motion Control, and Optimization, JIA to SAMCON 2021, Chiba, Japan, March 2021.

## Conference Proceedings (Japanese)

1. 前 匡鴻, 大西 亘, 藤本 博志, “2段アクチュエータHDDベンチマーク問題における外乱抑圧のための周波数応答データ駆動型共振フィルタ設計”, 2022年メカトロニクス制御研究会「精密サーボシステムと制御技術」, MEC-22-005, pp25-30, 東京, 2022年9月
2. 前 匡鴻, 大西 亘, 藤本 博志, “高次共振系に対する積と和の分解を用いたマルチレートフィードフォワード制御の比較検討”, 2021年メカトロニクス制御研究会「精密サーボシステムと制御技術」, MEC-21-004, pp19-24, オンライン, 2021年9月
3. 前 匡鴻, 大西 亘, 藤本 博志, “2慣性系に対するモード正準形に基づくマルチレートフィードフォワード制御における指令値に合わせたモード選択の検討”, 2020年メカトロニクス制御研究会「モーションコントロール, 精密サーボ, 実世界ハプティクス」, MEC-20-040, pp105-110, オンライン, 2020年12月
4. 前 匡鴻, 大西 亘, 藤本 博志, “2慣性系の駆動側と負荷側の制御入力および状態変数に着目した多入力多出力系に対するマルチレートフィードフォワード制御”, 2019年メカトロニクス制御研究会「精密サーボシステムと制御技術」, MEC-19-011, pp61-66, 東京, 2019年9月
5. 前 匡鴻, 大西 亘, 藤本 博志, “多入力多出力系に対する完全追従制御における特異値分解を用いた状態変数軌道生成”, 2018年メカトロニクス制御研究会「精密サーボシステムと制御技術」, MEC-18-014, pp.71-76, 東京, 2018年9月

## Magazines

1. 藤本 博志, 前 匡鴻, “電気学会技術報告 第1485号 精密サーボシステムにおける共通基盤技術 4.1 多入力多出力系に対するマルチレートフィードフォワード制御”, 一般社団法人 電気学会 産業応用部門 メカトロニクス制御研究会, 2020年6月

## Awards

1. 前 匡鴻, “2021年産業応用部門研究会優秀論文発表賞本部表彰”, 一般社団法人電気学会産業応用部門, 2022/03/31



2. 前 匡鴻, “メカトロニクス制御技術委員会優秀論文発表賞”, 一般社団法人電気学会産業応用部門メカトロニクス制御技術委員会, 2022/01/06
3. 前 匡鴻, “2019年産業応用部門研究会優秀論文発表賞部門表彰”, 一般社団法人電気学会産業応用部門, 2020/03/31
4. 前 匡鴻, “先端エネルギー工学優秀賞”, 東京大学大学院新領域創成科学研究科先端エネルギー工学専攻, 2020/03/23
5. 前 匡鴻, “メカトロニクス制御技術委員会優秀論文発表賞”, 一般社団法人電気学会産業応用部門メカトロニクス制御技術委員会, 2020/01/10
6. Masahiro Mae, “Finalist of the IFAC Mechatronics 2019 Young Author Award”, The International Federation of Automatic Control, 2019/09/05
7. 前 匡鴻, “令和元年度原島博学術奨励賞”, 公益財団法人電気電子情報学術振興財団, 2019/06/25
8. 前 匡鴻, “電気学会東京支部電気学術奨励賞”, 一般社団法人電気学会東京支部, 2018/03/31
9. 前 匡鴻, “平成29年度優秀卒業論文賞”, 東京大学工学部電気電子工学科, 2018/03/23



# Abstract 概要

## Multivariable High-Precision Motion Control with Structured Modeling and Data-Driven Convex Optimization

(構造的モデル化とデータ駆動凸最適化による  
多変数超精密位置決め制御)

精密位置決め制御は、半導体や液晶パネルを製造する露光装置、工作機械、産業用ロボット、ハードディスクドライブなどの産業装置に欠かせない技術である。社会を支える産業装置の高性能化は、我々の豊かな生活に直結している。高性能化の要求に伴い、制御対象の複数共振モードや複数入出力を考慮した制御手法が必要不可欠であるが、従来の制御手法では複数共振モードを無視した剛体系に基づく制御や、複数入出力を無視した単入出力系の制御が用いられることが多く、制御性能を悪化させる要因となっていた。

本論文では、複数共振モードや複数入出力といった多変数系のダイナミクスを考慮した精密位置決め制御手法を提案した。多変数系を構造的にモデル化することにより、制御対象や設計される制御器のダイナミクスを見通し良くエンジニアが解釈できる形に定式化する。また、多変数系の制御器に対して凸最適化を用いたデータ駆動の制御器設計手法を用いることで、多数の制御器パラメータの調整の難しさを解消する。これらの制御手法を、精密位置決めステージ、2慣性系モータベンチ、ビーム型装置、ハードディスクドライブなどの実システムに応用し、計算機シミュレーションおよび実験を通じて有効性を明らかにした。

本論文の内容と構成は以下のようになっている。

第I部において、第1章で高性能化するメカトロニクス制御装置の産業応用における要求と課題を明らかにした。産業界のメカトロニクス制御装置における先進的な精密位置決め制御の性能要求は年々高まっており、高性能化のために複雑化した制御装置の多くは、剛体以上の自由度を持つ複数モード系や、複数の入出力を持つ多入力多出力系であるため、それらのダイナミクスや冗長性を考慮した制御器設計が必要である。このような背景を踏まえ、多変数系の精密位置決め制御において冗長性を有効活用することで高い制御性能を実現し、モデルベース制御器設計で培われた物理的な意味づけをデータ駆動制御器設計の枠組みに拡張することを本論文の目標とした。本論文の前半（第2・3・4・5章）では、マルチレートフィードフォワード制御を用いた連続時間軌道追従性能の改善を複数モード系や多入力多出力系に対する枠組みに拡張し、より高い制御性能を実現することを目標とした。本論文の後半

(第4・5・6・7章)では、多変数系のような複雑でモデル化に手間のかかる制御対象に対して、設計後の物理的解釈が可能なエンジニアに優しい制御器の設計手法をデータ駆動凸最適化で実現することを目標とした。

第II部において、制御対象の状態変数に追従させることにより連続時間軌道追従性能を改善するマルチレートフィードフォワード制御器を、複数モード系や多入力多出力系といった冗長性を持つ制御対象のモデルに基づいて設計する手法を提案した。

第2章で、マルチレートフィードフォワード制御を複数モード系に拡張する具体的な手法を示した。複数モード系のマルチレートフィードフォワード制御では、複数モード系の冗長性や連続時間の零点のダイナミクスを考慮した制御器設計が必要となる。まず、マルチレートフィードフォワード制御で用いる状態変数軌道生成を、多入力多出力系の一般的な枠組みに拡張した。加えて、和と積の2種類のモード分解により、複数モード系の冗長性を有効に活用したマルチレートフィードフォワード制御器を設計し、連続時間軌道追従性能を改善した。複数の共振モードを持つ精密位置決めステージを制御対象とした検証により、指令値や制御対象に合わせた制御器設計指針を示した。

第3章で、マルチレートフィードフォワード制御を多入力多出力系に拡張する具体的な手法を示した。多入力多出力系のマルチレートフィードフォワード制御の課題として、複数の入力ごとに用いるサンプリング周期の選び方に冗長性が存在することがある。そこで、マルチレートフィードフォワード制御の多入力多出力系への拡張のために、一般化可制御性指数の選び方における可制御性の強さを指標とした、制御対象のダイナミクスに合わせた適切な入力サンプリング周期の選び方を提案した。2慣性系モータベンチと6軸の精密位置決めステージで検証を行い、入力サンプリング周期の適切な選び方による制御性能の改善を確認した。

第III部において、従来はモデルに基づいて設計されてきた状態追従型サンプル値フィードフォワード制御器をデータ駆動で設計する枠組みを提案した。

第4章で、調整パラメータに対して線形なフィードフォワード制御器において、サンプル値制御に基づいた微分器を導入することにより、連続時間軌道追従性能を改善する手法を提案した。従来のマルチレートフィードフォワード制御器は、制御対象のモデルの逆系として設計されるため、実験装置に合わせたパラメータの直感的な調整、実験データを用いたパラメータの更新が困難であった。そこで、状態追従型サンプル値フィードフォワード制御をデータ駆動化するために、パラメータに線形な構造のフィードフォワード制御器を提案した。基底関数型フィードフォワード制御の枠組みを取り入れることにより、調整パラメータに線形な形でフィードフォワード制御器を定式化した。零次ホールドのダイナミクスを考慮したサンプル値微分器を導入することにより、連続時間応答を考慮した離散時間の基底関数を設計した。2慣性系モータベンチにおける検証により、従来の零次ホールドのダイナミクスを考慮しない基底関数型フィードフォワード制御器よりも制御性能が改善することを確認した。

第5章で、第4章で提案した調整パラメータに対して線形なサンプル値フィードフォワード制御器を、多入力多出力系の複数モード系においてパラメータの物理的解釈が可能な形で定式化し、反復学習制御を用いてパラメータをデータ駆動で更新する手法を提案した。多入力多出力系のフィードフォワード制御器設計において、干渉を考慮するためには多入力多出力系のモデルが必要となるが、静的な非干渉化を行った後の干渉成分のモデリングは物理的解釈も難しく、グレーボックスモデリングにおいてもパラメータ同定が非常に難しいことが問題とされていた。そこで、多入力多出力の複数モード系に対する構造化されたフィードフォワード制御を用いることで、位置決め制御において支配的な低周波数の誤差に着目し、調整パラメータが物理的に解釈

可能な形でフィードフォワード制御器を定式化した。反復学習制御により、モデリングの難しい多入力多出力系に対するフィードフォワード制御器のパラメータを、実験データと対角の剛体モデルのみから反復的に更新し誤差を最小化した。ビーム型装置における検証により、干渉を考慮しない従来のフィードフォワード制御器と比較して制御性能が改善することを確認した。

第IV部において、精密位置決め制御対象の外乱抑圧のために、制御対象のパラメトリックモデルを必要とせず周波数応答データを直接用いて構造的なフィードバック制御器を凸最適化により自動設計する手法を提案した。

第6章で、ロバスト性能に主眼をおいた外乱抑圧のための制御器設計問題に対して、周波数応答データを直接用いて凸最適化する手法を提案した。従来のフィードバック制御器自動設計において、誤差の改善を直接目的関数として定式化した例は多くは見られなかった。外乱抑圧性能をより向上させるためには、制御対象の複数の変動モデル、複数周波数の外乱に対処するフィードバック制御器を設計する必要がある。そこで、複数の外乱周波数に合わせたフィードバック制御器を、制御器の構造を保ったまま調整パラメータに線形な形で定式化した。制御対象と外乱の周波数応答データを直接用いることで、誤差の改善を目的関数とした制御器設計問題を定式化し、逐次線形化により凸最適化の繰り返し計算として求解した。ハードディスクドライブのベンチマーク問題における検証により、外乱が抑圧され誤差が改善することを確認した。

第7章で、ロバスト安定性に主眼をおいた外乱抑圧のための制御器設計問題に対して、周波数応答データを直接用いて凸最適化する手法を提案した。露光装置の精密位置決めステージの外乱抑圧のためのフィードバック制御器設計は、多入力多出力の制御対象のパラメトリックモデルを同定する難しさと、フィードバック制御器設計において干渉を考慮してロバスト安定な制御器を設計する難しさを持つ。特定周波数への外乱抑圧は、その周波数で制御器がハイゲイン化することから、多入力多出力系におけるロバスト安定性の保証と実際の装置への実装に課題があった。そこで、多入力多出力系の軸間の干渉を考慮した周波数応答データを直接用いたロバスト制御器設計問題を定式化し、逐次線形化により凸最適化の繰り返し計算として求解した。実際に産業界で使用されている商用の液晶露光装置の精密位置決めステージにおける検証により、自動設計したフィードバック制御器の実装に成功し、誤差の改善を確認した。

第V部において、第8章でまとめとして本論文を振り返り、本論文を通じた研究成果と研究分野における位置づけを述べた。本論文は、多変数系の精密位置決め制御における制御性能と実用性の両立を目標として、「物理的解釈の可能な従来のモデルベースの制御器設計」と「制御性能のさらなる向上とモデリングコストの低減を目的としたデータ駆動制御器設計」の両面を組み合わせた、多変数の精密位置決め制御系のための制御器設計の枠組みを提案し、実際の実験装置による性能検証を行った。理論と実験によりその有効性を示した本論文は、学术界と産業界のどちらにも資する価値を生み出し、その重要性は今後も高まるものであると言える。

なお、本文は英語により記述されていることを付記する。



# Acknowledgment 謝辞

本研究を進めるにあたり、多くの方々に大変お世話になりました。

まず始めに、指導教員として普段から熱心なご指導と的確なご助言を頂いた藤本博志教授に深く感謝申し上げます。忙しい中でも学生と向き合うことを忘れない藤本先生の姿勢に惚れて研究室の一員となり、学部課程から修士課程を経て博士課程まで指導して頂いたことを誇りに思います。現在は東京理科大学で教鞭をとられている堀洋一教授には、2021年3月に東京大学を定年退職されるまで研究室発表会等の場でご指導頂き心から感謝しております。学部3年生のときに履修した堀先生の担当されていた制御工学第一の講義で制御工学の面白さに魅せられた後も、研究者としての姿勢はもちろん、人との関わり方や人生論など、堀先生から学んだ多くの考え方は、今も私の生きる道標となっております。大西亘講師には、私が学部4年生として卒業研究で堀・藤本研究室に配属された1年目は博士3年生の学生として、その後は教員として沢山の議論をさせて頂き、ありがとうございました。研究生活の楽しさやその先に広がる可能性を大西先生に身近で見せて頂いたおかげで、自分なりに挑戦を続けることができました。私の博士論文審査にご参加頂き、多くの鋭いご指摘やご助言を頂きました古関隆章教授、橋本樹明教授、坂井真一郎教授に熱く御礼申し上げます。審査員の先生方に、多角的視点からご意見頂いたことで、私の博士論文はより充実したものとなりました。

共同研究において、株式会社ニコンの坂田晃一様、原篤史様に大変お世話になりました。極限性能を引き出すために制御工学を産業装置へ応用することの難しさと面白さを同時に経験することができました。電気学会の精密サーボ委員会には幹事補佐として関わらせて頂き、熱海武憲教授、藪井将太准教授に大変お世話になりました。先生方の持つ産業界と学術界の両方の経験談から、それらを繋ぐことの重要性和難しさなど多くのことを学ばせて頂きました。

I would appreciate Prof. Tom Oomen for the fantastic collaboration during my research stay at Eindhoven University of Technology, the Netherlands from October 2021 to July 2022. I also want to thank the office mates in gemz -1.138, Max van Haren, Noud Mooren, Nard Strijbosch, and Nic Dirkx. I have a great memory of the office dinner, lab trips, and a lot of fun talking during the coffee break and lunch walk with CST and D&C members at TU/e every day. Dank je wel!

研究室のメンバーには6年間大変お世話になりました。研究室の先生方である、清水修特任講師、藤田稔之特任講師、永井栄寿特任助教、グエンビンミン特任助教、山田翔太特任助教には、日頃の発表会での指摘はもちろん、研究プロジェクトを進めていく姿勢や博士課程の過ごし方など多くのことを学ばせて頂きました。研究室の秘書の方々には、オランダでの研究滞在や国際学会参加のために多くの海外出張をするにあたり、大変お世話になりました。同じ時間を博士課程で過ごした皆様と苦楽を分かち合えたおかげで、多くの困難を乗り越えることができました。特に、研究室同期の林拓巳さん、古関・大西研究室の三好正太さんを始めとするEEIC2016の博士課程同期

の存在のおかげで、COVID-19による生活の変化や実験TAの準備、博士論文の執筆など、大変な時期であっても研究を続けることができました。研究室の社会人博士の北吉良平さん、角谷勇人さん、柳達也さんには、学生と会社員の双方の立場を理解した多くのアドバイスを頂き、研究や人生相談など、多くの部分で助けて頂きました。布施空由さんは、学部の頃から1学年上の先輩として背中から多くのことを学ばせて頂きました。後輩の松本諒さんは、私が留学中、そして博士3年になってから研究室内の博士課程の役割を引き継いで研究室運営の柱となって来て頼もしい限りです。私が博士課程の間に修士課程を修了した鈴木智順さん、野口生那さん、稲垣由寛さんとは、共著で論文誌に研究結果をまとめることができ、後輩を指導する難しさや、一緒に研究を進める喜びを経験する事ができました。また、ここには書ききれませんが、研究室の先輩、同期、後輩の全員が、日々の研究に関する議論はもちろん、研究以外の他愛もない時間も含めて、毎日充実した研究生活を送るためには欠かせない存在でした。

博士課程における経済的援助として、特別研究員をさせて頂いた日本学術振興会、リサーチアシスタントをさせて頂いた東京大学大学院工学系研究科、株式会社ニコン、ダイキン工業株式会社、株式会社安川電機に熱く御礼申し上げます。また、本研究の一部は科研費（21J13196）の助成を受けたものであることを付記します。

最後に、学ぶ機会を与えて頂き、故郷の広島から暖かく応援してくれた両親に心から感謝申し上げます。

December 2022  
Masahiro Mae



# Curriculum Vitae

Masahiro Mae was born on July 7, 1995, in Hiroshima, Japan. After finishing his secondary education at Hiroshima University High School in Hiroshima, Japan, in 2014, he studied at the Department of Electrical and Electronic Engineering, Faculty of Engineering, The University of Tokyo, Japan, and received his Bachelor of Engineering degree in 2018 under the supervision of Prof. Yoichi Horii and Prof. Hiroshi Fujimoto. He continued researching at the Department of Advanced Energy, Graduate School of Frontier Sciences, The University of Tokyo, Japan, and received his Master of Science degree in 2020 under the supervision of Prof. Hiroshi Fujimoto. From August 2018 to September 2018, he was a visiting researcher at Technische Universität Ilmenau, Germany, collaborating with Prof. Johann Reger.



In April 2020, Masahiro Mae started his Ph.D. research at the Department of Electrical Engineering and Information Systems, Graduate School of Engineering, The University of Tokyo, Japan, under the supervision of Prof. Hiroshi Fujimoto. From October 2021 to July 2022, he was a visiting researcher at Eindhoven University of Technology, Netherlands, collaborating with Prof. Tom Oomen. The main results of his research are included in this thesis and focus on multivariable high-precision motion control for mechatronic systems in industrial applications. He was also a Research Fellow of Japan Society for the Promotion of Science from April 2021 to March 2023. This work was partly supported by JSPS KAKENHI Grant Number 21J13196.





